Functional Heterointerfaces via Electromodulation Spectroscopy

Siong-Hee Khong

A dissertation submitted for the degree of Doctor of Philosophy

June 2010

University of Cambridge, Trinity Hall

To Dr. Daisaku Ikeda
In Commemoration of My Mentor's 290th Academic Awards

To Stephanie Rou Huey Tang
For safekeeping my sanity

ABSTRACT

Functional heterojunctions in organic electronic devices are interfaces formed either between a conducting electrode and an organic semiconductor or between two different organic semiconductors in blended and multilayered structures. This thesis is primarily concerned with the energy level alignment and the interfacial electronic structures at functional heterojunctions encountered in electronic devices made with solution-processable semiconducting polymers. Investigations on the electronic structures across these heterointerfaces are performed with the combined use of electromodulation and photoemission spectroscopic techniques.

Electromodulation and ultraviolet photoemission spectroscopic techniques enable direct determination of the surface work functions of electrodes at the electrode/semiconducting polymer interfaces. We overcame the inherent problems faced by electromodulation spectroscopy, which undermine accurate determination of interfacial electronic structures, by performing electroabsorption (EA) measurements at reduced temperatures. We showed in this thesis that low-temperature EA spectroscopy is a surface sensitive technique that can determine the interface electronic structures in electrode/polymer semiconductor/electrode diodes. Using this technique, we demonstrated that the energy level alignments in these solution-processed organic electronic devices are determined by the surface work functions of passivated metals rather than by those of clean metals encountered in ultrahigh vacuum.

This thesis also discloses our studies on the electronic structures in polymeric diodes with type II donor-acceptor heterojunctions using the EA spectroscopy. We showed that minimising meausurement temperature and attenuating EA illumination intensity enable accurate determinations of the electronic structures in these devices. We demonstrated that the electronic structures and the performance characteristics of multilayered polymer light-emitting diodes are determined by the surface work functions of passivated metals. Our investigations also confirmed that electronic doping of the organic active layers, rather than minimisation of the Schottky barriers at electrode/polymer contacts, holds the key in realising high-performance organic light-emitting devices.

PREFACE

Except where specific reference is made to the involvement of others, the material contained in this dissertation is original and is the result of my own work. This dissertation has not been omitted in whole or in part for the award of a degree at this or any other university and does not exceed 60,000 words in length.

Siong-Hee Khong
February 2010

CONTENT

CHAPTER 4   Electroabsorption Studies on Single-Layer Polymer Diodes

CHAPTER 1

Interfacial Energetics in Organic Electronic Devices

1.1   Semiconducting Conjugated Polymers

Polymers have traditionally been known to be insulating materials and are commonly used in numerous applications e.g. as electrical wire insulation or insulating interlayer in capacitors. Such conventional understanding of the electronic properties of polymers has been overturned by the landmark discovery of doped poly(acetylene) *[1]* that exhibits metallic conductivity *[2]*. But it was not until the pioneering discovery of semiconducting characteristics and electroluminescence (EL) from poly(p-phenylenevinylene) (PPV) *[3]* in Cambridge that polymer electronics attracted strong interest from the scientific community.

Amongst the key properties that contribute to strong attention on conjugated polymers is their solution processability. This unique property enables easy, cheap fabrication of polymer-based light-emitting diodes (PLEDs) *[4]*, photovoltaic cells *[5-7]* and field-effect transistors in open air *[8-10]* over large areas. Important progress in device fabrication technologies *[4, 8-14]* has been achieved over the last two decades.

Like fluorescent organic small molecules *[15]*, conjugated polymers are composed of sp^2 – hybridised carbon atoms that are often assembled in cyclic structures. Electronic wave functions in sp^2 orbitals are highly localised in σ bond formations with adjacent carbon atoms and do not contribute to electrical conductivity of the material. But the unhybridised p_z orbitals of neighbouring carbon atoms, which are orthogonal to sp^2 orbitals, laterally overlap with each other to form an extended π-system with a filled valence band along the polymer chain. In the case of trans-poly(acetylene) with alternating sequences of carbon-carbon single and double bonds, π-electrons are delocalised along the direction of the polymer chains. This gives rise to the macroscopically observed electrical conductivity of trans-poly(acetylene). But the π bonds inhibit rotations around the C-C axis and contribute to the high rigidity of the polymer chains.

This latter property favors ordered packing of the polymer chains over extended distance and leads to highly crystalline materials of low solvation entropy, which is commonly observed for most conducting polymers.

To increase the solvation entropies and hence solubilities of conjugated polymers in organic solvents, extended hydrocarbon side chains are grafted onto their backbones to disrupt the crystalline packing of the materials. Side chain grafting also modifies the π-π^* energy gaps of the polymers *[16]* through modifying the chemical structures of the materials. As the π-π^* gap critically affects optical and electronic properties of the materials, structural modification of the conjugated polymers opens up opportunities for tuning the π-π^* energy gaps of materials. Indeed advances in organic chemical synthesis *[17]* have produced a wide range of materials with different luminescent properties and energy gaps ranging from 1 eV to 4 eV (see ref. *[4]* for a comprehensive review of electroluminiscent conjugated polymers).

Unlike band-like, crystalline inorganic semiconductors, the electronic properties of conjugated polymers cannot be described using Bloch's wave function of the electronic states due to absence of long or medium range structural order. Since conjugated polymers are molecular solids comprising weakly interacting polymer chains (via van der Waals forces), it is useful to consider the evolution of electronic structure when two and more carbon atoms approach each other. When carbon atoms come together to form a molecular solid, the electronic structure resembles that shown in Fig 1.1. The lateral overlap of adjacent p_z orbitals results in an energy spread of both the bonding and anti-bonding electronic wavefunctions. By occupying the quasi-continuous valence "band" in the system, the π-electrons are delocalised along the polymer chain. Owing to the weak van der Waals interchain interactions, the electronic structure of a conjugated polymer largely preserves that of a molecule or a single chain.

To reflect their correspondence with the molecular state, the top of the occupied valence band (E_v) and the bottom of the unoccupied conduction band (E_c) are often denoted as the highest occupied molecular orbital (HOMO) and the lowest unoccupied molecular orbital (LUMO), respectively [see Fig. 1.1]. As in the case of a molecule, the ionisation energy (I_p) and electron

affinity (χ_s) of an organic molecular solid are defined as the energy separation of the HOMO and the LUMO from the vacuum level, respectively. Nevertheless the concept of Fermi level is valid as the π-electrons in conjugated polymers fill the energy levels following the Fermi statistics.

It must be emphasised that the conventional band diagram is problematic in describing the electronic properties of organic semiconductors (OSCs). One of the complications that interfere with the energy-band description of OSCs is that electrons and excitons are much more strongly bound [18] and localised than those in inorganic semiconductors. As polymer OSCs have low dielectric constants (typical values ~ 3 – 4 [19]), the excitonic states resemble Frenkel-excitons that are strongly bound and localised instead of the delocalised Wannier-excitons. Furthermore effective conjugation lengths of polymer OSCs rarely extend across the entire chain but only along several monomer units since the overlapping of the p_z orbital is often disrupted by structural imperfections (owing to chemical impurities from polymer synthesis) and conformational kinks [20].

The large difference of conjugation lengths also leads to inhomogeneous broadening of the HOMO-LUMO gap, which is reflected in broadened absorption and emission spectra. Another characteristic of polymer OSCs is the strong coupling between electronic charge carriers and molecular geometries of the material, which gives rise to pronounced polaronic characters of charge carriers in the polymers. This latter feature has important implications to the electronic properties of polymer OSCs and will be discussed in detail in subsequent sections.
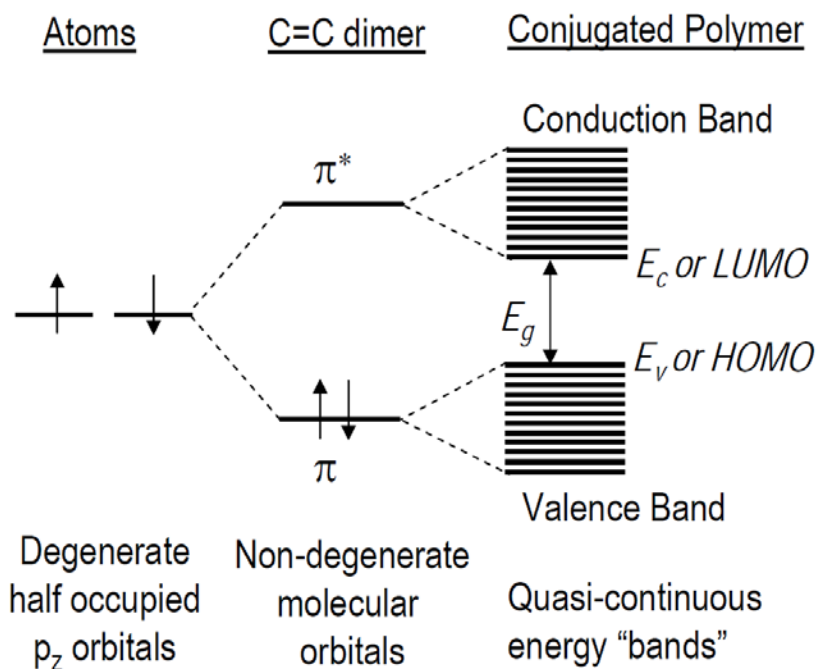
Figure 1.1: Schematic energy diagram showing the effects of repeated energy level splitting in conjugated polymers. When two sp^2 carbon atoms approach each other, their p_z orbitals split into bonding and anti-bonding molecular π orbitals. When a large number of p_z orbitals overlap, quasi-continuous bands form with a "band" gap, E_g smaller than the initial π - π^* energy gap of the C=C dimer.

1.2 Charge Carriers in Conjugated Polymers

EL of π-conjugated polymers is critically affected by the materials' electrical conductivities and thus their ability to transport electrical charges. Like inorganic semiconductors, molecular and polymer OSCs can be made conducting by chemical doping *[21, 22]* or electrical doping (i.e. charge injection from electrodes). Chemical doping in the context of polymer OSCs means charge transfer, be it by oxidation (p-type doping) or reduction (n-type doping), as well as the insertion of a counter ion into the vicinity of the polymer. In optoelectronic devices, however, the polymer OSC used as the active layer is highly pure *[23]* and doped by charges injecting from electrical contacts or generated from optical excitations.

Unlike band-like inorganic semiconductors, charges in polymer OSCs are not delocalised in a three-dimensional crystal lattice but spatially confined to the polymer chains *[19]*. Moreover polymer OSCs exhibit strong electron-phonon coupling, so adding an electron (or a hole) to the anti-bonding LUMO (or the bonding HOMO) induces structural relaxation of the polymer chains in its immediate vicinity to energetically lower conformations.
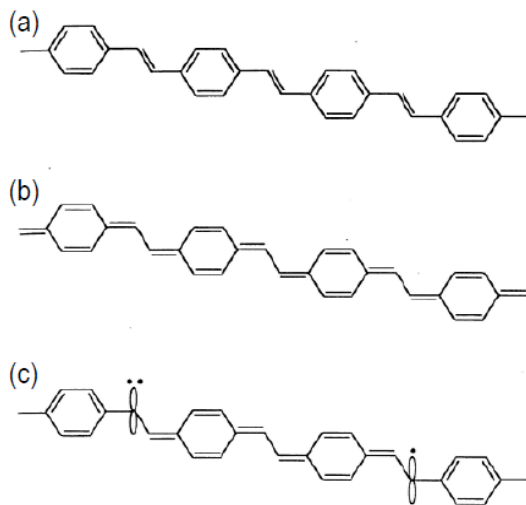
Figure 1.2: Schematic representation of the (a) benzoid, (b) quinoid and (c) electron polaron bond configurations in poly(p-phenylenevinylene) (PPV). An extra electron is added to form a lone pair [left of 1.2(c)), which disrupts the lower energy benzoid bond scheme. Also shown is an unpaired p_z orbital [left of 1.2(c)] resulting from switching from the higher energy quinoid configuration back to the benzoid configuration.

This phenomenon is schematically illustrated in Fig. 1.2 using the case of poly(p-phenylenevinylene) (PPV) that possesses a non-degenerate ground state *[24, 25]* like many other conjugated polymers used in the work presented here. Electrical doping of PPV (via injection from electrodes) can be seen as adding one extra electron to a p_z orbital of the PPV chain, which creates a lone electron pair and disrupts the alternating double bonds along the polymer backbone. To lower the overall energy of the system, a quinoid-like resonance structure that has higher affinity for electrons than the aromatic benzoid structure *[24, 25]* is created by local geometrical relaxation of the PPV chain in the vicinity of the charges (see Fig. 1.2b). In the absence of electrical doping, a PPV chain adopts either benzoid or quinoid structure via

resonance; but adding an electronic charge leads to a PPV chain (Fig. 1.2c) that possesses both the benzoid and quinoid structures. The fact that the quinoid structure of PPV (and many other conjugated polymers *[24, 25]*) has a lower ionisation potential and higher electron affinity leads to local lattice distortions via geometrical relaxation upon doping of the polymer chain.

It is important to emphasise that such local lattice distortions affect the electronic structures of the polymer in that they lead to an upward shift of the HOMO (in the case of hole doping) and a downward shift of the LUMO (in the case of electron doping) [see Fig 1.3]. In other words the HOMO and LUMO should not be taken as the transport levels for electronic charges in the OSCs. Rather the relevant charge transport levels that determine the interface energy line-up and charge-injection barriers lie within the HOMO – LUMO gap *[24, 26-29]* [see also section 1.5.4 for relevant discussions]. Such charges are commonly called polarons (i.e. a radical ion of spin ½ with local lattice distortion) and their electronic states in the gap are termed polaron states. Further addition or removal of electrons leads to spinless, doubly charged excitations called bipolarons (i.e. dications with lattice distortion) *[21, 24, 25, 30, 31]* that is created by the pairing of two polarons.

Polaron states are important as they are responsible for electrical conduction in molecular and polymer OSCs *[15]*. It is worth noting that the polymer materials differ from crystalline inorganic semiconductors in that they are ensembles of polymer chains with different conjugation lengths and random conformations. Electronic wavefunction does not delocalise along the entire polymer chain but only across several monomer units as structural imperfections, chemical defects (from polymer synthesis) and conformational kinks disrupt the orbital overlaps *[20, 32]*. The low effective conjugation length unfavorably limits the intrachain charge transport mobilities.
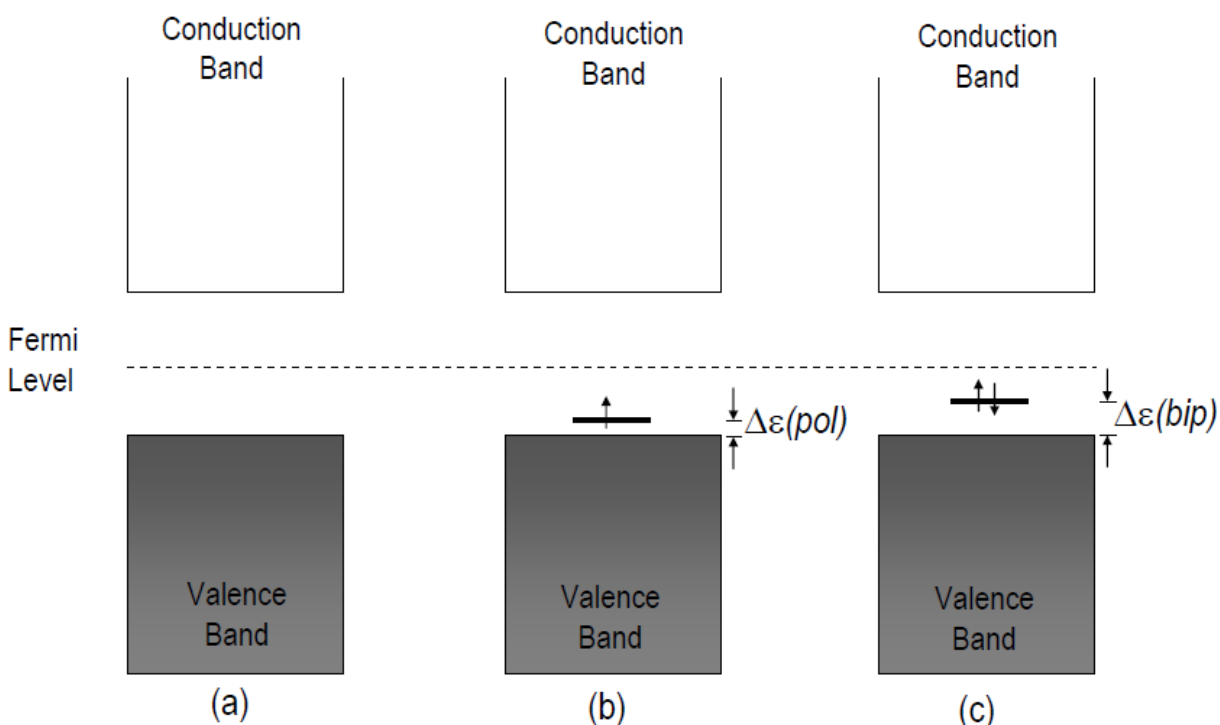
Figure 1.3: Illustration of the electronic band structure of a polymeric chain (a) without formation of polaron, (b) with the formation of a polaron and (c) with the formation of a bipolaron. Fermi level is taken as the reference level and $\Delta\varepsilon$ (pol) (or Δ(bip)) denotes the relaxation energy that stabilises the polaron (or bipolaron) on the polymer chain. [Figure adapted from ref. *[24]*]

Another key feature of charge transport in polymer OSCs is that polaronic charge carriers need to hop from one polymer chain to another in addition to moving along the chains. The latter process is the rate-limiting step that determines the macroscopic conductivity measured in experiments. Indeed, interchain charge hopping through a manifold of localised molecular states has been described as the main model for charge conduction in PLEDs *[33-36]*. The widely varied conjugation length, structural and conformational defects result in an energy spread of the charge-transport levels, which usually can be modeled with a Gaussian distribution. Hopping through localised polaronic states results in dispersive charge transport *[37-40]* with low charge carrier mobilites μ ($\sim 10^{-10} - 10^{-1}$ cm^{2}V^{-1}s^{-1}), which are often dependent on the applied electric field F ($\ln\mu \propto F^{1/2}$). Charge carrier mobilites in polymer OSCs are also strongly dependent on the charge carrier densities *[41-44]*. Tanase *et. al.* *[42]* showed that the experimental hole mobilities of hole-only diodes and field-effect transistors (FETs), both of which comprise

identical amorphous polymeric OSC materials, can differ by three orders of magnitude. Other diode and field-effect transistor measurements of different PPV derivatives *[44]* show that hole mobilities remain constant when charge carrier densities are less than $\sim 10^{22}$ m^{-3} but increases with a power law for charge carrier densities above $\sim 10^{22}$ m^{-3}. The phenomenon described above agrees well with independent studies, which shows that charge transport in solution-processed amorphous pentacene *[43]* and disordered OSCs in general *[41]* are inherently dependent on the charge density.

Polaron relaxation and structural disorder also critically affect the EL properties of conjugated polymers. The localisation of the polaron states and the strong interaction with the chain causes large Stokes' shift separating the peaks of emission and absorption spectra, and are also central to the existence of strongly bound excitons. The binding energies of polaron excitons are found to be of about several tenths of eV *[28, 45]* or considerably higher than kT (~ 25 meV) at room temperature. Therefore polaron excitons do not readily undergo thermal dissociation, making important spectral features observable even at room temperature. The terms "electron" and "exciton" will be used in subsequent sections of this dissertation with the unstated implication that they are of polaronic character.

1.3   Basic Physical Processes in Polymeric Light-Emitting Diodes (PLEDs)

Since the pioneering discovery of EL in conjugated polymers *[3]*, PLED technology has made dramatic progress in terms of materials design *[17, 38, 39, 46]* and device engineering *[11, 12, 47, 48]*. Although many PLED applications are in advanced stage of development with some already commercially available, the original multilayer device structure shown in Fig. 1.4 remains to be the fundamental architecture current devices are based on. The structure essentially comprises a thin conjugated polymer layer ($\sim 75 - 100$ nm) sandwiched between a glass substrate pre-coated with a transparent conductor (e.g. indium tin oxide, ITO) and a thermally-deposited metal electrode that is patterned via shadow mask. An important characteristic feature of a PLED is its requirement for energetically asymmetric electrodes to achieve highly power-

efficient EL. As such, low work-function cathode (e.g. calcium *[11, 47, 49]*, barium *[50]* or lithium fluoride *[48, 51]*) and high work-function anode (e.g. the conducting polymer poly(styrene sulphonate)-doped poly(3,4-ethylenedioxythiophene), PEDOT:PSSH *[52-54]*) are often employed. Upon applying a voltage across the two electrodes, an electric field is built up that drives a bipolar current through the polymer film. Subsequent radiative recombination of charge carriers in the polymer layer leads to EL.
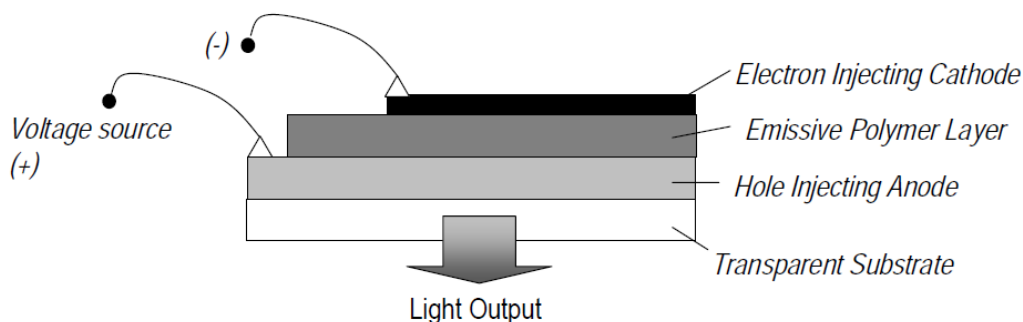
Fig. 1.4: Schematic structure of single-layer PLED.

Fig 1.4 depicts the energy level diagram for an organic LED under forward bias. This diagram illustrates the main processes governing the physics and operation of a PLED, namely: (a) charge injection from the electrodes into the polymer layer, (b) charge transport via drift/diffusion towards the opposite electrode under influence of the applied electric field, (c) formation of a neutral coulombically-bound excited state (termed exciton) and (d) radiative recombination of a fraction of these excitons that lead to light emission.

Excitons in conjugated polymers are generally considered to be more strongly localized than excitons in band-like semiconductors mainly because the exciton is substantially confined to a single polymer chain *[4]*. Formed from the pairing of two spin 1/2 electronic charges, the spin wave function of the exciton can be either singlet ($S = 0$) or triplet ($S = 1$) depending on how electron and hole pair with each other. Spin-allowed radiative emission (fluorescence) comes from the singlet excitons only. Owing to exciton confinement in the polymer chain, the exchange energy between singlet and triplet is large and cross-over between the two systems is

unlikely. Therefore triplet excitons do not produce light emission through recombination but via indirect processes such as triplet-triplet annihilation or phosphorescence.
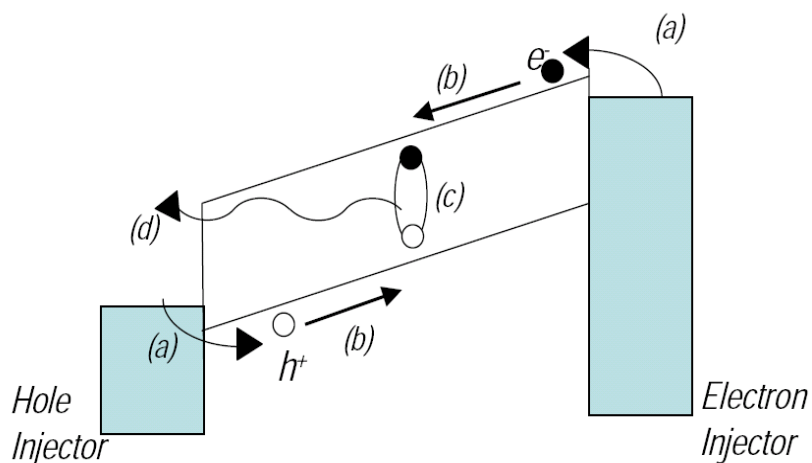
Figure 1.5: Schematic representation of the four main physical processes governing physics of PLED operations at forward bias: (a) charge injection, (b) charge transport, (c) exciton formation and (d) radiative decay of the exciton.

An important device parameter that takes into account the above mentioned processes is the internal quantum efficiency η_{int}, which is defined as the ratio of number of photons produced within the device to the number of charges injected through the PLED *[4]*:

$$\eta_{int} = \gamma r_{st} \eta_{PL} \qquad (1.1)$$

where γ is the proportion of injected charge carriers that form excitons in the polymer-emitting layer instead of passing through the PLED, r_{st} is the fraction of excitons that is formed as singlets and η_{PL} is the efficiency of radiative decay of these singlet excitons (i.e. photoluminescence efficiency). Indeed technological and scientific progresses in organic electronics revolve around maximising the internal quantum efficiency. Achieving this objective requires careful optimisation of charge injection *[47, 55, 56]*, realisation of good balance of electron and hole currents *[11, 47, 57]*, enhancement of the probability of singlet exciton formation *[47, 57, 58]* and minimisation of non-radiative recombination pathways *[59, 60]*.

Amongst the most notable strategies devised for optimising η_{int} are the use of multilayered structure to adjust the energy levels of the polymer components to those of the electrode *[11, 16, 47, 53, 54, 61]* with which they are in contact. This strategy also has the virtue of separating the recombination zone from electrode that injects the minority, low-mobility charge carriers and preventing majority carriers from traversing the diode without recombination *[47, 62]*.

The use of conjugated-polymer blends and copolymers with alternating molecular units of different electronic characteristics has also lead to high-performance PLEDs of high power efficiency and low operational voltage *[5, 12, 63]*. The possibility of using different polymers as spacers or charge blocking layers *[11, 47, 64]* for controlling the position of charge recombination zone has also been explored. The readers are referred to in-depth reviews of these and other issues in PLED research *[4, 5, 26, 65-68]*.

Primary focus in this dissertation will be directed on the metal/OSC heterojunctions as the energetics of these interfaces crucially affect charge injection and hence PLED performances. This involves controlling the height of the charge injection barrier, which is a key parameter determined by the mismatch between the electrode's Fermi level and the relevant transport levels of the OSC. Theoretical models and issues pertaining to the alignment of energy levels at electrode/OSC interfaces are explored in subsequent sections.

1.4 Charge Injection and Transport in PLEDs

As discussed in the above section, charge injection and collection processes are highly critical to the operation of polymer optoelectronic devices. These processes depend heavily on the size of charge injection barriers at metal/semiconductor heterojunctions. Unfortunately, these energy barriers across inorganic semiconductor/metal *[69, 70]* and small molecule OSC/metal interfaces *[4, 71, 72]* exhibit little dependence on the *bulk* electronic characteristics of metal contacts. This is because physical and/or chemical interactions usually occur at the junctions formed between two dissimilar materials, which can modify the *interfacial* electronic structures that determine charge injection barrier heights. The highly reactive nature of inorganic semiconductor surfaces can be generally attributed to dangling bonds on these surfaces *[73]*. Likewise, organic small molecular solids tend to interact with metal electrodes through various physisorption and/or chemisorption processes, which can induce interface dipoles of over 1 eV *[71, 74]*. In contrast, Schottky barrier heights across undoped conjugated polymer/metal interfaces depend much more strongly on the electronic characteristics of the metal contacts *[27, 29, 75-77]*. Consequently charge injection in PLEDs is more predictable and controllable by proper choice of electrode materials.

Unlike band-like inorganic semiconductors, mechanisms of charge injection into organic solids are less well established. Borrowing from conventional inorganic device physics, functional relationships of current with injection barrier height, have been described by two models *[69]*: a) Fowler-Nordheim (FN) quantum mechanical tunneling and b) thermionic emission. Assuming the case of an electron-injection barrier (Δ_e) [i.e. dashed line in Fig. 1.6], Fowler-Nordheim (FN) tunneling predicts the injection current to be:

$$I \propto F^2 \exp\left(\frac{-\kappa\Delta_e^{3/2}}{F}\right)$$

(1.2)

where I is the current, F is the electric field, and κ is a constant dependent on the charge carrier effective mass. Based on the simple assumption of vacuum level alignment at the

metal/semiconductor interface shown in Fig. 1.6, Δ_e is simply the difference between bulk work function of the metal (Φ_m) and electron affinity of the semiconductor (χ_s).
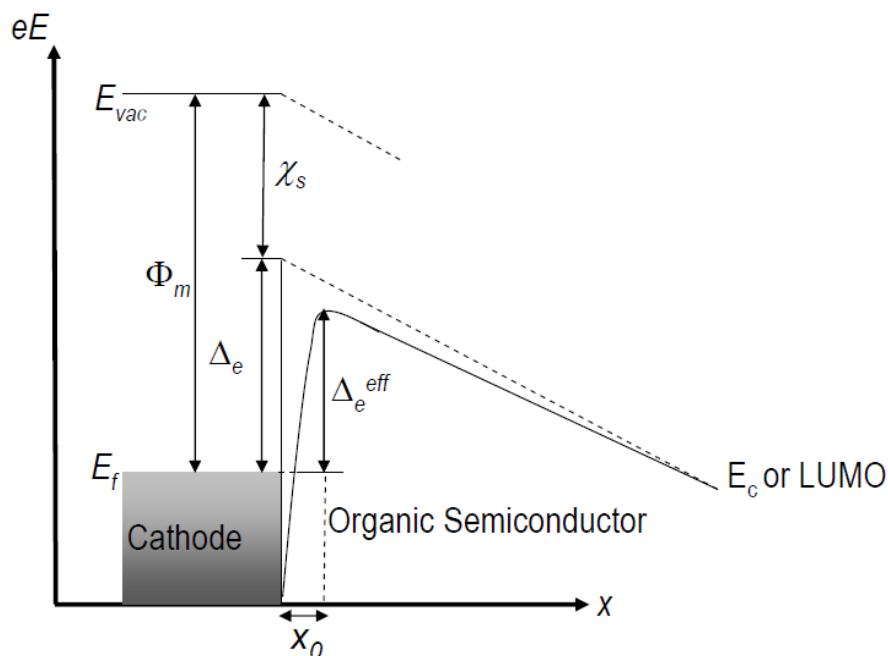
Figure 1.6: Schematic energy diagram of the metal/organic semiconductor (OSC) interface with an external electric field applied across the heterojunction. E_{vac} denotes the vacuum levels of both metal and semiconductor, Φ_m is the work function of the metal, Δ_e is the electron-injection barrier at zero electric field, X_0 is the distance from the metal at which the barrier is maximum, and χ_S is the electron affinity of the semiconductor. The solid line represents the energy minimum of the LUMO level, E_c. The potential is the sum the potential created by the applied field and that of the image force of the injected charge. The interface potential reduces the injection barrier from Δ_e to Δ_e^{eff}.

Although it reasonably estimates the functional dependence of injected current at high electric fields and barriers *[76, 78]*, eq. (1.2) cannot quantitatively explain the experimental I-V characteristics *[78-80]* at low applied field. This problem has been attributed to strong image force effect that commonly occurs across OSC/metal junctions during charge injection *[34, 79, 81, 82]*. The latter phenomenon reduces Δ_e across the heterojunction and renders Δ_e field-dependent. This effect is not considered by the FN tunneling expression shown in eq. (1.2).

This limitation leads to the use of Richardson-Schottky (RS) thermionic emission to describe charge injection across a metal/semiconductor heterojunction:

$$I = AT^2 \exp\left(\frac{-\Delta_e^{eff}}{kT}\right)$$

(1.3)

where *A* is the *effective* Richardson constant. Eq. (1.3) considers modified electron-injection barrier height (Δ_e^{eff}) at the interface *[69, 83]*, which is reduced by image force potential of an injected charge [solid line in Fig. 1.6]. Another key characteristic of eq. (1.3) is the inverse, exponential dependence of injection current on device operational temperature. Organic diodes with reduced Δ_e^{eff} are found to exhibit thermally activated and temperature-dependent injection behaviour in excellent agreement with thermionic emission *[80]*. But RS thermionic emission cannot quantitatively predict the magnitude and field dependence of the measured current *[78, 80]* because charges in disordered organic solids do not propagate freely in extended states as in inorganic crystalline semiconductors. Rather bulk charge transport in organic solids occur through hopping amongst the localised electronic states *[33-35, 37, 78-81]*, the energy distribution of which are approximated by Gaussian function *[27, 35, 81]*. The physical principles outlined in Fig. 1.6 can be extended to hole injection into a p-type semiconductor.

Owing to the strong charge localisation, most charge carriers are first injected into molecules adjacent to the metal contact. For conduction to occur, these carriers have to overcome the random energy barriers caused by material disorder *[81]* and crucially the coulombic energy well that arises from their image potentials (*x < x₀* shown in Fig. 1.6) in which they are trapped *[83]*. But only few charge carriers can overcome these barriers at low electric fields. Most carriers end up recombining at the metal/OSC interfaces so current is considerably lower than that predicted by theoretical models *[33, 34, 79-81, 84]* . But increasing the electric field strongly enhances the possibilities of charge carriers surmounting the barriers and drifting towards the counter electrode under the influence of the electric field applied across the bulk of polymer layer. Extensive research *[76, 77, 84, 85]* has also highlighted the strong dependence of injection

current on the barrier height for charge-injection (Δ), which represents the energy difference between the metal's Fermi level and average conduction levels of a multitude of energetically distributed polaronic states *[34]*.

Importantly, reducing charge-injection barrier height does not necessarily increase current passing through the device. Studies on hole-only diodes with poly[2-methoxy,5-(2'-ethyl-hexyloxy)-1,4-phenylene vinylene] (MEH-PPV) *[84, 86]* and on FETs with poly(3-hexyl thiophene) (P3HT) and poly(9,9-dioctylfluorene-alt-bithiophene) (F8T2) *[10, 87]* reveal two limiting regimes for injection current. When Δ is larger than $0.3 - 0.4$ eV, current traversing the device is limited by rate of carrier injection (i.e. injection-limited) from electrode into the polymer; but when Δ is less than $0.3 - 0.4$ eV current is limited by bulk charge transport rate in the polymer (i.e. space-charge limited, SCL regime). SCL current is inherently limited by local accumulation of space charges that affects the electric field distribution in the device due to the low carrier hopping mobilities in polymer OSCs ($\sim 10^{-6}$ cm^{2}V^{-1}s^{-1} for PPV and its derivatives). Note that ohmic contact is not the only condition realising SCL injection. In organic diodes with Schottky contacts, injection current can exhibit injection-limited behaviour at low fields and SCL behaviour at high fields *[88]*.

1.5 Energy Level Alignment at Metal/Semiconductor Interfaces

We have demonstrated that charge injection depends heavily on the Schottky barrier height or the energy difference between the *surface* Fermi level of the metal contact and the relevant conduction levels in the organic semiconductor (OSC) adjacent to the contact. As such it is essential to understand the alignment of such energy levels across the metal/OSC interfaces present in optoelectronic devices. Accurate prediction and control of the injection barrier heights Δ_h are necessary for designing high-performance optoelectronic devices.

Ideally experimental determinations of Δ with accuracy on the order of kT ($\sim$ 25 meV at room temperature) are needed to quantitatively predict transport and optoelectronic properties of PLED devices. In reality, such experimental accuracy remains unattained despite progress made over the years *[27, 71, 74]*. But experimental techniques and general theoretical models *[69, 89, 90]* of $\sim$ 100 meV accuracy have been developed, permitting qualitative understanding of energy alignment at such interfaces.

This difficulty is further complicated by the fact that in reality metal/OSC heterojunctions are not ideal interfaces with abrupt discontinuities in chemical composition and electronic structure *[26, 68, 71, 91-93]*. Studies on metal/OSC interfaces *[26, 68, 71]* have in fact shown that they can be complex systems with unknown material composition, interdiffusion of ions/atoms, partial or integral charge transfer and/or defect state formation. Moreover, these processes are highly sensitive on the materials forming the interfaces and can in many cases modify the interfacial electronic structure *[71, 74, 92, 93]*. These complications have inevitably prohibited full understanding of the energy level alignment at metal/OSC and OSC/OSC interfaces present in state-of-art organic optoelectronic devices. As such no reliable interface-design criteria are available to device manufacturers even though organic optoelectronic devices are already commercially available or in an advanced stage of development.

Nevertheless, extensive research on inorganic semiconductor systems has yielded well-controlled theoretical models that can reproduce or predict interfacial energy alignment in a range of $\sim$ 100

meV. In the subsequent sections, three major theories borrowed from inorganic semiconductor physics *[69]* which account for the interface energy lineup will be presented.

1.5.1 Schottky-Mott Model and Vacuum Level Alignment

One of the earliest models proposed for metal/semiconductor heterojunction is the Schottky-Mott model, which assumes no interaction between the two dissimilar materials. This approximation is valid as long as one neglects interfacial dipole layers (see section 1.5.2 for discussions) or charged interface sub-gap states that may present at the interface. The situation for a contact between a metal and an n-type semiconductor is shown in Fig. 1.7. Although Fig. 1.7 concerns electron injection into an n-type semiconductor, similar physical principles affect hole injection into a p-type semiconductor. In the case of electron injection, Δ_e is the difference between the work function of the metal, Φ_m and the electron affinity of the semiconductor, χ_s:

$$\Delta_e = \Phi_m - \chi_s \qquad (1.4)$$

Eq. (1.4) applies to interfaces where E_{vac} of the metal aligns with E_{vac} of the semiconductor (i.e. Schottky-Mott model) *[94]*. Similarly the Schottky-Mott model predicts that hole-injection barrier height, Δ_p is determined by the difference between work function of the metal, Φ_m and the ionisation potential of the semiconductor, I_p:

$$\Delta_p = I_p - \Phi_m \qquad (1.5)$$

In obtaining eq. (1.4) and (1.5) several important assumptions are made, namely: (i) the surface dipole contributions to Φ_m and χ_s do not change when both metal and semiconductor are brought into contact (or at least the difference between them does not change), (ii) there is no localised state on the surface of the semiconductor as mentioned earlier, and (iii) there is perfect contact between the semiconductor and the metal. If all these assumptions are valid, vacuum levels of both metal and semiconductor align with each other upon forming the interface.

Figure 1.7: Energy alignment between a metal and an n-type semiconductor (a) before contact formation and (b) after intimate contact formation (based on Schottky-Mott model), (c) a narrow gap exists at the interface due to surface passivation or oxidation of the metal. In (c), the Schottky-Mott limit is still reasonably accurate in describing the interface energy line-up. W is the width of the charge depletion layer within the semiconductor; whereas eV_{bi} denotes the energy of the built-in potential arising from the equilibration of Fermi level (E_f) throughout the heterojunction. E_v and E_c denote the valence band maximum and conduction band minimum of the semiconductor, respectively; while Φ_s denotes work function of the semiconductor.

Eq. (1.4) and (1.5) imply that Schottky barrier height for hole or electron injection (i.e. Δ) is linearly dependent on the electrode's work function Φ_m such that:

$$\left| \frac{\partial \Delta}{\partial \Phi_m} \right| = S = 1 \qquad (1.6)$$

where *S* is known as the interface parameter *[69, 73]*. In the case of an electron-injection barrier Δ_e can be predicted and controlled simply by changing the *surface* work function of the metal electrode *[55, 56]*, which may be achieved by changing the nature of the electrode or chemical/physical modification of the metal's surface *[27]*. It is worth noting that polymer OSC-on-metal contacts in devices deviate largely from the ideal situation shown in Fig 1.7 (b) because the metal is unavoidably passivated by a layer of hydrocarbons (organic solvents of the polymer OSCs) or a thin oxide layer (due to oxidation by moisture and/or oxygen in atmospheric ambient). Therefore metal/semiconductor heterojunctions encountered in working devices resemble Fig. 1.7 (c), in which a thin insulating layer separates the semiconductor from the metal. Nevertheless, the insulating barrier tends to be sufficiently thin such that charges can tunnel through quite easily. Fig. 1.7(c) is thus almost indistinguishable from Fig. 1.7(b) in energy level alignment as far as the electrons are concerned.

The Schottky-Mott model represents an ideal situation that assumes the electrode-semiconductor interface to be simply a junction of two non-interacting semi-infinite and two-dimensional solids. For most inorganic semiconductor/metal contacts *[69-71, 74]*, however, this is usually not the case as there exists unsaturated dangling bonds at metal and/or semiconductor surfaces, charge rearrangement or charge transfer across the interfaces formed between metal and/or semiconductor. These processes can significantly alter energy level alignment by introducing a discontinuity in the electrostatic potential at the interface (i.e. an interfacial dipole layer) *[69, 73]*, which is not taken into account by the Schottky-Mott model. The limitations of the Schottky-

Mott model in predicting charge-injection barriers in actual devices led to the proposal of another model by Bardeen *[90]* as discussed below.

Owing to spontaneous charge transfer to maintain equilibration of E_f, an internal, a built-in field that leads to the localised band bending adjacent to the metal-semiconductor heterojunction is induced upon contact formation. As illustrated in Fig. 1.7 (b) – (c), this electrically spontaneous process creates a charge-depletion region in the semiconductor with width W (depletion width) that is deprived of mobile charge carriers except immobile ionised donors. In the case of a metal/n-doped semiconductor heterojunction, negative ions in the charge-depletion region are counter balanced by positive charges at the metal surface to maintain charge neutrality. Spontaneous electron transfer sets up a contact potential or V_{bi} along the width of charge-depletion region in the semiconductor, which prevents further n-doping of the semiconductor adjacent to the metal contact. The built-in field in the metal is localised at the near surface region. In the case of a non-interacting metal/semiconductor interface where E_{vac} alignment prevails (i.e. $S = 1$) [see Fig. 1.7 (b) – (c)], V_{bi} is determined by work functions of the metal (Φ_m) and the semiconductor (Φ_s) by:

$$eV_{bi} = \Phi_m - \Phi_s \qquad (1.7)$$

1.5.2 Bardeen's Model and Fermi Level Pinning

As mentioned earlier, the vast majority of practical metal/inorganic semiconductor contacts do not obey Schottky-Mott limit and their interface parameters S tend to be significantly lower than unity *[69, 70, 73, 90]* or approach zero. In these cases charge injection barrier heights are not controlled by the metal's work function and accurate prediction of Schottky barrier height Δ for most systems is not possible. To account for the independence of injection barrier on the electrode's work function, Bardeen *[90]* proposed a model where the electrode's Fermi level E_f is "pinned" to the localised electronic states present on the semiconductor's surface through spontaneous electronic transfer [i.e. surface states in Fig. 1.8 (a)]. This process creates an

interface dipole, δ that aligns E_f of the metal electrode with the energy level of the surface states [i.e. Φ_0 in Fig. 1.8 (a)] present at semiconductor/metal interfaces.

If the density of such surface states, D_s is infinitely high (i.e. $D_s \rightarrow \infty$) charges from the electrode are fully accommodated causing E_f to be completely pinned to the surface states (i.e. $S = 0$). In this case, the Schottky barrier height for electron injection (i.e. Δ_e) is:

$$\Delta_e = \Phi_0 \tag{1.8}$$

and the Schottky barrier height for hole injection (i.e Δ_p) is:

$$\Delta_p = I_p - \Phi_0 \tag{1.9}$$

Eq. (1.8) and (1.9) are known as the Bardeen limit. A key assumption of the Bardeen's model is that Φ_0 of surface states is an intrinsic property of the semiconductor and is not related to the work function of the metal. Accordingly the height of charge-injection/charge-extraction barrier is controlled entirely by Φ_0 of the semiconductor but not by Φ_m of the metal:

$$\left| \frac{\partial \Delta}{\partial \Phi_m} \right| = S = 0 \tag{1.10}$$

In the case of a metal/semiconductor interface where E_f pinning prevails (i.e. $S = 0$) [see Fig. 1.8], V_{bi} is no longer determined by Φ_m of the metal but solely by material properties of the semiconductor. Therefore Schottky barrier height is not controllable by varying E_f of the metal electrode:

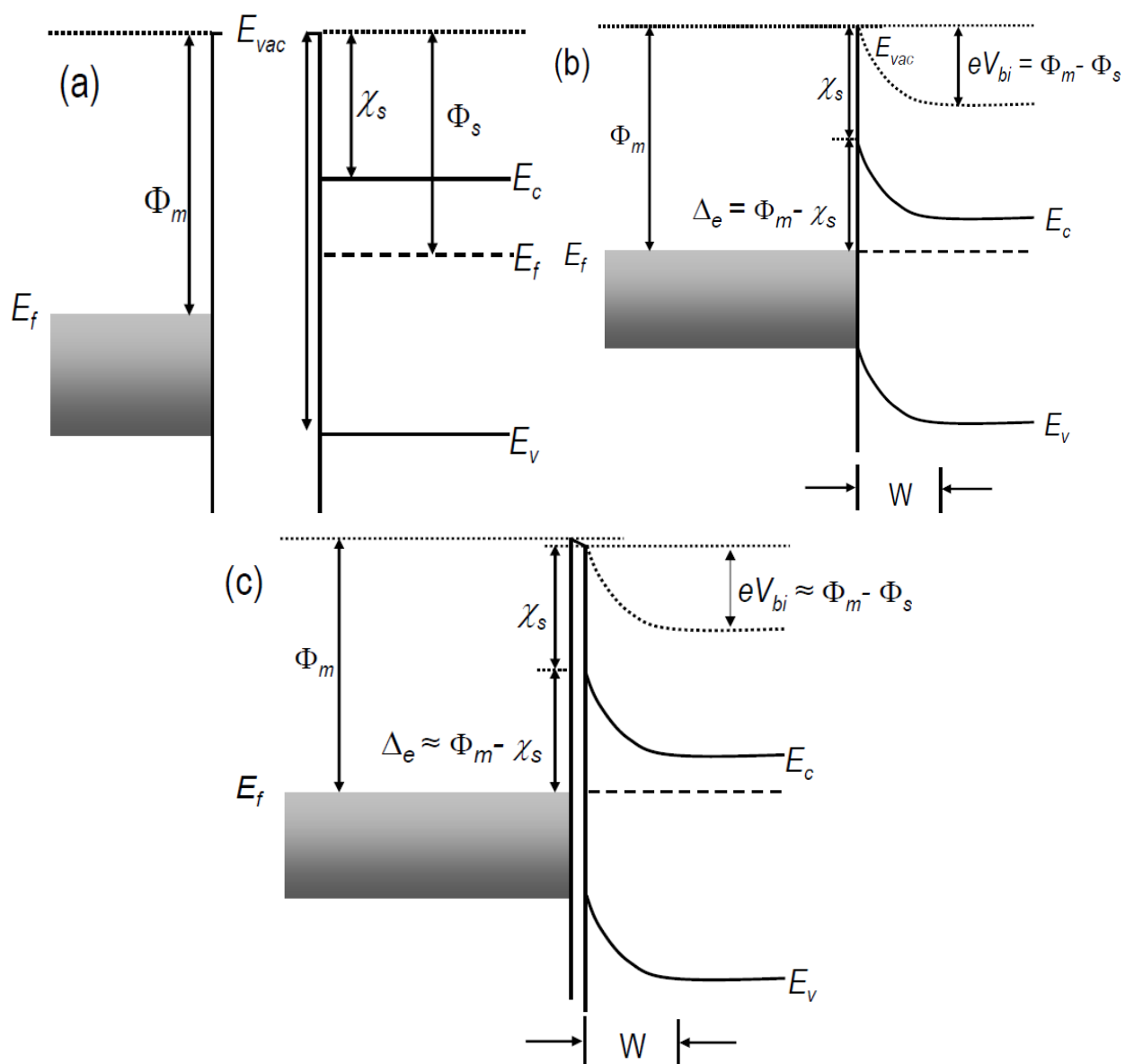$$eV_{bi} = \Phi_s - \chi_s - \Phi_0 \tag{1.11}$$
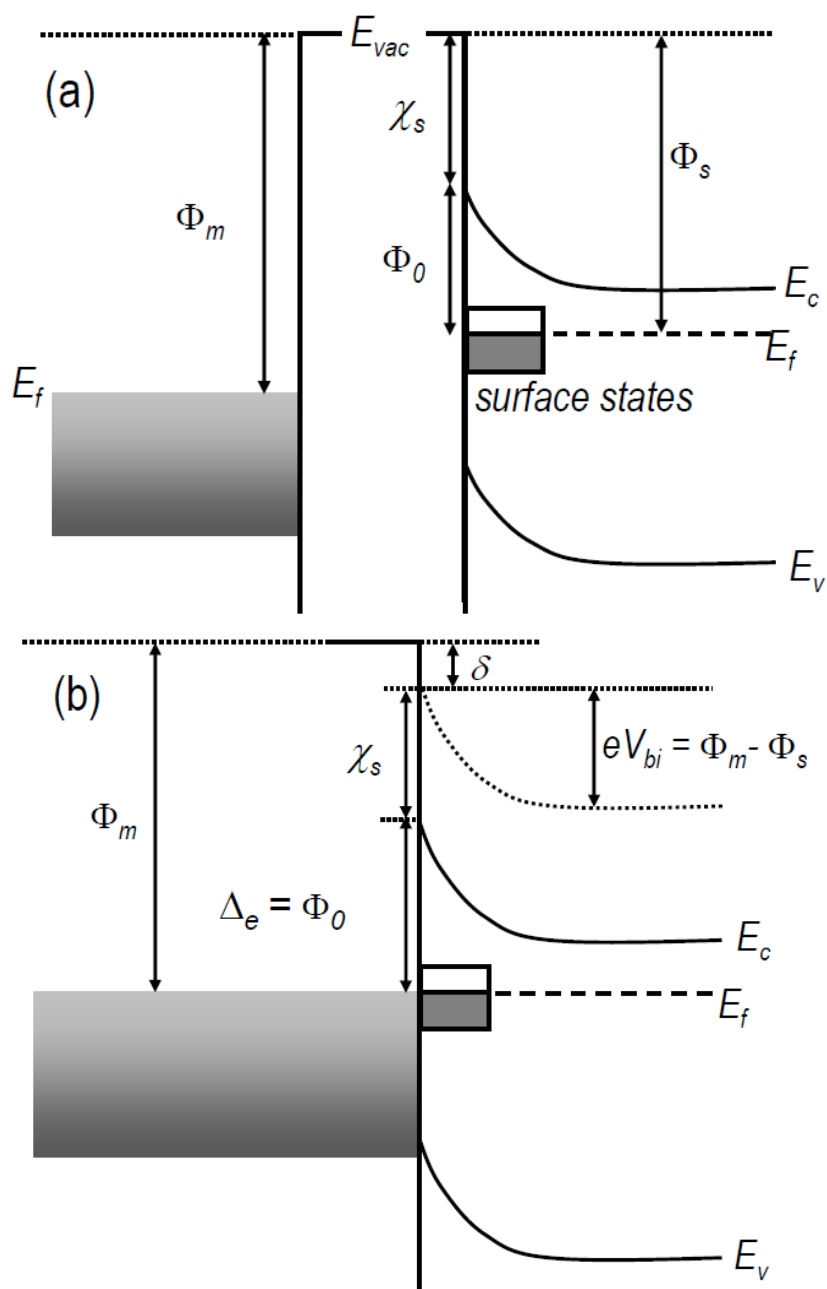
Figure 1.8: Schematic of energy alignment across the interface of a metal and an n-type semiconductor (a) before contact formation and (b) after contact formation (based on Bardeen's model). The surface states of the semiconductor are completely pinned to the electrode's Fermi level via electron transfer, thereby rendering the injection barrier height Δ_e independent of the metal's work function. E_f pinning leads to the formation of dipole δ at the interface. E_v and E_c denote the valence band maximum and conduction band minimum of the semiconductor, respectively. Φ_0 denotes the pinning level with respect to E_c of the semiconductor; while Φ_s denotes work function of the semiconductor.

Importantly E_f pinning can also occur despite absence of electronic state on a semiconductor surface. Electronic transfer will occur spontaneously by tunneling when Φ_m of a metal is lower (or higher) than χ_s (or I_p) of a semiconductor, thereby causing the continuum state at or near the metal's E_f to pin with the semiconductor's E_c (or E_v). The resulting contact is called an ohmic junction and is shown in Fig. 1.9. Since there are free charges accumulating near semiconductor/metal interface upon contact formation, accumulated charges traverse from a "virtual contact" where $|dV/dx| = 0$ into the bulk of semiconductor at electrical equilibrium [see Fig. 1.9 for illustration]. Therefore charge injection at positive bias (with respect to the semiconductor) is not limited by Δ_e at the metal/semiconducting interface. On the other hand, applying a negative bias to the metal (relative to the semiconductor) decreases interfacial charge density and causes the "virtual contact" to converge with the pinning level at the metal/semiconductor interface. When the "virtual contact" coincides with the pinning level, charge injection is limited by Δ_e at the interface *[95]*.
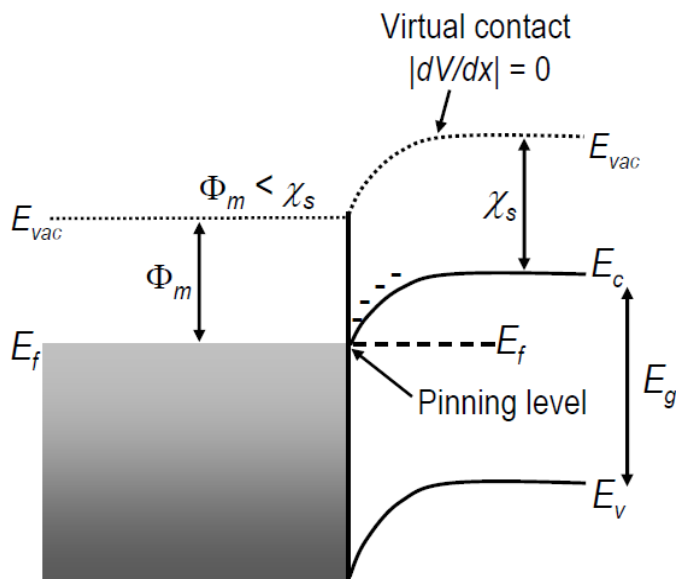
Figure 1.9: Ohmic contact between a metal and a semiconductor.

By invoking the concept of surface electronic states, Bardeen's model accounts for the weak dependence or independence of Δ on Φ_m of different heterojunctions *[73, 90]*. For metal/semiconducting interfaces, incomplete E_f pinning is expected due to the low density of states (i.e. $D_{s,semiconductor}$) on the semiconductor surface (i.e. $0 < D_{s,semiconductor} < \infty$) when

compared with that on the metal surface (i.e. $D_{s,metal}$). In the case of a metal/metal heterojunction formed between two metals with different Φ_m, high density of states on both metal surfaces ($D_{s,metal} \rightarrow \infty$) enable their E_f to completely align with each other. Accordingly an interface dipole layer of a few angstroms in thickness is spontaneously formed upon the metal/metal contact formation *[69]*. Although Bardeen's model provides qualitative explanations for the weak dependence of Δ on Φ_m of metal electrodes *[69, 73, 90]*, it cannot quantitatively predict Φ_0 of a semiconductor and hence Δ at a metal/semiconductor heterojunction. Accordingly the interface parameter S is considered to be an empirical parameter and must be determined on a case-to-case basis.

1.5.3 Integer Charge-Transfer Model

Schottky-Mott's and Bardeen's models were developed to account for energy level alignment across inorganic semiconductor/metal junctions made in ultrahigh vacuum (UHV) ($\sim 10^{-9}$ mbar) environment. But charge-injecting/collecting interfaces in organic optoelectronic devices are prepared either fabricated in high vacuum (HV) ($\sim 10^{-6} - 10^{-7}$ mbar) or by solution processing of conjugated polymers *[4, 47]* or small molecule precursor *[96]* (e.g. spin coating, ink-jet printing and screen printing) in chemically inert atmospheres or open air. Such interfaces are characterised by a negligible hybridisation of π-electronic molecular orbitals and substrate electronic wave functions because the substrate surfaces are inevitably passivated by a thin layer of oxide (due to oxidation caused by exposure to atmospheric ambient) or a residual hydrocarbon layer from organic solvents during device fabrication *[26, 71]*.

Since the intervening oxide/hydrocarbon layer decouples π-electrons of a solution-processed OSC layer from electrons near the E_f of underlying metal electrodes, electronic interactions that lead to formation of interface dipoles and/or interfacial sub-gap electronic states are unlikely. Furthermore these OSCs have negligible concentrations of surface states compared to inorganic semiconductors because chemical bonds are not broken in forming OSC surfaces. These characteristic features mean that OSC/OSC and OSC-on-metal contacts encountered in solution-processed organic electronic devices are Schottky-Mott interfaces formed between two weakly-

interacting or non-interacting solids. Nevertheless electrically spontaneous charge transfer can occur through quantum mechanical tunneling so long as the passivating oxide/hydrocarbon layers at these junctions are sufficiently thin. The phenomena of charge transfer-induced E_f pinning in working solution-processed metal/OSC/metal diodes *[27, 97-99]* and metal/OSC bilayer structures *[26, 29, 68, 75, 100, 101]* have been extensively reported over the last decade.

Recently Tengstedt *et. al. [26, 29, 102]* proposed an Integer Charge-Transfer (ICT) model to describe energy level alignment across non-interacting metal/OSC and OSC/OSC interfaces. According to the ICT model in Fig. 1.10, charge transfer occurs via tunneling only if Φ_{sub} is greater (or smaller) than the formation energies of positive (or negative) polaron states in the OSC layer. Quantum mechanical tunneling implies transfer of integral amount of charge, one charge at a time, from the metal into well-defined polaron levels (i.e. E_{ICT+} and E_{ICT-}) in the OSC material. The formation energies of the positive polaron (E_{ICT+}) or negative polaron states (E_{ICT-}) has taken into account electrostatic screening from the substrate as well as electronic and geometrical relaxation of the OSC material. Since hole polaron relaxation energies, $\Delta\varepsilon(pol)$ of different OSCs correspond to energy differences between the HOMO edges and E_{ICT+} of the materials [see Fig. 1.3 for illustration], the ICT model enables direct measurement of $\Delta\varepsilon(pol)$ for different heterojunctions.

Fig 1.10 shows the mechanisms underlying energy level alignment at a hypothetical OSC/metal interface using the ICT model, where the OSC layer has an energy gap defined by E_{ICT+} and E_{ICT-} of ~ 1.4 eV. Fig. 1.10 predicts that work function at the OSC-on-metal substrate contact ($\Phi_{org/sub}$) exhibits a characteristic "Z" dependence with metal substrate's work functions (Φ_{sub}). This characteristic "Z" dependence is depicted in Fig. 1.11 where abrupt transitions between Schottky-Mott limit ($S = 1$) and Bardeen's limit ($S = 0$) occur as Φ_{sub} coincides with E_{ICT+} and E_{ICT-} of the OSC layer. Theoretical predictions of ICT model have been experimentally verified by varying Φ_{sub} of metal substrate beneath a polyfluorene APFO-Green1 polymer (with E_{ICT+} − E_{ICT-} gap ~ 1.3 eV) over an energy range of 2.5 eV [see Fig. 1.12 and ref. *[75]*]. Fig. 1.12 shows that when Φ_{sub} is larger than 4.6 eV (i.e. E_{ICT+}), $\Phi_{org/sub}$ is pinned at ~ 4.6 ± 0.1 eV (i.e. $S = 0$). When Φ_{sub} lies between 4.0 eV and 4.6 eV, $\Phi_{org/sub}$ corresponds exactly to Φ_{sub} as a result of E_{vac}

alignment (i.e. $S = 1$). When Φ_{sub} lies below ~ 3.6 eV and ~ 4.0 eV, $\Phi_{org/sub}$ is pinned at these levels due to electron tunnelling from metal to the polymer. Fig. 1.12 shows that APFO-Green1 has two different E_{ICT-} values at $\sim 3.6 \pm 0.1$ eV and at $\sim 4.0 \pm 0.1$ eV. These values were assigned to be the energy levels of singly charged polarons and doubly charges bipolarons, which are expected to be of different energies in polymer OSCs *[24, 75]*.

It is worth noting that a full "Z" variation of $\Phi_{org/sub}$ - Φ_{sub} plot is rarely observed in most other OSC/metal bilayer systems *[29, 103-106]* mainly because the $E_{ICT+} - E_{ICT-}$ energy gaps of many OSCs are often larger than the degree of variation in Φ_{sub} achievable in practice [see Fig. 1.13]. Fig. 1.12 and 1.13 show that energy level alignment at weakly interacting or non-interacting OSC/OSC and OSC/metal interfaces are not determined by the HOMO and LUMO levels but by E_{ICT+} and E_{ICT-} of the OSC materials. We emphasise that Φ_{sub} referred to in the ICT model represent the *surface* work functions of the metal substrates encountered in finished, working organic electronic devices, which can be very different from their respective work functions determined in ultrahigh vacuum environment. Work function modification can be attributed to repulsion of electrons at the tail of surface states *[26, 71]*, surface passivation *[101, 107]* and/or contamination *[108, 109]* as well as interfacial chemical modifications *[56, 101, 102, 110]*.
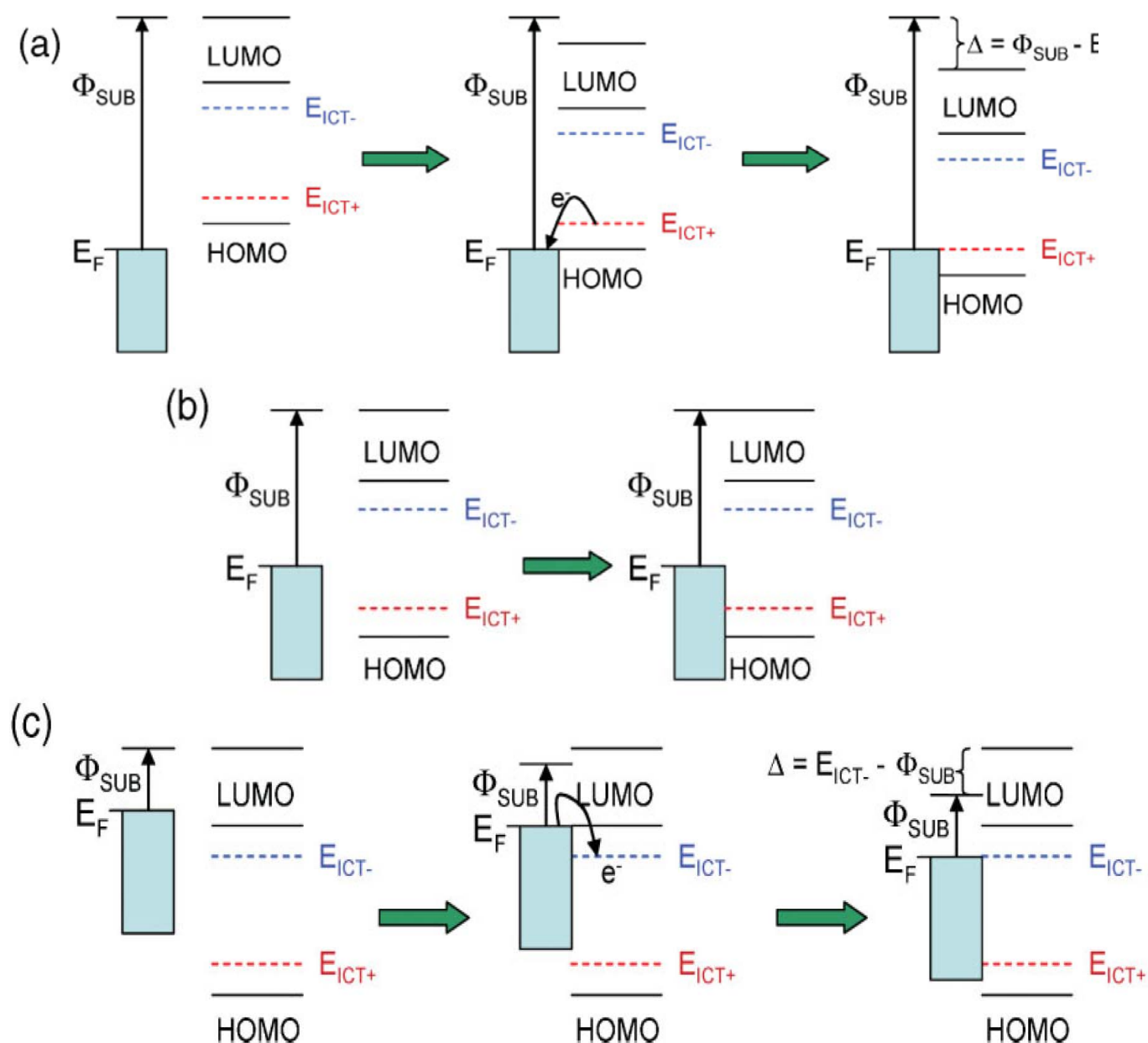
Figure 1.10: Schematics showing evolution of the energy level alignment across a molecular or polymeric OSC-on-metal interface under three possible conditions:-

a) $\Phi_{sub} > E_{ICT+}$: E_f pinning to a positive ICT state (Bardeen's limit, i.e. $S = 0$),

b) $E_{ICT-} < \Phi_{sub} < E_{ICT+}$: E_{vac} alignment (Schottky-Mott limit, i.e. $S = 1$), and

c) $\Phi_{sub} < E_{ICT-}$: E_f pinning to a negative ICT state (Bardeen's limit, i.e. $S = 0$).

Charge transfer-induced shift in vacuum level, Δ is shown where applicable. [Figure adapted from ref. *[26]*]
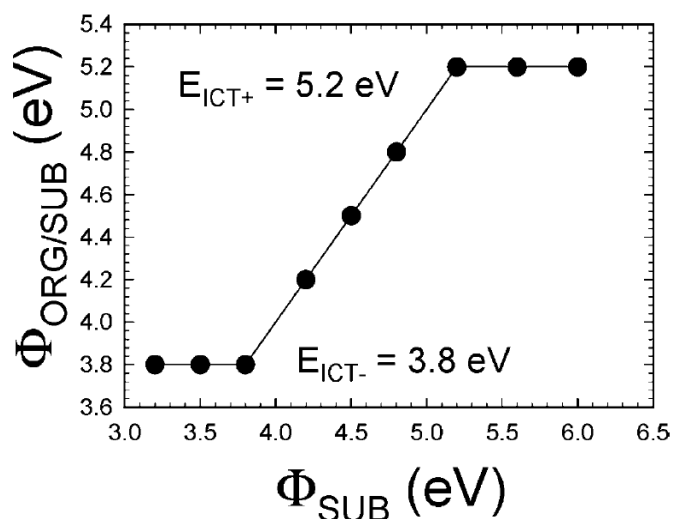
Figure 1.11: General dependence of work functions of OSC-on-substrate interface, $\Phi_{org/sub}$ with the underlying substrate's work functions, Φ_{sub} according to the ICT model. [Figure adapted from ref. *[26]*].
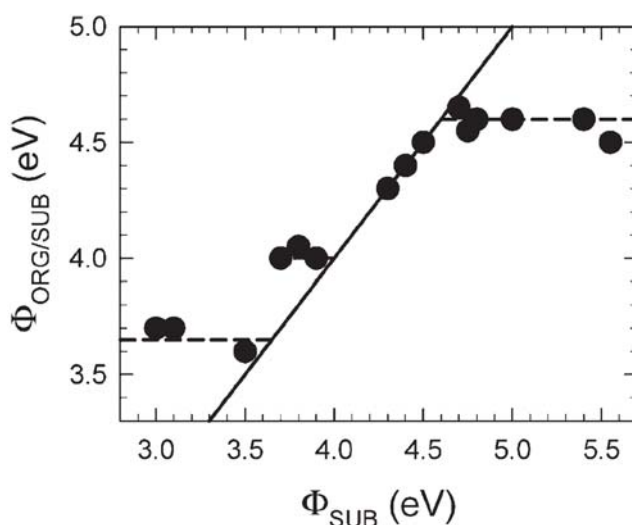
Figure 1.12: Work function at APFO-Green1/metal interfaces, $\Phi_{sub/org}$ as a function of work function of bare metal substrates, Φ_{sub}. The solid line is added as a guide to the eye, illustrating the $S = 1$ dependence expected for E_{vac} alignment. The dashed lines are added as guides to the eye, illustrating the $S = 0$ dependence expected for E_f pinning [Figure adapted from ref. *[75]*].

1.5.4 Metal/Organic Semiconductor (OSC) Interfaces in Electronic Devices

The ICT model predicts that metal/OSC heterojunctions encountered in actual organic electronic devices obey Schottky-Mott limit (i.e. $S = 1$) if Φ_{sub} of an underlying metal substrate lies within $E_{ICT+} - E_{ICT-}$ energy gap of an OSC overlayer. On the other hand, raising the metal E_f above (or below) E_{ICT-} (or E_{ICT+}) of the OSC leads to interface dipole formation through spontaneous, integral charge-transfer. The ICT model provides a unified theory that applies to OSC-on-metal and metal-on-OSC interfaces *[26, 101]* prepared by vacuum deposition or solution processing techniques so long as strong electronic interactions across the heterojunctions are minimised by intervening layers that passivates the OSC and/or metal surfaces.

Fig. 1.13 shows the effects of varying Φ_{sub} on $\Phi_{org/sub}$ values at interfaces formed between different metal substrates and conjugated polymers with a large range of I_p (4.5 − 5.8 eV) *[26, 111]*. Values of Φ_{sub} and $\Phi_{org/sub}$ are determined by ultraviolet photoemission spectroscopy (UPS) before and after coating the metal substrates with polymer OSC films. When Φ_{sub} of the metal lie above the hole polaron level (or E_{ICT+}) of the polymer OSC overlayer, $\Phi_{org/sub}$ and hence charge-injection/charge-extraction barrier heights (i.e. Δ_h) are solely determined by Φ_{sub} of the metal. These phenomena are independent on the chemical nature of the polymer OSCs and confirm that E_{vac} of different polymer OSCs align with E_{vac} of the substrates upon contact formation (i.e. $S = |\partial\Delta_h/\partial\Phi_{sub}| = 1$).

But when Φ_{sub} exceeds the threshold energy values corresponding to E_{ICT+} of the polymer OSCs overlayer, $\Phi_{org/sub}$ and charge-injection/charge-extraction barrier heights are not dependent on Φ_{sub} of the metal (i.e. $S = 0$ or Bardeen's limit) due to pinning of E_f with E_{ICT+} of the material. In other words the interface dipole at metal/OSC interfaces is simply the difference between $\Phi_{org/sub}$ and Φ_{ub} (i.e. $\Phi_{org/sub} - \Phi_{sub}$). Accordingly interface dipole arising from spontaneous charge transfer across a P3HT-on-metal interface can be as large as 2.1 eV [see Fig. 1.13]. Similar phenomenological dependence for small molecule OSCs are reported and discussed in ref. *[105, 112]*.
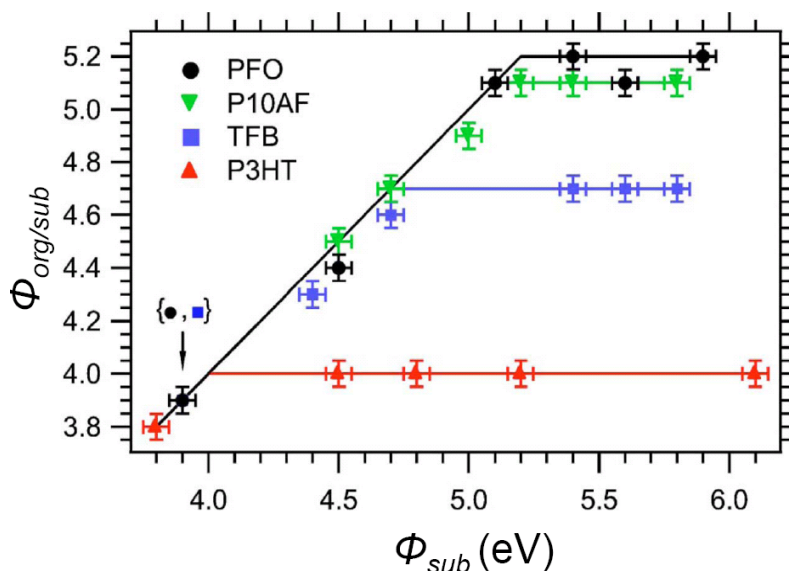
Figure 1.13: Dependence of work function at OSC/metal substrate interface, $\Phi_{org/sub}$, on the work function of the bare substrate, Φ_{sub}, for P3HT, TFB, P10AF and PFO. The solid line is only a visual guide to illustrate $S = 1$ dependence expected for vacuum level alignment and $S = 0$ dependence for Fermi-level pinned interfaces. PFO: poly(9,9'-dioctylfluorene); P3HT: poly(3-hexylthiophene); P10AF: poly(9-(1'-decylundecylidene) fluorene); TFB: poly(9,9'-dioctylfluorene-alt-N-(4-butylphenyl)diphenylamine). [Figure adapted from ref. *[29]*].

Since HOMO edges of polymer OSCs can be measured by UPS, the ICT model enables direct measurement of polaronic relaxation energies in different polymer OSCs through measuring the energy differences between their E_{ICT+} and HOMO values (i.e. E_{ICT+} − HOMO). E_{ICT+} can be readily measured by determining $\Phi_{org/sub}$ at different polymer OSC/metal heterojunctions through systematically varying Φ_{sub} values of the underlying metals. Using this technique, E_{ICT+} of different polymer OSCs are found to be ~ 400 − 700 meV *[26, 111]* above the HOMO edges of these materials [see Table 1.1]. Although the ICT model shows that E_{ICT+} coincides with the E_f pinning levels at metal/OSC interfaces that obey Bardeen's limit, this view is challenged by Hwang *et. al. [68, 100]* who have shown that E_{ICT+} of OSCs should be ~ 200 meV and that E_f pinning levels should lie at ~ 400 − 500 meV above the OSC HOMO edges. The ~ 200 − 300 meV difference between E_f and E_{ICT+} is attributed to the geometrical relaxation energies of the charged molecular ions, which is not measurable by UPS technique *[26, 100]*. Interestingly Hwang's hypothesis agrees well with independent measurements on polymeric OSC *[113]* and molecular OSC *[114]*. These results highlight the confusion of current understanding on electronic structures at weakly-interacting metal/OSC heterojunctions.

OSC	IP [±0.1 eV]	Polaronic energy [±0.05 eV]	Relaxation energy [±0.05 eV]
P3HT	4.5	4.0	0.5
TFB	5.4	4.7	0.7
P10AF	5.5	5.1	0.4
PFO	5.8	5.2	0.6

Table 1.1: Estimates of essential parameters characterizing the energetics at the interface, as deduced from UPS measurements: IP, polaronic energy (i.e. E_{ICT+}), and polaronic relaxation energy. [Table adapted from ref. *[29]*].
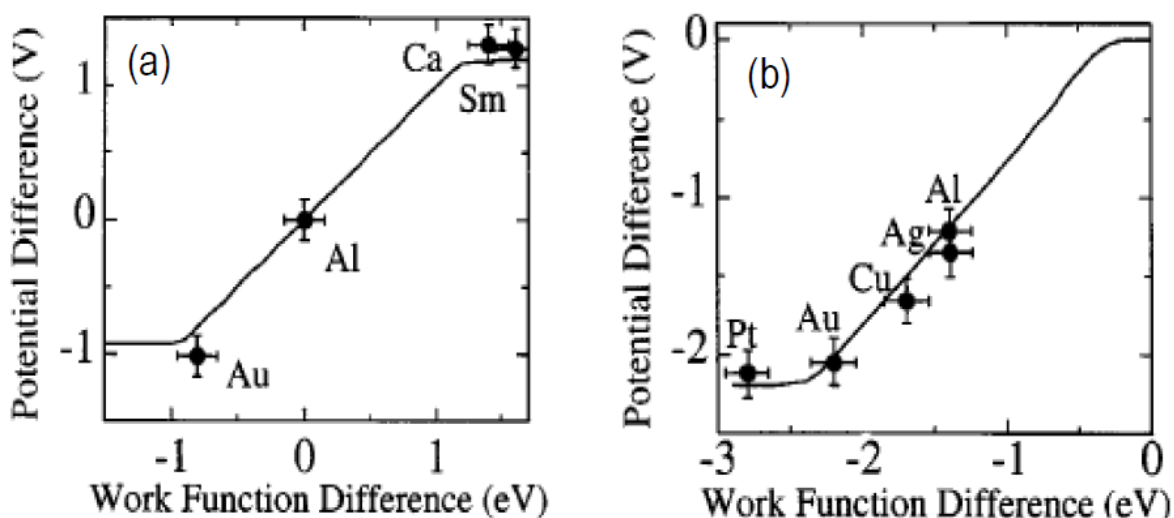
Figure 1.14: Calculated (solid line) and experimental (points) built-in potential V_{bi} across (a) metal/MEH-PPV/Al structures and (b) metal/MEH-PPV/Ca structures as a function of the work function difference of the metal contacts [Figure adapted from ref. *[27]*].

The ICT model is also supported by device data and has its origin in electroabsorption (EA) studies on metal/polymer/metal sandwich structures *[27]*. Fig. 1.14 shows that built-in potential (V_{bi}) measurements on metal/MEH-PPV/metal devices using EA spectroscopy yields characteristic "Z" dependences on Φ_{sub}, which is predicted by the ICT model outlined earlier. In a metal/polymer OSC/metal structure where the electrodes' work functions lie within the

polymer's energy gap defined by E_{ICT+} and E_{ICT-}, V_{bi} is given by the difference in work functions of the electrodes. Therefore if the work function of one of the electrodes remains unchanged, changes in V_{bi} correspond to variations in Schottky barrier height (i.e. Δ) at an electrode/polymer interface. The "Z" shape dependences of V_{bi} measurements in Fig. 1.14 clearly show that the ICT model is applicable in describing the interface energylevel alignment in working devices.

1.6 Built-in Fields in Metal/Polymer OSC/Metal Structures

Built-in field distribution in a metal/OSC/metal diode structure at equilibrium is heavily influenced by width of the charge-depletion layer W in the OSC layer, which can be approximated as follows *[69]*:

$$W \approx \sqrt{\frac{2\varepsilon_r \varepsilon_0 V_{bi}}{qN_D}} \tag{1.12}$$

where N_D denotes dopant concentration in the OSC layer; while ε_r and ε_0 denotes relative dielectric constant and vacuum permittivity, respectively. Using the "abrupt" approximation built-in potential decreases only across the charge-depletion's width and the bulk of the semiconductor remains field-free. Therefore the built-in field in diodes with a thick semiconductor active layer (i.e. $d \gg W$, where d denotes semiconductor's thickness) occurs near the metal/semiconductor interfaces. But if separation between the two electrodes is shortened, there exists a critical OSC thickness that corresponds to the sum of the electron and hole depletion regions for which a built-in field extends across the entire structure.

Eq. (1.12) enables estimation of this critical thickness value in polymer OSCs based on their ε_r, N_D and V_{bi}. Most organic diodes are fabricated with OSCs of relatively high purity *[4, 16, 27, 115, 116]* although unwanted impurity dopants of small concentration may remain from their chemical synthesis. Therefore N_D in polymer OSCs are significantly lower compared to n-doped or p-doped inorganic semiconductors. Indeed photoemission spectroscopic measurements *[23]*

on poly(9,9'-dioctylfluorene) detects no band bending across the polymer with d approaching 110 – 160 nm, implying that typical length scale of W in polyfluorene OSCs is in the micrometer range *[23, 117]*. Using eq. (1.12) simple estimation of W with typical values of V_{bi} in PLEDs (~ 1 – 2 V), dopant concentration of 10^{14} cm^{-3} and the ε_r of polyfluorene-based OSCs (~ 3 *[19]*) leads us to conclude that W is ~ 1.8 μm, which is ten times larger than typical polymer thicknesses found in diode structures *[115, 118-120]*. Therefore polyfluorene-based OSCs in devices at electrical equilibrium resemble charge-free dielectrics. Interestingly eq. (1.12) shows that W of a polyfluorene OSC layer comprising dopants up to 10^{16} cm^{-3} (~ 180 nm) is still larger than typical thickness for active layer in PLEDs (~ 100 nm *[115, 118-120]*), so internal fields may extend across the entire active layers in working devices at such condition.

Another possible source of dopant in polymer OSCs is charges localised at the electronic trap states, which is determined by the density of the traps in the polymer. Davids *et. al. [121]* performed detailed simulations to study effects of trapped charges on band profile in a metal/MEH-PPV/metal diode at electrical equilibrium. It was found that introducing a trap density of ~ 10^{16} cm^{-3} (and lower) at $\pm$ 0.6 eV from the middle of the band gap did not affect the depletion width of MEH-PPV. Therefore the diode structure is fully depleted and that the built-in field is uniformly distributed in the bulk of the polymer layer in reverse or weak forward bias. This simulation agrees well with experimental measurements on MEH-PPV diodes *[122]* and highlights the fact that W is larger than the thickness of polymer OSCs in diode structures. These observations clearly show that energy bands of polymer OSC layers in diode structures can be approximated by rigid bands. Accordingly the built-in field F_{bi} is extended through the entire OSC layer:

$$F_{bi} = \frac{V_{bi}}{d} \tag{1.13}$$

Eq. (1.13) shows that the V_{bi} of an OSC layer in a metal/OSC/metal structure is the difference in Φ_m of the two metal electrodes. Using eq. (1.13), the energy band diagrams of different metal/OSC/metal structures can be determined by measuring the V_{bi} of the specimens *[97, 123]*.

CHAPTER 2

Introduction to Electroabsorption Spectroscopy

2.1 Introduction to Modulation Spectroscopy

Modulation spectroscopy *[124]* is commonly used to study the fundamental physics of heterostructures and bulk semiconductors. Compared to such techniques as photoemission spectroscopy, modulation spectroscopy can study properties of electronic devices in their actual form under working conditions, thereby yielding data that is directly correlated to the performance characteristics of the devices *[51, 52, 125-127]*. Modulation spectroscopy is a pump-probe spectroscopic technique that relies on the use of a pump source in the form of periodically oscillating perturbation to excite the device. The modulated perturbation can take the form of electric field *[128]*, magnetic field, mechanical stress or photon pulse etc. Such excitations induce modulated changes in optical transitions that may be detected by a probe beam in the form of static monochromatic light.

Since optoelectronic devices are driven by an externally applied electric field, electromodulation or electroabsorption (EA) spectroscopy that uses electrical perturbation is useful in studying the physics of such working devices. In the context of organic optoelectronic devices, EA spectroscopy presents another unique advantage as it can probe internal electric fields of individual components embedded in mutilayered organic electronic devices *[123, 129]*. This makes EA spectroscopy an attractive technique for studying the physical mechanisms underlying the operations of polymer-based optoelectronic devices. For this reason, an EA system has been constructed and used as the primary investigation technique for this dissertation. Practical details of the EA spectrometer are disclosed in chapter 3.

2.2 Electroabsorption Spectroscopy

Like other modulation spectroscopic techniques, EA spectroscopy measures the normalised change in light transmittance through (or reflectance from) a sample (in this case a polymer light emitting diode), which is subjected to excitation by an electric field. Ignoring multiple reflections and interference within the sample, the transmitted intensity of light, I_t normally incident through a sample can be expressed as:

$$I_t = I_o (1-R)^2 e^{-\alpha d} \tag{2.1}$$

where I_o is the incident light intensity, R is the reflection coefficient (assumed to be identical for both front and back surfaces), α is the absorption coefficient and d is the distance light traverses through the material.

The absorption and reflection coefficients change when an electric field F is applied across a polymer layer. Such field-induced change of the transmitted light intensity $\partial I_t/\partial F$ is given by:

$$\frac{\partial I_t}{\partial F} = -I_o e^{-\alpha d} \left[d(1-R)^2 \frac{\partial \alpha}{\partial F} + 2(1-R)\frac{\partial R}{\partial F} \right] \tag{2.2}$$

Since the EA signal is detected in the form of a normalised change in light transmittance or reflectance, the relationship governing the EA signal strength can be derived by dividing eq. (2.2) with the unperturbed transmitted light intensity, I_t given in eq. (2.1):

$$\frac{\Delta T}{T} = \frac{\Delta I_t}{I_t} = -d\Delta\alpha + \frac{2}{(1-R)}\Delta R \tag{2.3}$$

For typical operating conditions of EA experiments, the second term in eq. (2.3) may be neglected for the sake of approximation:

$$\frac{\Delta T}{T} = \frac{-\Delta R}{R} \approx -d\Delta\alpha \qquad (2.4)$$

As shown in eq. (2.4), the magnitude of the normalised field-induced change of both transmittance ($\Delta T/T$) and reflectance ($\Delta R/R$) depends on both the thickness of the sample and the field-induced change in absorption coefficient ($\Delta\alpha$).

2.3 Electroabsorption: A Field-Induced Nonlinear Optical Effect

The change in extinction coefficient due to electric field perturbation ($\Delta\alpha$) is a non-linear optical effect. In a semiclassical description, such a phenomenon can be described by envisioning the interactions of external electric fields with individual atoms of a target material. Specifically the electron-cloud (that can be seen as a point charge, q) surrounding the nucleus of an atom interacts with the electric field of an electromagnetic wave, $\vec{F}$ through an electrostatic force ($q\vec{F}$) that displaces the center of electron density away from the nucleus. This leads to a local charge separation and thus a field-induced dipole μ on the atomic scale.

For the case of macromolecules that consist of ensembles of atoms, average vectorial summation of all such dipole moments lead to a bulk polarisation, $\vec{P}$ that represents an intrinsic characteristic of a material. $\vec{P}$ shows a linear response with the electric field $\vec{F}$:

$$\vec{P} = \varepsilon_o \cdot \chi \cdot \vec{F} \qquad (2.5)$$

where ε_o is the vacuum permittivity and χ is the dielectric susceptibility that quantifies the polarisability of the bulk material.

For ideal linear optical materials, dielectric susceptibilities tend to be independent of strength of the electric field. But such a linear dependence is only valid over a limited range of light

intensity. By subjecting a material to strong electric field $\vec{F}$ or intense light illumination, dipoles can be introduced in the material, thereby causing $\vec{P}$ to vary nonlinearly with $\vec{F}$. In this case, one can express the dielectric susceptibility χ_{eff} as a power series in terms of F:

$$\chi_{eff} = \chi^{(1)} + \chi^{(2)} \cdot \vec{F} + \chi^{(3)}.\vec{F}^2 + ... \tag{2.6}$$

where $\chi^{(n)}$ is the nth order dielectric susceptibility. For most materials, orders higher than $\chi^{(3)}$ are very difficult to measure. Moreover, $\chi^{(2)}$ vanishes in materials with inversion symmetry such as conjugated polymers *[128, 130]* and fullerene molecules *[131, 132]*. The reason for this phenomenon is that the changing direction of the electric field across such materials changes only the signs but not the absolute values of $\vec{P}$. Therefore, both equations:

$$\vec{P}_2 = \varepsilon_o \cdot \chi^{(2)} \cdot (+\vec{F}_l)^2 \quad \text{and} \quad -\vec{P}_2 = \varepsilon_o \cdot \chi^{(2)} \cdot (-\vec{F}_l)^2$$

have to hold true, which is only possible if $\vec{P} = 0$ and $\chi^{(2)} = 0$. As such, $\vec{P}$ of conjugated polymers can be simply written as:

$$\vec{P} = \varepsilon_o \cdot \chi_{eff} \cdot \vec{F} = \varepsilon_o \cdot (\chi^{(1)} + \chi^{(3)} \cdot \vec{F}\vec{F}) \cdot \vec{F} \tag{2.7}$$

where $\chi^{(3)}$ remains to be the highest order dielectric susceptibility that can be measured. For eq. (2.7) to be useful, however, a correlation needs to be drawn between $\chi^{(3)}$ and $\Delta R/R$ measured in practical EA experiments. This can be achieved by considering the relationship between χ_{eff} and the relative dielectric constant ε_r of the material:

$$\varepsilon_r = 1 + \chi_{eff} = 1 + (\chi^{(1)} + \chi^{(3)} F^2) \tag{2.8}$$

and the Maxwell relation that correlates the relative dielectric constant to the refractive index, N of the material:

$$\varepsilon_r = \varepsilon_{r,1} + i\varepsilon_{r,2} = N^2 = (n+ik)^2 \tag{2.9}$$

In eq. (2.9), n is the real component of the refractive index whilst k is the attenuation factor or extinction coefficient that measures the loss in power of an electromagnetic wave while propagating through a material. The real component of relative dielectric constant Re (ε_r) in eq. (2.9) can be written as:

$$\text{Re}(\varepsilon_r) = \varepsilon_{r,1} = n^2 - k^2 \tag{2.10}$$

while the imaginary component of the dielectric constant Im (ε_r) can be written as:

$$\text{Im}(\varepsilon_r) = \varepsilon_{r,2} = 2nk \tag{2.11}$$

Combining eq. (2.8) and (2.9), the variation of χ_{eff} with F can be expressed as:

$$\Delta\chi_{eff} = \chi_{eff}(F) - \chi_{eff}(0) = \chi^{(3)}F^2 = 2N\Delta N = \Delta\varepsilon_r \tag{2.12}$$

The relationship between Im(ε_r) and α can be understood by considering Maxwell's electromagnetic theory, which describes the propagation of a planar electromagnetic wave (light in the case of EA) along the x-axis direction with a fixed velocity v ($v = c/n$) through a material medium with refractive index N as:

$$E = E_0 \exp\left[i\omega\left(\frac{Nx}{c} - t\right)\right] = E_0 \exp\left[i\omega\left(\frac{nx}{c} - t\right)\right]\exp\left(\frac{-\omega kx}{c}\right) \tag{2.13}$$

where c/N and x represents the speed and the distance of light propagation in the material, respectively; c denotes the speed of light propagation in vacuum (where refractive index, $N=1$). The last term $[-(\omega kx)/c]$ in eq. (2.13) measures the attenuation factor k of the material, which is related to the refractive index, N by eq. (2.9).

Transmittance of a light wave that propogates through a material medium with refractive index N can be obtained by considering the damping factor term and the optical power (P). P or illumination intensity (I) of a light wave is determined by the conductivity (σ) of the material and the electric field vector (E) (i.e. $P=\sigma E^2$) of the light wave. Therefore transmittance of a light wave (i.e. I_t/I_0) that propagates from the surface of a material (where $x=0$) with conductivity (σ) through its thickness (where $x=d$) is given by:

$$T = \frac{I_t}{I_0} = \frac{P(d)}{P(0)} = \frac{E^2(d)}{E^2(0)} = \exp\left[\frac{-2\omega kd}{c}\right]$$

(2.14)

where k in eq. (2.14) is proportional to the material's absorption coefficient (α) and the wavelength of the light (λ) by $\alpha = (4\pi k)/\lambda$. This latter relationship, when compared with eq. (2.11), leads to the following expression for molecular solids like conjugated polymers:

$$\alpha = \frac{4\pi}{\lambda}k = \frac{2\pi}{n\lambda}\operatorname{Im}(\varepsilon_r)$$

(2.15)

Eq. (2.15) shows that the imaginary component of the third order dielectric susceptibility, $\operatorname{Im}\chi^{(3)}$ is proportional to the change in absorption coefficient, $\Delta\alpha$ and hence the change in fractional reflectance, $\Delta T/T$:

$$\Delta\alpha \propto \Delta\operatorname{Im}(\varepsilon_r) \propto \operatorname{Im}\chi^{(3)}F^2$$

$$\Rightarrow \frac{-\Delta T}{T} \approx d\Delta\alpha \propto \mathrm{Im}\,\chi^{(3)} F^2 \qquad\qquad (2.16)$$

Eq. (2.16) reveals an important characteristic: EA is a third order non-linear effect that exhibits quadratic dependence on applied electric field F. This is indeed the case for EA signals found in practical experiments conducted for this dissertation and provides an important theoretical basis for the accurate determination of charge injection barrier heights via built-in voltage (V_{bi}) measurements. The EA responses may be correlated to the macroscopic non-linear properties of the material using a semiclassical approach, thereby allowing us to understand the factors affecting the magnitude of the EA responses. Understanding the EA spectral line shapes, however, requires us to consider the physical mechanisms contributing to the electric field induced red shifts of optical transitions (i.e. Stark shifts).

2.4 Electroabsorption (EA) Response and the Stark Shift

Compared to three-dimensionally bonded inorganic semiconductors, electronic states in organic molecular solids and most conjugated polymers *[4, 35]* are localised to a higher degree. Therefore electric field-induced changes in the absorption coefficient of macromolecular solids can be generally ascribed to Stark shifts of optical transitions amongst possible molecular energy levels. In practice several transitions were found to contribute to the experimental Stark shift observed in most conjugated polymers. In particular a three-level system as shown in Fig 2.1 seems to be applicable to many conjugated polymers with inversion symmetry *[128]*. It consists of a ground state of even parity $1A_g$, an excited state of odd parity $1B_u$ and further states of either parity at higher energy that may form a continuum. Linear optical transition from the ground state $1A_g$ to the odd parity state $1B_u$ is allowed with oscillator strength f; whereas the transition from the $1A_g$ to the nA_g state is optically forbidden. Static electric field couples electronic states of different parity, thereby causing a miniscule decrease (typically few tens of μeV) in energy gap separating the $1A_g$ and $1B_u$ states if the $1A_g$ ground state is well separated from the excited $1B_u$ state. Consequently the allowed $1A_g \rightarrow 1B_u$ transition shows a red shift due to its transition dipole moment $\vec{\mu}$ to the relatively closely neighbored excited state nA_g. At the same time, the

application of an electric field induces a relaxation of the selection rules by transferring oscillator strength to the optically forbidden nA_g excited state.
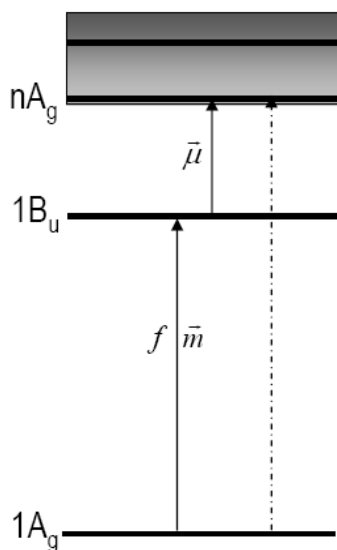
Figure 2.1: Schematic diagram of energy levels contributing to the Stark effect seen in most conjugated polymeric materials. Dotted line denotes field-induced transition while solid lines represent optical transitions that contribute to EA spectral absorptions.

Using a semi-classical approach, the red shift in energy level $\Delta E_j^{(1)}$ in molecular or macromolecular materials caused by a permanent dipole moment $\vec{m}_j$ can be expressed as follows:

$$\Delta E_j^{(1)} = -\vec{m}_j \cdot \vec{F} \tag{2.17}$$

where $\vec{F}$ denotes electric field in the material. On the microscopic level, a permanent dipole in centrosymmetric conjugated polymers can arise from charge transfer states, structural defects or disorders that introduce a local asymmetry in charge distribution along a polymer chain segment *[133-135]*. Eq. (2.17) illustrates the linear Stark shift of the molecular energy levels owing to the linear dependence on $\vec{F}$.

With the exception of highly ordered *[134, 135]* or single crystalline polymeric systems *[136]*, spin-cast macromolecular films generally possess an ensemble of polymer chains that are randomly oriented in three dimensional space. Accordingly linear Stark shifts are not generally observed as spatial averaging of all local permanent dipoles inevitably nulls their contributions towards the spectral shift of an optically isotropic polymer *[128]*. Therefore, the EA response of bulk conjugated polymer films $\Delta E_j^{(2)}$ is usually dominated by the field-induced dipole contribution *[128, 130, 135, 137, 138]* that varies quadratically with $\vec{F}$:

$$\Delta E_j^{(2)} = -\frac{1}{2} p_j \cdot \vec{F}^2 \tag{2.18}$$

where p_j is the polarisability that varies with the nature of the excitonic state and degree of crystallinity of the material*[130]*. This term, commonly known as the quadratic Stark effect, originates from the presence of a macroscopic dipole moment induced by the electric field and is responsible for causing the red shift of the $1A_g \rightarrow 1B_u$ excitonic transition energy gap.

In principle, absorption spectra of conjugated polymers may be affected by both the linear and quadratic field-induced Stark effects *[128, 133]*. The electric field-induced change in the transition energy, $\Delta E(F)$ can thus be expressed as a combination of both terms shown in eq. (2.17) and (2.18) *[138]*:

$$\Delta E = E(F) - E(0) = -(\vec{m}_f - \vec{m}_i) \cdot \vec{F} - \frac{1}{2} \Delta p \cdot \vec{F}^2 \tag{2.19}$$

where $\vec{m}_f$ and $\vec{m}_i$ are the dipole moments in the final excited state and initial ground state typically induced by disorder *[133]*. Similarly, Δp is the change in polarisability of the excited state induced by electric field perturbation.

The field-induced change in reflectance measured in EA experiments can be expressed in terms of change in molecular state's energy level ΔE in the form of a MacLaurin series truncated at the second order term due to the miniscule spectral shifts (typically tens of µeV for conditions encountered in EA experiments *[52, 137]*):

$$\Delta\alpha = \left\langle \frac{\partial\alpha}{\partial E}\Delta E \right\rangle + \frac{1}{2}\left\langle \frac{\partial^2\alpha}{\partial E^2}\Delta E^2 \right\rangle \tag{2.20}$$

Inserting eq. (2.19) into eq. (2.20) yields the change in absorption coefficient $\Delta\alpha$ in terms of the modulating electric field *F*. As mentioned earlier, isotropic averaging of the randomly oriented molecular dipoles nulls the $\left\langle \Delta\vec{m}\cdot\vec{F} \right\rangle$ contribution to the first order term $\partial E/\partial F$ in eq. (2.20). Therefore the first-order derivative term of eq. (2.20) contains only field-induced dipole moment contribution (i.e. ½ ΔpF^2), which is always present in disordered macromolecular materials.

In contrast, isotropically averaging the square of randomly-oriented permanent dipole moments yields non-zero contribution to second order term $\partial^2 E/\partial F^2$ and can be written as:

$$\left\langle \left(\Delta\vec{m}\cdot\vec{F}\right)^2 \right\rangle = \frac{1}{3}(\Delta m F)^2 \tag{2.21}$$

Change in exciton polarizability in conjugated polymers typically ranges from $10^{-19} - 10^{-18}$ eV m^2/V^2, so the contribution of the square of the field-induced dipole moment (i.e. $\Delta p^2 F^4$) to the field-induced spectral shifts is too small and may be safely neglected. Using these approximations, the field-induced change in absorption $\Delta\alpha$ can therefore be rewritten in terms of linear and quadratic Stark effects:

$$\Delta\alpha = \frac{1}{2}\left[-\left\langle \Delta p \right\rangle \frac{\partial\alpha}{\partial E} + \frac{1}{3}(\Delta m)^2 \frac{\partial^2\alpha}{\partial E^2} \right]F^2 \tag{2.22}$$

A third contribution that needs to be added to eq. (2.22) is the transfer of oscillator strength to the higher lying excited states, which are normally forbidden in unperturbed optical transition. Such a field-induced relaxation of the selection rules is predicted by the Stark effect *[135, 137]* and also varies quadratically with electric field *F*.

$$\frac{\Delta f_{ij}}{f_{ij}} = e^2 F^2 \frac{\left|\left\langle \Psi_j \left|z\right| \Psi_i \right\rangle\right|^2}{\left(E_i - E_j\right)^2}$$

(2.23)

In isotropically conjugated polymers, the term in eq. (2.23) can be approximated with a contribution that follows the line shape of the absorption spectrum.

By combining eq. (2.22) and (2.23), shapes of EA spectra of isotropic conjugated polymers *[128, 130]* can be modelled as a linear combination of field-induced spectral absorptions, its first order derivative and its second order derivatives as well as bleaching of allowed optical transitions:

$$\Delta\alpha = a\alpha + \frac{1}{2}\Delta p F^2 \frac{\partial\alpha}{\partial E} + \frac{1}{6}\Delta m F^2 \frac{\partial^2\alpha}{\partial E^2} + \alpha'$$

(2.24)

The first term in eq. (2.24) describes field-induced bleaching of absorption due to transfer of oscillator strengths from allowed to forbidden transitions (i.e. $a < 0$); while α' denotes field-induced absorption. By fitting experimental EA spectra with eq. (2.24), important parameters such as Δp of an excitonic state, which is proportional to conjugation length of the OSC *[130, 136]*, may be extracted. In general, the EA spectrum of a conjugated polymer comprises contributions from all components. Nevertheless, relative contribution of the second order derivative term $\partial^2 E/\partial F^2$ to the spectral line shape depends greatly on the degree of crystallinity in the polymer film.

Analysis based on Stark effect on localised molecular states is found to work well for many luminescent and non-luminiscent conjugated polymers*[128]*, especially at wavelength ranges close to the excitonic absorption edges of these materials. But other effects may become

important depending on the exact material and experimental conditions. For instance, in inorganic semiconductors where the excitonic wavefunction is truly delocalised and a continuum of states is present, the line shape follows the third order derivative of absorption spectrum in the low-field region *[139]*. For higher electric fields the quantum mechanical approach of Franz and Keldysh may become necessary as the latter is dominant in crystalline inorganic semiconductors but not readily visible for molecular or polymeric solids that have relatively short coherence length *[135]*. Nevertheless, Franz-Keldysh oscillations have been seen in high quality polydiacetylene single crystals *[136, 138]*.

It is important to emphasise that the hallmark of Stark shifts of excitonic transitions in conjugated polymers is its quadratic dependence on electric field *F*. As will be discussed in the following section, this dependence is critical in determining V_{bi} across organic-metal and organic-organic heterojunctions in polymer light-emitting diodes (PLEDs). Accurate measurement of V_{bi} is the key to monitor the variation in charge injection/extraction barrier height within *finished* devices under operational conditions in a non-destructive manner.

2.5 Measurements of EA Signals in Conjugated Polymers

As described in the previous section, EA measures the normalised change in reflectance of light passing through a material when subjected to an electric field. EA studies on conjugated polymers have been carried out with two different sample structures: the interdigitated electrode geometry *[128, 137]* and the multilayer geometry closely resembling that of working optoelectronic devices *[4, 27, 52, 130, 140]*. The first structure involves depositing metal electrodes over a transparent substrate in the interdigitated array geometry shown in Fig 2.2 and polymer films are then spin-coated over the electrodes. During EA measurement, a probe beam illuminates the sample in the direction perpendicular to the polymer surface, traverse through the material between the electrode fingers and is subsequently collected by a photodetector at the other side of the substrate. Meanwhile a voltage has to be applied across the electrode to create an electric field in the polymer layer, which gives rise to an EA signal that varies with applied electric field *F* and the imaginary, third order dielectric susceptibility Im $\chi^{(3)}$ as follows *[128]*:

$$\frac{-\Delta T}{T} = \frac{\Delta R}{R} \approx d\Delta\alpha \propto \mathrm{Im}\,\chi^{(3)} F^2 d \tag{2.25}$$

Typical values of $\chi^{(3)}$ for conjugated polymers are in the range of 10^{-12}–10^{-10} esu *[141]*, therefore an electric field as high as ~ 0.1 – 1 MV/cm has to be applied across the sample to amplify $\Delta R/R$ signal to a range between 10^{-7} and 10^{-4} so that signal can be detected by the lock-in amplifier. Although the interdigitated electrode geometry remains the preferred structure for studying electronic excitations and non-linear optical properties of conjugated polymers *[128, 133-137]*, it necessitates the use of high sinusoidal voltage of 10^2-10^3 V for generating a measurable signal. Moreover it is not closely related to the multilayered structure commonly found in optoelectronic devices *[4, 140]*.
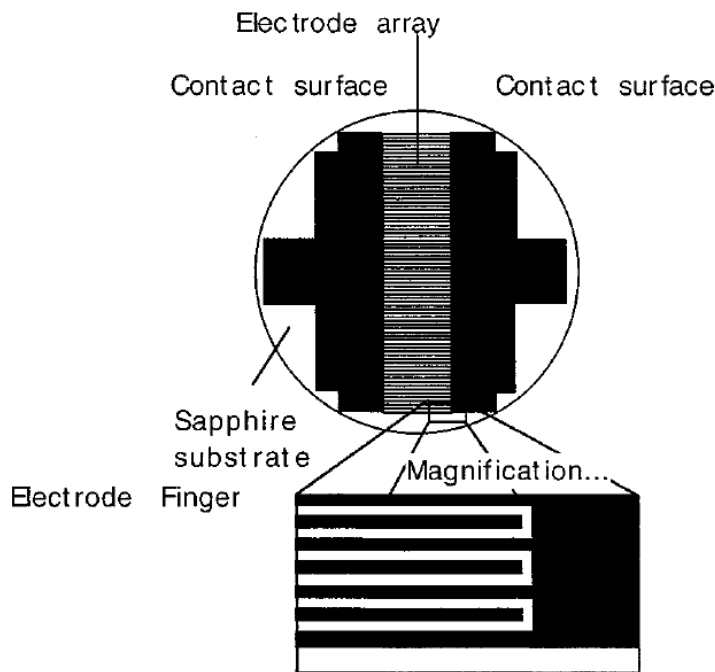
Figure 2.2: Plan view of the interdigitated electrode configuration used in EA experiments. [Figure adapted from ref. *[128]*]

Pioneered by the work of Campbell *et. al. [27]*, EA experiments have also been extended to multilayered metal/polymer/metal sandwich structures *[48, 49, 51, 52, 130]* [see Fig. 2.3]. In this geometry, one or both of the electrodes needs to be transparent or semitransparent for light to optically excite the conjugated polymer (that may comprise more than one layer) sandwiched between the two electrodes. After passing through the polymer layer, light is then transmitted through, or reflected by, the second metal electrode over the polymer layer. In practice, only one semitransparent electrode is necessary since light illuminating the sample can be specularly reflected at $\sim 45^0$ by the back electrode that acts as a mirror. This sample structure has the virtue of increasing the distance that photons have to travel through the polymer layer. Note that the metal/polymer/metal structure is identical to those of organic LEDs and organic photovoltaic devices, making EA a powerful technique as it enables direct correlation of EA results with the performance characteristics of the device.
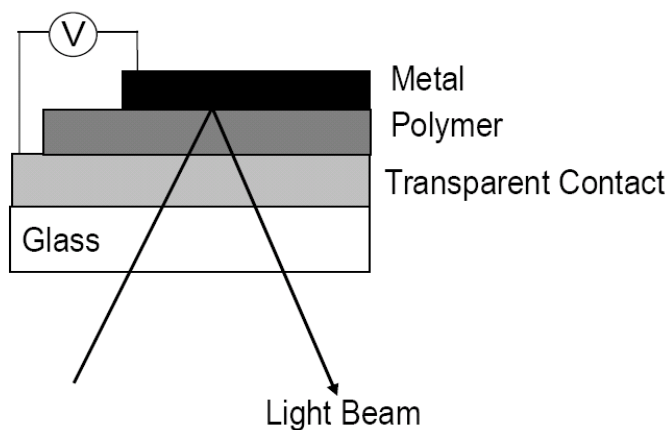
Figure 2.3: Side view of the multilayered sample geometry resembling that of working optoelectronic devices. A monochromatic probe beam enters the diode through the glass substrate and travels through polymer layer twice before exiting the sample.

Another important advantage of the multilayered sample geometry is that the built-in electric field (F_{bi}) across the active polymer layer can be as high as $0.01 - 0.1$ x 10^6 V/cm since the thickness of the conjugated polymer layer only ranges between 70 nm and 100 nm. This means that sinusoidal voltages ($10^{-1} - 10^0$ V) much lower than that required in the interdigitated

geometry can be used. These advantages make the multilayered structure ideal for investigating the interfacial energy level alignment *[48, 51, 52, 97, 142, 143]*, internal electric field distribution *[49, 98, 123]* and polaronic charge transport levels of conjugated polymers *[27]* in *finished* optoelectronic devices. Since interfacial electronic structure plays a decisive role in understanding, controlling and improving device performance characteristics, this dissertation focuses on studying interfacial electronic structures found in working polymeric devices with multilayered geometry using the EA spectroscopy.

EA technique involves applying an electric bias that comprises a linear combination of a DC and a sinusoidal AC component $V = V_{dc} + V_{ac} \sin(\omega t)$ across the polymer layer. Assuming charge depletion within the polymer layer, the combined electric field in the polymer layer is:

$$F = F_0 + F_{ac} \sin(\omega t) \tag{2.26}$$

where F_0 is the DC field component and F_{ac} is the AC field component modulated at fundamental frequency (1ω). The EA response to such a composite electric field can be deduced by inserting eq. (2.25) into eq. (2.26), yielding the following expression after simple trigonometric manipulations:

$$\frac{\Delta R}{R}(h\nu) \propto \mathrm{Im}\,\chi^{(3)}(h\nu)\left\{F_0^2 + 2F_{ac}F_0 \sin(\omega t) + F_{ac}^2[\frac{1 - \cos(2\omega t)}{2}]\right\} \tag{2.27}$$

Eq. (2.27) shows that the electrical perturbation causes $\Delta R/R$ to be modulated at both fundamental and second harmonic (2ω) frequencies. Employing a phase sensitive lock-in amplifier allows one to separately measure the 1ω component of the EA signal:

$$\frac{\Delta R}{R}(h\nu) \propto 2\,\mathrm{Im}\,\chi^{(3)}(h\nu)F_{ac}F_0 \sin(\omega t) \tag{2.28}$$

where the DC field component F_o is a linear combination of F_{bi} that arises from equilibration of the electrodes' Fermi levels (i.e. E_f) and externally applied electric field F_{dc}. Most conjugated polymer OSCs used for optoelectronic device fabrication are of high-purity, so DC field (F_o) is uniformly distributed along the vertical thickness d of the polymer [i.e. $F_0 = (V_{bi} + V_0)/d$]. Therefore the 1ω EA signal of a polymer OSC that is depleted of charges is given by:

$$\frac{\Delta R}{R}(h\nu, \omega) \propto 2\,\text{Im}\,\chi^{(3)}(h\nu)V_{ac}(V_{dc} + V_{bi}) \tag{2.29}$$

Eq. (2.29) indicates that at electrical equilibrium, the V_{bi} is simply the DC bias needed to null the 1ω EA signal. In practice F_{bi} across the polymer layer is strongly influenced by local charge accumulation that may arise from electrical injection [49, 50, 98], electrical [144] or chemical doping [145], which affect the long-term operational stability of optoelectronic devices [146]. This makes EA spectroscopy uniquely suited to investigating physical processes affecting polymer-based device degradation [146] and performance characteristics.

Similar analysis leads us to conclude that the 2ω EA signal of a polymer layer varies quadratically with the AC field and hence V_{ac}:

$$\frac{\Delta R}{R}(h\nu) \propto \frac{1}{2}\text{Im}\,\chi^{(3)}(h\nu)F_{ac}^{2}\cos(2\omega t)$$

$$\Rightarrow \frac{\Delta R}{R}(h\nu, 2\omega) \propto \frac{V_{ac}^{2}}{2} \tag{2.30}$$

Deviation of 2ω EA response from eq. (2.30) is useful in confirming the presence of space charge that modifies the electric field distribution in the polymer active layer of the device. In this way the 2ω EA signal measurement gives additional information on current injection complementary to V_{bi} determination [49, 50], which provide insights into the operational mechanisms of PLEDs.

2.6 EA as Tool for Studying Interface Energetics in Organic Electronic Devices

Independent studies done by Campbell *et. al. [27]* and Salaneck et. al. *[29]* have shown that Schottky-Mott limit is valid in explaining the energy level alignment across various metal-polymer junctions, so long as the metal's E_f lies within the energy gap of the conjugated polymer. As illustrated by Fig 2.4 (a), the V_{bi} across a metal/polymer/metal structure is equal to the difference in work function ($\Delta\Phi_m$) of the two metal contacts:

$$V_{bi} = \frac{\Delta\Phi_m}{q} \pm \delta \tag{2.31}$$

δ in eq. (2.31) represents experimental error inherent in EA measurements. One of the distinguishing characteristics of PLEDs is their reliance on energetically asymmetric charge-injecting electrodes to optimise electroluminescence (EL) efficiency *[47]* through balancing the electron and hole current. Such a requirement led to the use of low work function cathodes e.g. calcium ($\Phi \sim 2.85$ eV) and high work function anodes e.g. gold ($\Phi \sim 5.1$ eV) as electrodes, resulting in V_{bi} that exceed 2 V in some cases. Since the thicknesses of light-emitting OSC layer in PLEDs are typically $\sim 70 - 100$ nm, eq. (2.31) indicates that the OSC active layers are subjected to large F_{bi} ($\sim 10^5 - 10^6$ V/cm) at electrical equilibrium. This large internal field has the virtue of amplifying the EA signals for accurate determinations of interfacial electronic structures across metal/polymer heterojunctions *[27, 48, 51, 52]*.

Accurate measurements of interfacial energy alignment hinge on the assumption that metal/polymer/metal structures resemble capacitors with negligible space charge trapped in polymer OSC layers. The validity of this assumption is proven by capacitance measurements conducted on samples comprising a homopolymer (i.e. one single polymer component) sandwiched between two metal electrodes *[48, 121, 122]*. Nevertheless, no similar measurements have been conducted on polymer-based optoelectronic devices having two or

more polymer components that form type II organic-organic heterojunctions. Results of electrical impedance measurements on such devices cannot directly correlate with the EA results owing to the inherently charge-generating nature of type II organic-organic heterojunctions upon light illumination *[147]*.

Fig 2.4 illustrates the physical meaning of V_{bi} in a metal/polymer/metal sandwich structure measured from EA technique using rigid band approximation. Consider the case when E_f of both metal electrodes lie within the energy gap defined by the highest occupied molecular orbitals (HOMO) and lowest occupied molecular orbitals (LUMO) of the polymer layer [Fig 2.4 (a)]. If vacuum level alignment occurs at both metal/polymer junctions, the measured V_{bi}, which arises from E_f equilibration across the sandwich structure, is simply the difference in work functions of the electrodes in accordance with eq. (2.31). Meanwhile V_{bi} scales linearly with the difference in the electrodes' work functions (i.e. Schottky-Mott limit).

On the other hand, if the work function of the cathode is less than the electron affinity of the organic layer, the E_f at the cathode will be pinned close to the LUMO of the polymer *[27]*. A similar process occurs at the anode if the work function of the anode is greater than the ionization potential of the organic layer. When E_f pinning occurs at both metal/polymer junctions, the measured V_{bi} is close (but *not* identical due to exciton binding energies) to the optical gap of the electrically doped polymer layer [Fig 2.4(b)]. The V_{bi} does not change with the work functions of metal electrodes ($S = 0$) but is limited by the energy gap of the polymer layer.

It is critical to point out that the exact pinning levels of metal-polymer heterojunctions are highly sensitive to the nature of the materials and exact conditions of device fabrication. Moreover, the pinning levels may deviate substantially from the HOMO and LUMO levels of the neutral polymers owing to the polaronic/bipolaronic nature of charge carriers in doped systems *[27, 29]*. The exact pinning levels of conjugated polymers remain to be a subject of considerable debate and are under continual investigation. Nevertheless, EA spectroscopy has been demonstrated to be useful in detecting pinning levels in finished metal/polymer/metal structures of various material combinations *[27, 50, 52, 99, 148]*.

One point worth investigation is the phenomenon of charge transfer across metal/polymer junctions that results from E_f pinning [Fig 2.4 (d)]. Accurate V_{bi} measurement requires that the metal/polymer/metal structure resembles a capacitor with the polymer film depleted of charges. Yet Fig. 2.4 (d) highlights that formation of ohmic contact(s) invariably leads to electrical doping of the polymer chains near the interface by charges transferred from metal electrode(s).

Therefore the assumption of charge depletion in polymer film is probably incorrect for diode structures having ohmic junction(s) at one or both interfaces. This problem is further complicated by the presence of type II organic-organic heterojunctions in optoelectronic devices *[129, 147]* that can facilitate photogeneration of space charges upon light illumination. The influence of this problem on accurate V_{bi} determination by EA spectroscopy will be explored and a solution to overcome this limitation will be presented.

The physical meaning of V_{bi} measured by EA spectroscopy and its relationship with both electrodes' work functions and energy gap of the polymer layer has been illustrated for two different cases. The following section will briefly describe the current state of understanding derived from EA studies on interfacial energetics at organic/metal and organic/organic interfaces (with an emphasis on conjugated polymers), which is the main objective of this dissertation.
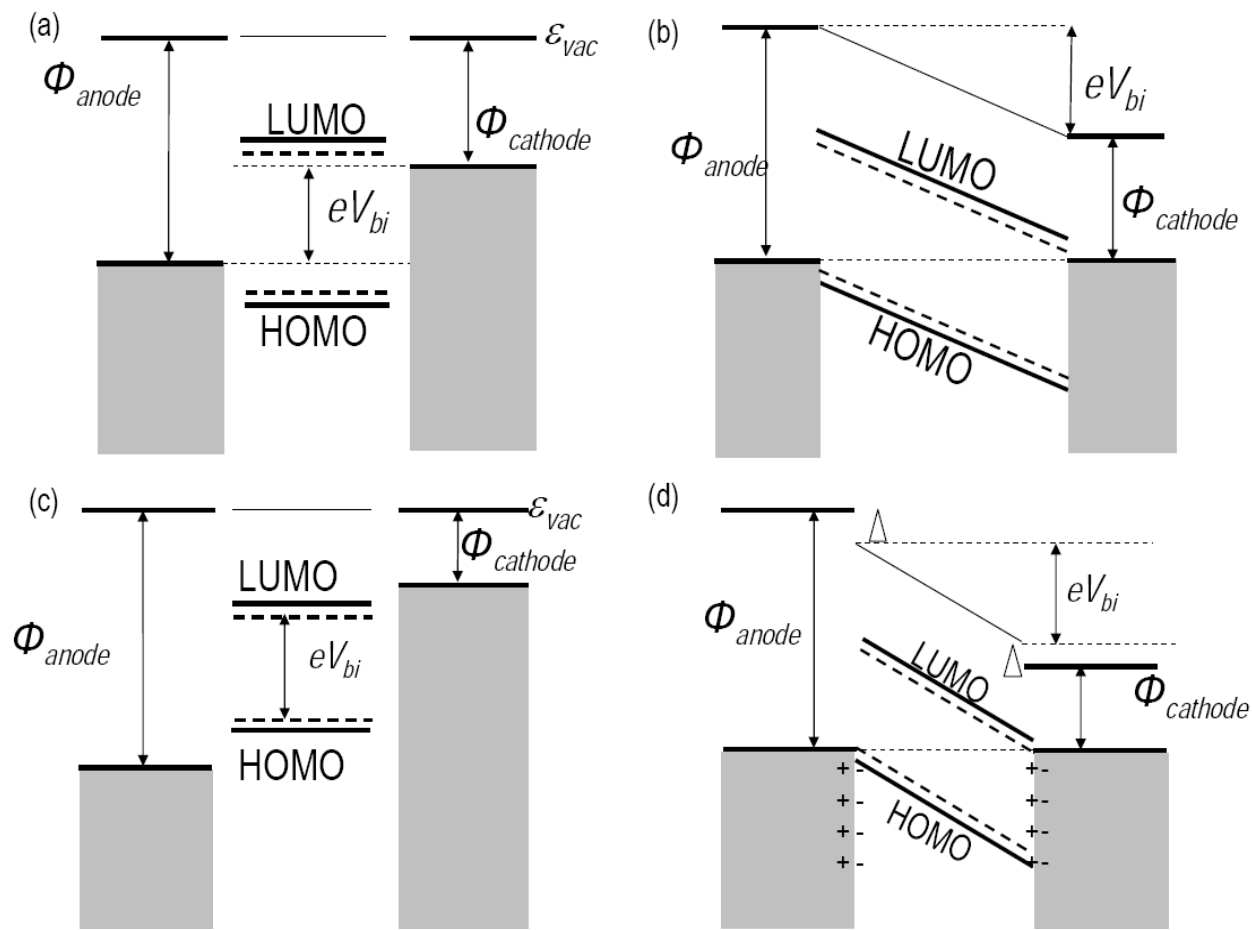
Figure 2.4: Schematic diagram showing the relationship between the V_{bi}, the electrode work functions, and the energy gap of an organic semiconductor. (a) The energy levels when no E_f pinning is expected. (b) The energy levels of a completed device structure with no E_f pinning. (c) The energy levels when E_f pinning of both electrodes is expected. (d) The energy levels of a completed device structure with E_f pinned (owing to charge transfer) at both electrodes/polymer interfaces. Δ represents the energy shift of the vacuum level ε at both interfaces. Exact pinning levels (dotted line) vary with nature of the polymer. [Figure adapted from ref. *[97]*]

2.7 EA Studies on Functional Heterojunctions in Organic Electronic Devices

EA spectroscopic studies on interfacial energy alignment across metal/polymer heterojunctions in *finished* devices were first conducted by Campbell *et. al.*[27] on a series of metal/MEH-PPV polymer/metal structures. The measured F_{bi} values were compared against those derived from difference in work functions [see eq. (2.31)]. The resulting V_{bi} measurements are summarised by Fig. 1.14 in Chapter 1. These results, together with Schottky barrier height measurements obtained by internal photoemission spectroscopy (IPES), demonstrate that energetics across most metal/MEH-PPV junctions can be aptly described by the Schottky-Mott limit since the V_{bi} scales linearly with the difference in electrodes' work functions. But for metals whose bulk E_f lies beyond the energy gap of MEH-PPV, the V_{bi} saturate instead of scaling with work function difference (i.e. $V_{bi} \neq \Delta\Phi/q$). Interestingly, theoretical calculations[27] [solid line in Fig 1.14] show that the E_f of low-work function (Ca and Sm) and high work function metals (Pt) are pinned close to the bipolaronic levels of MEH-PPV.

Nevertheless, comparison of the V_{bi} and IPES measurements on Schottky energy barriers show that the binding energy of bipolaron (deduced from V_{bi} measurements) is almost identical to that of the single particle polaron (determined from IPES) within the ~ 100 meV error limit of these techniques. With this observation, it was concluded that bipolarons are not strongly bound *[27]* and not likely to significantly affect device performance. This observation, however, is not consistent with recent ultraviolet photoemission spectroscopic (UPS) studies *[26, 29, 75]* that suggest the bipolaronic binding energies in conjugated polymers to be 400 meV to 700 meV.

EA spectroscopic studies have also been extended to working PLED structures employing a commercially important conducting polymer poly(3,4-ethylenedioxythiophene) doped with poly(styrenesulfonate) (PEDOT:PSSH) *[52]* instead of metal anodes [see Fig. 2.5]. Measurements were conducted on two different devices that share a common cathode but of two different transparent anodes (indium tin oxide, ITO or PEDOT:PSSH). Fig. 2.5 shows that the V_{bi} increases by 0.5 V when PEDOT:PSSH is inserted between the ITO electrode and the

polymer emissive layer, thereby indicating a 0.5-eV reduction in the anode barrier height at the PEDOT:PSSH/polymer interface that accounts for the improvements in EL efficiency and operational lifetime.
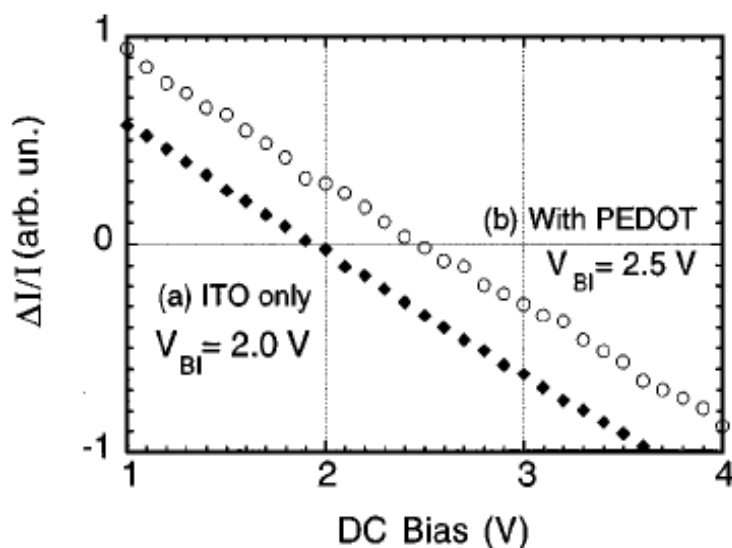
Figure 2.5: EA (1ω) response at 2.95 eV as a function of applied DC bias for the (a) ITO/PDPV/Ca–Al and (b) ITO/PEDOT:PSS/PDPV/Ca–Al structures. The increase in V_{bi} is attributed to lowering of the anode barrier height due to PEDOT:PSSH insertion [Figure taken from ref. *[52]*].

Further studies of the effects of PEDOT:PSSH on the PLED performance characteristics were conducted with EA spectroscopy *[50, 98]*. These studies show that the superior EL efficiencies of PLEDs containing PEDOT:PSSH is not only caused by the lowering of the hole injection barrier but also partly by the electron blocking ability of PEDOT:PSSH. This unique characteristic of PEDOT:PSSH results in *in-situ* formation of an ohmic junction within *finished* PLEDs upon significant electron injection from a low-work function cathode *[149]*. Since this interface dipole is caused mainly by the accumulation of electrons near the PEDOT:PSSH/polymer interface, it cannot be observed through UPS study on non-device structures (PEDOT:PSSH/polymer). Rather it forms only in *complete* device structures (i.e. PEDOT:PSSH/polymer/metal) and requires the presence of a low work-function cathode (e.g. Ca, Sm and Ba). Similar phenomenon has been observed in several independent studies *[64, 149, 150]* on different metal/polymer/metal structures with the use of current-voltage measurements

and/or device modeling. These studies therefore highlight the unique role of EA spectroscopy in deducing interfacial energy alignment in finished structures and understanding the operational mechanisms of high-performance optoelectronic devices.

Brown *et. al. [48, 51]* has also employed EA spectroscopy to study the effects of incorporating a thermally evaporated LiF layer between Al and the polymer film on the cathode barrier heights in working diodes. It was found that having a thin LiF interlayer (7 – 10 nm) between Al and the polymer emissive layer leads to a 1.1-eV reduction in cathode barrier height. These observations were used to account for the vast reduction in EL turn-on voltage and improvement in EL efficiency. V_{bi} measurements of Brown *et. al. [48, 51, 52]* on metal/polymer/metal structures effectively established EA spectroscopy as a pertinent tool in extracting energy alignment information that is highly relevant to various functional parameters of PLEDs of one single polymer system. But highly emissive PLEDs typically have two or more polymeric components to form type II organic/organic heterojunctions *[11, 47]* to achieve optimal balance in charge injection and electron-hole recombination.

EA spectroscopic determination of the pinning level in photovoltaic devices with type II organic/organic heterojunctions has been reported by Heller *et. al.[99]*. Systematic investigations were conducted on C_{60}-doped MEH-PPV bulk heterojunction photovoltaics by studying the variation of V_{bi} with electrodes' work functions. Fig 2.6 shows the energy level diagrams of pristine MEH-PPV and C_{60}-doped MEH-PPV diodes. In the case of undoped MEH-PPV, metal E_f are pinned close to the polaronic levels of the polymer. Upon doping with C_{60}, the E_f of the cathode is expected to pin close to the LUMO level of C_{60}. This is manifested as a 0.6V reduction in the measured V_{bi} values for diodes having anodes of different work functions. Accordingly the extent of the decrease in V_{bi} was used to deduce the electron polaron level of C_{60} in the device. It was shown that electron polaron level of the bulk C_{60} film (electron affinity ~ 3.3 eV*[132]* using inverse photoemission measurements) is lowered by 300 meV after blending with the MEH-PPV polymer host. The relative alignment of energy levels shown in Fig 2.6 can be similarly applied to that in a device comprising a bilayer organic/organic heterojunction, in

which case the V_{bi} is limited by the organic layer with the highest lying electron affinity (or LUMO level) and the organic layer with the lowest lying ionisation potential (or HOMO level).
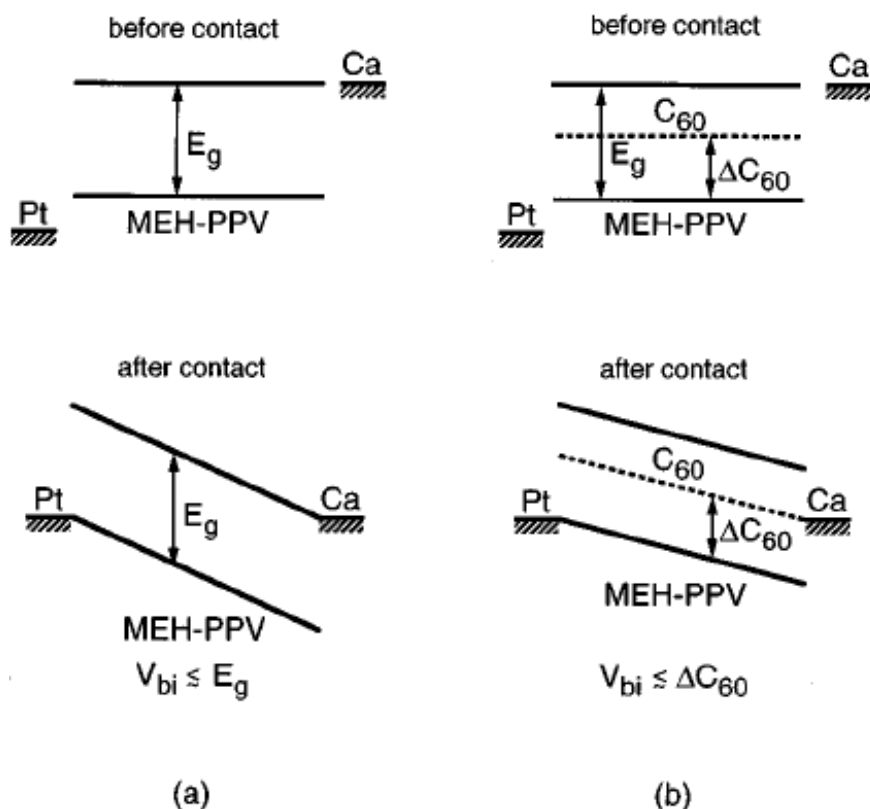
Figure 2.6: Schematic energy level diagrams showing the effects of incorporating a high-electron affinity component (in this case C_{60}) on the measured V_{bi} of the diodes. (a) In undoped MEH-PPV, the measured V_{bi} is limited by the energy gap of the polymer; (b) upon doping with C_{60}, the measured V_{bi} is limited by the difference between positive polaronic level of MEH-PPV and negative polaronic level of C_{60}. [Figure from ref. *[99]*]

EA spectroscopy has also been used to understand the electric field redistribution in organic small molecule LEDs under the condition of strong charge injection *[49, 50, 123]*. Interestingly, an EA study on multilayered small molecule organic LEDs reveals highly unequal electric field distribution across different organic layers *[123]*. The measured difference in electric field was used to estimate the density of accumulated charges across the interfaces of different

organic/organic heterojunctions, yielding areal accumulated charge densities ranging between ~ $3 \times 10^{11} - 2 \times 10^{12}$ cm^{-2}.
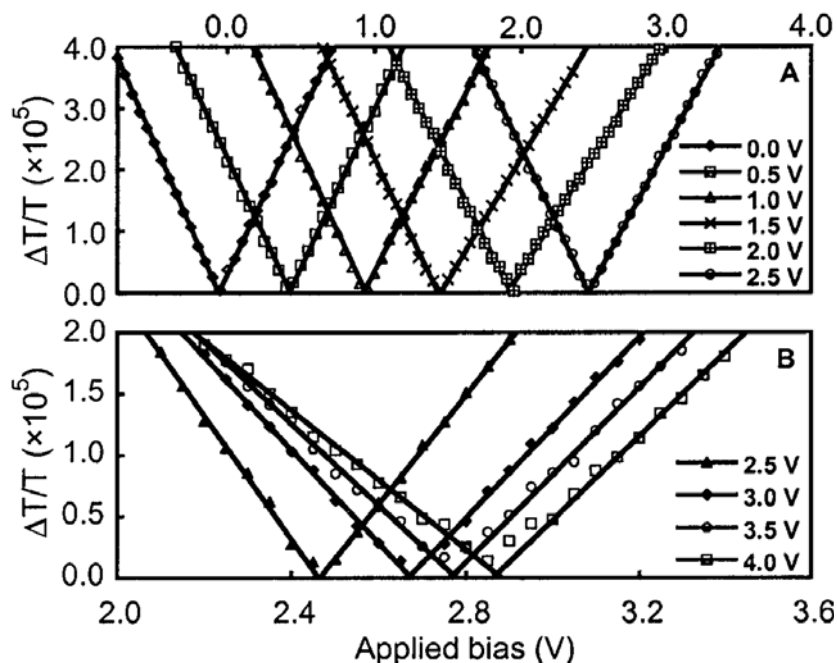
Figure 2.7: Variation of EA (1ω) response with DC offsets for LECs preconditioned at different pre-biases: (A) pre-biases applied to the LEC are lower than or identical to energy gap (2.5 eV) of the undoped polymer, nulling voltage of EA (1ω) signal matches the pre-bias indicating a zero-field polymer bulk during pre-biasing; (B) applying pre-biases higher than 2.5 V causes the nulling voltage to deviate from the pre-bias values owing to significant charge injection during pre-biasing. [Figure adapted from ref. *[145]*]

The phenomenon of internal field redistribution in ion-doped light-emitting electrochemical cells (LECs) was also investigated using EA spectroscopy *[145]* by de Mello *et. al*. In this study, EA spectroscopy directly confirms that the LEC can be seen as a cathode/doped-polymer/polymer/doped polymer/anode structure under certain operational conditions. An anion concentration of ~ 10^{20} cm^{-3} was used that was found to completely screen the bulk electric field of the LEC. This was ascribed to the migration of mobile ions toward the two electrodes in response to the externally applied electric field. By cooling the LEC to a low temperature while applying a fixed, *reverse* DC bias across the device, the positive (and negative) ions can be

frozen near to both anodes (and cathodes). In this case, the electrodes' E_f are pinned to the LUMO and HOMO level of the *undoped* polymer layer since the doped-polymer layers adjacent to both electrodes are highly conducting and can be seen as metals themselves. This is experimentally proven by bias dependences of EA (1ω) at different DC pre-bias in Fig 2.7, which demonstrate that bulk internal voltages equal the pre-biases applied across the LEC before cooling.

Fig 2.7 shows that applying pre-biases larger than that corresponding to the HOMO-LUMO energy gap (see Fig 2.4 for explanation) causes the internal field to be partially screened by injected electronic charges that have a higher mobility than the ions at low temperature. As such, the internal field at low temperature no longer equals the applied pre-bias but saturates at a certain upper limit. This interesting study clearly demonstrates that EA spectroscopy is an effective technique in understanding the underlying operational mechanisms of optoelectronic devices.

Similar phenomenon related to electric field redistribution in PLEDs is reported by Lane *et. al.* *[49]*. In this study, the bias dependences of EA (1ω) [and EA (2ω)] was used to provide clear evidence of DC (and AC) field screening at voltages corresponding to the threshold value for current injection (refer to Fig 3.10 for details). This phenomenon is attributed to accumulation of trapped charges at the counter electrode, which gives rise to the strong excited state absorption signals observed in the electromodulation spectrum under forward bias. Using eq. (2.4), the thickness of the surface charge layer is estimated to be roughly ~ 0.5 – 1 Å for 25% doping (n $\approx$ 10^{20} cm^{-3}) of the accumulation layer, showing that the observed electric field screening can be explained by a thin surface charge layer of approximately one monolayer in thickness.

CHAPTER 3

Design and Development of Electromodulation System

3.1 Overview

In a practical electroabsorption (EA) experiment, several main processes are involved: 1) illumination of specimen (in the form of a working device) placed in vacuum with monochromatic probe light, 2) application of electrical excitation in the form of a periodically oscillating voltages across the sample, and 3) detecting the intensity of reflected light and its change due to electrical perturbation. The overall EA signal is then computed and presented as a ratio between the two detected probe signals and thus measures the field-induced normalised change in light reflectance. Since field-induced variations of reflectance of a material are small (10^{-4} - 10^{-6} range), a lock-in technique is required to detect the EA signals.

Fig. 3.1 shows the schematic representation of the EA spectrometer designed and constructed for this thesis. A similar EA spectrometer has been designed and built previously for built-in potential (V_{bi}) measurements *[125]*, but several important differences were made to the setup described here. The probe beam originates from a xenon arc lamp (white light source used for probing the electrically modulated sample) and is fed into a monochromator. The dispersed monochromatic light is guided by an optical fiber and subsequently focused by a set of lens assemblies through the cryostat windows onto the polymer light emitting diode (PLED) sample. The monochormatic light illuminate the PLED through the transparent glass/ITO anode of the device at an angle of 45^0. After traveling through the polymer layer, the light is then reflected by the metallic cathode on the other side of the polymer, passed through the cryostat windows and refocused by a lens onto an amplified silicon photodiode. Meanwhile, a signal generator within the lock-in amplifier provides a linearly combined DC and AC sinusoidal bias in the form of $V = V_{dc} + V_{ac} sin\ (\omega t)$ that are usually modulated at 0.2 kHz.
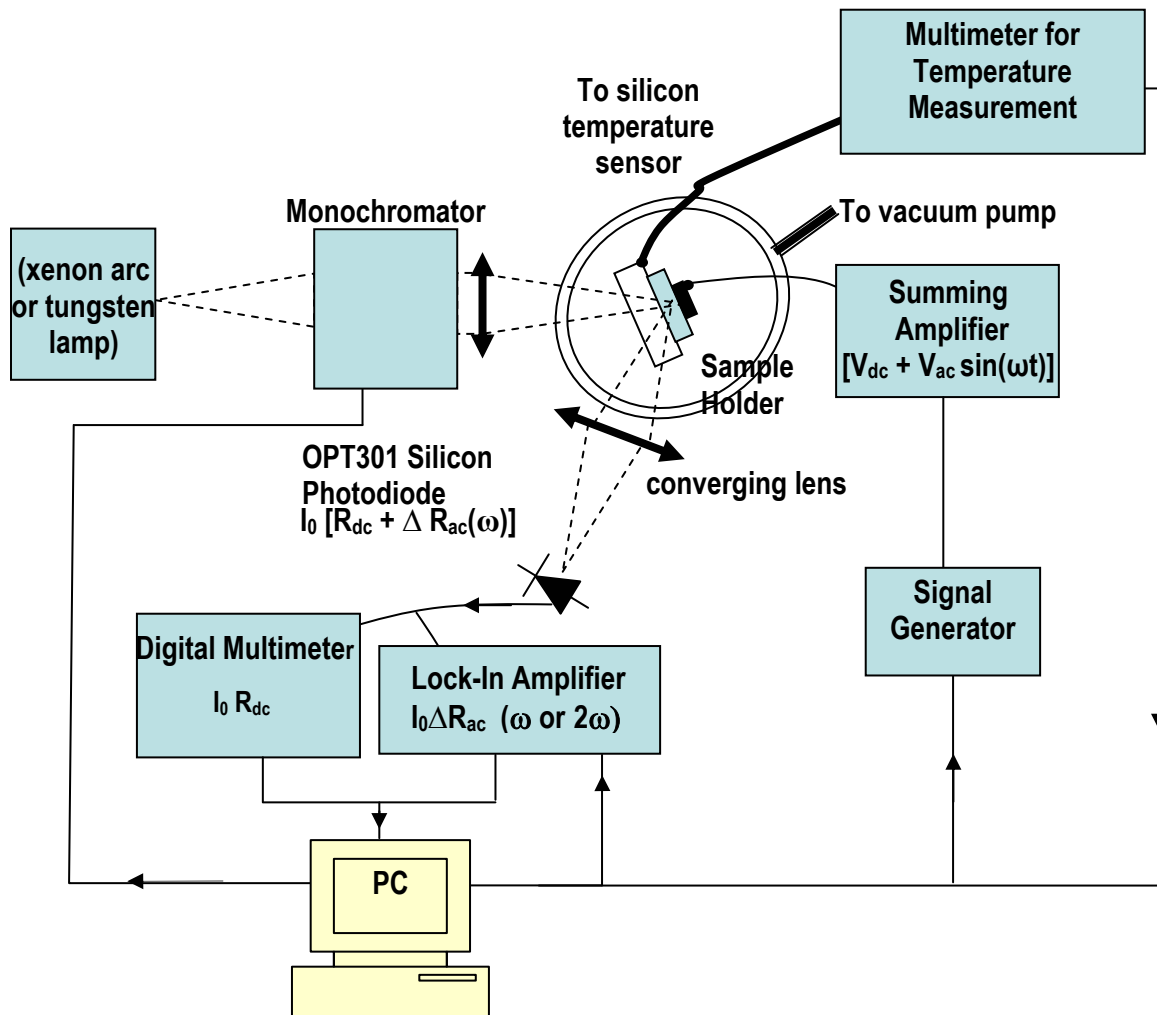
Figure 3.1: Schematic configuration of EA setup. Light exiting monochromator is outcoupled and directed by an optical fiber (not shown) towards sample in cryostat. As described in the text, a silicon temperature sensor is placed next to the sample in the cryostat for temperature monitoring and the signal generator shown in the schematic is an integral part within the lock-in amplifier.

The combined biases are applied across the PLED sample in order to induce a perturbation of the absorption coefficient of the semiconducting polymer. The DC and AC components of the composite photodetector output are then separately measured by a HP34401A digital multimeter and a SR-830 dual-channel lock-in amplifier, respectively. The digital multimeter measures the

DC reflectance (R) of the sample whereas the lock-in amplifier measures the change in reflectance (ΔR) that is induced by the applied modulating AC bias.   These two signals are then fed into a computer that calculates the ratio ΔR/R and presents the final signal. Since ΔR/R is a normalised signal, it is not affected by the abrupt variations of light reflectance caused by the sharp molecular transitions of xenon arc lamp at specific wavelength ranges.

The sample is mounted by a sample holder that is custom built for the cryostat of the EA system and can monitor temperatures ranging from 500 K to 1.4 K although the maximum allowable temperature is restricted at 310 K by the cryostat heater controller. Further details on temperature control and sample holder will be given in later section within this chapter. As shown in Fig. 3.1, the EA system is assembled from various components. As such, it will be useful to break it down into these components and discuss briefly on the design and construction of each of them in the following section.

3.2 Optical Setup of Electromodulation System

3.2.1 Light Source

Unlike the previous EA setup constructed by Brown *[125]* that used 450 W xenon arc lamp as the only light source, we used a 150 W xenon arc lamp (Oriel 6253) and a 50 W quartz tungsten halogen lamp (Oriel 6332) for the current EA system. Both lamps are controlled by their respective current regulated power supplies (Oriel 68938 and Oriel 68806) that ensure constant current and hence power of the lamps while in operation. The output of these power supplies changes by less than 0.02 % even for large swings in the line voltage. The controlled current serves to maintain a constant irradiance of the emission sources over the course of experiment. Despite the lower power of our lamp sources relative to the previous setup, high irradiance and signal strength can be readily obtained owing to the optimisation of lens assemblies that will be discussed in later section.

The xenon arc lamp is highly desirable as a probe beam source as it produces high irradiance in the ultraviolet (UV) and visible wavelength range (300 – 700 nm) where spectral features of

many technologically important conjugated polymers for optoelectronic applications occur. On the other hand, the quartz tungsten halogen lamp has smooth continuous irradiance across the visible and near infrared (IR) region and does not have discreet molecular transitions in the visible wavelength range. Most experiments undertaken for this thesis were conducted with xenon arc lamp as the illumination source.\
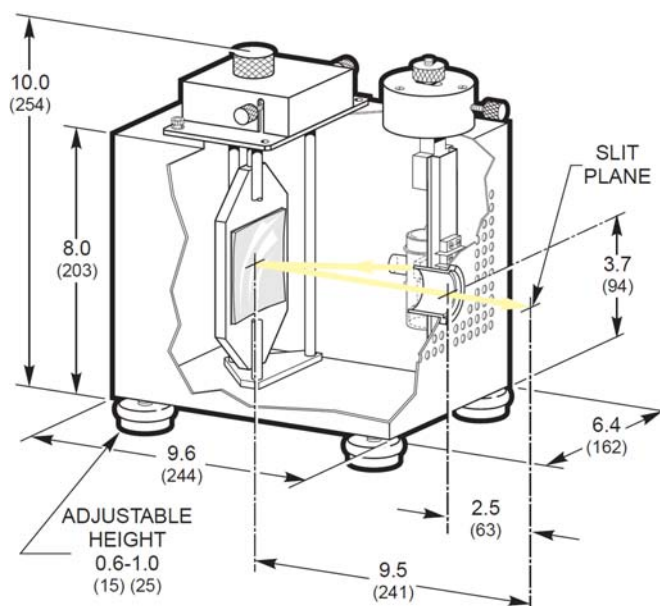
Figure 3.2: Schematic of monochromator illuminator in which a mirror and both lamp sources are housed. [Figure taken from ref. *[151]*]

Both xenon and quartz tungsten halogen lamps are housed within a metallic monochromator illuminator (Newport 7340), which also contains a concave Al mirror that is coated with AlMgF for high reflectance over the 200 nm to 40 μm region. By adjusting the lateral position of the mirror, one can switch between the two lamp sources without dismounting either lamp source. The detailed design and dimension of the monochromator illuminator is shown in Fig. 3.2.

3.2.2 Monochromator

We used a Bruker Optics 250is/sm Imaging Spectrograph/Scanning Monochromator equipped with three diffraction gratings (600 g/400 nm, 1200 g/250 nm and 300 g/1000 nm), an aperture ratio of f/4.0, entrance and exit slits with variable widths (0 – 2 mm) and a controllable wavelength from 250 nm to 10 μm. The linear dispersion of the equipment is 2.5 nm/mm, which yields full-width-half-maximum of instrument bandpass function upon multiplying the linear dispersion with the slit width. Although resolution is inversely proportional to the slit width, narrowing the slits decreases light and hence signal intensity, resulting in low signal-to-noise ratio and unwanted increase in error limit of V_{bi} measurement. In all the EA experiments presented in this thesis, a good compromise between signal-to-noise ratio and resolution was obtained with the widths of both entrance and exit slits fixed at 2 mm. Fully opening both slits of the monochromator enables us to obtain an EA signal of high magnitude despite the varying thickness values of the PLED samples and nature of the materials (i.e. magnitude of their nonlinear dielectric susceptibilities). Schematic diagram of the optical design of a triple grating monochromator is shown in Fig. 3.3.
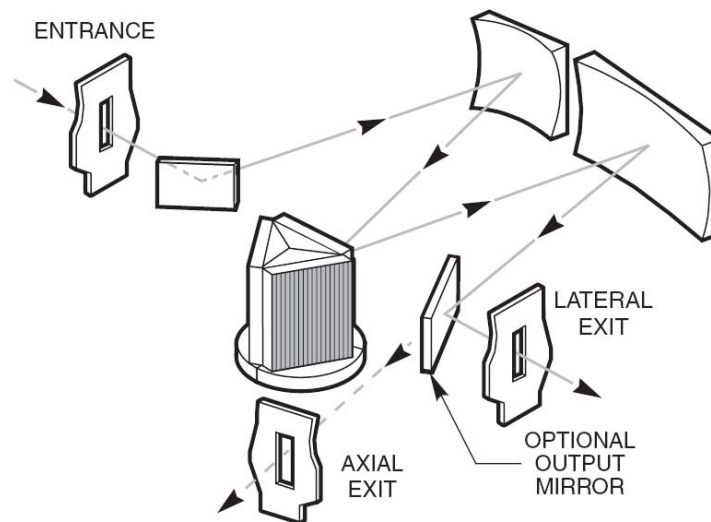
Figure 3.3: Optical design of a three-grating monochromator used in the EA experiments. [Figure taken from ref. *[151]*].

The wavelength of the monochromator output light is controlled by varying the angle of rotation of the grating. This was achieved by a stepping motor connected to the computer via GPIB interface. Unlike the previous setup, we use only one monochromator instead of two monochromators. The second monochromator in the EA setup of T.M. Brown *[125]* was formerly used to prevent signal contamination due to modulated electroluminescence (EL) or electromodulated photoluminescence (PL). In all experiments conducted for this dissertation, signal contamination of modulated EL was avoided by electrically driving devices below the turn-on voltage. On the other hand, the electromodulated PL contribution is dispersed over all half space (2π steraradians) and only constitutes $\sim$ 1 % of light reflectance detected by photodiode at absorption edges of conjugated polymers. Since V_{bi} measurements are normally conducted near absorption edges of the samples, electromodulated PL contamination is insignificant and one monochromator is sufficient.

Nevertheless, having a second monochromator is useful for investigating the electric field distribution of technologically important, highly emissive PLEDs*[11]* or multilayered small-molecule white organic LEDs*[152]* under strong charge injection conditions. Such measurements will enable better understanding on the spatial distribution of space charges within these highly emissive systems under operational conditions. With an additional monochromator, interesting studies on the effects of photoexcitation on the open circuit voltages of different components in polymer-based F8BT:PFB photovoltaic or state-of-the-art tandem polymer solar cells *[68]* can also be studied.

3.2.3 Motorised Filter Wheel

In this setup, a high-precision motorised filter wheel (Thorlabs FW102) that is fitted with long pass filters is used to remove higher order harmonics that can otherwise contribute to our measured signal at the intended wavelength. The same GPIB connection used for connecting the monochromator is also used to run the motor that controls the filter wheel system. This enables automatic selection of appropriate filter in response to changes in wavelength of monochromatic light exiting the monochromator. While the previous EA system constructed by Brown*[125]*

uses only two long pass filters, we incorporate five long pass colored glass filters (1-inch diameter) with cut-on wavelengths at 309 nm, 400 nm, 570 nm, 780 nm, and 1000 nm.

Since these cut-on wavelengths correspond to only 50% of the light transmittance of the respective filters, changing filters at these specific wavelengths will led to unwanted dips in EA signal strengths during the experiments. This practical limitation causes us to change filters at wavelengths slightly larger than their respective cut-off wavelengths to ensure that reflected light remains fully transmitted throughout the EA spectral range. For the reader's information, the transition wavelengths are set by the Labview 8.0 software programme to be 350 nm, 450 nm, 590 nm, 830 nm and 1300 nm. The initial attempt to connect the filter wheel to the opening of the monochromator illuminator led to premature damage of motorised filter wheel system as the irradiated heat at the illuminator's opening is too high for proper functioning of filter wheel's circuit system. As such, a new filter wheel was installed between the cryostat and focusing lens assembly before the probe beam impinges upon the evacuated sample.

3.2.4 Optical Lens System

In this current setup, the light beam exiting the monochromator is focused into a 600 μm-diameter optical fiber (Ocean Optics QP600-2-UV Vis) by a focusing beam probe assembly (Oriel 77646) that houses two plano convex lenses (Newport 77646 and 41230). In order to transmit most of the light through the optical fiber, a magnification of 0.5 is required. This is achieved by using two fused silica plano convex lenses (Newport 77646 and 41230), with the first lens (L_1) having focal length, f_1= 38 mm, and the second lens (L_2) having focal length, f_2 = 19 mm. L_1 was placed away from the monochromator's exit slit at a distance equal to f_1 in order to collimate the beam, which is then focused by L_2 onto the optical fiber placed at a distance of f_2. Combination of the two conjugated lenses results in magnification of 0.5 as intended. The diameters of both lenses are chosen to be 12.5 mm ± 0.015 mm in order to best match the f-number of L_1 (f/# = 3.4) to that of the monochromator (f/# = 4), this enables collection of the maximum amount of light while minimising lens diameter and cost. Both lenses and the optical fiber are housed in the same spacer tube.

Rather than using free-space optics *[125]*, we use fused-silica optical fibers (f/# = 2.3) with proper matching of f-number with that of lens L_2 to outcouple light from monochromator to our sample. This allows us to optimize light transmission while reducing stray light collection, and enables us to obtain strong signals despite the low power of the lamp sources. The light beam exiting the optical fiber is eventually magnified by a dual plano-convex fused silica lens system (lenses L_3 and L_4), with both lenses having diameters of 25.0 mm ± 0.015 mm (Melles Griot 01-LQF-028 and 01-LQF-078). Both L_3 and L_4 are housed in the same spacer tube. The focal lengths of these lenses are chosen to be 50 mm and 100 mm such that image magnification is 2 and the light beam shining onto the pixel of our sample has the same size as that of the lamp source image exiting the monochromator. The f-number of the first collimating lens (f/# = 2) nearer to the optical fiber is chosen to best match that of the optical fiber. With optimal alignment of the light outcoupling and focusing lens systems, a monochromatic probe beam having an intensity of about 0.7 – 0.8 mW/cm^2 can be obtained. With the use of long-pass filters, however, the intensity of the probe beam tends to drop further by another 10 %. It is important to note that the exact intensity varies with photon energy owing to the differential outcoupling efficiency of monochromator's grating.

The light beam incident on the pixel of interest passes through the polymer layer, reflects from the metal electrode, exits the cryostat windows and is then focused by a UV fused silica plano convex lens L_5 of focal length 100mm and diameter 50.8mm (Thorlabs LA 4545) onto a silicon photodiode detector (see section 3.3 for discussions). Although the f-number of the reflected light beam (f/# = 4) is larger than that of L_5 (f/# ≈ 2), the signal we obtained does not suffer from stray light contamination. In our case, the 100mm focal length lens is the optimal lens system due to the constraints introduced by the limited range of lens choices and small working space of the optical table. A concave mirror coated with AlMgF coating (Newport 7292 reflector) was initially used as to redirect the reflected light beam to the photodiode. But, the signal strength thus obtained was found to be very sensitive on the angle of incidence of the reflected light beam. Moreover, small angle of incidence is required for optimal signal strength, putting practical constraint on the position of the photodiode. These limitations prompted us to use an optical lens system to replace the concave mirror.

Deviations from ideal performance of lenses are called aberrations and can be relatively strong for low f-number lenses, where large ray angles are present. Although such problems as chromatic aberrations and wavelength-dependent focal length are associated with optical lens systems, use of more expensive achromatic lenses was found to be not necessary to minimise the aberrations in our experiments. This is because i) the active area of device under study (1.5 mm x 3.5 mm or 3 mm x 3.5 mm depending on the shadow mask used for evaporation) are similar or larger than that of the probe beam (~ 1.3 mm in diameter) and ii) EA signal, $\Delta R/R$ is a normalised quantity and the wavelength dependences affecting both ΔR and R are cancelled out at each wavelength.

3.3   Photodetection Setup and Electrical Excitation Source of Electromodulation System

The field-induced variations in reflectance of PLED samples monitored by EA experiments, $\Delta R/R$ are extremely small (~ 10^{-4} – 10^{-6} range). As such, reduction of noise levels is of paramount importance. For this reason, special efforts were put into designing and constructing a modulating voltage source and a stable, low-noise photodetector.

3.3.1   Photodetection Setup

Since the optical absorption of most conjugated polymers lies within the range of 250 nm and 700 nm, a silicon photodiode with spectral wavelength ranging between 250 nm to 1000 nm to cover the absorption range of PLED samples is desired. Accordingly we used a Burr Brown OPT 301, which comprises an integrated optoelectronic circuit containing a silicon photodiode (2.3 mm x 2.3 mm) and a transimpedance amplifier on a single dielectrically isolated chip. Fig. 3.4 shows the spectral responsivity of the OPT 301 silicon photodiode unit. The transimpedance amplifier consists of a precision FET-input op-amp and an on-chip metal film internal gain resistor that is laser trimmed to 1 MΩ ± 2 %. The OPT 301 derives its voltage output by multiplying the photodiode current with the resistance of the gain resistor, resulting in an output voltage responsivity of approximately 0.45V/μW at 650 nm illumination wavelength. This

photodiode is operated at zero bias in photovoltaic mode to optimise linearity in output photocurrent and minimise dark current. The dark voltage of OPT 301 unit is 2 mV and the noise level is less than 1 μV (at 700 – 800 nm wavelength range) at 1 Hz measurement bandwidth. Although the offset bias of the op-amp circuit leads to non-zero dark voltage, offset circuit is not included to eliminate this problem as the output voltages due to reflected light illumination are at least three orders of magnitude higher than the dark voltage. Circuit diagram of the Burr Brown OPT301 photodiode unit can be found in reference *[153]*.
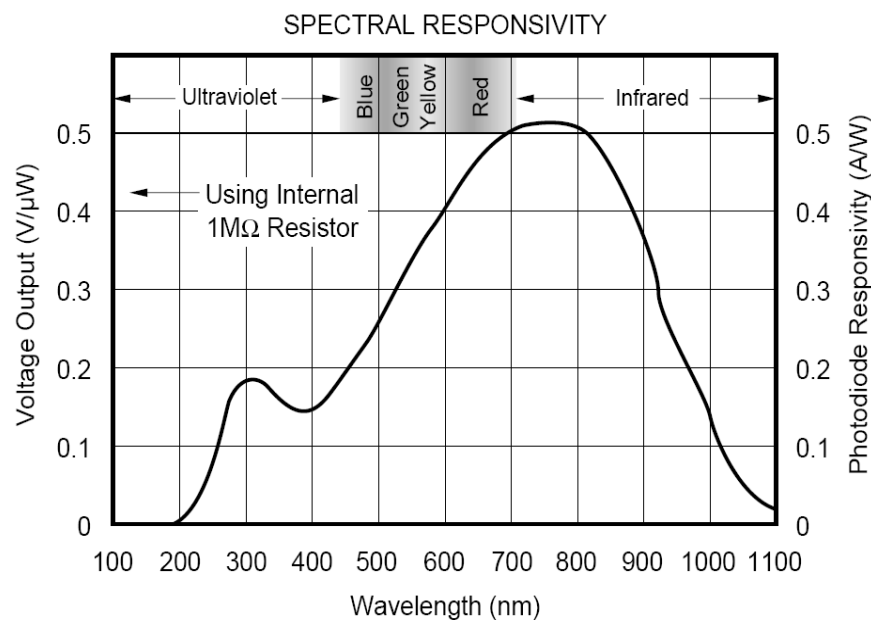
Figure 3.4: Sensitivity of the Burr Brown OPT 301 photodetector across deep UV to far IR wavelength range. [Figure taken from ref. *[153]*]

The photodiode unit has the advantage of operating over a wide voltage supply range ($\pm$ 2.25 V to $\pm$ 18 V) and supply current is only 400 mA. It is packaged in a hermetic TO-99 metal package with a glass window, and is specified for a wide range of operational temperature (– 40°C to 85 °C) although noise level will increase with temperature and can present problems for measurements that require higher gain resistance. The integrated combination of photodiode and transimpedance amplifier on a single chip eliminates problems commonly encountered in discrete designs such as leakage current errors, noise pick-up and gain peaking due to stray

capacitance. The OPT 301 photodiode and operational amplifier are enclosed in a 10-pin TO-5 package. Circuit elements other than that disclosed above were purchased separately and mounted or soldered onto a printed circuit board.

The low spectral responsivity (0.15 A/W to 0.48 A/W) of the OPT 301 silicon photodiode between 400 nm and 680 nm [see Fig. 3.4] may hinder accurate V_{bi} measurements for thick PLED specimens comprising blue-emitting conjugated polymers. To solve this problem, the photodiode system was modified by connecting two additional feedback resistors (0.1 MΩ and 10 MΩ) in parallel to the pre-existing op-amp circuit that was integrated with the OPT 301 unit. The lower detection limit is usually determined by the noise level of the amplifier circuit instead of the OPT 301 photodiode itself. Accordingly the operational amplifier and the transimpedance amplifying circuit are deliberately placed in close physical proximity to the OPT 301 unit to realise a low-noise photodetector unit as noise level can increase significantly with distance from the silicon photodiode detection source. Such close proximity is a necessary design feature as both noise and signal are equally amplified by the feedback circuits.

Unlike the previous EA setup that used a variable gain resistor for its photodetector *[125]* (which introduces additional noise to photodetection system), we decided to use high precision resistors with fixed gain resistances (and hence amplifications) as fixed-gain resistors can achieve much higher signal-to-noise ratio compared to a variable resistor. To avoid gain peaking and stabilise the output voltage at amplification lower than 1 V/μA, we used an external phase-compensation capacitor that is connected in parallel with these resistors. With this modification, gain settings can be manually changed to optimise detected signal strength. The as-modified photodetection system is enclosed in a small metallic box to screen the system from external electromagnetic field. The desired gain setting can be chosen by dip switches installed on the box that is mounted on a xyz translation stage. Circuit diagram of the modified photodiode setup is shown alongside with that of the summing amplifier in the appendix. Construction of the summing amplifier is described at length in section 3.3.2.

Fig. 3.5 depicts the bandwidths of our modified photodiode system, which is measured by electrically modulating a LED source at different frequencies ranging from 1 Hz to 50 kHz. The detected signal is presented as normalised change in intensity ΔI/I on a logarithmic scale. With the use of the internal 1 MΩ amplification, the measured bandwidth is 3.8 kHz and is limited by the op-amp section of the photodiode *[153]*. At 10 MΩ amplification, the measured bandwidth of the photodiode unit decrease to 0.3 kHz due to the increase in feedback resistance. But when amplification is set at 0.1 MΩ, the measured bandwidth is not 40 kHz but 4.6 kHz because it is inherently limited by the frequency response of the electrical circuits of OPT 301.
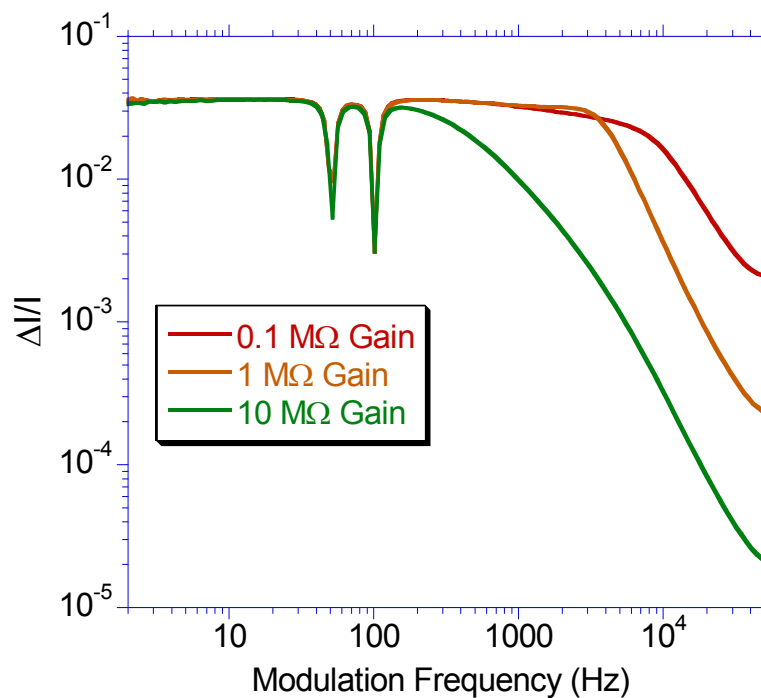
Figure 3.5: Electromodulated optical signal as a function of modulation frequency at the three fixed amplification settings available on the custom-built silicon photodetector unit of EA spectrometer. ΔI/I is the normalised intensity measured at an arbitrary frequency supplied by the lock-in amplifier.

In practice, the 0.1 MΩ-amplification setting was never used as high signal-to-noise ratio is critical for accurate measurement of V_{bi}. Depending on the intensity of the reflected light, 10 MΩ and 1 MΩ amplifications were used in all experiments conducted for this dissertation. The

sharp dips in ΔI/I seen at 50 Hz and 100 Hz are due to large interfering noise picked up from the main line and first harmonic frequencies. This problem can be eliminated by powering the photodiode with batteries instead of the power supply unit (coupled to the AC main line). Alternatively, one can also circumvent this limitation by avoiding the use of 50 Hz and its odd number harmonic frequencies. In our case, all experiments were conducted at about 216 Hz modulation frequency which represents the optimal setting that yields EA signals with the highest signal-to-noise ratio. Measurements of EA signal against modulation frequency will require a photodiode that has bandwidth higher than 4 kHz. Our Si photodiode is electrically connected to a HP6410A digital multimeter via BNC cable for photovoltage measurement. The photodiode unit shares the same low-noise dc power supply as the summing amplifier.

3.3.2 Electrical Excitation Source

Since the SR830 digital lock-in amplifier (LIA) can source out both DC (- 10.5 V to 10.5 V with a resolution of 1 mV) and AC sinusoidal voltage (4 mV$_{rms}$ to 5 V$_{rms}$ with a resolution of 2 mV) in a range suitable for EA experiments on PLED samples, a summing amplifier was custom designed and built to linearly combine LIA-sourced DC and AC biases. The linear summing amplifier circuit is built using the printed circuit board processes outlined earlier with high precision and low noise op-amps and resistors. The summing amplifier unit is encased in a metallic die-cast box for electromagnetic field screening and electrically driven by a power supply unit rather than 9 V batteries. The box was furnished with two input BNC connectors (AC and DC) and one connector supplying an output equal to the sum of the input biases [V_{dc} + $V_{ac} sin (\omega t)$]. The use of mains DC for driving power supply unit was found to not increase the electrical noise level.

We have confirmed that bandwidth of the linear summing amplifier is more than 10 kHz thereby allowing us to modulate PLED samples up to 10 kHz without unwanted loss in optical signal. By using the LIA reference voltage output as AC excitation source, we simplify our setup as the reference frequency source is now kept to "internal" and the use of an external frequency source can be avoided. The combination of low-noise photodetector, voltage modulation source, SR830

digital LIA, close-space optics guided by optical fibers and various optical components with careful matching of their f-numbers ultimately enables us to detect EA signal down to 5 x 10^{-7}. Circuit diagram of the constructed summing amplifier is shown alongside with that of the modified photodiode setup in the appendix.

3.4 Temperature Control Setup and Sample Holder of Electromodulation System

Since the aim of this dissertation is to study the interfacial energy level alignment across different heterojunctions, there is a need to conduct measurements across a wide range of temperatures.   At low temperatures, the EA spectral features of PLED samples tend to become sharper and the V_{bi} may also reveal interesting insights into the electric field distribution of finished devices.   As such, efforts were put into constructing a system that can operate from room temperature down to 4 K.

3.4.1 Sample Holder and Temperature Measurement Setup

The sample holder was based on a design by Dr. Lay-Lay Chua and worked upon by me. The holder was constructed by the metal workshop technical officer. To enable efficient thermal transfer, the sample holder is made of copper with a 13 mm-diameter circular hole for mounting 15 mm-diameter spectrosil substrates.   In order to mount 12 mm x 12 mm ITO-coated glass substrates (commonly used for both PLED and photovoltaic), we constructed a 12.5 mm x 12.5 mm square trough (with a depth of 1 mm) on the same position of the circular hole.   The sample position can be secured by up to four M3 nylon screws and washers on the sample holder for EA measurements although only two nylon screws are needed to secure the sample in practice.

The mounted sample in the cryostat can be electrically connected to the exterior via two BNC connectors (RG 178/BU from Allied Electronics).   In all EA experiments conducted for this dissertation, electrical connections are readily made by connecting the metallic cathode of PLED with the BNC live connector using copper wire. The ITO anode is electrically connected to the

BNC earth connector that is also grounded to the cryostat and optical bench. Electrical bias is then applied to the metallic cathode with respect to the electrically grounded anode.

To monitor and control the temperature of the PLED sample, a silicon temperature sensor (DT-670-SD from Lakeshore) that is connected to a 9-pin connector is manually installed near to the sample trough on the reverse side of the holder. The DT-670 silicon sensor functions by measuring the forward voltage drop across a p-n junction biased at a constant current (typically 10 μA). The potential drop is measured by a Keithley 2000 digital multimeter and recorded by the Labview 8.0 software program, which presents the final temperature readings in Kelvin scale by converting them using the temperature response data table (installed in the computer).

By placing the silicon sensor close to the PLED sample, we can monitor the temperature of the sample more accurately than the rhodium-iron temperature sensor pre-installed (near the heat exchanger) in the cryostat. The difference in temperatures measured by both sensors is found to be as large as 5 K - 10 K although it tends to diminish upon reaching thermal equilibrium after cooling for 10 minutes. Owing to the greater accuracy of the DT-670 silicon diode temperature sensor, it is routinely used for low-temperature EA experiments.

3.4.2 Cryostat, Vacuum Setup and Temperature Control System

During the course of EA experiments, the PLED device and sample holder is placed in high vacuum environment ($\sim 10^{-6} - 10^{-7}$ mbar) to avoid its exposure to atmospheric oxygen and moisture. Both oxygen and moisture are known to introduce bulk traps in the polymeric active layer and thus induce rapid degradation of the device performance [146]. A high vacuum environment is also necessary to avoid condensation of moisture in the ambient and ice formation during low-temperature EA measurements. To realise a high vacuum environment, we use a combination of an oil-free, diaphragm backing pump (Divaco 8T) and a turbo molecular pump (TW 70) purchased from Oerlikon Leybold UK. We purposely choose an oil-free pumping system for such sensitive measurement as EA experiments as it is essential to avoid sample contamination by residual hydrocarbons from the pump. The oil-free pump system

is connected to the cryostat (Optistat CF from Oxford Instruments) that houses the sample holder and device.

The Optistat CF vacuum cryostat achieves sample cooling by continually drawing liquid cryogen (helium or nitrogen) from a separate helium or nitrogen dewar and circulating them through a heat exchanger (cooling coil) in the cryostat. The circulating cryogen does not come into contact with the sample during cooling. Rather the sample is cooled by conduction through helium gas that fills the separate central exchange gas space. The amount of dry helium gas directed into the sample chamber space can be controlled using a needle valve (that forms part of the helium circulation line custom built by R. Beadle) before cooling. To maximise the EA signal magnitude, the material for all cryostat windows was chosen to be spectrosil B (transmission ~ 90 – 95 % between 200 nm – 2 μm wavelength range) that is a synthetic vitreous silica purchased from Oxford Instruments.

Since a single optical scan may take several tens of minutes to complete, it is critical to keep the sample's temperature constant over entire course of the experiment. Moreover, since the system is dynamically changing with time and experimental conditions, an effective temperature control system is required. We control the temperature by manipulating the flux of cryogen circulating through the system or by the heater preinstalled in the cryostat. To achieve precise control over the flux of cryogen (liquid helium), we connect a needle valve (VC31 from Oxford Instruments) to the oil-free rotary pump (GF4 from Oxford Instruments) that is dedicated for extracting the liquid helium. As mentioned above, the temperature in the sample space can be measured by a rhodium-iron temperature sensor located near the heat exchanger and/or Lakeshore DT-670 silicon diode mounted on sample holder. An ITC503 Intelligent Temperature Controller is used to record the temperature registered by the rhodium-iron sensor.

In addition to the cooling system, a heater pre-installed in the cryostat is used to raise temperature of the sample. The heater is also coupled to the rhodium-iron temperature sensor to actively control or maintain the temperature of the sample during the course of EA measurements. In this way, the ITC503 Temperature Controller sources out an appropriate

amount of power to the heater to manipulate the system. For each EA signal recorded by the SR830 LIA, the heater power is continually adjusted based on the temperature reading registered by the rhodium-iron sensor. Functionalities of the heater hinge on the control algorithm of a Proportional-Integral-Derivative (PID) controller (an integral part of ITC503 temperature controller) that is commonly used for temperature controlling system. Details of PID algorithm can be obtained in reference *[125]*.

Combining the heating and cooling hardware systems allows us to carry out temperature-dependent EA experiments for studying the evolution of V_{bi} in polymer LEDs. The temperature achievable by this cryostat system ranges from 3.4 K up to 310 K. 310 K is the upper limit imposed by the ITC 503 temperature controller, therefore temperatures higher than 310 K are not recommended. By using liquid helium as the cryogen, temperatures as low as 3.4 K can be routinely achieved within 20 minutes.

3.4.3 System Interconnections, Automation and Measurement Settings

The different component parts are connected by GPIB cables with each other and to a desktop dedicated for automation and control of the EA spectrometer. A Labview 8.0 programme custom-written by Dr. Anoop S. Dhoot and subsequently modified by Dr. James C. Blakesley was used for controlling the different components of the system. All EA measurements in this dissertation were performed under steady state conditions in which in which the lock-in signal is measured 1.5 s after after initial application of modulating biases. A waiting time of 300 ms is subsequently introduced into the interval in between successive EA signal acquisition. Depending on the signal-to-noise ratios, each recorded EA signal is averaged over 50 data points to 100 data points.

By measuring the "dark" signal using a SR830 LIA over a wide range of modulation frequencies, we found the optimal electrical modulation frequency that leads to the highest signal-to-noise ratio to be 216.1 Hz, although it varies from day to day. All EA measurements are conducted upon manipulating the phase difference between reference and detected signals such that the EA signal lock-in measured by channel Y is zero. EA spectral measurements are conducted with

the phase difference adjusted by auto-phasing the signal at photon energy corresponding to the EA maximum.

3.5 Specification and Resolution of Electromodulation System

The main objective of this work is the determination of energy level alignment across metal/organic and organic/organic heterojunctions through accurate measurements of the V_{bi} of PLED devices. To ensure confidence in the results of my measurements, it is important to understand the accuracy limit, repeatability and performance of the constructed EA spectrometer. As outlined in the previous chapter, the electric field is uniformly distributed across the organic semiconducting layer if the amount of space charge in the polymer diode is negligible. Under this condition, the EA signal is linearly dependent on externally applied voltage owing to quadratic Stark effect. Shown in Fig 3.6 are (a) the first harmonic EA spectra taken at different applied dc bias and (b) the UV-Visible absorption spectrum of poly(2,7-(9,9-di-n-octylfluorene)-alt-(1,4-phenylene-((4-sec-butylphenyl)imino)-1,4-phenylene)), TFB that is sandwiched in between a calcium cathode and a poly(styrene sulfonate) doped poly(3,4-ethylenedioxythiophene) (PEDOT:PSSH)-coated-indium tin oxide anode. The PEDOT:PSSH film is spun from a commercially available aqueous dispersion (2 – 4 wt % in concentration) from Cambridge Display Technology, which has a weight ratio of 1 PEDOT :16 PSSH.

To study the exact dependence of EA signal on applied bias, the energy (*hv*) of the incident beam was fixed at 2.95 eV that corresponds to the EA maximum of TFB polymer (i.e. 2.92 eV based on Fig. 3.6). It is worth noting that in measuring the V_{bi}, the Stark-shift induced EA maximum at the lowest energy position is chosen *[27, 52]* as it gives the strongest signal-to-noise ratio and enables accurate determination of the energy level alignment across interfaces in finished devices. Another important reason is that optical absorption of the polymer is low at the energy level corresponding to the EA maximum [see Fig 3.6 (a) and (b)]. Positioning the probe beam at higher energies may generate significant PL and photoinduced charges in the polymer layer and is deliberately avoided as doing so may complicate the analysis of results.

The reflected signals also become weaker as the probe beam energy increases (due to the lower spectral sensitivity of the OPT 301 silicon photodiode), but this was found to have no effect on the V_{bi} thus measured as the decrease in reflectance affects both the electromodulated signal ΔR and non-modulated signal R to an equal extent. Nevertheless, the electronic noise contributed by the surroundings may still adversely decrease accuracy and repeatability of V_{bi} measurements if the reflectance is low. The noise floor of the SR 830 LIA of the EA setup is found to be 4 – 5 μV, so the EA signal (ΔR) should be at least 40 – 50 μV to achieve accurate V_{bi} measurement. Experiments conducted in this thesis have been carried out with optimised optical alignment, and EA signals (ΔR) ranging between 0.5 mV to 1 mV can be achieved.
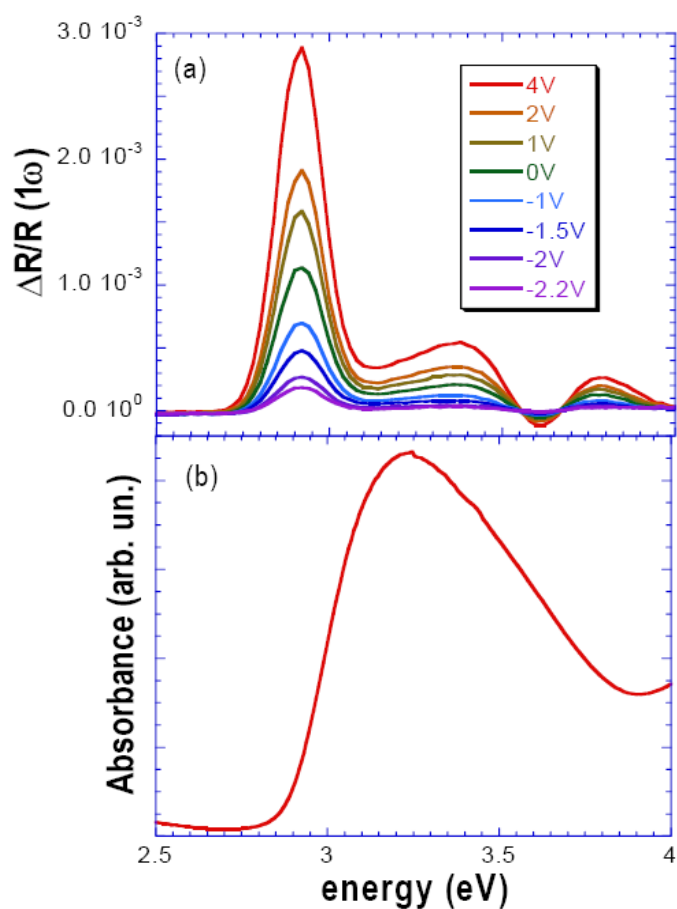
Figure 3.6:   EA spectra of a PEDOT:PSSH/TFB/Ca polymer diode measured at different externally applied V_{dc} (V_{ac} = 0.35V_{rms}, 216.1 Hz frequency) (b) Absorption spectrum of TFB polymer coated on a PEDOT:PSSH anode.

By fixing the probe beam energy, EA signal dependence on applied bias (V_{dc} and V_{ac}) can be studied. As mentioned in the previous chapter, a key characteristic feature of the EA signal is that signals measured by the lock-in amplifier at the fundamental modulation frequency, ω is linearly proportional to both the AC bias and the net DC bias in the organic active layer across which the potential drop is most pronounced:

$$EA(1\omega) = \frac{\Delta R}{R}(h\upsilon,\omega) = 2\,\mathrm{Im}\,\chi^{(3)}(V_{bi} - V_{dc})V_{ac} \qquad (3.1)$$

where $\mathrm{Im}\chi^{(3)}$ is the imaginary, third order dielectric susceptibility of the polymer. On the other hand, EA signals measured by the lock-in amplifier at twice the fundamental modulation frequency, 2ω, exhibit a quadratic dependence with AC modulation bias that are independent on the applied DC bias:

$$EA(2\omega) = \frac{\Delta R}{R}(h\upsilon,2\omega) = \frac{\mathrm{Im}\,\chi^{(3)}V_{ac}^{\,2}}{2} \qquad (3.2)$$

Therefore, the performance of the EA spectrometer can be best studied by investigating the effects of varying V_{ac}, V_{dc} and modulation frequency while keeping the rest of the parameters constant.

Fig. 3.7 shows the dependence of EA signals of a TFB-based diode at 1ω and 2ω on AC modulation bias amplitude. Both curves were fitted with generic power laws ($V_{ac}^{\,\alpha}$) so as not to constrain the results to the expected linear (1ω) and quadratic (2ω) dependences. Our results clearly show that both 1ω and 2ω EA experimental responses conform very well with eq. (3.1) and (3.2). Curve fittings of 1ω and 2ω EA signals yield $\alpha = 0.99$ and 2.02, respectively. The correlation coefficients in both cases, which measure the closeness of the fits with 1 being the perfect fit, are 0.99995.
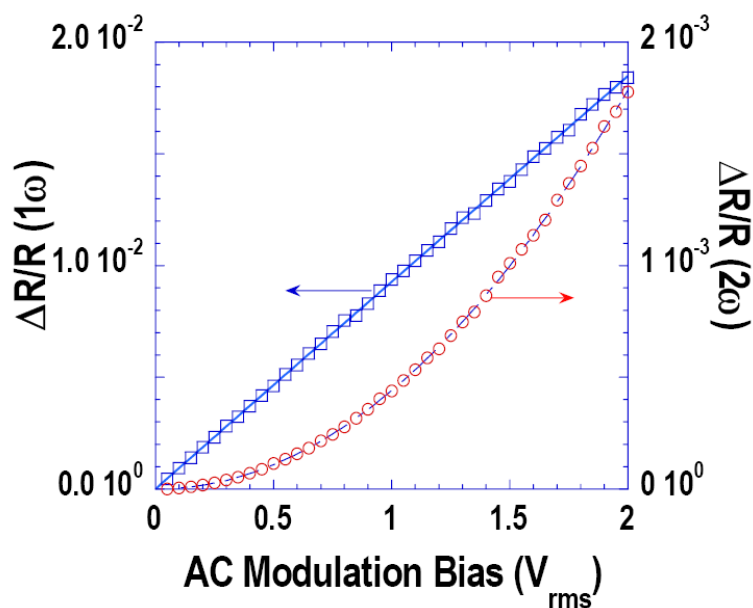
Figure 3.7: EA signals of a PEDOT:PSSH/TFB/Ca diode measured at fundamental (1ω) and second harmonic (2ω) frequencies as a function of applied AC bias (hv = 2.93 eV, V_{dc} = - 4 V, 216.13 Hz frequency).
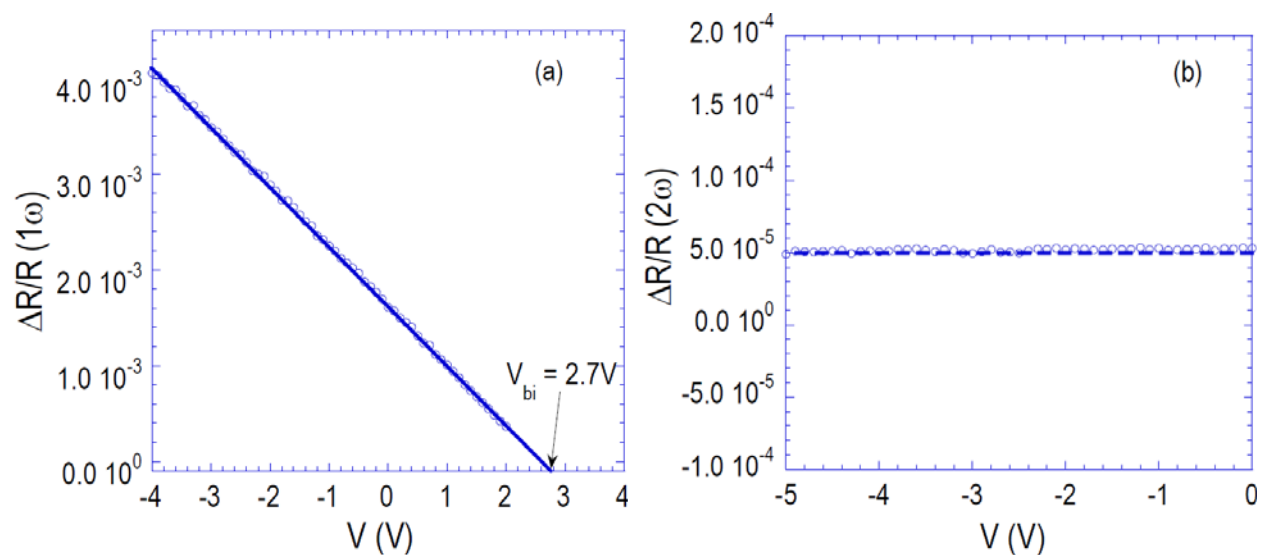
Figure 3.8: (a) EA signals of a PEDOT:PSSH/TFB/Ca diode modulated at 1ω (216.13 Hz, V_{ac}= 0.5 V_{rms}) and (b) at 2ω (V_{ac} = 0.4 V_{rms}) as a function of externally applied V_{dc}. The bias that corresponds to nulling of 1ω EA signal is the V_{bi} of the device.

Fig 3.8 shows the voltage dependence of the EA signal measured at 1ω. As described by eq. (3.1) and (3.2), the dependence of a PLED's EA response at fundamental freequency is linearly dependent on the applied DC bias; whereas the second harmonic frequency EA signal does not depend on the DC bias. This indicates that the electric field drops uniformly across the thickness of the semiconducting polymer layer under reverse bias and weak forward bias regimes where $V_{dc} \leq V_{bi}$. According to eq. (3.1), the V_{bi} across a conjugated polymer layer at electrical equilibrium is the DC bias needed to cancel the EA signal modulated at the fundamental frequency:

$$V_{bi} = -V_{dc}(h\upsilon, 1\omega, V_{ac})$$
(3.3)

Therefore the V_{bi} across PEDOT:PSSH/TFB/Ca device is 2.7 ± 0.1 V as is shown in Fig 3.8. The physical meaning of the V_{bi} value is discussed at length in Chapter 4. Linear fitting of the 1ω EA signal yields:

$$\frac{EA(1\omega)}{10^{-4}} = 16.27 + 6.23V_{dc}$$
(3.4)

with the regression coefficient, R = 0.99984. To determine the accuracy limit of the EA spectrometer, V_{bi} measurements with identical experimental conditions were repeated five times in succession on the same PEDOT:PSSH/TFB/Ca device. The values of V_{bi} thus measured fall within a narrow range of 2.64 V < V_{bi} < 2.76 V with a resolution limit of ± 12 mV, which is lower than the resolution limits of EA spectrometers (i.e. ~ ± 100 mV) reported in the literature *[27, 99]*.

State-of-the-art PLED devices have relied on the use of type II organic-organic heterojunctions to achieve balance in charge carrier injection and high electroluminescent efficiency *[12, 47]*. EA measurements on PLED devices with binary polymeric systems will yield important information on underlying device operational mechanisms. But the EA maximum of the higher energy-gap polymer component [e.g. TFB] may overlap with the UV-visible absorption

spectrum of the lower energy-gap polymer component [e.g. poly(9,9-dioctylfluorene-alt-benzothiadiazole) or F8BT]. In this case systematic V_{bi} measurements need to be carried out at attenuated probe beam intensities to avoid the possible interference of photoexcitation on the built-in field of higher energy-gap polymer (effects of photoexcitation on measured V_{bi} of bilayer PLEDs are discussed at length in Chapter 5). Accordingly it is important to first determine the resolution limit of V_{bi} measurements at attenuated EA probe beam intensities.

Repeated V_{bi} measurements were therefore carried out for five times in succession under identical experimental conditions on PLED with the structure of PEDOT:PSSH/F8BT:TFB (50:50 w/w)/Ca. In this case, the polymer active layer was made by spin casting from a F8BT:TFB (50:50 w/w) xylene blend solution. For samples comprising a total of 75 – 80 nm of semiconducting polymer layer, resolution limits of V_{bi} values measured at reduced probe beam intensities (by using OD 0.5 and OD 1 neutral optical filters) are ± 100 mV. For samples containing more than 100 nm semiconducting polymer layer, resolution limit of V_{bi} values measured at reduced probe beam intensity is ± 150 – 200 mV. It is important to emphasise that the resolution limit is highly dependent on the EA signal-to-noise ratio, which can vary if the experimental conditions (e.g. AC modulation bias, optical alignment of lens assemblies, sample temperature etc) are different. Therefore resolution limit of the EA spectrometer should be measured independently to ensure reliable V_{bi} measurements.

An alternative way to extract V_{bi} is by taking the ratio of EA (1ω)/EA (2ω) based on eq. (3.1) and (3.2):

$$V_{bi} = \left. \frac{EA(1\omega)V_{ac}}{EA(2\omega)4} \right|_{Vdc=0V} \tag{3.5}$$

Although this method is equally applicable in extracting V_{bi}, it is far from ideal for accurate determination of energy level alignment because the intensities of EA (2ω) spectral features are at least one order of magnitude lower (owing to its independence on DC bias) than those of EA

(1ω) spectral signals. As such eq. (3.5) introduces larger experimental errors into V_{bi} values than eq. (3.1) or eq. (3.3).

Although it is possible to increase V_{ac} to enhance signal-to-noise ratio of the EA (2ω) signal in principle, but high V_{ac} facilitates charge injection when the absolute magnitude of the applied DC bias approaches flat-band voltages of the PLED sample. Since charge injection disrupts the uniformity of the electric field distribution, EA (1ω) and EA (2ω) tend to deviate from eq. (3.3) and (3.4) near V_{dc} values required for charge injection. High V_{ac} is therefore not desirable and should only be used when either the background noise is higher than 10 % of intended signal or when V_{bi} of the device is significantly higher than the modulation bias.

It is important to emphasise that the EA response $\Delta R/R$ deviates from behaviours predicted by eq (3.1) and (3.2) earlier as V_{ac} increases. Significant charge injection invalidates the approximation of the polymer active layer behaving as a uniform dielectric with the electric field uniformly distributed across its thickness. Instead other charge-induced effects such as charge modulation, modulated EL, variation of refractive index or bleaching of ground state absorption become prominent. For PLED samples with relatively thin (75 – 80 nm) polymer active layer, excited state absorption (ESA) features due to injected or trapped charges can be measured at frequencies similar to that used for EA measurements[154]. Spectral overlap of EA and ESA features inevitably contaminates the intended EA signal, thus rendering accurate V_{bi} measurements difficult due to non-linear bias dependence of the ESA signal[49, 97, 126]. This phenomenon is particularly common with diodes or PLED samples that have ohmic junction(s) at one or both sides of the electrode/polymer interfaces[97, 142, 154, 155].

Solutions to overcome the problem described above include conducting EA measurements at high modulation frequencies [49, 154] ($\geq$1 MHz) or at low temperatures. Increasing modulation frequencies can minimise ESA contribution because injected/trapped charges have a finite lifetime that is on the order of microseconds to milliseconds. Unfortunately increasing modulation frequency is not practically feasible in our case as the bandwidth of the OPT 301 photodiode (at 1 MΩ gain setting) of our constructed EA system is only 3.8 kHz.

On the other hand, the mobility of trapped/injected charges is significantly lower at cryogenic temperatures so the electrically modulated signal detected at low temperature is dominated by EA components. This reason prompted me to conduct EA experiments on both single layer and multilayer samples at temperature as low as 8 – 10 K. Low-temperature EA measurements are found to be ideal (or necessary in some cases) for accurate determination of the V_{bi}. While extracting V_{bi} from the EA (1ω) linear dependences, care was taken to carefully fit the data only in the reverse to weak forward bias regime. Discussions on the parasitic effects of charge induced absorption signals and low temperature EA measurements on measured EA results will be presented in subsequent chapters.
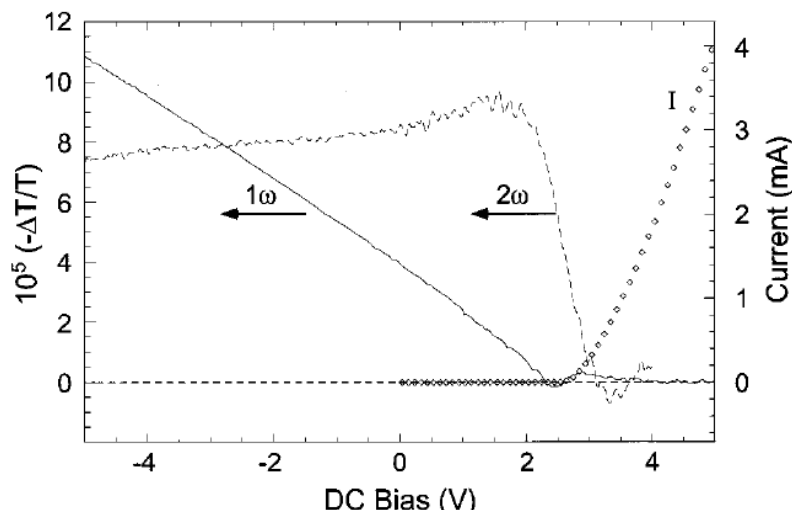
Figure 3.9: DC bias dependences of EA (1ω) (solid line) and EA (2ω) (dotted line) signals of a PLED sample of PEDOT:PSSH/F8 : F8BT (95%:5% w/w)/Ca/Al structure. The EA (2ω) is multiplied by a factor of 4 for ease of comparison. Injected current is proportional to EL intensity [Figure taken from ref. *[49]*]

It is useful to explore the variation of EA signals at DC biases larger than the V_{bi}. Fig. 3.9 illustrates the effects of charge injection on EA (1ω) and EA (2ω) spectral signals of a PLED sample comprising a blend of 95 % F8 (poly(9,9'-dialkyl-fluorene-2,7-diyl)) and 5% F8BT as the active layer *[49]* . EA (1ω) completely disappears upon reaching flat-band voltage at 2.4 V (i.e. the flat band voltage) showing that the integral built-in field in the polymer active layer is

fully screened by injected charges. Further increase in DC bias enhances charge accumulation near the metal/polymer interface. As a result the AC field-induced EA (2ω) signal drops abruptly to zero at 2.8 V indicating that there is no AC electric field in the bulk of the polymer active layer.

The channel Y component of the EA (1ω) signal may also provide a good indication on the presence of charges that disrupt the electric field distribution in the device. With the uniform distribution of electric field, the channel Y signal is zero in the reverse and weak forward bias regime. But channel Y signal deviates from zero as the V_{dc} approaches near the flat-band voltage or V_{bi}, indicating that a component caused by injected/trapped charges has been picked up by the lock-in amplifier of the EA spectrometer and the phase of the signal has varied. This phenomenon is particularly common for diodes having small injection barrier height or ohmic contact at one and/or both metal-polymer heterojunctions.
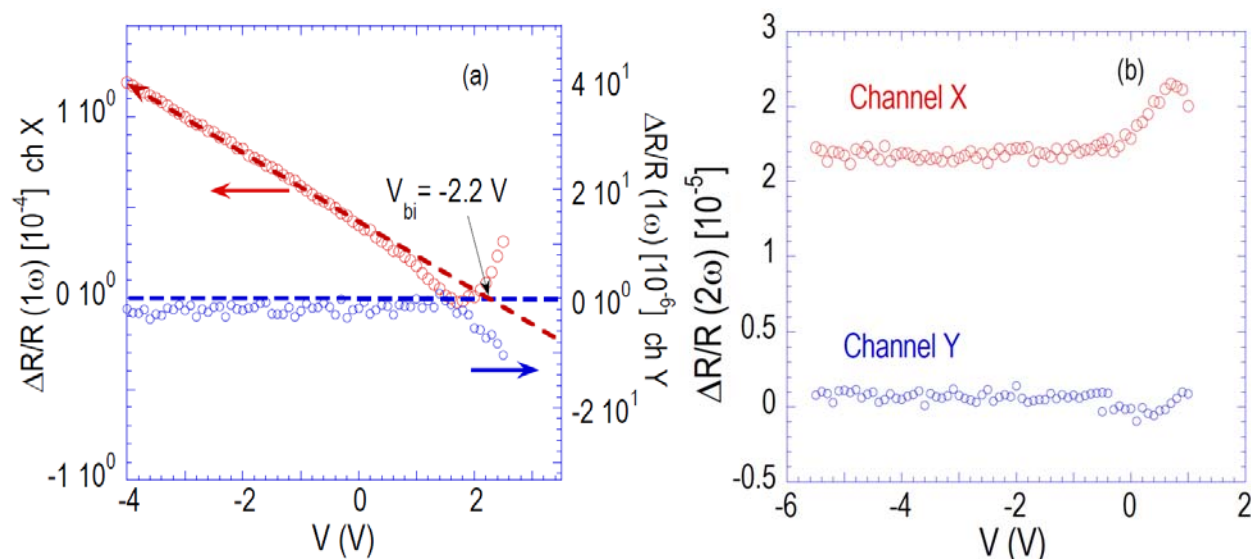
Figure 3.10: Channel X and Y components of the (a) EA (1ω) and (b) EA (2ω) signals of a PEDOT:PSSH/regioregular P3HT/Ca diode versus applied V_{dc}. Dotted lines in 3.10 (a) represent the EA responses arising from quadratic Stark effect.

Fig. 3.10 illustrates the effects of charge injection across the ohmic contacts on electromodulated signals. Fig. 3.10 (a) shows the 1ω electromodulated signals of a PEDOT:PSSH/regioregular P3HT(rr-P3HT)/Ca diode, which comprises ohmic contacts at both the electrode/polymer

interfaces. By virtue of eq. (3.3), the V_{bi} of this sample is found to be - 2.2 V. But in Fig. 3.10 (a), the channel X component of 1ω signal deviates from linearity when V_{dc} approaches 1 V. This phenomenon may be attributed to: i) the doping of rr-P3HT due to E_f pinning at both of the electrode/polymer interface; and ii) the application of V_{ac} (0.25 V_{rms}) in addition to externally applied V_{dc} to the device during EA measurement. Effects of E_f pinning on 1ω measurements are discussed in detail in Chapter 5. Further increase in V_{dc} to 1.98 V causes the channel X signal to decrease to zero showing that the inner electric field is completely screened due to the significant accumulation of charges near the cathode/polymer interface. Beyond 1.98 V, the modulated EL predominates causing the channel X signal to increase; while the channel Y signal decreases rapidly to negative values upon the commencement of modulated EL. Fig. 3.10 (b) shows the 2ω electromodulated signals of the same device measured by the two lock-in amplifier channels. V_{ac} used for the 2ω measurement is 0.5 V_{rms}, thereby causing the 2ω electromodulated signals to deviate from respective constant values when applied V_{dc} approaches - 0.4 V.

Recently Lane *et. al.* [49, 127] have also investigated the effects of charge injection on EA spectra of PLED samples with polymeric blend as the active layer. Their studies reveal that ESA spectral features predominate over the EA spectrum of the lower energy-gap polymer component during charge injection [49, 127]. But the EA spectral contribution dominates the electromodulation signals under low charge-injection conditions. This limitation unavoidably decreases the bias range useful for extracting V_{bi} from the DC bias dependence of EA (1ω) response. Similar problems were encountered while measuring the V_{bi} of multilayered PLEDs [see Chapter 5] because charge injection leads to deviation of EA (1ω) response from linearity.

Spectral contamination of subgap spectral features [49, 154, 155] in the absence of charge injection can also lead to inaccurate V_{bi} determination. Deviation from the correct V_{bi} values by as much as 0.5 V has been observed in our experiments [see Chapter 5]. To solve this problem, V_{bi} measurements were again conducted at low temperatures to minimise or eliminate subgap spectral contribution. Low-temperature EA measurement has been proven effective in yielding reliable V_{bi} values [see Chapters 4 and 5]. This approach, in conjunction with photoemission

spectroscopic studies, has enabled better systematic studies on the energy level alignment in working PLEDs.

Fig 3.11 summarises our discussions by showing the rigid band diagrams of a metal/polymer/metal diode at different bias regimes. The rigid band model and eq. (3.1) and (3.2) serve as a good approximation to correctly understand the energy level diagram of the device with no or minimal charge injection. With the commencement of charge injection, however, the rigid band approximation is no longer valid to describe the internal field distribution in the diode. Injected charges accumulate near the metal/polymer interface, which disrupts uniformity in the electric field distribution across the active polymer layer. Accordingly the device has to be subjected to reverse bias during EA measurement to accurately determine the V_{bi}.

Electric field redistribution may also occur if extrinsic charge carriers are introduced via chemical doping *[132, 145, 156, 157]*, moisture-induced interfacial interactions *[158]*, unwanted exposure to atmospheric ambient *[158-160]* or space charge generated by light illumination *[161-163]*. These problems may occur when the conjugated polymeric active layer in the device contains a significant concentration of impurities/trap states or is subjected to prolonged current injection *[159, 164]*. In such cases the 1ω $\Delta R/R$ signal is highly nonlinear with applied bias and/or varies with time *[146, 161]*. These problems are not discussed in this dissertation as they often arise from conditions or parameters that not commonly encountered in state-of-the-art, high performance PLEDs.

This dissertation focuses on studying polymer-based devices for which the rigid-band approximation is valid, a condition that requires the use of high-purity polymeric materials. Fortuitously all polymers used in the work presented here belong to the polyfluorene family, which is known to exhibit high purity *[117]* and can give rise to repeatable and excellent device performance characteristics *[116, 165]*. Another critical advantage of using high-purity polymers as active layers is that it enables systematic investigations on different types of charge-transfer interactions that may occur upon the formation of charge-injecting polymer/electrode

interfaces in working devices. Results of EA measurements of single-layer PLEDs with high-purity polymer OSC active layers are presented in Chapter 4.
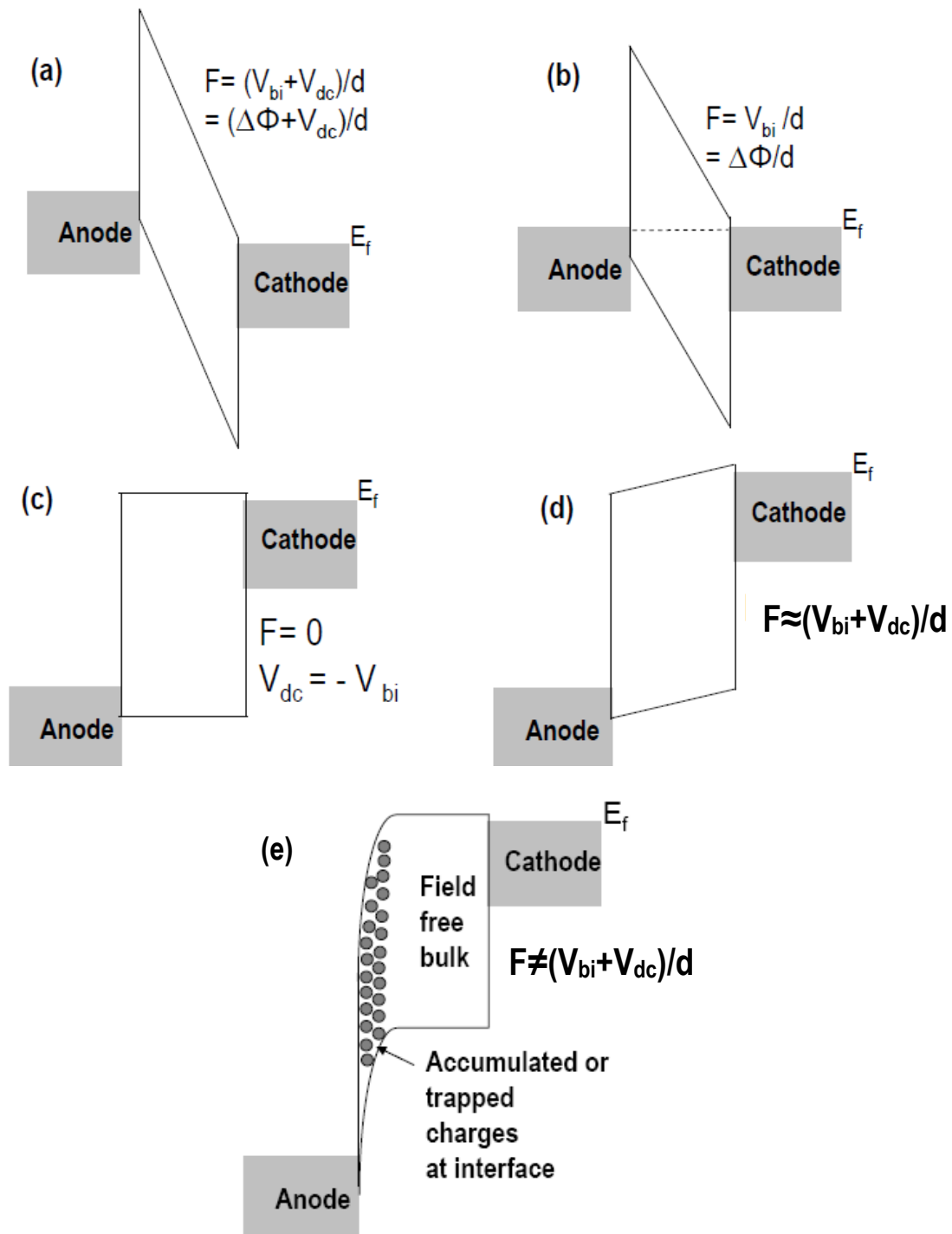
Figure 3.11: Schematic energy diagrams of PLED samples at different biases. Electric field, F is contributed by applied V_{dc} and V_{bi} that compensates for difference in electrodes' work functions $\Delta\Phi$. The rigid band model is a good approximation when there is no significant charge injection in the device [(a)-(d)]. But under strong forward bias [(e)] charges accumulate at the anode/polymer interface and F tends to be heavily or completely screened. In the case of (e), the rigid band model cannot be used to correctly describe the bulk field distribution in the device.

CHAPTER 4

Electroabsorption Studies on Single-Layer Polymer Diodes

This chapter reports the results of electroabsorption (EA) measurements on polyfluorene-based light-emitting diodes with vapour-deposited metals as cathodes; and poly(3,4-ethylenedioxythiophene) doped with polystyrene sulphonic acid, PEDOT:PSSH, as anodes. Ultraviolet photoemission spectroscopy (UPS) measurements were conducted on a series of PEDOT:PSSH/polyfluorene structures, followed by EA measurements of the V_{bi} of PEDOT:PSSH/polyfluorene/metal diodes at 10 K. Results of low-temperature EA measurements were found to bear little consistency with those obtained using UPS, indicating that the work functions of clean metal surfaces are not applicable in describing the interfacial electronic structures in finished devices. The experimental results presented in this chapter enable the mapping of energy level alignment across different metal-on-polyfluorene-on-PEDOT:PSSH structures, which comprise vapour-deposited metals of different work functions (Ca, Al, Ag or Au). Results shown in this chapter serve as prelude to studying interfacial energy level alignment in bilayer polymer diode structures, which will be discussed in the following chapter.

4.1 Overview and Motivation

4.1.1 Electrode Materials and Interface Energetics

Although substantial efforts have been directed towards developing high-performance light-emitting diodes (OLEDs) *[4, 47, 52, 54, 166]*, no reliable interface-design criteria are available due to the limited understanding of the electronic structures at metal/organic semiconductor (OSC) *[4, 71, 109]* and OSC/OSC interfaces *[26, 100, 108]*. Achieving control over these functional heterojunctions has become one of the most important factors in determining the eventual success of organic electronics *[26, 102, 108, 115]*. Amongst the challenges facing interface engineering is the lack of electrode materials that exhibit air stability, suitable work functions, solution processability, high optical transparency and mechanical flexibility. In particular ohmic contacts between metals and polymer OSCs are needed for balanced charge

injections *[47, 55]*, making low work-function cathodes and high work-function anodes necessary to realise high-performance PLEDs.

Significant progress has been made in developing "ideal" anodic materials. The development of water-borne poly(styrene sulfonate) doped poly(3,4-ethylenedioxythiophene) (PEDOT:PSSH) hole-injecting interlayer *[46, 52, 166]* has led to high-performance PLEDs with long operational lifetime *[47, 54, 115, 119, 166-168]*. PEDOT:PSSH is also widely used in making high-performance organic electronic devices (e.g. transistors and photovoltaics) *[4, 169, 170]*. Nevertheless PEDOT:PSSH is hydrophilic and cannot be easily deposited over the hydrophobic polymer OSC film, thus restricting its use as the bottom electrode in most cases.

"Ideal" cathode materials with low work functions are harder to obtain. Despite much efforts in developing alternative electrodes *[48, 51, 143, 171, 172]*, vapour-deposited metal thin films (e.g. Ca, Ba, Al, Cs and Mg:Ag alloy) are still used as *top* electrodes for organic electronic devices. But some of these metals may chemically dope the polymer OSC underlayer *[143, 156, 173-178]* and can have detrimental effects on device performance characteristics *[179-181]*. Moreover they are highly susceptible to oxidation by atmospheric oxygen and moisture found in high-vacuum (HV) environment ($\sim 10^{-6} - 10^{-7}$ mbar), thereby necessitating hermetic encapsulation with noble metals and/or epoxy resin for device protection.

The actual fabrication procedures and fabrication environments can have decisive effects on interface energetics in finished devices. The polymer OSC-on-metal interface is prepared by exposing metal electrode to polymer solutions and is compositionally abrupt *[66]*. But metal-on-polymer OSC interface fabrication involves depositing vapourised metal atoms onto polymer surfaces, which yields compositionally graded interfaces where metal atoms diffuse through the top few OSC monolayers *[26, 174, 182, 183]*. Metal atoms that penetrate the OSC may further interact with the surrounding organic matrix *[100, 156, 175, 176, 178, 184]*, resulting in modified electronic structures that affect device performance characteristics.

4.1.2 Studying Interface Energetics by Electroabsorption (EA) Spectroscopy

Although interfaces encountered in real devices obviously differ in nature from those found in a ultrahigh vacuum (UHV) environment *[26, 108, 180, 182]*, interface energetics are often studied by photoemission spectroscopy in an UHV environment (pressure $\leq$ 1 x 10^{-9} mbar) *[26, 65, 66, 100]*. Therefore EA spectroscopy is useful to determine the actual electrode work function and thus charge injection barrier heights in working devices *[52, 97, 126, 142, 155, 168]*.

The phenomenon of barrierless contact across PEDOT:PSSH/polymer interfaces in *finished* PLEDs has recently been studied using EA spectroscopy by Lane *et. al.* *[97]*. This study measures the built-in voltages (V_{bi}) of PLEDs that comprise PEDOT:PSSH as the anode and vapour-deposited Al, Ca or Ba as the cathode. In particular, two notable observations on devices with one or more conjugated polymers (i.e. blended binary system) were made: i) regardless of the metal cathode used, the effective work function of PEDOT:PSSH (deduced from V_{bi} measurements) is found to coincide with the highest occupied molecular orbital (HOMO) levels of the polyfluorene active layer; and ii) the EL turn-on voltages of PLEDs comprising a low work-function cathode and PEDOT:PSSH anode are identical to their V_{bi} values measured by the EA technique.

To explain these phenomena, Lane *et. al.* *[97]* claim that E_f pinning occurs across the PEDOT:PSSH/polymer interface as a result of *electrons* trapped near the polymer/PEDOT:PSSH interface. These trapped electronic charges shift the interfacial HOMO level of the polymer towards the E_f of PEDOT:PSSH by as much as 0.7 eV, thereby eliminating the hole-injection barrier height across the polymer/PEDOT:PSSH heterojunction. But no discussion is made on the exact source contributing to the trapped electrons in the devices, although electron accumulation is thought to be related to the electron-blocking behaviour of the PEDOT:PSSH surface *[64, 98, 126, 154, 168]*.

Polyfluorene and polyfluorene derivatives are known to exhibit high chemical purity with minimal ion contamination *[185]*, so polymer contamination is unlikely to be the cause of charge

trapping. Low work-function, vacuum-deposited metals may dope the polymer with charges through E_f pinning, but the amount of charges thus introduced is unlikely to give rise to such a large vacuum level misalignment across PEDOT:PSSH/polyfluorene interface. In fact the V_{bi} measurements on PEDOT:PSSH/poly (9,9'-dioctylfluorene)/Al by Lane *et. al. [97]* suggest that elimination of hole injection barrier may occur even when vapour-deposited Al is used as cathode.

We believe that EA studies described above *[50]* highlight the lack of complete understanding of energy level alignments across metal/polymer heterojunctions that govern operational parameters of PLEDs. A possible contribution for charges trapped at PEDOT:PSSH/polymer interface is hole-transfer that pins the PEDOT:PSSH's E_f to the positive polaron levels of the polymer *[29, 155]*. This process may lead to local band bending at PEDOT:PSSH/polymer interface *[68]* or an abrupt interface dipole *[26]* that eliminates the hole-injection barrier height in a finished device, thereby reducing the V_{bi} in the device. Motivated by EA studies of Lane *et. al.[97],* we attempt to provide alternative explanations to their observations in this chapter.

In this chapter, we present direct evidences of sizeable changes ($\geq$ 0.5 eV) in cathode work functions brought about by their surface passivations and/or oxidations during vapour deposition. Using both EA spectroscopy and ultraviolet photoemission spectroscopy (UPS), we show that V_{bi} of single layer diodes are governed by the *surface* work functions of vapour-deposited metals and PEDOT:PSSH. Information derived from these measurements enables us to construct full energy alignment schematics for various single layer diodes.

4.2 Materials and Experimental Procedures

The devices presented here are of PEDOT:PSSH/polymer OSC/metal structures. Polymer OSCs used here are polyfluorene and its derivatives. As shown in Fig. 4.1, some materials used are alternating ABAB co-polymers with A being the poly(9,9'-dioctylfluorene) (F8) unit. Using Suzuki condensation coupling, B monomer of different chemical structures can be attached to the poly(9,9'-dioctylfluorene) unit to yield chemically stable, high-purity conjugated polymers with

tunable HOMO and lowest unoccupied molecular orbital (LUMO) levels *[38-40, 186-188]*. This makes polyfluorene-based OSCs ideal materials for studying the effects of varying HOMO/LUMO levels on the V_{bi} in organic optoelectronic devices.

To ensure consistency, polymers used for ultraviolet photoelectron spectroscopic (UPS) and EA measurements are of the same batch and were obtained from Cambridge Display Technology Ltd. Number average molecular weights (M_n) and polydispersity indices (PDI) of polyfluorene-based OSCs are given in Fig. 4.1. UPS studies were conducted with the use of 21.21-eV He I radiation in an ESCALab Mk-II spectrometer at a base pressure lower than 10^{-9} mbar. The experimental resolution of the UPS spectrometer is $\pm$ 150 meV, which is determined from the width of Fermi step of a Au reference specimen. HOMO values of the polymer OSCs were taken from independent UPS studies conducted by Dr. M. Zhou (National University of Singapore). All specimens were made in N_2 environment and transferred for UPS characterizations without exposing to atmospheric ambient.

Vapour-deposited Ca, Al, Ag and Au are used as the metal electrodes and PEDOT:PSSH as hole-injecting anode for all samples. The transparent substrate used here is indium tin oxide (ITO), which was subjected to successive wet cleaning with acetone and with iso-propanol and then dried with nitrogen. This is followed by 10-minute oxygen plasma etching (250 W) to eliminate residual photoresist on the surface. The plasma-etched ITO substrates were subsequently rinsed with deionised water and iso-propanol to remove residual ionic contaminants that may present on their surfaces. Immediately after these cleaning procedures, ~ 60nm thick PEDOT:PSSH films were spin coated from aqueous dispersion (3 wt % concentration) over ITO substrates follow by baking at 150^0C (in N_2 glovebox with $pO_2, H_2O < 1$ ppm) for 10 minutes.

All polymer solutions (concentrations ~ 14 – 16 mg ml^{-1}) were prepared in a N_2 environment. 75nm-thick polymer OSC films from either anhydrous 1,2-dichlorobenzene (for F8) or anhydrous xylene solutions (for F8BT, TFB and PFB) were deposited over PEDOT:PSSH [see Fig. 4.1 for their chemical structures]. This was followed by baking at either 130^0C (F8BT, TFB

and PFB films spun from xylene) or 180^0C (F8 film spun from 1,2-dichlorobenzene) in N_2 glovebox (pO$_2$, H$_2$O < 1 ppm) for 15 minutes. Metal thin films were thermally evaporated at a base pressure of ~10^{-6} to 10^{-7} mbar to define 4.27 mm^2 diodes through a shadow mask.

For EA measurements, the samples were mounted onto the sample holder of a closed-cycle He cryostat (Optistat CF from Oxford Instrument) in N_2 environment, transferred to the cryostat and evacuated to ~10^{-6} mbar without exposure to atmospheric ambient throughout this process. A sinusoidal voltage V_{rms} (216.1 Hz modulation frequency, 1ω) that is superimposed onto a static dc bias was applied across the diode. Monochromatic light was focused onto the diode from the glass substrate at 45^0, the reflected light is then collimated and focused through lens optics onto a Si photodiode with a transimpedance gain of 10^6 V/W. The electromodulated reflectance signal ΔR was then measured at 1ω and demodulated by a dual channel lock-in amplifier (SR 830 from Stanford Research Systems). Results are then recorded as fractional change in reflectance ΔR/R by the Labview 8.0 programme. All specimens were subjected to current-voltage-luminance (I-V-L) measurements in high-vacuum after V_{bi} measurements to ensure they are in working condition. Current density and luminance versus applied voltage were measured using Keithley 195 electrometer and Keithley 230 source-meter, respectively. Luminance measurements were conducted with a calibrated reference Si photodetector (Thorlabs FDS1010-CAL) located in the forward direction.
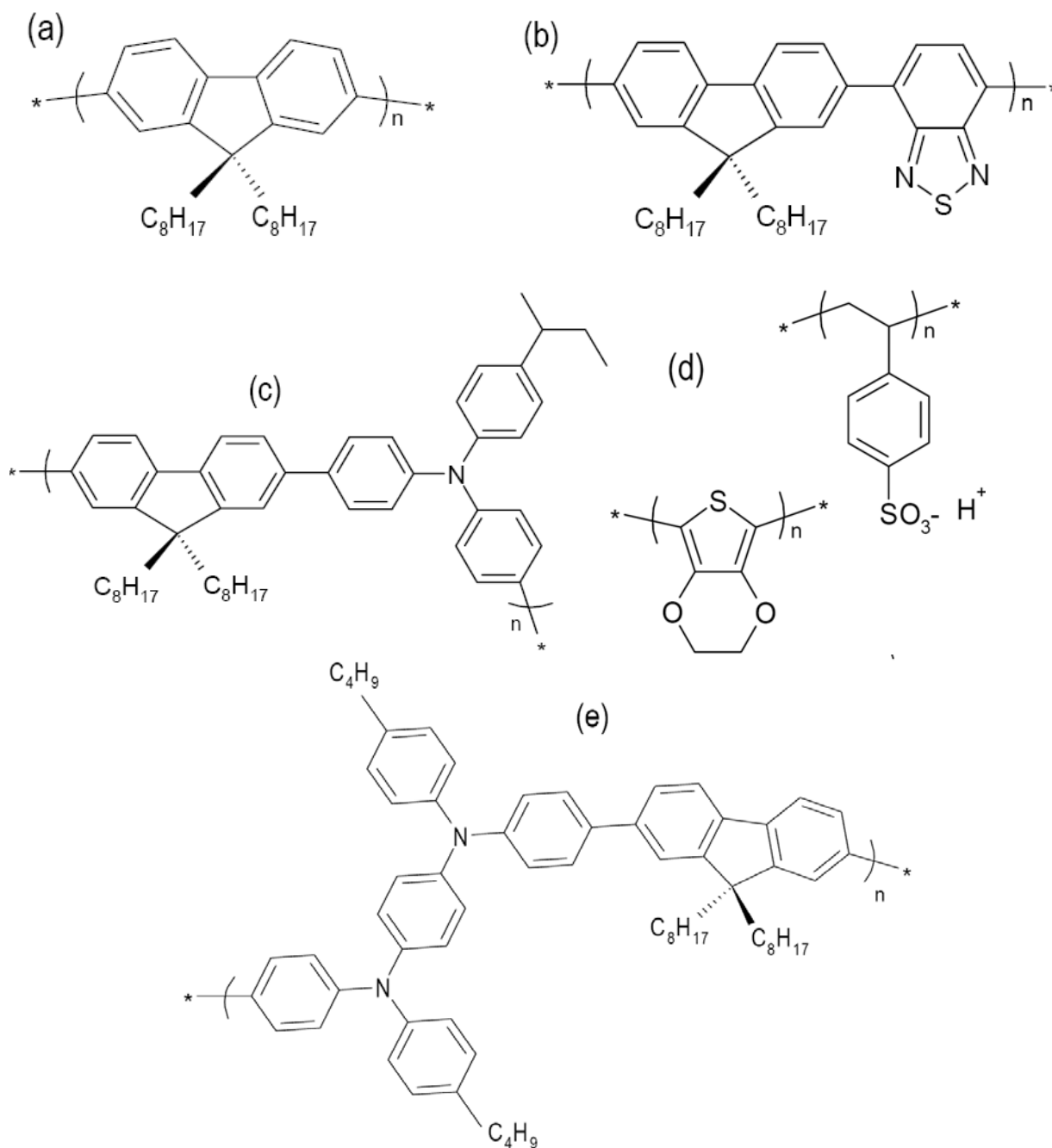
Figure 4.1: Chemical structures of (a) poly(9,9'-dioctylfluorene), F8 (M_n = 112 kg/mol, PDI = 2.10) (b) poly(9,9'-dioctylfluorene-alt-benzothiadiazole), F8BT (M_n = 97 kg/mol, PDI = 1.93) (c)poly(2,7-(9,9'-di-n-octylfluorene)-alt-(1,4-phenylene-((4-sec-butylphenyl)imino)-1,4-phenylene)), TFB (M_n = 55 kg/mol, PDI = 2.75) (d) poly(styrenesulfonate) doped poly(3,4-ethylenedioxythiophene), PEDOT:PSSH conducting polymer and (e) poly(9,9'-dioctylfluorene-alt-bis-N,N'-(4-butylphenyl)-bis-N,N'-phenyl-1,4-phenylenediamine), PFB (M_n = 60 kg/mol, PDI = 2.80) used in EA studies on devices of metal/polymer organic semiconducting (OSC)/metal structure.

4.3   Ultraviolet Photoemission Spectroscopic Studies of Electrode/Organic Semiconductor Interfaces

4.3.1 Operational Principles of the Ultraviolet Photoemission Spectroscopy (UPS)

Ultraviolet Photoemission Spectroscopy is a form of photoelectron spectroscopy used to study the band structure of material systems and their interactions at the surface. Photoelectron spectroscopy involves ionising a specimen via photoexcitation using photons of different wavelengths. By analysing energy distribution of the emitted photoelectrons, one can determine elemental composition (X-ray Photoemission Spectroscopy or XPS) or the characteristics of the band structure like density of states and work function (UPS). The figure given below illustrates the fundamental difference between XPS and UPS.
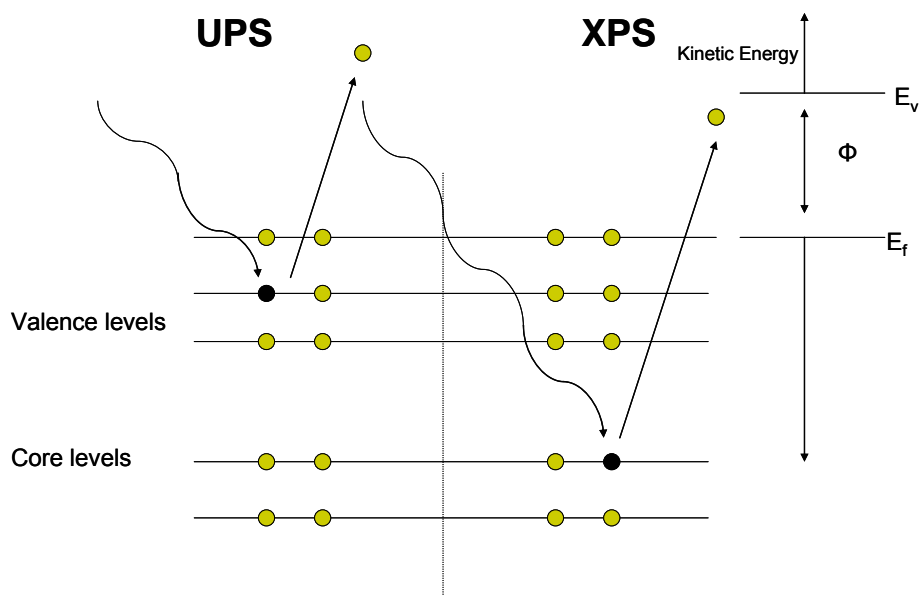
Figure 4.2: Schematic of physical processes underlying the operations of XPS and UPS techniques.

X-ray radiation that is used in typical lab-based XPS experiments is of much higher energy (typically 1200 eV) can knock out electrons from the core levels and hence can be used for

elemental composition determination. On the other hand, UV irradiation can knock out only the valence electrons and hence is primarily used for determination of properties like work function, density of states etc. As the name of UPS implies, UV irradiation obtained by high voltage gas discharge of helium gas, is used to knock out electrons. The energy of the incident UV photons (hv) of He I irradiation source is 21.21 eV. The kinetic energy (E_{kin}) of the photoemitted photoelectrons is dependent on their binding energies and can be obtained by $E_{kin} = hv - E_{binding}$, where $E_{binding}$ denotes the binding energy of the photoemitted electrons. The advantage of using UV irradiation over X-ray is that very narrow line width of the radiation can be obtained and the high flux of photons is available from simple discharge sources.

Cr/Au substrates are used for UPS so as to provide a conducting surface to avoid sample charging. The substrates are held onto Al stubs by electrically conducting carbon tapes. Ag tagging is performed at the sides of the Al stubs to prevent as-mounted samples fromn undergoing electrical charging, which would result in modification of $E_{binding}$. In a UPS measurement, samples are irradiated by UV light in a UHV chamber and photoemitted electrons are detected by an electron hemispherical analyser. During the course of UPS measurements, an electrical bias of -10 V (with respect to the UHV chamber of the spectrometer) is applied to the sample. This is useful while studying the secondary electron cascade where electrons have near-zero kinetic energy. Fig. 4.3 shows typical UPS spectra in forms of density of photoemitted electrons over a fixed E_{kin} energy range. The Fermi level (E_f) used for calibrating all UPS spectra is that of a metallic sample, usually Au or Ag. The finite density of states at the E_f is seen as a step-like spectral feature and is commonly referred to as the Fermi step.

Sample's work function Φ is given by:

$$\Phi = hv - (E_f - E_{LECO}) \tag{4.1}$$

where E_{LECO} is the lowest secondary electron energy as detected by the analyser, E_f denotes the kinetic energy of the electrons emitted from E_f of the sample and hv being the He I irradiation energy (i.e. 21.21 eV). Note that the vacuum level was obtained from the secondary-electron cutoff in the high binding energy regime of the UPS spectra; whereas ionisation potential was

approximated by the intersection of a linear extrapolation of the HOMO edge and the background signal in the low binding energy regime.

4.3.2 UPS Studies on PEDOT:PSSH/Polyfluorene Interfaces

We conducted systematic UPS measurements on different metal/polyfluorene OSC structures to understand the interface energetics across these heterojunctions. Figure 4.3 (a) – (d) shows the results of our UPS measurements conducted on a series of polymer OSC film-on-PEDOT:PSSH specimens. In most cases we examined polymer OSC films of two different thicknesses coated on top of PEDOT:PSSH, which were prepared in the glovebox environment typically used for actual device fabrications. The right panels of Figure 4.3 depict the UPS spectra near E_f of the PEDOT:PSSH and E_f of the polymer OSC films. The left panels compare the *surface* vacuum levels of the bare PEDOT:PSSH substrate and of the polymer OSC overlayers. The middle panels show the UPS spectra of these materials over the full energy range of interest.

Figure 4.3 (a) – (b) indicate that the positions of the surface vacuum levels remain unchanged (within the error limit of UPS, which is ± 150 mV) before and after coating the PEDOT:PSSH with a layer of F8 or F8BT film. These observations indicate vacuum level alignments (i.e. interface parameter, $S = 1$) at both F8-on-PEDOT:PSSH and F8BT-on-PEDOT:PSSH interfaces and show no interfacial charge transfer across these heterojunctions, which are consistent with results of recent UPS measurements *[68, 100, 111]*. We attribute the Schottky-Mott limits across these polymer-on-PEDOT:PSSH interfaces to the fabrication environments and the deep HOMO levels of F8 and F8BT. Preparing these interfaces involve exposing the PEDOT:PSSH to polymer solutions in glovebox environments, where the electrode surfaces are inevitably passivated with saturated hydrocarbons. The large ionisation potentials of F8 (~ 5.8 eV) and F8BT (~ 5.9 eV) also lead to deep hole polaron levels that lie *below* the E_f of the PEDOT:PSSH (~ 5.15 eV) *[68, 109]*. Consequently interfacial charge transfer is not likely to occur at thermodynamic equilibrium condition.
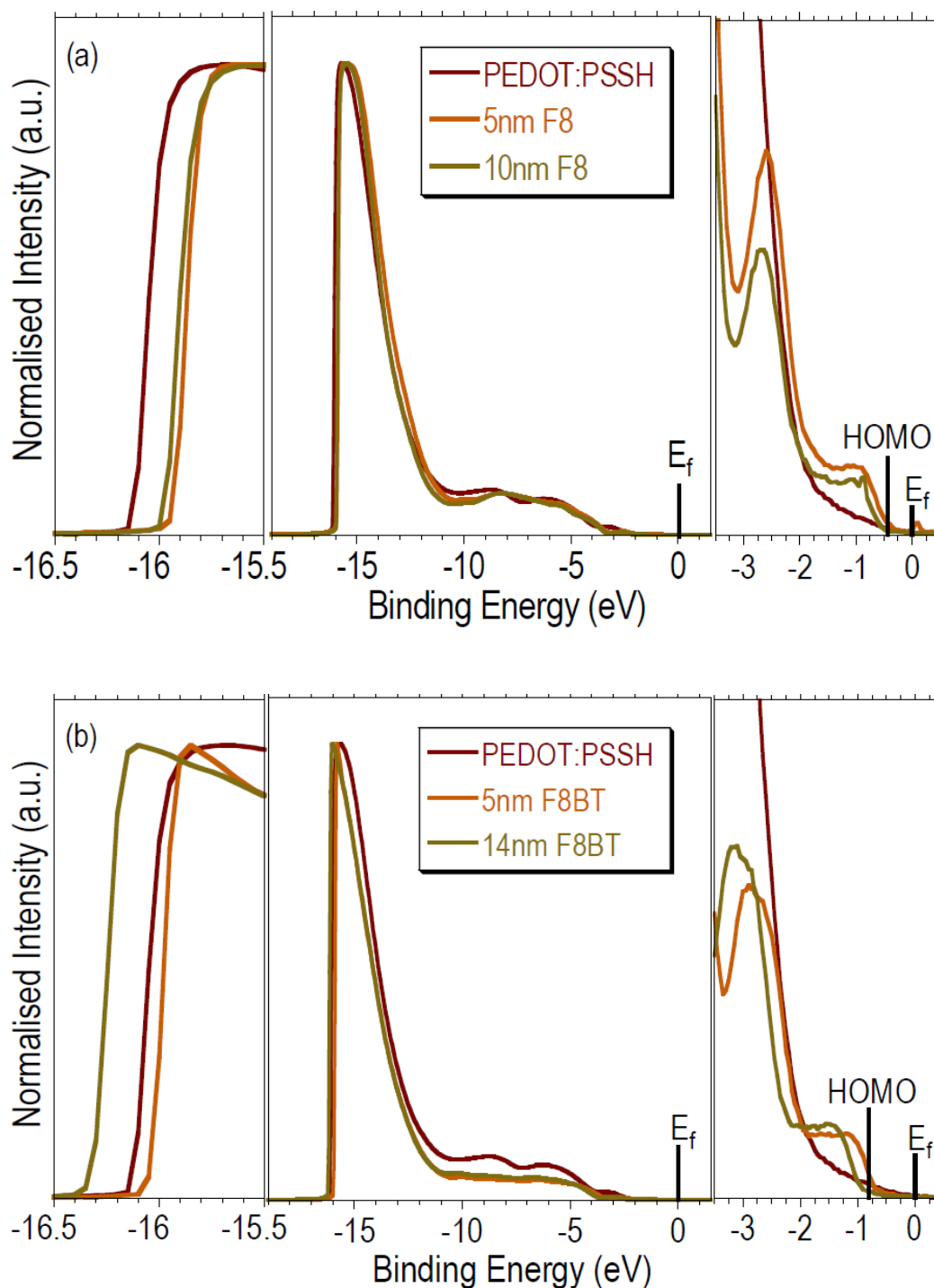
Figure 4.3: UPS spectra of (a) F8 and (b) F8BT spin coated over PEDOT:PSSH (~ 63 nm in thickness). The left panel compares the surface vacuum level positions of PEDOT:PSSH substrate before and after polymer deposition; wheareas the right panels show the magnified views of spectral regions near E_f of the materials. The energy scale is relative to the gold substrate's E_f.
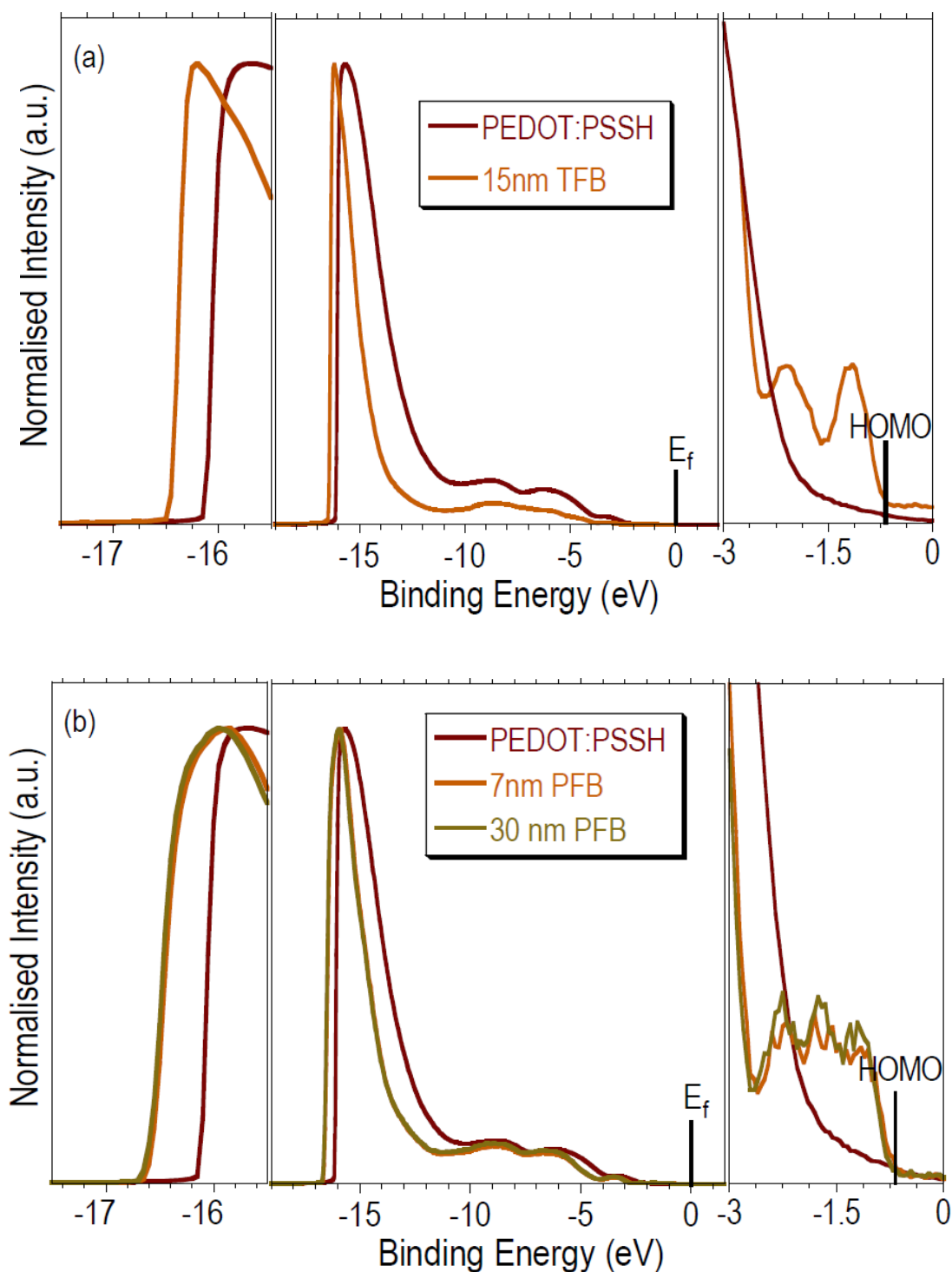
Figure 4.4: UPS spectra of (a) TFB and (b) PFB films spin-coated over PEDOT:PSSH (~ 63 nm in thickness). The left panel compares the surface vacuum level positions of PEDOT:PSSH substrate before and after polymer deposition; wheareas the right panels show the magnified views of spectral regions near E_f of the materials. The energy scale is relative to the gold substrate's E_f.

We have also conducted UPS measurements on TFB and PFB polymers that are coated on top of the PEDOT:PSSH substrates. Figure 4.4 shows the results of our UPS measurements. Interestingly, we found that the HOMO levels of TFB (~ 5.50 eV) and PFB (~ 5.30 eV) are ~ 0.2 eV lower than the HOMO levels reported by Moons *[5]*, which may be attributed to the use of different measurement techniques. The left panels of Fig. 4.4 show that $E_{binding}$ of secondary electrons emitted from the TFB and PFB surfaces are *higher* than $E_{binding}$ of the secondary electrons emitted from the PEDOT:PSSH film, showing that the polymer OSC vacuum levels lie *below* that of the PEDOT:PSSH. Our observations indicate polaronic hole transfer from the PEDOT:PSSH to the polymer OSC chains adjacent to the interfaces, which contributes to vacuum level misalignments of ~ 0.33 ± 0.20 eV and ~ 0.45 ± 0.20 eV between PEDOT:PSSH and TFB and PFB, respectively.

Although UPS data in Figure 4.4 shows that the HOMO levels of TFB (~ 5.50 eV) and PFB (~ 5.30 eV) lie *below* the E_f of PEDOT:PSSH (~ 5.15 eV), the Integer Charge Transfer (ICT) model suggests that hole polaron levels of these polymer OSCs lie *above E_f* of the PEDOT:PSSH *[26, 111]*. Using the ICT model, hole polarons may spontaneously tunnel across the interface and electronically dope the interfacial TFB or PFB chains *[26, 100, 108, 155]*. By assuming that the E_f of the PEDOT:PSSH aligns with the hole polaron levels (E_{P+}) of the polymer OSC at equilibrium, E_{P+} of TFB and PFB are estimated to be ~ 4.82 ± 0.17 eV and ~ 4.70 ± 0.17 eV, respectively. This implies that the electronic contribution of the polaron relaxation energies, which is measured as energy differences between the pinning level and the HOMO edge by UPS, is as large as 0.6 – 0.7 eV.

We believe polaron relaxation energies for polymer OSCs should be ~ 0.2 eV *[24, 27, 28]*. Hwang *et. al. [68]* propose that the electrode E_f is pinned with the tail of the broadened electronic states within the HOMO–LUMO gap of the polymer OSCs. This explanation has been verified by measurements on polymer and molecular OSCs *[113, 114]*, which confirm the presence of significant density of states at about 0.2 – 0.3 eV from the HOMO edges measured by UPS. The results of Hwang *et. al. [68]* suggest that: i) the E_f pinning level is likely to be ~ 0.4 – 0.5 eV from the HOMO edges and ii) vacuum level misalignments are probably due to

local band bending rather than abrupt interface dipole *[68, 155]*. The nature of vacuum level misalignment does not affect our result interpretations because we focus on thick polymer OSC film (thickness ~ 75 − 80 nm) typically encountered in working diode structures. Figure 4.4 reveals no subgap feature near to the HOMO features showing no chemical interactions between PEDOT:PSSH and the polymer OSCs. This observation is consistent with the presence of electronic charge transfer across the interfaces.

4.4 Energy Level Alignments in Polymer Diodes via EA Spectroscopy

We have shown that EA spectroscopy can be used to accurately determine the V_{bi} in finished working PLEDs. This can be achieved simply by measuring the applied DC bias, V_{dc} needed to null the EA signal modulated at the fundamental frequency 1ω using the following relationship:

$$\frac{\Delta R}{R}(h\nu,1\omega) \propto 2\,\mathrm{Im}\,\chi^{(3)}V_{ac}(V_{dc}+V_{bi})$$

(4.2)

The V_{bi} originates from the alignment of E_f throughout the heterostructure within a PLED. Owing to the different work functions of the two electrodes, electrons are transferred from the E_f of the thermally evaporated top metal cathode to the lower-lying E_f of anode (in this case PEDOT:PSSH). In a metal/OSC/metal sandwich structure (in which the OSC resembles a charge-free insulator), this spontaneous self-discharge process is limited by an opposing electrostatic field (i.e. the built-in field) that offsets the difference in electrode's work function to attain electrical equilibrium. Importantly Schottky barrier height (ϕ_b) is related to the difference between the electrode's E_f and the relevant transport levels of OSC at the metal/OSC interface. This follows from the general relationship between the energy gap of the polymer OSC (i.e. E_g), the measured V_{bi} and ϕ_b at both polymer OSC/metal heterojunctions:

$$\phi_{b,cathode} + eV_{bi} + \phi_{b,anode} = E_g$$

(4.3)

$\phi_{b,cathode}$ and $\phi_{b,anode}$ represent barrier heights at the cathode/polymer and the anode/polymer interfaces, respectively. Eq. (4.3) enables EA spectroscopy to be used for measuring variations in barrier heights ($\Delta\phi_b$) of finished PLEDs with different work functions. In the ideal case where vacuum levels align at both the metal/polymer OSC interfaces and the built-in electric field is uniform across the polymer OSC layer [see Fig. 4.5 (a)], V_{bi} is the difference in work functions of the electrodes. When interface dipole layer(s) δ exist at one or both metal/OSC heterojunction(s)

[see Fig. 4.5 (b)], V_{bi} reflects the net difference in the electrode's work functions and dipole layer(s). In both cases eq. (4.3) is valid in describing the relationship between the measured V_{bi}, ϕ_b and E_g because ϕ_b have taken the interface dipole(s) δ into consideration [see eq. (4.4) and (4.5)]. Fig. 4.5 schematically depicts the relationship between these parameters for metal/OSC/metal structures. In general, $\phi_{b,cathode}$ and $\phi_{b,anode}$ at metal/OSC interfaces can be written as:

$$\phi_{b,anode} = I_p - \Phi_{anode/OSC} + \delta_{anode/osc} \tag{4.4}$$

$$\phi_{b,cathode} = \Phi_{cathode/OSC} - \chi_s + \delta_{cathode/osc} \tag{4.5}$$

where $\Phi_{cathode/OSC}$ (or $\Phi_{anode/OSC}$) denotes the work function of the cathode (or the anode) at the polymer OSC/electrode interface. We emphasise that $\Phi_{cathode/OSC}$ should be differentiated from $\Phi_{cathode}$, which represents the work function of a bare cathode surface encountered in UHV environment. Discrepancies between $\Phi_{cathode/OSC}$ and $\Phi_{cathode}$ are discussed at length in subsequent sections.

It is worth noting that relevant transport levels of polymer OSCs consists of a manifold of electronic states broadened by structural disorders *[34, 36, 113]*. This material characteristic invariably leads to ambiguity in the definition of Schottky barrier height. In internal photoemission measurement, for instance, ϕ_b is defined as the difference between the metal's E_f and the polymer OSC's lowest (or highest) electron (or hole) polaron level *[56]*. When a distribution of molecular states is considered, charge transport levels in the polymer OSC are approximated to be some average molecular levels amongst the manifold polaronic states *[34]*. In the case of disordered polymer OSCs, non-uniform conjugation lengths can further affect positions of the relevant transport levels. We emphasise that the uncertainty on the exact position of the transport level do not affect our discussions in this chapter because we determine the cathode's E_f from the *changes* in the electron-injection barrier height ($\Delta\phi_{b,cathode}$) and the built-in potential (ΔV_{bi}) of the metal/OSC/metal structures.

Fig. 4.5 illustrates the methodology employed to achieve accurate determinations of $\Delta\phi_b$ and $\Phi_{cathode/OSC}$ of different metals prepared by vapour deposition. Using this method, a series of diode structures that use PEDOT:PSSH as anode but with different polymer OSC materials (i.e. E_g = constant and Φ_{anode} = constant) are constructed. Metal cathodes of different UHV work functions ($\Phi_{cathode}$) are deposited by vapour deposition over the polymer OSC layer. For diodes with identical polymer OSC layer and PEDOT:PSSH anode, $\Phi_{cathode}$ is correlated to the V_{bi} since ΔV_{bi} indicates an opposite change in $\phi_{b,cathode}$ of equal magnitude *[143]*:

$$e\Delta V_{bi} = -\Delta\phi_{b,cathode} \qquad (4.6)$$

Eq. (4.3) – (4.6) enable direct measurements of $\Phi_{cathode/OSC}$ through determining the ΔV_{bi} by EA technique. This is useful because injection barriers at the metal-on-polymer interfaces are more difficult to determine than those at the polymer-on-metal interfaces by photoemission spectroscopy. In UPS measurements, ϕ_b at the metal-on-polymer interface are given by difference between the E_f of the metal and the energy of the frontier HOMO orbitals (i.e. HOMO edge) of the polymer OSC *[71]*. But UPS signals from the incrementally deposited metal overlayer often rapidly mask the UPS signals of the OSC underlayer *[66]*, thereby making accurate determination of ϕ_b difficult in many instances.

The actual interfacial chemistries found in working devices are also different from those detected by UPS technique since the electronic structure across metal-on-polymer interface is highly sensitive to the actual device fabrication environment (e.g. partial pressure of oxygen and moisture) *[4, 26, 100, 109, 174, 180]*. Metal-on-polymer interfaces are often diffuse with metal diffusion *[66, 174]* and may have various chemical interactions *[4, 66, 92, 174, 189, 190]* taking place. In the case of poly(phenylene-vinylene), PPV systems, Ca deposition in UHV environment leads to bulk or interfacial doping of the polymer OSCs and generation of bipolaron states in the forbidden energy gap of the polymer OSC *[174, 191]*. Depositing Ca over PPV systems in HV environment (~ 1 x 10^{-6} mbar) leads to the formation of a 20 – 30 Å CaO_x layer between Ca and the polymer *[4, 174]*. Such a passivating oxide layer is known to eliminate

photoluminescence quenching sites (due to Ca–OSC interactions) and enhance radiative recombination efficiencies of many organic LEDs (OLEDs) *[4, 180, 192]*; whereas OLEDs fabricated in UHV environment (~ 1 x 10^{-9} mbar) often exhibit lower efficiencies and inferior operational stabilities *[180, 181, 192, 193]*. These observations show that UPS measurements conducted in UHV environment may not yield information that is directly correlated to the performance behaviours of real working devices. Therefore there is a need to examine the metal/OSC heterojunctions encountered in working PLEDs fabricated in a practical environment.

The combination of UPS and EA measurements gives us the possibility to determine the work functions of vapour-deposited metals at the metal/OSC interfaces (i.e. $\Phi_{metal/OSC}$) in working devices. $\Phi_{metal/OSC}$ can be estimated based on:

$$\Phi_{cathode/OSC} = \Phi_{anode/OSC} - eV_{bi} - \delta_{anode/OSC} \qquad (4.7)$$

where $\Phi_{cathode/OSC}$ and $\Phi_{anode/OSC}$ in eq. (4.7) denote the interface work functions of cathode and anode (i.e. PEDOT:PSSH), respectively. Interface work functions are defined with respect to the polymer OSC's vacuum level; while V_{bi} and interface dipole $\delta_{anode/OSC}$ can be accurately measured by EA and UPS, respectively.

The EA response of a polymer OSC film (~ 100 nm in thickness) in a MIM structure at electrical equilibrium is identical to that of a dielectric film that is depleted of charges. To determine V_{bi} we concentrate on eq. (4.2), which shows that the EA signal, in the form of normalised reflectance $\Delta R/R$ ($h\upsilon, 1\omega$), modulated at the fundamental frequency 1ω is linearly related to the effective DC voltage ($V_{dc} + V_{bi}$) across the polymer OSC and is cancelled when $V_{dc} = -V_{bi}$. It is also linearly dependent on the applied AC voltage. In this chapter, we show that EA spectroscopy is an ideal technique to measure the *interface* work functions of technologically-important electrodes of different materials (vapour-deposited polycrystalline metals, amorphous metal oxide films and conducting polymer) in working devices. In conjunction with the UPS technique, our approach shed lights on the nature of interfacial electronic structures that are of practical relevance for device interface engineering.
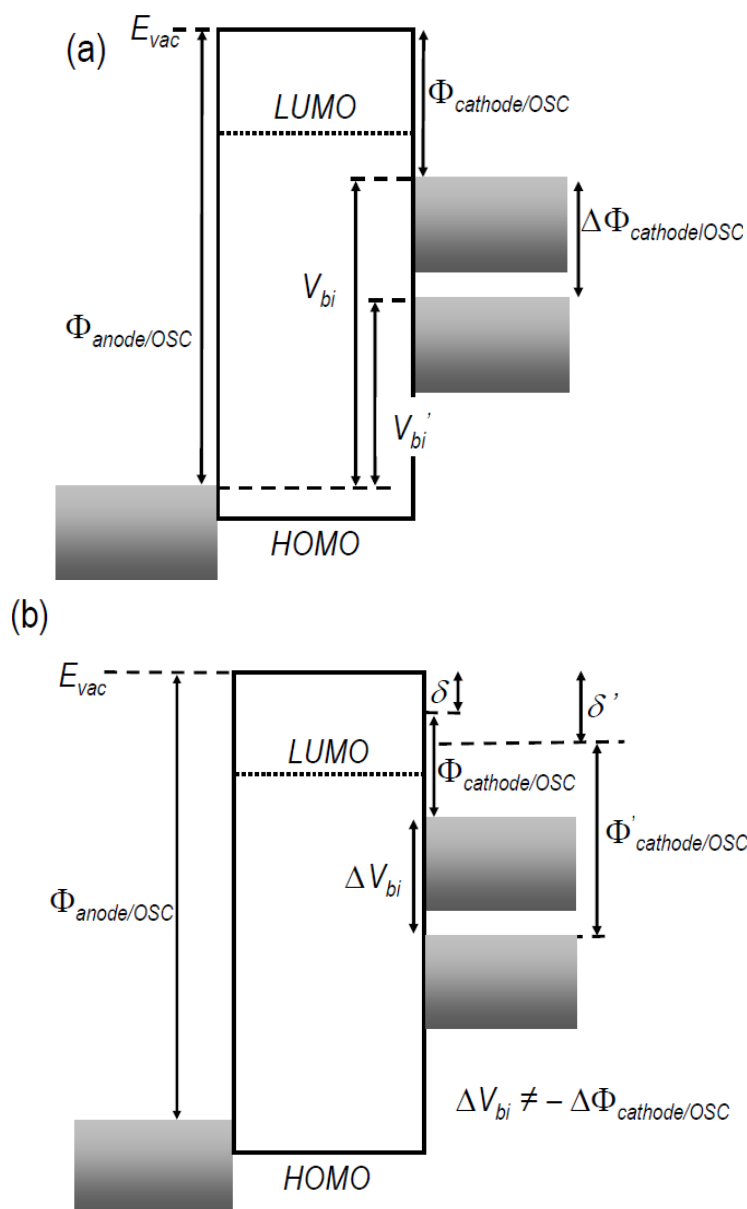
Figure 4.5: Energy levels of anode/polymer OSC/cathode (MIM) structures at flat band condition. $\Phi_{cathode/OSC}$ denotes the cathode work function at the metal/OSC interface measured by EA. E_f equilibration generates a built-in potential (V_{bi}) through the structure.
(a) MIM structure with vacuum level (E_{vac}) alignment at both metal/OSC interfaces enable direct determination of $\Phi_{cathode/OSC}$ from variation in V_{bi} (i.e. ΔV_{bi}). This enables measurement of the charge-injection barrier height at the cathode/OSC interface ($\phi_{b,cathode}$) using the relationship:
$\Delta V_{bi} = -\Delta\Phi_{cathode/OSC} = -\Delta\phi_{b,cathode} = -(\Phi_{cathode/OSC} - \text{LUMO})$.
(b) MIM structure with E_{vac} *misalignment* at one of the metal/OSC interfaces due to localised interface dipole. $\Delta V_{bi} \neq -\Delta\Phi_{cathode/OSC}$ in different MIM structures with a common anode (i.e. PEDOT:PSSH), but $|\Delta V_{bi}| = |\Delta\phi_{b,cathode}|$ in all cases. The latter relationship applies even if E_{vac} misalignments exist at both anode/OSC and cathode/OSC interfaces.

4.5 Results of EA Studies on PEDOT:PSSH/Polyfluorenes/Metal Diodes

4.5.1 Influences of Temperature on EA Measurements

At room temperature the 1ω electromodulated $\Delta R/R$ ($h\upsilon,1\omega$) spectrum taken at room temperature contains both the EA and charge modulated [or excited state absorption (ESA)] components *[49, 126, 154]*, which may lead to inaccurate determination of the V_{bi}. Fig. 4.6 illustrates the effects of temperature on EA spectra of a PEDOT:PSSH/TFB/Ca device, which are measured at room temperature and 10 K while subjecting the device to different externally applied V_{dc}. Fig. 4.6 (a) and 4.6 (c) show that the EA spectra of the same device over a wide energy range (1.5 eV to 3.74 eV) at 298 K and 10 K, respectively. Fig. 4.6 (b) depicts a strong subgap spectral feature between 2.0 eV and 2.7 eV measured at at 298 K that becomes saturated as the V_{dc} approaches forward bias; but upon cooling to 10 K [see Fig. 4.6 (d)] the intensity of this subgap feature is significantly attenuated and becomes less dependent on V_{dc}.

Recent studies have attributed the origin of this subgap feature to either electron trapping at the PEDOT:PSSH/polymer OSC interface *[142, 154]* or "delta-state" interfacial doping of the polymer OSC by PEDOT:PSSH *[155]*. The V_{bi} values shown here are of ± 0.05 V accuracy limit as it has taken into the non-zero spectral background interferences with the nulling voltages (V_{null}) into consideration. V_{null} measurements conducted with identical experimental conditions but at room temperature (not shown) reveal that V_{null} are generally lower than respective V_{bi} values by 0.1 – 0.2 V and may be attributed to temperature-dependent ESA spectral contamination. To circumvent this problem, all V_{bi} measurements on metal/OSC/metal structures are conducted at temperature as low as 10 K to eliminate or minimise the ESA spectral contributions to the $\Delta R/R$ ($h\upsilon,1\omega$) *[155, 194]*.
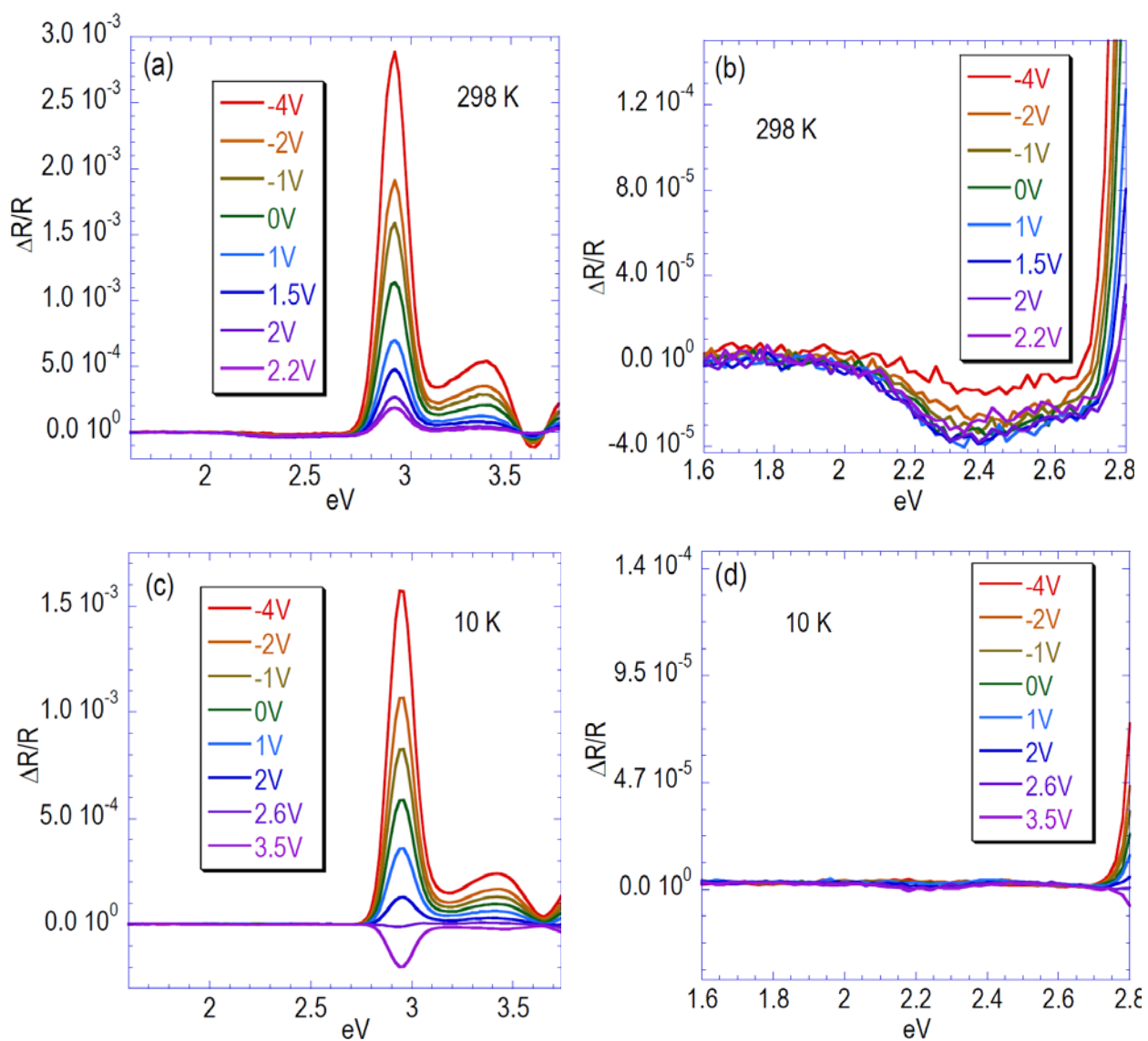
Figure 4.6: 1ω EA spectra of 60 nm-PEDOT:PSSH/75 nm-TFB/50 nm-Ca diode at dfferent temperatures and externally applied V_{dc}. The device is electromodulated with a V_{ac} of 0.35V_{rms} at 216.1 Hz frequency.

4.5.2 Measurements of V_{bi} in PEDOT:PSSH/Polyfluorenes/Metal Diodes

The 1ω EA spectrum of a typical 60 nm-PEDOT:PSSH/75 nm-F8BT/metal at V_{dc} = 0 V and 10K is shown in the inset of Fig. 4.7. The fact that 1ω EA spectrum is not zero when V_{dc} = 0 V indicates the presence of a built-in field that originates from E_f alignment throughout the heterostructure. In order to extract the V_{bi}, monochromatic probe beam of photon energy corresponding to the 1ω EA maxima was illuminated onto the metal/OSC/metal diode, which is subjected to electrical modulation of a fixed sinuidoidal voltage (0.5 V_{rms}). At the same time, the 1ω EA signal is monitored and measured as a function of V_{dc} applied across the device. Fig. 4.6 shows the 1ω EA responses of the PEDOT:PSSH/75 nm-F8BT/metal (metal = Ca, Al, Ag or Au) devices at 10 K, which vary linearly with V_{dc}. Using eq. (4.2), the V_{bi} values are measured as the bias needed to null the 1ω EA signals in these devices.

Figure 4.7: 1ω EA responses of 60 nm-PEDOT:PSSH/75 nm-F8BT/metal (metal = Ca, Al, Ag or Au) diodes at 10 K and 2.45 eV as a function of V_{dc}. Devices are electrically modulated with a sinusoidal V_{ac} of 0.5V_{rms} at 216.1 Hz frequency. A typical EA spectrum of the device is shown in the inset.

Several important observations can be made from Fig. 4.7. The 1ω EA responses are linearly dependent on the V_{dc} indicating that the rigid band approximation is valid in describing electric field distribution in these devices. Based on eq. (4.2), we find that the V_{bi} of the PEDOT:PSSH/F8BT/Ca diode is 2.44 V and the V_{bi} of the PEDOT:PSSH/F8BT/Al diode is 1.99 V. These observations are qualitatively consistent with the fact that polycrystalline Al has a higher bulk work function (4.2 - 4.3 eV *[27, 100, 183, 195, 196]*) than that of polycrystalline Ca (2.8 – 2.9 eV *[27, 196, 197]*). Similarly replacing Al with noble metals of higher work functions causes further decrease in V_{bi} of the devices. Specifically the V_{bi} of the PEDOT:PSSH/F8BT/Ag diode is found to be 1.40 V; whereas V_{bi} of PEDOT:PSSH/F8BT/Au diode is only 0.40 V. Interestingly ΔV_{bi} is *not* identical to the corresponding differences in the UHV work functions of these metals (i.e. $\Delta V_{bi} \neq -\Delta\Phi_{cathode}$) even though all devices comprise the same anode material (i.e. PEDOT:PSSH) of identical work function. The discrepancies between our V_{bi} measurements and the reported UHV metal work functions are discussed in detail in section 4.6.

Figure 4.8: 1ω EA responses of 60 nm-PEDOT:PSSH/75 nm-TFB/metal (metal = Ca, Al, Ag or Au) diodes at 10 K and 2.96 eV as a function of V_{dc}. Devices are modulated with a sinusoidal V_{ac} of 0.5V_{rms} at 216.1 Hz frequency. A typical EA spectrum of the device is shown in the inset.

We observe similar phenomena for PEDOT:PSSH/TFB/metal devices in which Ca, Al, Ag and Au are used as four different metal electrodes. Fig. 4.8 depicts the 1ω EA spectrum of a typical PEDOT:PSSH/TFB/metal diode and their 1ω EA responses as a function of applied V_{dc} at 10 K. The V_{bi} values decreases in the order of Ca, Al, Ag and Au, which is consistent with the respective work functions of these metals determined in UHV *[100, 123, 198, 199]*. But V_{bi} values for PEDOT:PSSH/TFB/metal diodes are different compared to V_{bi} values of F8BT-based diode that employs the same electrode combinations [see Fig. 4.8]. Another notable observation is that the change in V_{bi} of the PEDOT:PSSH/TFB/metal device is *not* identical to the difference in the UHV work functions of these metals. To better understand the correlation between V_{bi} values and the nature of the polymer OSC, it is important to conduct EA measurements on diodes with polymers with similar chemical structures as active layers. Accordingly F8 and its derivatives PFB are ideal candidate polymers as they share similar chemical structures with F8BT and TFB but have different HOMO values *[5, 68, 100]*.
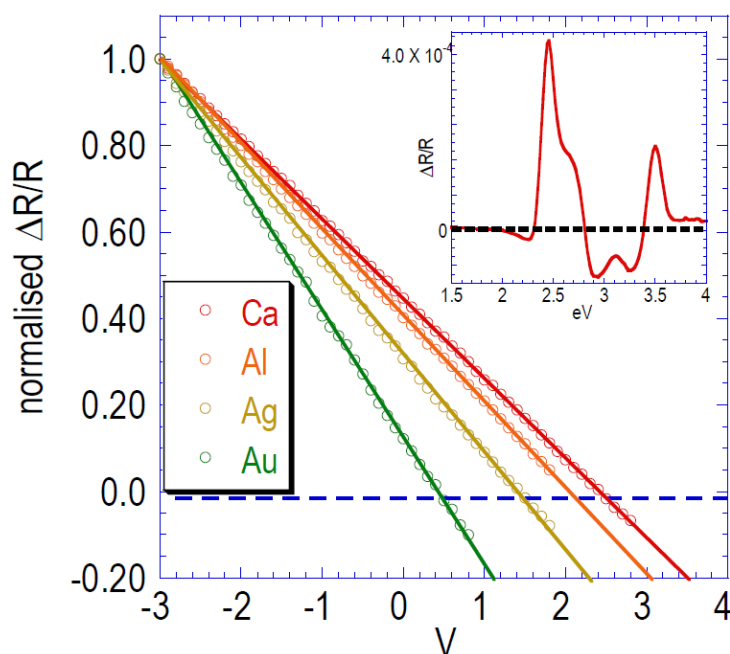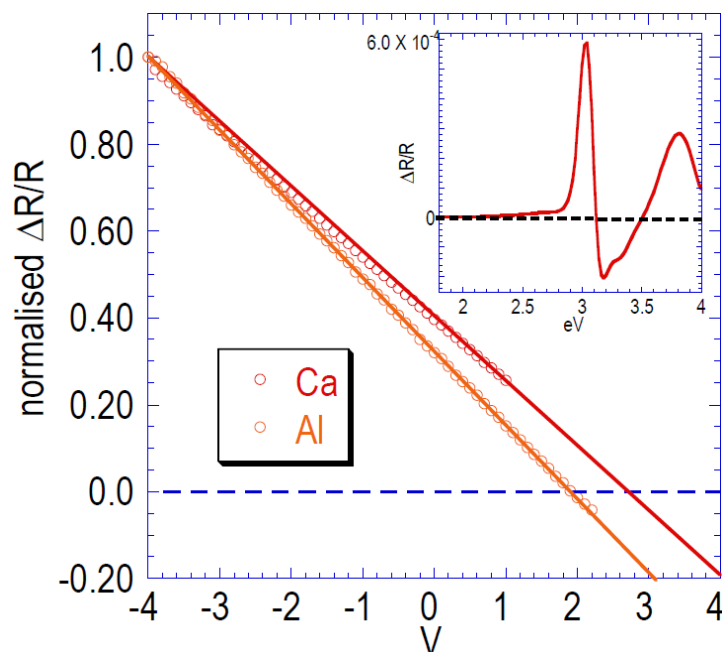

Figure 4.9: 1ω EA responses of 60 nm-PEDOT:PSSH/80 nm-F8/metal (metal = Ca and Al) diodes at 10 K and 3.05 eV as a function of V_{dc}. The devices are modulated with a sinusoidal V_{ac} of $0.5V_{rms}$ at 216.1 Hz frequency. A typical EA spectrum of F8 is shown in the inset.

Fig. 4.9 and 4.10 depict the 1ω EA responses of PEDOT:PSSH/F8/metal and PEDOT:PSSH/PFB/metal, respectively. Fig. 4.9 shows that the V_{bi} of PEDOT:PSSH/F8/Ca is 2.74 V. But replacing Ca with Al electrode reduces the V_{bi} to 1.90 V, which is consistent with the results shown in Fig. 4.7 and Fig. 4.8. Importantly the decrease in V_{bi} upon replacing Ca with Al is *less* than the difference in UHV work functions of the two metals. The V_{bi} of PEDOT:PSSH/F8/Al device is identical to that reported by Lane *et. al. [97]* but 0.30 V smaller than that recent measurements reported by Zhou *et. al.[200]*. Reasons contributing to such inconsistencies are discussed in section 4.6. Fig. 4.9 shows the 1ω EA responses for PEDOT:PSSH/PFB/metal diodes at 10 K, where vapour-deposited Ca or Al is used as the metal electrodes. The V_{bi} of PEDOT:PSSH/PFB/Ca is 2.30 V but replacing Ca with Al electrode reduces the V_{bi} to 0.99 V. In this case, the 1.31 V difference in V_{bi} coincides with the difference in work functions of polycrystalline Al (~ 4.2 eV) and polycrystalline Ca (~ 2.9 eV). These results clearly show that the V_{bi} values are markedly affected by the HOMO levels of the polymer OSC materials. Results of our EA measurements shown in Fig. 4.7 – 4.10 are summarised in Table 4.1.
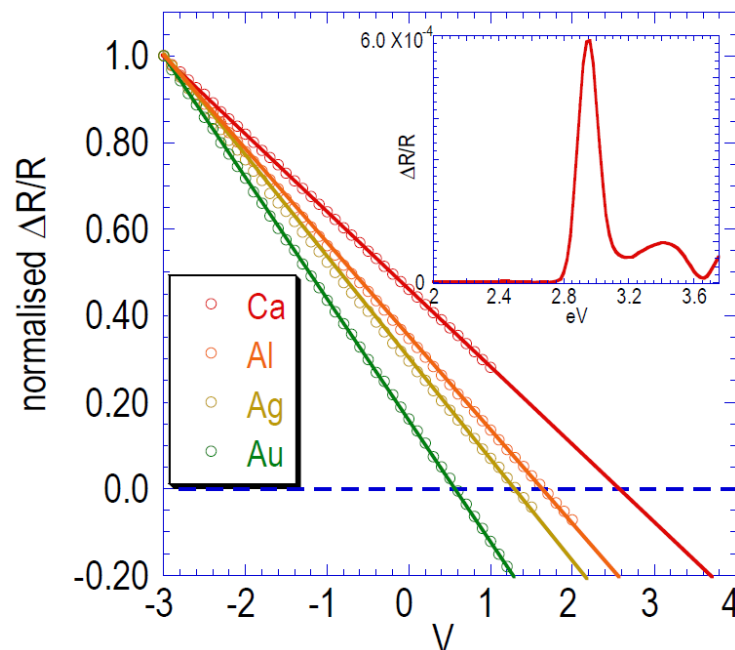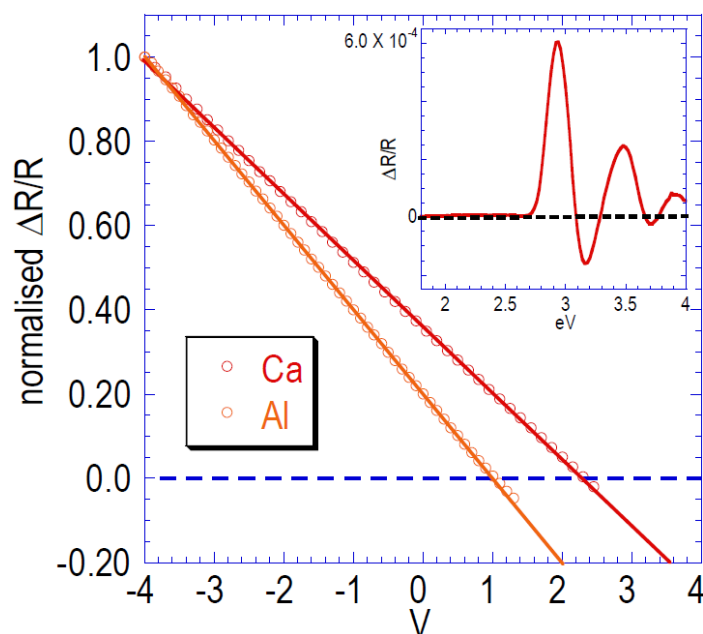

Figure 4.10: 1ω EA responses of 60 nm-PEDOT:PSSH/75 nm-PFB/metal (metal = Ca and Al) diodes at 10 K and 2.90 eV as a function of V_{dc}. The devices are modulated with a sinusoidal V_{ac} of 0.5V$_{rms}$ at 216.1 Hz frequency. A typical EA spectrum of PFB is shown in the inset.

Device structure	Metal cathode	$\delta_{PEDOT/OSC}$ (± 0.20 eV)	V_{bi} (± 0.05 V)	$\Phi_{cathode/OSC}$ (± 0.25 eV)
PEDOT:PSSH/F8BT/cathode	Ca	0.0	2.44	2.71
	Al		1.99	3.16
	Ag		1.40	3.75
	Au		0.40	4.75
PEDOT:PSSH/F8/cathode	Ca	0.0	2.74	2.41
	Al		1.90	3.25
PEDOT:PSSH/TFB/cathode	Ca	0.33	2.59	2.23
	Al		1.64	3.18
	Ag		1.29	3.53
	Au		0.56	4.26
PEDOT:PSSH/PFB/cathode	Ca	0.45	2.30	2.40
	Al		0.99	3.71

Table 4.1: Results of UPS and V_{bi} measurements as well as the work functions of different vapour-deposited metals over different polyfluorene OSCs (i.e. $\Phi_{cathode/OSC}$). $\Phi_{cathode/OSC}$ and the uncertainties inherent in $\Phi_{cathode/OSC}$ are determined based on eq. (4.7).

4.6 Energy Level Alignments in PEDOT:PSSH/Polyfluorene OSCs/Metal Diodes

4.6.1 PEDOT:PSSH/OSC/Ca (or Al) Diodes (OSC = F8 or F8BT)

To correctly understand our results, we first examine the energy level alignment across the PEDOT:PSSH/F8/metal diodes. The deep HOMO level (5.8 eV) of F8 *[100, 111, 187]* leads to vacuum level alignment *[100, 111, 183, 201]* with the underlying PEDOT:PSSH anode. UPS measurements were conducted on PEDOT:PSSH surfaces that were exposed to organic solvents used for dissolving polymer OSCs. The work function of such a "passivated" PEDOT:PSSH surface, Φ_{PEDOT} is confirmed to be 5.15 ± 0.05 eV and is in excellent agreement with reported literatures *[52, 100, 109, 201, 202]*. Using these information, V_{bi} measurements derived from the EA technique enable direct determinations of the interface work functions of vapour-deposited Ca and Al. Using eq. (4.7), we estimated the interface work function of vapour-deposited Ca, $\Phi_{Ca/F8}$ to be given by ~ 2.41 eV ($\approx 5.15 - 2.74$ eV). The same analysis for vapour-deposited Al yields $\Phi_{Al/F8}$ to be ~ 3.25 eV ($\approx 5.15 - 1.84$ eV). In both cases $\Phi_{Al/F8}$ and $\Phi_{Ca/F8}$ are considerably lower than their respective bulk work functions [determined by UPS, see *[96, 178, 194]*] of polycrystalline Ca and polycrystalline Al.

Several reasons contribute to lowering of metal work functions. Although work function of polycrystalline Al has been widely assumed to be $4.1 - 4.3$ eV *[27, 97, 100, 183, 195, 196]*, such values are taken via UPS technique in UHV environment ($\sim 1 \times 10^{-9}$ mbar) in which the surface of the Al film is atomically clean. Depositing Al on clean *oxygen-free* surfaces of polymer OSCs is known to induce interfacial chemical interactions *[88, 89, 96, 201, 202]*, which break π-conjugations of polymer OSCs *[89, 96]* and result in chemically diffuse heterojunctions with thicknesses on the scale of electron tunneling lengths *[92, 174]*.

But Al vapour deposition in actual device fabrications are conducted in high vacuum environment ($\sim 1 \times 10^{-6}$ mbar) in which the polymer OSC surfaces are passivated by a thin layer of physisorbed oxygen and/or hydrocarbon molecules *[4, 26, 174, 180]*. A thin AlO$_x$ layer ($\sim 20 - 30$ Å in thickness *[4, 174]*) is formed during the early stage of Al deposition over the polymer

(F8 in this case), which may prohibit polymer-metal interactions and modify the interface work function of Al. This observation is consistent with independent UPS studies on AlO$_x$ surfaces, which confirm that AlO$_x$ work function varies from 3.3 eV to 3.8 eV *[103, 203, 204]*. Early studies of oxygen adsorption on polycrystalline Al surface at room temperature *[204, 205]* report a strong correlation between the Al surface oxide formation and its work function, which decreases by up to ~ 0.8 eV upon oxygen exposure. Similarly vapour deposition of Ca over polymer OSC is known to be preceded by the formation of a thin CaO$_x$ passivating layer *[4, 174, 180]*, resulting in PEDOT:PSSH/F8/CaO$_x$/Ca heterojunction in a finished device. Therefore surface oxide formation may account for the relatively low values of $\Phi_{Ca/F8}$ and $\Phi_{Al/F8}$.

Another factor that may also lead to the lowering of Al and Ca work functions is the "push-back" effect of the metal's surface electrons, where the electron density that spills outside the metal surface is repelled by that on the OSC surface. This phenomenon reduces the metal's work function and can be as large as 0.5 – 0.8 eV *[101, 108, 195, 204]*, which may explain the 0.8 – 1.0 eV deficit of $\Phi_{Al/F8}$ (3.25 eV) as compared to the reported work function of Al (4.1 – 4.3 eV). The same reasoning can be applied to the F8/Ca interface because $\Phi_{Ca/F8}$ (2.41 eV) [see Table 4.1] measured by the EA technique is 0.4 – 0.5 eV lower than the reported work function of polycrystalline Ca (i.e. 2.8 – 2.9 eV *[196, 197]*).

It is not clear that E_f of the Ca is "pinned" with the F8 LUMO level due to the inconsistency over the reported LUMO values of F8 polymer *[68, 186, 187, 206]*. Our optical absorption measurement of F8 film (data not shown) shows that E_g of F8 is ~ 3.16 eV. The LUMO level of OSC can be estimated using the following relationship:

$$LUMO = HOMO - E_g - E_b \qquad (4.8)$$

where E_g and E_b denote optical absorption gap and exciton binding energy, respectively. By assuming that the HOMO level of F8 to be ~ 5.8 eV [see Fig. 4.3 and references *[68, 111, 187]*] and the E_b of F8 polymer as ~ 0.3 eV *[186]*, we estimate the LUMO level of F8 to be ~ 2.3 eV by using eq. (4.8), which is identical to $\Phi_{Ca/F8}$ measured by the EA technique (~ 2.41 eV) within

experimental errors. Since $\Phi_{Ca/F8}$ almost coincides with the F8 LUMO level, we conclude that there should be charge transfer at the Ca-on-F8 interface although charges may have to tunnel through a thin CaO_x interlayer. The effects of oxygen exposure on the Ca-on-F8 interface has been studied using photoemission spectroscopies *[173]*, which concluded that Ca diffuses into F8 and an injection barrier height of 0.5 eV exists at the Ca-on-F8 interface after oxidation. But these results are derived from *in-situ* oxidation of the Ca-on-F8 interface originally prepared in an UHV environment and does not correspond to actual fabrication environment. The Ca-on-F8 interface encountered in operational, finished devices is likely to be $Ca/CaO_x/F8$ with distinctive change in material composition across the junction.

Interestingly independent EA measurements on the PEDOT:PSSH/F8/Al diode *[97, 201]* yield results that are with our values. In particular, Zhou *et. al. [201]* reported a V_{bi} of 1.60 V while Lane *et. al. [97]* reported a V_{bi} of 1.90 V. Studies by Koch *et. al. [109]* have demonstrated that Φ_{PEDOT} can vary by 0.5 eV depending on the relative humidity of the processing environment, so the 0.30 V difference in V_{bi} may be caused by variations of PEDOT:PSSH work function and/or $\Phi_{Al/F8}$. This leads us to conclude that the exact value of $\Phi_{Al/F8}$ is likely to be uncertain and can change depending on the actual fabrication environment. Indeed it is not physically meaningful to ascertain the exact value of $\Phi_{Al/F8}$ because V_{bi} represents a macroscopic, spatially averaged parameter derived over the entire EA probe beam area *[143]*. As such $\Phi_{Al/F8}$ reported here should be taken as an estimate with fairly large uncertainty of ~ 0.2 eV.

We apply similar analysis to the PEDOT:PSSH/F8BT/metal diodes since our UPS data confirms that the vacuum level of F8BT (HOMO = 5.9 eV *[5, 207]*) aligns with that of PEDOT:PSSH ($\Phi_{PEDOT} = 5.15 \pm 0.05$ eV). For the case of PEDOT:PSSH/F8BT/Al, $\Phi_{Al/F8BT}$ is found to be $\sim$ 3.16 eV using eq. (4.7), which is identical to $\Phi_{Al/F8}$ within the error limit of the EA technique. Therefore, we conclude that in both cases interface work function of Al decreases by $0.8 - 1$ eV upon vapour deposition over the OSC underlayer.

The case of the PEDOT:PSSH/F8BT/Ca diode deserves more detailed examination. The value of $\Phi_{Ca/F8BT}$ (2.7 eV) is larger than that of $\Phi_{Ca/F8}$ (2.4 eV) due to charge transfer from the Ca's E_f

to the LUMO level of F8BT *[97, 207]*. Using eq. (4.8), Campbell *et. al.* *[207]* showed that the LUMO level of F8BT is 3.2 eV below the vacuum level *[40, 97]*. Moons *[5]* also reported the LUMO level of F8BT to be 3.5 eV. The large electron affinity of F8BT is consistent with quantum chemical calculations *[208]*, which show that the incorporation of electrophilic BT co-monomer units significantly lower the LUMO level of F8BT via spatial localisation of the LUMO electronic wavefunction *[208]*. Subsequent studies have therefore assumed 3.2 eV *[209]* or 3.5 eV *[5]* to be the LUMO levels and hence the "pinning levels" *[97]* of F8BT with low work-function metals.

But it is important to point out that the 3.2-eV-LUMO level of F8BT is derived from optical gap (E_g) measurement *[210]* with the assumption that E_b of F8BT is identical *[40, 207]* to that of F8 (i.e. ~ 0.3 eV, taken from reference *[186]*). We note that the F8BT E_g value reported by Fletcher *[210]* is 2.4 eV and is not consistent with the E_g (2.66 eV) reported elsewhere *[211]*. Therefore we conducted independent optical absorption measurement [see Fig. 5.2 (b)] of F8BT film, which shows that E_g is 2.7 eV and agrees well with 2.66 eV E_g reported in ref. *[211]*. We also note that previous studies *[40, 207]* may have underestimated E_b of F8BT by 0.1 – 0.2 eV since the incorporation of the electrophilic BT units result in optoelectronic properties *[208]* that are very different from those of F8. Unfortunately, E_b of F8BT has not been measured directly and is not known.

We attempt to deduce the LUMO level of F8BT by using 2.7 eV as E_g and by assuming that E_b is ~ 0.4 eV. UPS measurement shows that the HOMO of F8BT is 5.9 eV and confirms that the vacuum level of F8BT aligns with that of PEDOT:PSSH. Using eq. (4.8), we estimate the LUMO level of F8BT film to be ~ 2.8 – 2.9 eV, which is almost identical to $\Phi_{Ca/F8BT}$ within the error limits of the EA technique and of the E_b of F8BT. Therefore we conclude that the charge-transfer level of Ca (or other metals with work functions lower than F8BT's electron affinity) on F8BT is likely to be ~ 2.8 – 2.9 eV rather than 3.2 eV. Using 2.8 ± 0.1 eV as $\Phi_{Ca/F8BT}$ and 2.44 ± 0.05 V as V_{bi}, leads us to deduce that PEDOT:PSSH interface work function, $\Phi_{PEDOT/F8BT}$ is ~ 5.2 ± 0.11 eV or identical to Φ_{PEDOT}.
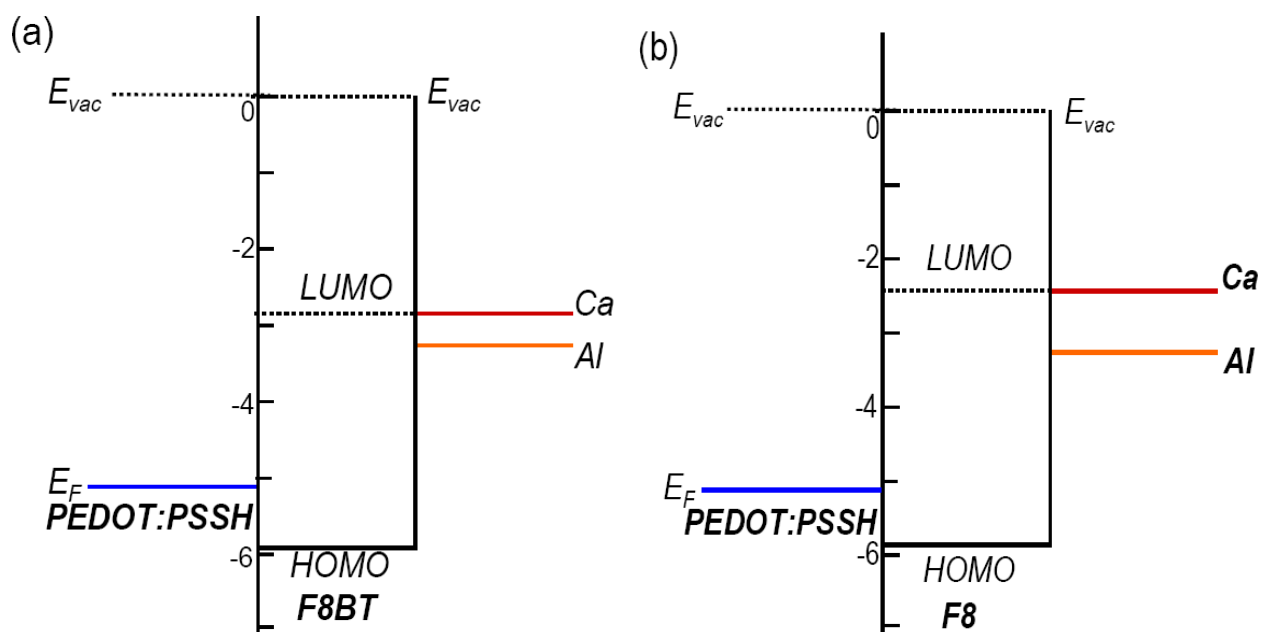
Fig. 4.11: Schematic energy level diagrams of diodes with (a) PEDOT:PSSH/F8BT/metal and (b) PEDOT:PSSH/F8/metal structures. Note that the positions of the E_f of Ca and Al are deduced from V_{bi} measured using the EA spectroscopy. HOMO levels of the polymer OSCs are obtained from UPS measurements; while LUMO levels derive from their respective E_g values based on their optical absorption spectra. E_{vac} denotes the vacuum level of a material. E_{vac} of the vapour-deposited metals are not shown since dipoles may present at the metal-on-OSC contacts.

Figure 4.11 summarises our discussions in the form of schematic energy level diagrams of diodes with F8 or F8BT as active layer. Our results here point towards a new understanding of the energy level alignment of F8BT (or F8)-based diodes. Previous EA measurements *[49, 97]* on PEDOTPSSH/F8:F8BT(95:5w/w)/Ca and PEDOT:PSSH/F8:F8BT(95:5 w/w)/Ba yield 2.4V for V_{bi} values. Using 3.2 eV as the charge-transfer level of Ca-on-F8BT interface, Lane *et. al.* *[97]* suggests that PEDOT:PSSH forms ohmic contact with F8BT and F8. The PEDOT:PSSH's E_f was suggested to converge to the HOMO levels of F8 and F8BT at the interfaces, thereby giving rise to a measured V_{bi} of 2.4 V. This interpretation is not consistent with UPS results that confirm vacuum level alignment at the F8BT/PEDOT:PSSH and F8/PEDOT:PSSH interfaces (see Fig. 4.3 and references *[29, 96, 198]*). We attempt to reconcile the inconsistencies between UPS and EA results on F8 and F8BT by proposing that: i) the work functions of vapour-deposited Ca and Al on these OSCs are ~ 2.4 – 2.7 eV and ~ 3.2 eV [see Table 4.1], respectively and ii) PEDOT:PSSH forms Schottky contacts with F8 and F8BT in PEDOT:PSSH/OSC/metal

diodes that use vapour-deposited Ca or Al as cathodes. Interestingly $\Phi_{Al/OSC}$ in polyfluorene-based PLEDs (~ 3.2 eV) is consistent with an independent V_{bi} measurement of PEDOT:PSSH/OC$_1$C$_{10}$-PPV/Al diode *[201]*, which shows that the interface work function of Al at the OC$_1$C$_{10}$-PPV/Al interface is ~ 3.0 eV. The excellent consistency between these two independent measurements suggests that the Al-on-polymer OSC interface work functions are mainly affected by the "push-back effect" and AlO$_x$ formation due to oxidation of the vapour-deposited Al atoms.

Early studies by Greenham *et. al.[16]* on a cyano-substituted poly(p-phenylene vinylene) derivative, CN-PPV, reported that ITO/CN-PPV/Ca diodes exhibit similar internal quantum efficiency as ITO/CN-PPV/Al. We suspect that vapour-deposited Al may form an ohmic contact with CN-PPV since the polymer's LUMO level (3.2 – 3.5 eV, from ref. *[209, 212]*) may be almost identical to $\Phi_{Al/CN-PPV}$. On the other hand, poly(p-phenylene vinylene), PPV (LUMO = 2.7 eV, from ref.*[209]*) forms ohmic contact with Ca but not with vapour-deposited Al. This may explain why replacing Ca contact with Al causes a 10-fold reduction in internal quantum efficiency of ITO/PPV/metal diodes *[16]* since there exists ~ 0.5 – 0.6 eV injection barrier at the Al-on-PPV interface.

4.6.2 PEDOT:PSSH/OSC/Ca (or Al) Diodes (OSC = TFB or PFB)

Understanding the interfacial electronic structures of F8-based and F8BT-based diodes enables us to extend our analysis to TFB and PFB-based diodes. Unlike F8 and F8BT with deep HOMO levels at 5.8 – 5.9 eV, the arylamine co-monomer units of TFB and PFB shift their HOMO levels to 5.5 eV *[96, 182, 198]* and 5.3 eV *[183]*, respectively. The small and medium ionisation potential I_p of these polymers leads to vacuum level *misalignment* at their interfaces with PEDOT:PSSH *[26, 111]* although both their HOMO edges lie below E_f of the PEDOT:PSSH.

For the case of TFB/PEDOT:PSSH interface, UPS studies *[26, 68, 111]* indicate that vacuum level of TFB is downshifted from that of PEDOT:PSSH. But the exact nature contributing to such a phenomenon is under considerable debate. Hwang *et. al. [64, 96]* demonstrated that there is a local band bending region that extends from the TFB/PEDOT:PSSH junction to ~ 16 nm into

the TFB bulk; whereas studies based on the ICT model [see Chapter 1 and ref. *[110, 111]*] suggest that an abrupt interface dipole with flat, rigid band extending throughout the TFB is more likely. As a result, Schottky barrier heights at the PEDOT:PSSH/TFB interface ranging from ~ 0.35 eV *[68]* to ~ 0.7 eV *[111]* have been reported. Our UPS measurement on 25 nm TFB-on-PEDOT:PSSH reveals a 0.30 eV vacuum level misalignment between TFB and PEDOT:PSSH, which is in good agreement with the result reported by Hwang *et. al. [68]*.

We emphasise that the confusion over the exact nature of vacuum level misalignment does not affect our interpretations as follows because: 1) the EA measures the built-in electric field integrated over the entire OSC layer and 2) the V_{bi} depends on difference in electrodes' work functions, which is unaffected by the nature of vacuum level misalignment. For the sake of simplicity, we assume that an abrupt interface dipole $\delta_{anode/TFB}$ of ~ 0.30 eV exists and that flat band conditions prevail across the TFB/PEDOT:PSSH heterostructure. Using eq. (4.7) and Φ_{anode} (i.e. Φ_{PEDOT}) as 5.15 ± 0.05 eV, we estimated $\Phi_{Ca/TFB}$ and $\Phi_{Al/TFB}$ to be ~ 2.40 eV and ~ 3.20 eV, respectively. These results are very consistent with those of F8-based diodes.

For the case of PFB/PEDOT:PSSH interface, our UPS measurements indicate a 0.45-eV vacuum level misalignment across the heterostructure in good agreement with the reported result by Hwang *et. al. [68]*. Applying the same analysis outlined above yields $\Phi_{Ca/PFB}$ and $\Phi_{Al/PFB}$ to be ~ 2.40 eV and ~ 3.71 eV, respectively. Although $\Phi_{Al/PFB}$ is not consistent with our earlier results, it is still significantly lower than the clean Al surface work function (i.e. 4.3 eV). The main reason contributing to the inconsistency is the high oxygen partial pressure in the vacuum deposition environment. Indeed $\Phi_{Al/PFB}$ (~ 3.8 eV) coincides with the reported work function of AlO_x *[96, 204]*. Independent measurement *[201]* on another PEDOT:PSSH/PFB/Al diode found that $\Phi_{Al/PFB}$ is ~ 3.5 eV. These observations highlight that there is no universal $\Phi_{Al/OSC}$ value and $\Phi_{Al/OSC}$ is highly sensitive to the actual fabrication environment.
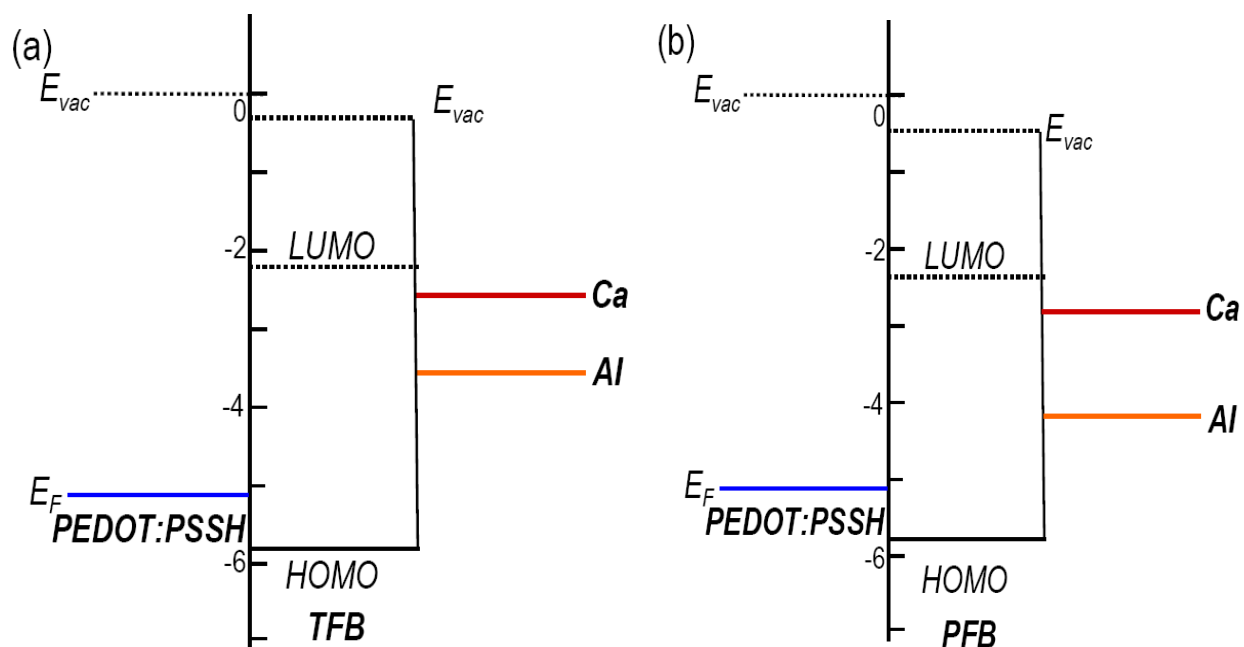
Fig. 4.12: Schematic energy level diagrams of diodes with (a) PEDOT:PSSH/TFB/metal and (b) PEDOT:PSSH/PFB/metal structures. Note that the positions of the E_f of Ca and Al are deduced from the V_{bi} values measured using EA spectrocopy. HOMO levels of the polymer OSCs are obtained from UPS data; whereas LUMO levels are derived from E_g value obtained via optical absorption measurements and by assuming E_b to be $\sim 0.1 - 0.2$ eV. E_{vac} denotes vacuum level of a material. E_{vac} of the vapour-deposited metals are not shown since dipoles may present at the metal-on-OSC contacts.

Fig. 4.12 summarises our results and discussions in the form of schematic energy level alignments of TFB and PFB-based diodes. Note that although TFB and PFB share similar chemical structures, the V_{bi} values of PEDOT:PSSH/TFB/Ca (or Al) diodes are larger than those of PEDOT:PSSH/PFB/Ca (or Al) diodes. Using eq. (4.7), the V_{bi} differences can be fully accounted for by taking their respective $\delta_{anode/OSC}$ into consideration, the accuracy limit of the EA technique and the chemical/electronic inhomogeneity of the metal-on-polymer OSC interfaces. Our observations shown in Fig. 4.12 suggest that metal-on-polymer OSC interfaces in finished devices resemble Schottky-Mott junctions with small or negligible vacuum level misalignment. This is not surprising since the interaction between the metal and the polymer OSC is probably decoupled by a thin physisorbed hydrocarbon and/or oxygen layer at the interfaces. This gives us confidence that the low $\Phi_{metal/OSC}$ values are mainly due to the "push-back" effect and/or surface oxidation at the interfaces.

4.6.3   PEDOT:PSSH/OSC/Ag (or Au) Diodes (OSC = F8BT or TFB)

It is interesting to determine the energy level alignment of noble metals-on-polymer OSC interfaces. We restrict our studies on F8BT-based and TFB-based diodes with PEDOT:PSSH as the anode and vapour-deposited Ag or Au as the counter electrode. The fact that PEDOT:PSSH/F8BT interface obeys Schottky-Mott limit (i.e. $\delta_{PEDOT/F8BT}$ = 0) allows us to compare it against the PEDOT:PSSH/TFB interface, which exhibits vacuum level misalignment with $\delta_{PEDOT/TFB}$ ~ 0.30 eV. F8BT and TFB are also ideal as model OSCs since they are commonly used to achieve high-performance PLEDs *[47, 63, 116]*.

We first examine PEDOT:PSSH/OSC/Ag diodes (where OSC = F8BT or TFB). Our EA measurement results [refer to Fig. 4.6 (a) and (b)] show that $\Phi_{Ag/F8BT}$ and $\Phi_{Ag/TFB}$ is ~ 3.75 eV and ~ 3.60 eV, respectively. These values are 0.5 – 0.7 eV smaller than the reported surface work function of clean polycrystalline Ag (4.26 eV) *[27, 196]*. The 0.5 – 0.7 eV change in work function at the Ag-on-OSC interface may be attributed to the "push-back" effect *[26]* or chemical interactions between the Au atoms and the polymers, which may contribute to the formation of an interface dipole *[100]*. The 0.2 eV-variation in $\Phi_{Ag/OSC}$ may be attributed to: 1) the chemically and/or electronically inhomogeneous Ag/polymer OSC interfaces and/or, 2) work function variation of PEDOT:PSSH caused by inhomogeneity in its surface morphology *[109]*. Recent UPS studies *[100]* also suggest that there may be a 0.2 eV dipole at the vapour-deposited Ag-on-polymer interface.

For the case of PEDOT:PSSH/OSC/Au diodes (where OSC = F8BT or TFB), our results in Table 4.1 show that $\Phi_{Au/F8BT}$ and $\Phi_{Au/TFB}$ is ~ 4.75 eV and ~ 4.26 eV, respectively. These values are about 0.4 – 0.9 eV lower than the surface work function of clean, polycrystalline Au (5.2 eV) *[107, 196, 213]* and correspond to the work functions of naturally passivated Au (i.e. 4.4 – 4.7 eV) *[101, 107, 108, 170, 214]*. Recent UPS measurement conducted by Osikowicz *et. al.* *[26, 101]* on delaminated Au-on-TFB interface (prepared in UHV environment) show that the work function of the vapour-deposited gold is 4.35 ± 0.10 eV, which coincides with $\Phi_{Au/TFB}$ measured by EA. Independent UPS studies *[68]* confirm the absence of chemical reactions between

vapour-deposited Au and TFB underlayer prepared in UHV environment although the Au atoms diffuse into TFB and induce hole traps near the Au-on-TFB interface. Therefore we conclude that the low $\Phi_{Au/TFB}$ value is due to the compression of electron density tail of the vapour-deposited Au atoms by TFB.

Although $\Phi_{Au/F8BT}$ ($\sim$ 4.8 eV) lies close to work functions of passivated Au surfaces (i.e. 4.4 – 4.7 eV), vapour-deposited Au atoms may diffuse into F8BT and chemically react with the F8BT polymer. Depositing "hot" Au atoms onto F8BT may result in a highly-doped interfacial region of distinctive electronic structure, so the V_{bi} measured by the EA technique may be determined by the work function of this chemically-modified interfacial region. Alternatively strong charge-transfer interactions may occur between the BT units and the diffused Au atoms, thereby forming an interface dipole that downshifts the E_f of Au. UPS and XPS would be useful in clarifying effects of interfacial interactions on electronic structures of Au-on-F8BT contact.

Figure 4.9 summarises our results in the form of schematic energy level alignments of different bapour-deposited metals (Ca, Al, Ag and Au) on TFB and F8BT films. The surface work functions of atomically clean metals in UHV are shown as references. $\Phi_{metal/OSC}$ taken by EA spectroscopy is *lower* than Φ_{metal} taken in UHV by at least 0.4 eV. The substantial work function modifications can be explained by: 1) surface oxide formation and/or, 2) repulsion of the vapour-deposited metal surface electrons by the OSC or the hydrocarbon adsorbates on the OSC surface. Our results are highly consistent with independent UPS studies *[26, 100, 101, 108]* and indicate a lack of strong interfacial interactions at a wide range of technologically important metal-on-polymer OSC interfaces. These results suggest that the ICT model may be useful in approximating the electronic structures at polymer OSC-on-metal and metal-on-polymer OSC heterojunctions in real working devices.
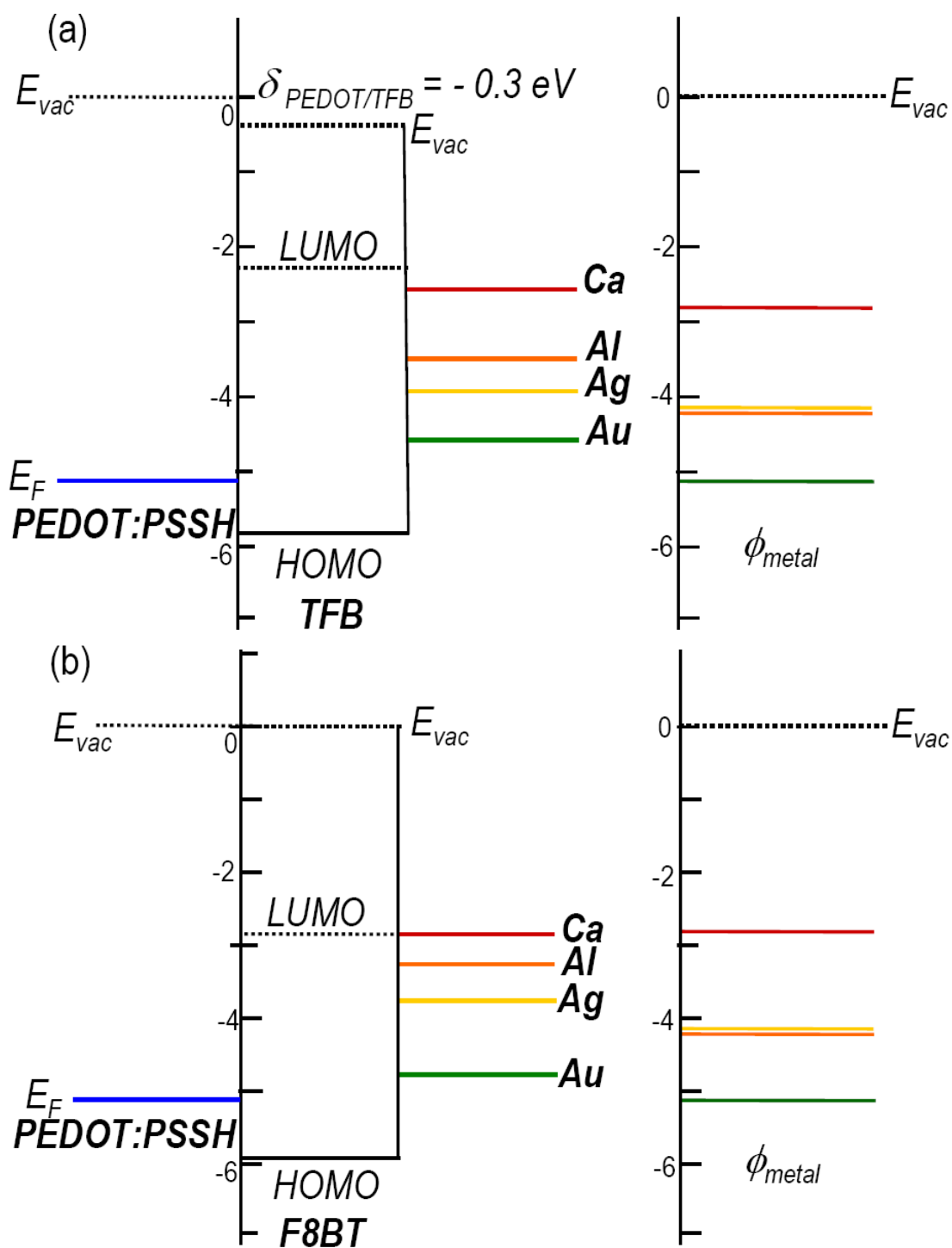
Fig. 4.13: Schematic energy level diagrams of diodes with (a) PEDOT:PSSH/TFB/metal and (b) PEDOT:PSSH/F8BT/metal structures. The interface metal work functions in the left panel are obtained from their respective V_{bi} values; while the surface work functions of atomically clean polycrystalline metals (Φ_{metal}) are shown for comparison. $\Phi_{metalOSC}$ is $0.4 - 1.0$ eV lower than their respective Φ_{metal}. E_{vac} denotes vacuum level of a material. E_{vac} of the vapour-deposited metals are not shown since dipoles may present at the metal-on-OSC interfaces.

4.7   Conclusion

Our results in this chapter have clearly shown that EA spectroscopy is a powerful tool to determine the *interface* work functions ($\Phi_{metal/OSC}$) of different metal-on-polymer OSC interfaces commonly found in finished optoelectronic devices.   Importantly $\Phi_{metal/OSC}$ at different metal/polymer interfaces of finished devices are found to be at least 0.4 eV *lower* than corresponding surface work functions, which are often cited for data interpretation in reported literatures.   The substantial reductions of work function are attributed to (a) surface oxide formation and/or (b) repulsion of surface electrons of the deposited metals by the OSC or hydrocarbon adsorbates on the OSC surface ("push back effect" or "pillow effect").

The relative contribution of these two factors towards work-function modification is likely to vary with the UHV surface work functions of the metals and the polarisabilities of the surface electron density tails. $\Phi_{metal/OSC}$ is also found to be highly sensitive to the actual fabrication environment, highlighting the need for careful control over detailed device fabrication procedures and conditions. With the combined use of UPS and EA techniques, we have shown that energy level alignments across different metal/polyfluorene/metal diode structures can be experimentally determined to within $\pm$ 0.1 eV accuracy limit. Our studies point towards the need to reexamine the interface energetics across polymer-on-PEDOT:PSSH and metal-on-polymer interfaces used for high-performance optoelectronic devices.

CHAPTER 5

Electroabsorption Studies on Blended and Multilayered Polymer Diodes

This chapter presents results of electroabsorption (EA) measurements on bilayer polymer light-emitting diodes (PLEDs) with vapour-deposited Ca or Al as the cathode and poly(3,4-ethylenedioxythiophene) doped with polystyrene sulphonic acid (PEDOT:PSSH) as the anode. We combined two different polyfluorene co-polymers, with either electron- or hole-accepting properties, to form an energetically staggered, type-II heterojunction as the polymer active layer. Systematic V_{bi} measurements are presented on bilayer devices at different temperatures and with different EA probe beam intensities. Low-temperature EA measurements with low illumination intensities were shown to yield the most reliable built-in voltages (V_{bi}) for bilayer devices. Results acquired by EA technique enable determination of energy level alignment across different bilayer PLED structures. Our V_{bi} measurements show that spontaneous electronic doping of the polymer active layers, rather than elimination of charge-injection barriers, contributes to realising PLEDs with high electroluminescent (EL) efficiencies and low EL turn-on voltages. Results of our analysis highlight the influence of interfacial electronic interactions on performance characteristics of organic electronic devices.

5.1   Overview and Motivation

As described in Chapter 1, the internal quantum efficiency of a polymer light-emitting diode (PLED) is determined by (a) the photoluminescence (PL) efficiency (η_{PL}) of the polymer organic semiconductors (OSCs), (b) the proportion of excitons that form singlets (r_{st}) and (c) the fraction of injected charge carriers that form excitons instead of traversing the device without recombination (γ) :

$$\eta_{\text{int}} = \gamma r_{st} \eta_{PL} \tag{5.1}$$

Eq. (5.1) highlights the different reasons underlying poor performances of single layer PLEDs: (1) imbalanced charge injection from electrodes causes the majority charge carriers to pass through the device without recombining into singlet excitons (i.e. low γ) and (2) differential mobilities of electrons and holes cause the radiative recombination zone to be located near a metal contact where dipole quenching and non-radiative losses occur *[4, 16, 115, 116, 180, 181]* (i.e. low η_{PL} and/or r_{st}). γ may be optimised by reducing or eliminating the Schottky-barrier heights through interface chemical modifications *[47, 55, 56]* and/or by employing different electrode materials *[48, 51, 52, 54, 215]*, but these solutions cannot be used to confine the charge carriers and control the position of recombination zone in PLEDs. To solve this problem, an additional polymer OSC interlayer may be used to separate the electrode from the light-emitting OSC. This strategy, which creates a bilayer PLED structure, has been extensively used *[16, 115, 116, 215, 216]* to realise high-performance PLEDs.

50 F8BT: 50 TFB (w/w) binary blends cast from xylene comprise a type II heterojunction and is the material of choice for realising PLEDs with high power conversion efficiencies *[12, 63, 115, 116, 118, 217]*. Excellent optoelectronic behaviour of the 50:50 blend system are related to vertical phase segregation during film formation *[63, 116]*, which enables spontaneous formation of a continuous poly(2,7-(9,9'-di-n-octylfluorene)-alt-(1,4-phenylene-((4-sec-butylphenyl)imino)-1,4-phenylene) (TFB) wetting layer near the poly(styrene sulfonate) doped poly(3,4-ethylenedioxythiophene) (PEDOT:PSSH) anode. Phase segregation leads to spontaneous formation of ohmic contacts at Ca/poly(9,9'-dioctylfluorene-alt-benzothiadiazole) (F8BT) and PEDOT:PSSH/TFB interfaces in a finished device [see Chapter 4]. This feature is further complemented by a large LUMO edge offset ($\sim$ 1 eV) across F8BT/TFB, which confines electrons near the heterojunction and promotes electric field redistribution to achieve balanced charge injections from both electrodes.

Phase separation studies of TFB/F8BT system motivated efforts to realise bilayer PLEDs with planar heterojunction to optimise device performances. Recent studies *[115, 116]* confirm that inserting a TFB interlayer ($\sim$ 10 − 15 nm in thickness) between PEDOT:PSSH and F8BT enhances electroluminescent (EL) efficiencies by isolating radiative recombination zone in F8BT

from the exciton-quenching PEDOT:PSSH contact. Careful optimisation of fabrication methods and electrode engineering produce bilayer PLEDs with exceptionally low turn-on voltages, superior EL efficiencies and extended operational lifetimes *[116, 215]*. Nevertheless understanding of the electronic structure of bilayer PLEDs remain incomplete due to the limited understanding on interfacial energetics in these devices.

The excellent performances of PLEDs with F8BT/TFB system are attributed to a "barrier-free electron hole capture" photophysical process that occurs across the type II heterojunction *[118]*. This process enables facile formation of long-lived exciplex states across the F8BT/TFB interface, which readily undergo thermal activation to regenerate singlet F8BT excitons that decay radiatively *[118, 218]*. To date efficient regeneration of excitons from long-lived interfacial exciplexes is widely assumed to have primarily contributed towards low EL turn-on voltages of finished PLEDs *[63, 116, 118, 218]*. This explanation implies that a TFB/F8BT or a type II OSC/OSC heterojunction is necessary to achieve PLEDs of high EL efficiencies.

Here we present V_{bi} measurements on PLEDs with a F8BT/TFB bilayer heterojunction sandwiched between PEDOT:PSSH and different metal electrodes. We show that measurement conditions of the EA technique (photoillumination intensity and temperature) can affect results of V_{bi} measurements and lead to misleading interpretation on electronic structures in these bilayer devices. This problem led us to propose an optimal measurement protocol to accurately study interfacial energetics across TFB/F8BT heterojunctions with different spatial orientations in working devices. Using this strategy and EA studies on single layer PLEDs [see Chapter 4], we have determined energy level alignments across different bilayer structures. Our studies show that polymers in bilayer PLEDs are doped with polarons *before* being subjected to charge injection. These observations indicate that interfacial electronic interactions, in addition to the photophysics across type II polymeric heterojunction, are playing crucial roles in realising low threshold voltages for current injection and EL. Furthermore it suggests that a TFB/F8BT or type II OSC/OSC heterojunction is not necessary to achieve PLEDs with exceptional performances *[219]* with proper optimisation in electrode materials. This conclusion explains recent research interests into realising single-layer PLEDs with transition metal oxide electrodes *[172, 220]*.

5.2   Materials and Experimental Procedures

Bilayer diodes presented in this chapter are of PEDOT:PSSH/polymer A/polymer B/metal structures, which are made by laminating two pre-spun, dissimilar polyfluorene films. For the purpose of our EA studies, we used TFB and F8BT as model polymer OSCs [see Fig. 4.1 for chemical structures].   Using Suzuki condensation coupling, structural moieties of different electron affinities are attached next to the poly(9,9'-dioctylfluorene) unit *[38-40, 186-188]* to yield polyfluorene-derivatives of various optoelectronic properties.   The differential optical energy gaps (E_g) and charge transport properties make F8BT-TFB an ideal type II heterostructure for EA measurements.   Bilayer F8BT-TFB heterostructures of controlled thicknesses and different orientations were fabricated by laminating the two pre-spun polymer OSC layers together.   Detailed fabrication procedures involve spinning a polymer OSC film of intended thickness on freshly-cleaned hydrophilic glass substrate exposed to O_2 plasma etching and floating the polymer off the substrate surface using high-purity deionised water (H949 ROMIL, electronic grade) [also see ref. *[120]* for fabrication procedure].   The floated polymer OSC layer is then transferred over another polymer OSC film on the PEDOT:PSSH-covered ITO substrate.   This technique yields a laminated bilayer polymer structure of well-defined thickness (confirmed by profilometry).

The bilayer F8BT-TFB structures were then placed in a vacuum oven ($\sim 10^{-6} - 10^{-7}$ mbar) at 110^0C for 6 hours to remove residual water and ensure intimate contact across the F8BT-TFB interface.   Care was taken to avoid annealing these samples at temperatures at or above 110^0C for a prolonged period to ensure formation of compositionally abrupt F8BT-TFB interface.   After annealing, these samples were then placed in an evaporator to undergo vapour deposition of Ca and/or Al at a pressure of $\sim 10^{-6} - 10^{-7}$ mbar.   All samples were subjected to Ca or Al deposition in the same time to achieve a uniform fabrication environment for electrode deposition.

The instrumental setup of the EA spectrometer and detailed procedures employed for EA measurements are given in Chapter 4.   Effects of illumination intensity on the V_{bi} of working bilayer diodes comprising type II OSC/OSC heterojunctions has been investigated during EA

measurements. A monochromatic EA probe beam of 1.3-mm in diameter (full width at half maximum) originated from a 150 W xenon-arc lamp is used for light-intensity dependent measurements. EA probe beam of average intensity (measured by optical power meter) ranging from ~ 0.06 – 1 mW/cm^2 was achieved by the use of neutral density optical filters and/or by varying the electrical power supplied to the 150W xenon-arc lamp. Multiple reflective losses of EA probe beam across the cryostat windows are considered while determining the average intensity of EA probe beam impinging the sample.

To ensure experimental consistencies, polymers used for EA and current density-voltage-luminance (J-V-L) measurements are of the same batch and obtained from Cambridge Display Technology Ltd. Current density-voltage (J-V) and luminance-voltage (L-V) characteristics were measured using a Keithley 195 electrometer and a Keithley 230 source-meter, respectively. Luminance measurements were conducted with a calibrated reference Si photodetector (Thorlabs FDS1010-CAL) located in the forward direction. Leakage currents of all samples subjected to – 4 V reverse bias are measured shortly before V_{bi} measurement with the EA technique. Time-integrated EL spectra of all devices were measured using an Ocean Optics Fiber-Optic Spectrometer (USB4000) with a 3648-element linear CCD-array silicon detector.

5.3 EA Studies on Polymer Light-Emtting Diodes (PLEDs) with F8BT/TFB Heterojunctions

There are practical issues concerning V_{bi} measurements in multilayer organic LEDs using EA spectroscopy. EA spectroscopy measures the integral electric field in an OSC based on electromodulated signals arising from the Stark shifted absorption edge of the material [see Chapter 2]. To correctly determine the V_{bi} in each OSC material within a binary or ternary system, optical absorption gaps of these OSC materials must be different so that their EA spectral features do not overlap in energy. Early EA measurements of internal fields in multilayered organic molecular LEDs show that overlap of EA spectral features undermines accurate determination of electric fields in the OSC active layers *[123]*. To ensure reliable EA studies on electronic structures in multilayered/blended devices, care must be taken to ensure that EA absorption maxima of polymer OSCs are well separated in energies. With these complications in mind, the F8BT/TFB heterojunction is ideal as a model OSC/OSC system as the EA maximum of F8BT (~ 2.48 eV) is well separated from that of TFB (~ 2.93 eV).
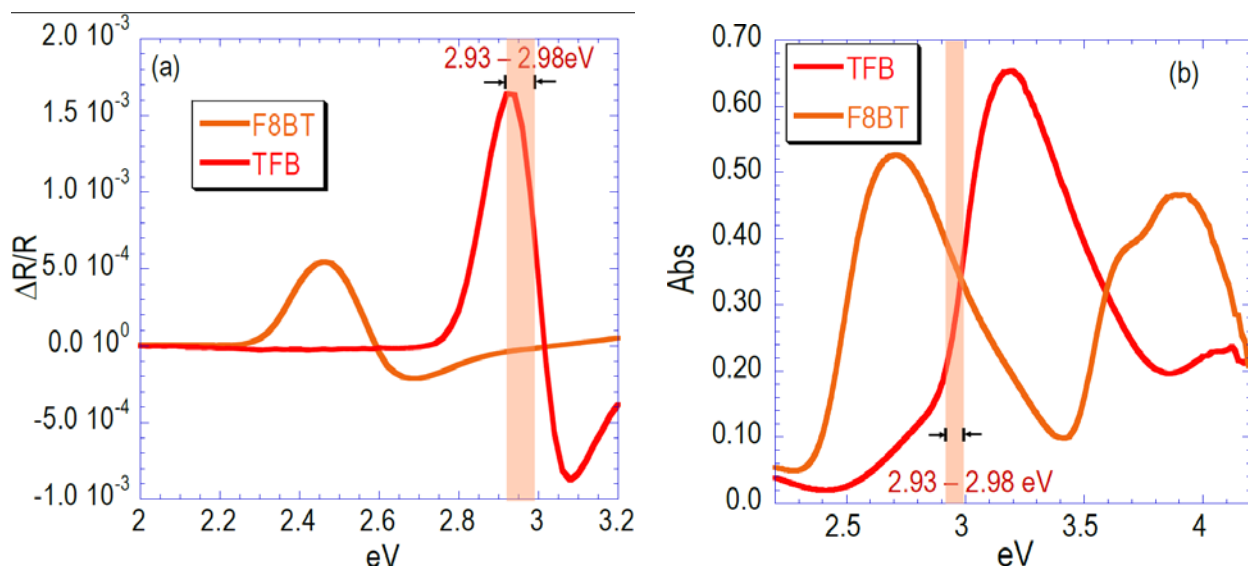
Figure 5.1: (a) EA spectra of the PEDOT:PSSH/F8BT/Al diode (red) and the PEDOT:PSSH/TFB/Al diode (orange) measured at 10K and - 2 V reverse bias. Both devices are electromodulated with a sinusoidal V_{ac} of 0.35 V_{rms} at 216.1 Hz frequency. EA spectral shapes of both polymers are unaffected by nature of the cathode. (b) Absorption spectra of the F8BT and the TFB films spin cast on PEDOT:PSSH. Note that the energy range corresponding to the EA maximum of TFB (~ 2.93 – 2.98 eV) overlaps with the absorption spectrum of the F8BT.

Fig. 5.1 (a) confirms that signal contamination due to EA spectral overlap is negligible because the contribution of F8BT EA spectral signal is minimal at the energy corresponding to the TFB EA maximum (~ 2.93 eV). But Fig. 5.1 also shows that the TFB EA maximum at ~ 2.93 – 2.98 eV overlaps with the optical absorption spectrum of F8BT. This is undesirable because the photons (with 2.93 – 2.98 eV in energy) introduced by the EA probe beam optically excite F8BT in a bilayer PLED, which may undermine accurate determination of the V_{bi}. We examine this problem in detail and propose practical solutions to correctly determine the electronic structure of multilayered and blended devices.
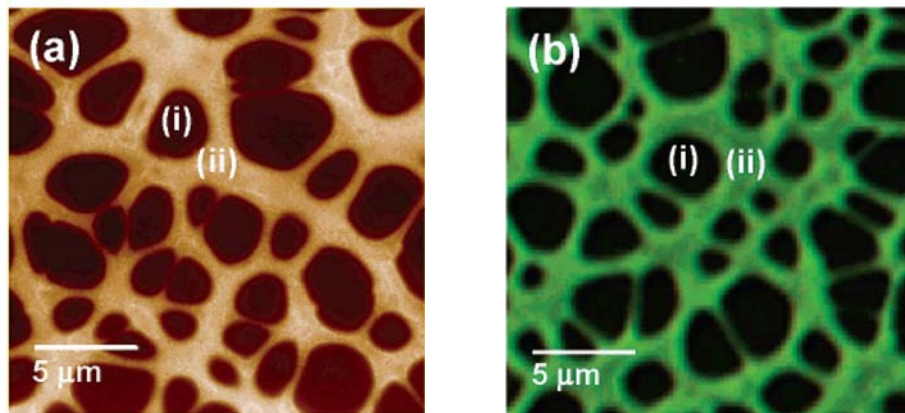
Figure 5.2: (a) AFM image and (b) PL image of a 100-nm thick F8BT:TFB (50:50 w/w) film. The PL image of the blend film confirms that the dark, low region in (a) is the TFB-rich domain [region (i)]; while the light, high region in (a) is the F8BT-rich matrix phase [region (ii)]. PL mainly occurs at interfaces between the two domains, showing that radiative recombination takes place preferentially at these interphase domain boundaries. [Figure adapted from ref. *[63]*].

EA spectroscopy is commonly used to study electronic structures in diodes comprising polymer blends as active layers *[49, 97, 142]*, but full understanding of interfacial energy level alignments in these devices remains elusive because polymer blends exhibit complex and uncontrolled phase separation behaviours during film formation, which are highly dependent on the polymer and solvent compositions as well as the actual processing conditions (temperature, postbake, etc.) *[63, 116, 221]*. Fig. 5.2 shows that the micron-length scale phase separations in

the 50:50 (w/w) F8BT/TFB blend make it hard to determine which polymer OSC forms the actual interfaces with the two opposite electrodes more preponderantly and results in multiple polymer OSC/metal interfaces near the same contact *[116]*. Accordingly, a polymer double layer with a compositionally abrupt and planar OSC/OSC interface is necessary as a model structure to gain understanding on electronic structures in multilayered devices. This understanding may be useful in understanding electronic structure in blended devices.

To the best of our knowledge, EA has not been employed to study the electronic structure across an abrupt polymeric OSC/OSC heterojunction because most polymer OSCs share similar solubilities in organic solvents. Spin coating a polymer layer over a polymer film inevitably dissolves the underlayer, thereby preventing formation of an abrupt interface between the two materials. To form a polymer OSC/OSC heterojunction, the polymer underlayer must not be soluble in any organic solvent.

Kim *et. al. [115]* showed that a 10 nm TFB layer spin-coated on PEDOT:PSSH is rendered insoluble after annealing it at 180 °C, which is above the T_g of TFB, for 1 hour in N_2 environment. This technique yields highly efficient bilayer TFB/F8BT PLEDs. Recently Jin *et. al. [216]* fabricated a bilayer TFB/F8T2 (poly(9,9-dioctylfluorene-alt-bithiophene) PLEDs with this technique and employed the EA technique to study the V_{bi} of F8T2 in these devices. But no disclosure was made on the V_{bi} in the TFB layer owing to low signal-noise ratio. Motivated by these studies, we have fabricated bilayer devices with a TFB/F8BT heterojunction by laminating two pre-spun polymer films together to create a compositionally abrupt F8BT/TFB interface [see section 5.2]. We then employed the EA technique to systematically measure the electronic structure of devices comprising TFB/F8BT bilayers with different orientations. Information gained from V_{bi} measurements are applied to understand the performance characteristics of these devices.

5.4   Device Characterisations of PLEDs with F8BT/TFB Heterojunctions

We compare the current density-voltage-luminance (J-V-L) behaviour of bilayer diodes with different TFB-F8BT orientations with respect to the charge-injecting electrodes. Fig. 5.3 depicts the J-V-L characteristics of (a) "normal bilayer" diodes (60nm-PEDOT:PSSH/40nm-TFB/40nm-F8BT/50nm-Ca) and (b) "reverse bilayer" diodes (60nm-PEDOT:PSSH/40nm-F8BT/40nm-TFB/50nm-Ca). Current density-luminance (J-L) characteristics derived from forward and backward voltage scan directions are depicted with solid and empty circles, respectively.

Fig. 5.3 (a) shows that the normal bilayer PLED exhibits a threshold voltage for current injection ($V_{injection}$) of ~ 1.45 V and EL turn-on voltage (V_{on}) of ~ 2.10 V with little hysteresis. $V_{injection}$ is defined as the voltage that yields a current density of 10^{-5} mA/cm^2 in the device. Although thicknesses of both TFB and F8BT layers are not optimised, the J-V-L performance of our device is close to those of the best-performing bilayer PLEDs reported in references *[115, 116]*. The unusually low $V_{injection}$ (~ 1.45 V) suggests that electronic charges are present in the active layer(s) *prior to* charge injection. This phenomenon may be related to electronic doping near the metal/polymer interfaces of the bilayer devices and is discussed in subsequent section. The increase in EL with driving voltages is less abrupt when compared to V-L characteristics of devices reported in literatures *[115, 116]* due to unoptimised TFB layer thickness in our devices.

On the other hand, reversing the F8BT/TFB bilayer orientation with respect to the PEDOT:PSSH and the Ca electrodes results in inferior J-V-L device performance due to: i) increased charge-injection barrier heights at both sides of the metal/polymer OSC interfaces and ii) poor electron (hole) mobility of TFB (F8BT) layers. Fig. 5.3 (b) shows that $V_{injection}$ increases to ~ 2 V and the reverse bilayer diode does not turn on until 4.4 V. At the same driving voltage, both injection current and EL intensity of the reverse bilayer diodes are at least an order of magnitude lower than those of normal bilayer PLEDs. Moreover considerable hysteresis in terms of J-V-L behaviour is observed in reverse bilayer diodes, indicating low stability in device operations. Further examination of Fig. 5.3 (b) reveals two step-like increases in injection current at ~ 2 V and ~ 3.5 V upon biasing the device from 0 V to 7 V. Similar J-L behaviours were observed in

other reverse bilayer diodes with the second step-like current injection occurring shortly before the device electroluminesces.
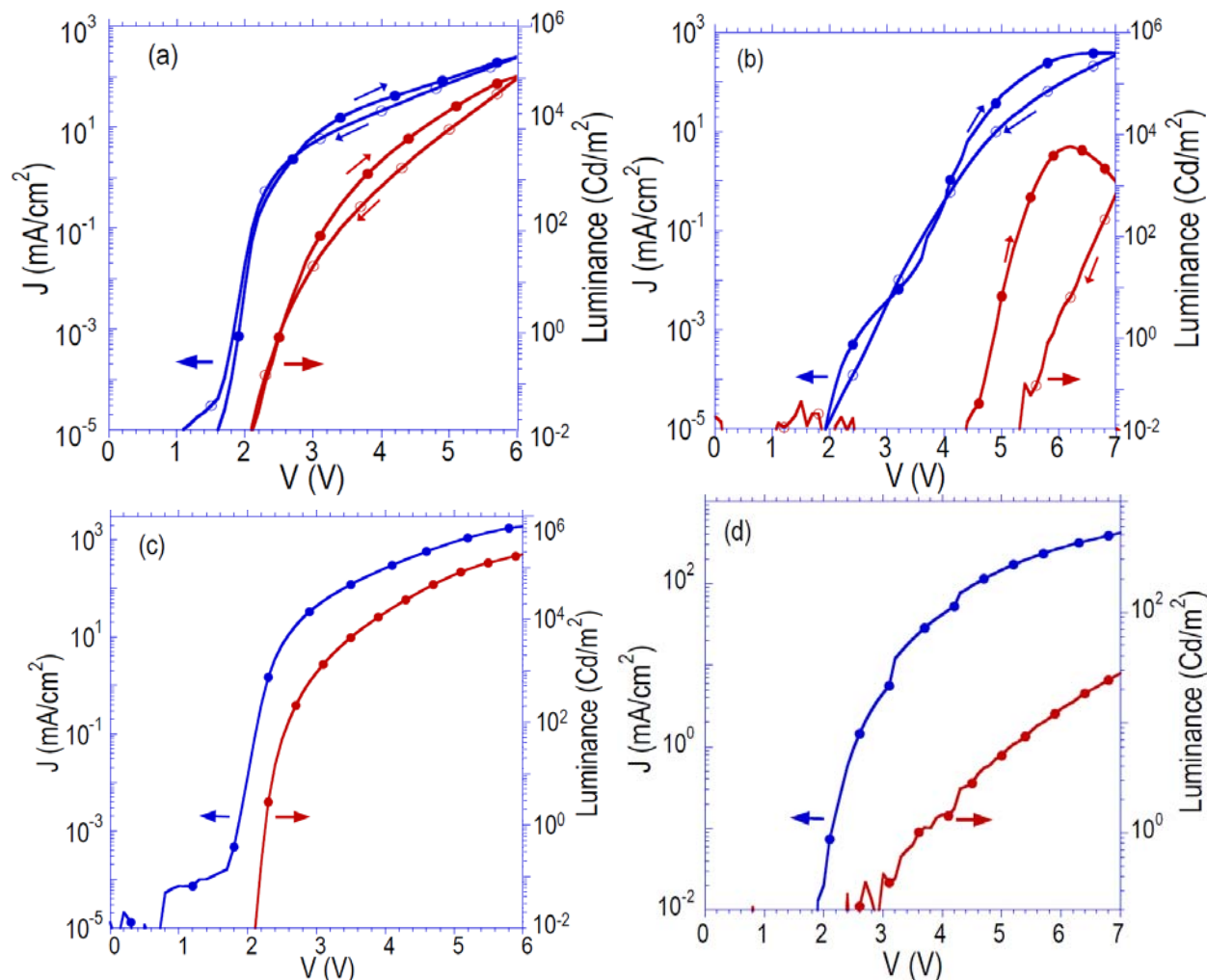
Figure 5.3: J-V-L characteristics of:
(a) 60nm-PEDOT:PSSH/40nm-TFB/40nm-F8BT/50nm-Ca bilayer diodes,
(b) 60nm-PEDOT:PSSH/40nm-F8BT/40nm-TFB/50nm-Ca bilayer diodes,
(c) 60nm-PEDOT:PSSH/50TFB:50 F8BT (w/w)/50nm-Ca diodes and,
(d) 60nm-PEDOT:PSSH/50TFB:50 F8BT (w/w)/50nm-Al diodes [courtesy of Dr. G. Pace].
J-V-L data with solid circles are obtained by sweeping applied bias from 0 V to 7 V; while J-V-L data with solid circles are obtained by sweeping applied bias from 7 V to 0 V.

EA measurements in Chapter 4 show that the charge-injection barrier height at TFB/Ca interface (~ 0.40 eV) is lower than that at the F8BT/PEDOT:PSSH interface (~ 0.75 eV), suggesting that *electrons* are first injected into the interface LUMO levels of TFB at ~ 2 V follow by *hole*

injection into the F8BT's interface HOMO levels at ~ 3.2 V. Electron accumulation at the F8BT-TFB interface in the reverse bilayer diode is likely due to the large LUMO offset (~ 1 eV), resulting in no EL until holes are injected from PEDOT:PSSH. Delayed EL seen at 4.4 V (rather than at the commencement of hole injection at 3.2 V) can be attributed to the inferior hole mobility of F8BT *[40, 207]* and field-assisted detrapping of hole charge carriers, which are probably entrapped adjacent to PEDOT:PSSH/F8BT interface *[40]*.
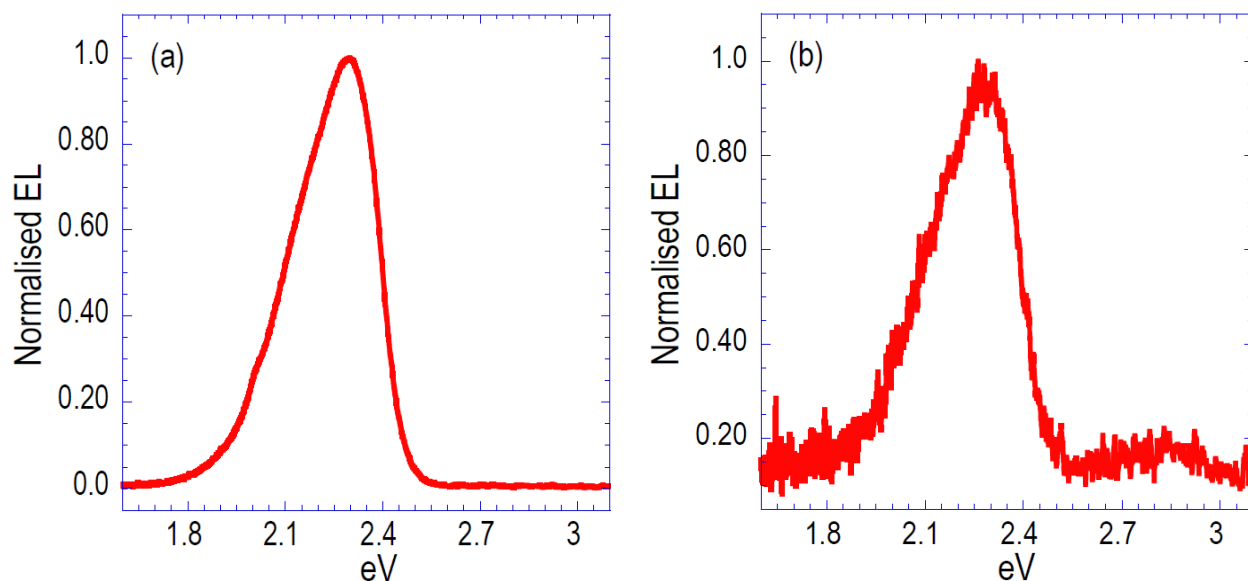
Figure 5.4: Normalised time-integrated EL spectra of (a) PEDOT:PSSH/TFB/F8BT/Ca (normal bilayer) diodes at 4 V applied bias and (b) PEDOT:PSSH/F8BT/TFB/Ca (reverse bilayer) diodes at 6 V applied bias. The shoulder EL peak at 2.0 eV in (a) may be due to electronic disorder in the F8BT film and/or interfacial chemical interactions between the vapour-deposited Ca and the F8BT *[143]*. EL of the F8BT (2.16 and 2.28 eV) and the TFB layers (2.69 eV and 2.88 eV) are present in (b).

Our hypothesis on the operational mechanisms of reverse bilayer PLED is supported by the time-integrated EL spectrum of the reverse bilayer device at 6 V in Fig. 5.4 (b), which also reveals very weak EL spectral contribution of TFB (at 2.69 eV and 2.86 eV) that decays rapidly with time. On the other hand, the time-integrated EL spectrum of the normal bilayer PLED (at 2.16 eV and 2.28 eV) at 4 V in Fig. 5.4 (a) has a much higher signal-noise ratio than the EL spectrum of the reverse bilayer device. Note that the EL spectrum of the normal bilayer PLED in Fig. 5.4 (a) closely resembles the EL spectrum of the PEDOT:PSSH/F8BT/Ca PLED *[222]*. This

phenomenon is attributed to field-assisted radiative exciton recombinations in the F8BT bulk *[223]* and/or endothermic excitations from the exciplex states at the F8BT/TFB interface *[118, 218, 223]*.

We had performed J-V-L measurements on PLEDs with blended PLEDs, which comprise 50 TFB: 50 F8BT (w/w) as the active layer and vapour-deposited Ca or Al as the cathode. Fig. 5.3 (c) – (d) shows the performance characteristics of these devices. J-V-L characteristics of a blended PLED with a Ca cathode [Fig. 5.3 (c)] is similar to that of normal bilayer PLED [Fig. 5.3 (a)] due to the vertical phase segregation behaviour in 50:50 blend during film formation *[63, 116]*. But the leakage current traversing blended PLED below 1.9 V is higher compared to bilayer PLEDs because 50:50 blend has a rough surface morphology with large thickness variation (~ 30 – 50 nm) *[63, 221]*. Replacing the Ca cathode with Al results in a blended PLED with much lower EL efficiency and higher EL turn-on voltage (~ 2.5 – 2.7 V) [see Fig. 5.3 (d)]. Interestingly the current density traversing the blended PLED with an Al cathode is close to that traversing the blended PLED with Ca as the cathode, suggesting that the Al/F8BT contact is nearly as ohmic as the Ca/F8BT contact. This phenomenon is discussed at length in section 5.5.

The J-V-L characteristics shown in Fig. 5.3 confirm that the bilayer PLEDs made by "water-floating" procedures are of optimal performances and highlights the importance of ohmic junctions in enhancing performance behaviours of PLEDs. This prompted us to use EA spectroscopy to investigate the correlations between built-in fields and J-V-L characteristics of normal bilayer PLEDs. But before doing so, we examine the effects of EA measurement conditions on internal fields in TFB and F8BT layers of these bilayer devices.

5.5 Results of EA Studies on on PLEDs with F8BT/TFB Heterojunctions

5.5.1 Effects of Temperature on EA Spectral Measurements
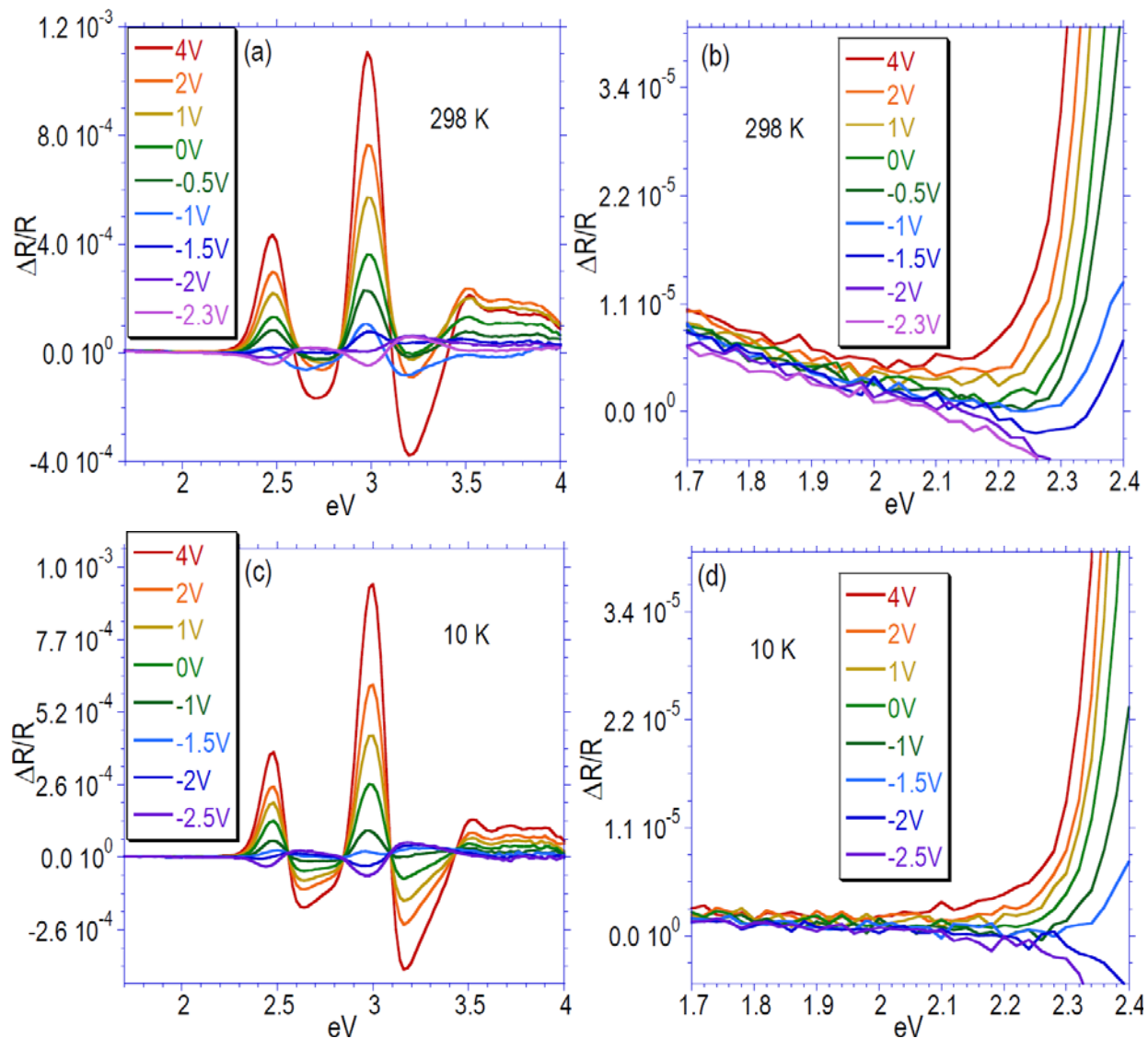
Figure 5.5: 1ω electromodulation spectra of a 60 nm-PEDOT:PSSH/40 nm-TFB/40 nm-F8BT/ 250nm Al PLED measured at different temperatures and externally applied V_{dc}. The device is electromodulated with a V_{ac} of 0.35V$_{rms}$ at 216.1 Hz frequency. Similar sub-gap spectral attenuation is observed in the electromodulation spectra of other bilayer devices with different configurations and metal electrodes.

We have studied the influence of measurement temperature on the electromodulated spectra of bilayer devices. Fig. 5.5 (a) and (c) compare the $\Delta R/R$ ($h\upsilon, 1\omega$) spectra of a PEDOT:PSSH/TFB/F8BT/Al bilayer PLED, which are measured at different temperatures and different applied DC biases (V_{dc}). At room temperature, a strong sub-gap spectral feature is observed between 1.7 eV and 2.15 eV [see Fig. 5.5 (b)]; but upon cooling to 10 K [see Fig. 5.5 (d)], the intensity of this sub-gap feature is significantly attenuated and the spectral signals beyond 2.2 eV that is measured with externally applied V_{dc} below - 1 V appear sharper. Recent room-temperature V_{bi} measurements on PLEDs comprising bilayer *[216]* and blended *[49, 142]* polyfluorene active layers have also reported strong sub-gap absorptions in their electromdulated spectra. Similarly EA measurements on single-layer diodes with ohmic charge-injecting interfaces have reported strong charge-modulation spectral features at room temperature *[97, 98, 126, 154, 168]*.

We observe similar effects of temperature on the EA spectra of other F8BT/TFB bilayer diodes with Ca electrode and with F8BT/TFB bilayers of different orientations. The physical origin of the strong sub-gap feature is unclear although recent studies have attributed it to electron trapping at the PEDOT:PSSH/polymer OSC interface *[142, 154]* or "delta-state" interfacial doping of the polymer OSC by PEDOT:PSSH *[155]*. We restrict our investigation on determining built-in fields and energy band diagrams in bilayer devices for the purpose of understanding their J-V-L characteristics.

Similar to the cases of single layer PLEDs in Chapter 4, Fig. 5.5 indicates that low-temperature EA measurement of bilayer devices is necessary for accurate determinations of the V_{bi} values in multilayered and blended PLEDs due to the substantial overlap between the temperature-dependent sub-gap spectral feature and the Stark-shift induced EA component *[142, 154, 155]*. The effects of temperature on V_{bi} measurements of the bilayer and the blended devices are discussed at length in subsequent sections. All V_{bi} measurements on different bilayer and blended diodes were performed at 10 K to ensure accurate determination of energy level alignment in these working devices.

5.5.2   Effects of Illumination Intensity and Temperature on EA Studies of Blended PLEDs

We have conducted EA measurements on PLEDs comprising a Ca electrode and a blended 50 F8BT:50 TFB (w/w) active layer ("blended PLED"), which is spin cast from a solution made with anhydrous xylene. Results of these measurements conducted at 10 K with different EA probe beam intensities ($\sim 0.06 - 1$ mW/cm^2) are presented in Fig. 5.6 and Table 5.1. Several notable features are observed from Fig. 5.6: firstly, the V_{bi} values of the F8BT and TFB components (~ 2.6 V) are identical but do not seem to correspond to differences in the surface work functions of vapour-deposited Ca ($\sim 2.3 - 2.4$ V) and PEDOT:PSSH (~ 5.15 V). Secondly, the V_{bi} values of the F8BT and TFB components are *not* affected by variation of the EA probe beam intensity. Lastly, the V_{bi} values of the F8BT and TFB components (~ 2.6 V) in the blended PLED lie within the voltage range ($1.45 - 2.77$ V) defined by the V_{bi} of the bilayer diodes, which comprise an F8BT/TFB heterojunction of different orientations. V_{bi} measurements of bilayer diodes will be disclosed in subsequent sections.

The last observation is consistent with the fact that the blended PLED can be seen as four different diodes (normal bilayer, reverse bilayer, single layer TFB and single layer F8BT) connected in parallel *[63, 116]*. Therefore the V_{bi} of the blended PLED is a composite value with V_{bi} contributions from these four diodes being directly proportional to their respective volume fractions in the blended film. But random spatial orientations of TFB/F8BT interfaces may partially offset the V_{bi} contributions from some diode components *[63, 116]*. Moreover phase separation behaviour of the TFB/F8BT blend varies with the actual deposition environment *[63]*. These complications make meaningful understanding of V_{bi} difficult.

We have also measured nulling voltages of the EA 1ω signals (V_{null}) of the same device to study the influence of sub-gap spectral features on V_{bi} determination at 298 K. Fig. 5.6 (c) and (d) show the V_{null} values measured at 298 K with probe beam intensities identical to that used at low temperature. Several observations are noted: firstly, when the EA probe beam intensity is fixed at $\sim 0.06 - 0.07$ mW/cm^2, the V_{null} of F8BT at 298 K (~ 1.5 V) is lower than its V_{bi} measured at 10 K by ~ 1 V; while the V_{null} of TFB at 298 K (~ 2.4 V) is lower than its V_{bi} at 10 K (~ 2.6 V)

by ~ 0.2 V. Secondly, the V_{null} of F8BT at 298 K can be decreased by ~ 0.6 V simply by decreasing the EA probe beam intensity over more than an order of magnitude, resulting in a large difference of V_{null} (~ 0.9 V) between F8BT and TFB. The phenomenon of light-intensity dependent V_{bi} is examined in greater detail in the following sections.
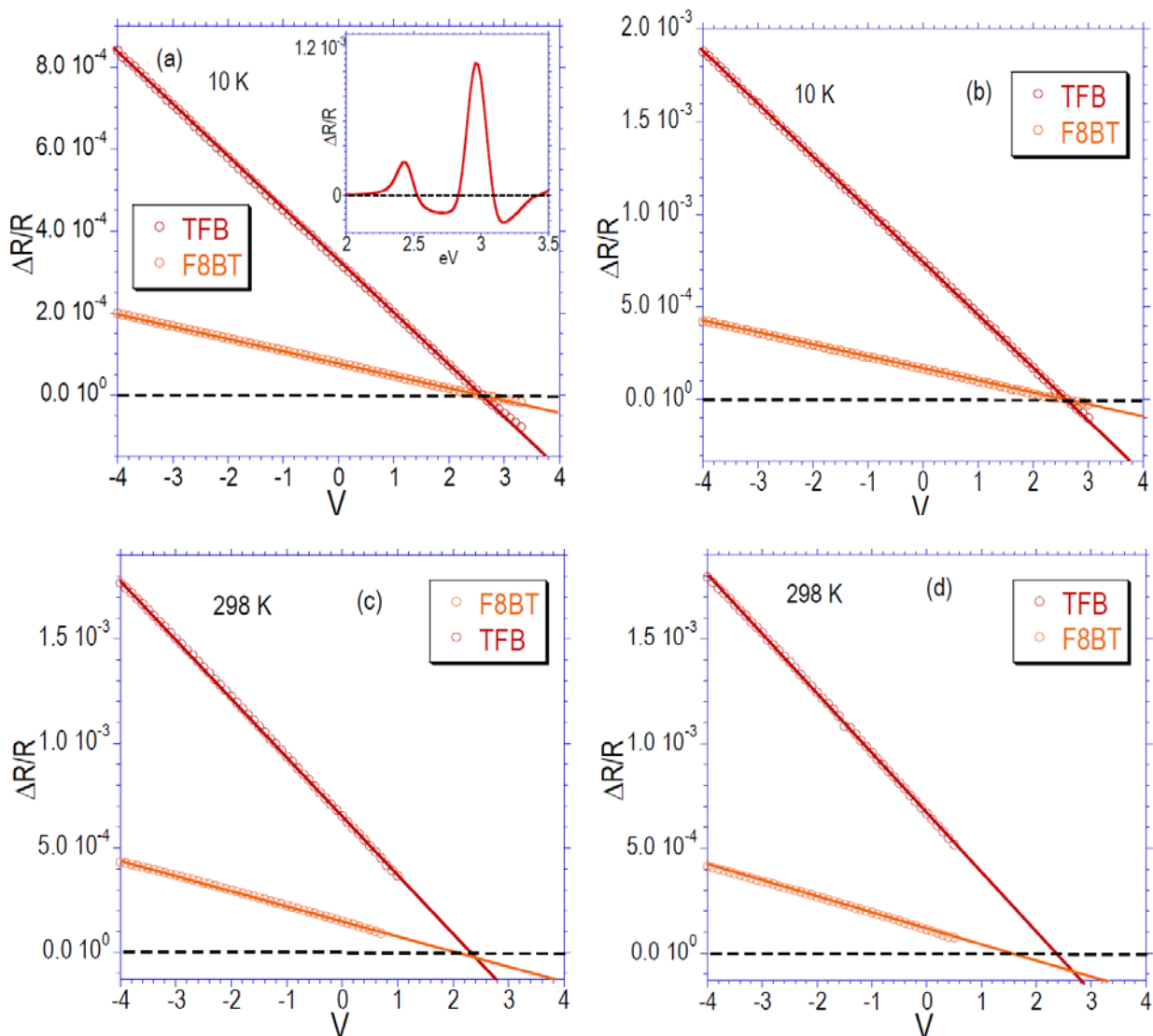
Figure 5.6: V_{bi} measurements of F8BT (2.44 eV) and TFB (2.93 – 2.96 eV) of a PEDOT:PSSH/50TFB:50F8BT(w/w)/Ca PLED at different temperatures. The monochromatic EA probe beam intensity is set at $0.8 – 1$ mW/cm^2 [(a) and (c)] and $0.06 – 0.07$ mW/cm^2 [(b) and (d)]. The device is modulated with $0.50 V_{rms}$ at 216.1 Hz frequency. Inset in (a) shows the EA spectrum of the PLED at - 4 V and 10 K.

Temperature (K)	Illumination Intensity (mW/cm^2)	Polymer OSC	V_{bi} or V_{null} (± 0.1 V)
298	0.8 – 1	F8BT	2.1
		TFB	2.3
	0.06 – 0.07	F8BT	1.5
		TFB	2.4
10	0.8 – 1	F8BT	2.6
		TFB	2.6
	0.06 – 0.07	F8BT	2.5
		TFB	2.6

Table 5.1: Results of V_{bi} or V_{null} measurements of PEDOT:PSSH/TFB:F8BT (50:50 w/w)/Ca PLEDs obtained with different EA probe beam intensities and at different temperatures.

The results in Fig. 5.6 clearly show that the V_{null} of polymer components in blended systems at 298 K deviate substantially from their respective V_{bi} values at 10 K. Even at room temperature, care must be taken to ensure that the EA probe beam intensity does not interfere with the V_{null} of blended or multilayered devices. Nevertheless, V_{null} measured at room temperature are commonly used to deduce interfacial energy level alignment in blended *[97, 142]* and multilayered devices *[216]* with two or more polymeric components. For reasons outlined here, we rely on V_{bi} measurements on bilayer diodes at 10 K to determine energy level alignment in devices disclosed in this chapter.

5.5.3 Effects of Illumination Intensity and Temperature on EA Studies of Bilayer Diodes

5.5.3.1 PEDOT:PSSH/F8BT/TFB/Al

Since F8BT/TFB forms a type-II heterojunction that enables photoinduced charge generation across its interface *[118, 218]*, intensities of the EA probe beam may interfere with the internal field of bilayer devices. To study the influence of photocharge generation (i.e. optical doping) on V_{bi} values, it is essential to conduct systematic V_{bi} meausurements with different EA probe beam intensities illuminated on the F8BT/TFB heterojunction. Effects of optical doping caused by the EA probe beam illumination is best determined by studying the *reverse* bilayer diode in which both metal/polymer interfaces obey the Schottky-Mott limit. This is achieved by conducting light-intensity dependent V_{bi} measurements on a "reverse bilayer" diode with a 60 nm-PEDOT:PSSH/40nm-F8BT/40nm-TFB/250nm-Al structure. The reverse bilayer configuration has the virtue of isolating TFB from PEDOT:PSSH, thereby preventing charge transfer-induced electronic doping across TFB/ PEDOT:PSSH interface [see Chapter 4 and ref. *[68, 111, 155]*]. Similarly depositing Al or Ca over TFB is unlikely to cause charge-transfer electronic doping of TFB LUMO levels due to the presence of AlO_x and CaO_x intervening layers as well as large Schottky barriers at the Al-on-TFB and Ca-on-TFB interfaces [see Chapter 4].

Fig. 5.7 and Table 5.2 show the results of V_{bi} measurements of PEDOT:PSSH/F8BT/TFB/Al device obtained with different EA probe beam intensities ($\sim 0.06 - 1$ mW/cm^2) and at different temperatures. Several important observations at 10 K can be noted by comparing Fig. 5.7 (a) with Fig. 5.7 (b). Firstly, the internal built-in field of bilayer diodes clearly varies with the EA probe beam intensity. Specifically the V_{bi} of TFB layer (~ 1.8 V) decreases by ~ 0.4 V when the probe beam intensity increases from ~ 0.06 W/cm^2 to ~ 1 mW/cm^2; while the V_{bi} of the F8BT layer (~ 2.2 V) remains unaffected by the same changes in . Consequently, photoexcitation at 10 K induces a V_{bi} offset of ~ 0.4 V across the TFB/F8BT heterojunction. Secondly, the V_{bi} of TFB (~ 2.2 V) is almost identical to that of F8BT (~ 2.3 V) at low EA probe beam intensities at 10 K, consistent with the equilibration of electrode's E_f through the bilayer structure.

Figure 5.7: V_{bi} measurements of F8BT (2.48 eV) and TFB (2.98 eV) components in a PEDOT:PSSH/F8BT/TFB/Al bilayer device at different temperatures. The monochromatic EA probe beam intensity is set at $0.8 – 1$ mW/cm^2 [(a) and (c)] and $0.06 – 0.07$ mW/cm^2 [(b) and (d)]. The device is modulated with $0.35V_{rms}$ at 216.1 Hz frequency. Inset in (a) shows the EA spectrum of the PLED at - 2 V and 10 K.

Temperature (K)	Illumination Intensity (mW/cm^2)	Polymer OSC	V_{bi} or V_{null} ($\pm$ 0.1 V)
298	0.8 – 1	F8BT	2.5
		TFB	2.1
	0.06 – 0.07	F8BT	2.4
		TFB	2.2
10	0.8 – 1	F8BT	2.2
		TFB	1.8
	0.06 – 0.07	F8BT	2.3
		TFB	2.2

Table 5.2: Results of V_{bi} or V_{null} measurements of PEDOT:PSSH/F8BT/TFB/Al bilayer devices obtained with different EA probe beam intensities and at different temperatures.

We have studied the effects of temperature on the V_{null} of the reverse bilayer device. Fig. 5.7 (c) and (d) show results of V_{null} measurements conducted on the device at 298 K. To ensure experimental consistency, intensities of EA probe beam employed in such measurements are identical to those used at 10 K. By fixing the EA probe beam intensity at ~ 0.8 – 1 mW/cm^2, we found that the V_{null} values of both TFB layer and F8BT layer at 298 K are ~ 0.3 V higher than respective V_{bi} values at 10 K. These results show that sub-gap spectral absorptions of reverse bilayer diodes at 298 K can undermine reliabilities of V_{null} values like the case of blended PLED outlined above. Interestingly the strong charge modulation components at 298 K appear to obscure the influence of the EA probe beam intensity on V_{null} of the device. As shown by Fig. 5.7 (c) and (d), changing the probe beam intensities over more than an order of magnitude at 298 K does not seem to vary the difference in the V_{null} of F8BT and TFB layers. These observations highlight the importance of low-temperature EA measurement in ensuring reliable determinations of the built-in fields in bilayer devices.

5.5.3.2   PEDOT:PSSH/F8BT/TFB/Ca

We have performed similar measurements on PEDOT:PSSH/F8BT/TFB/Ca reverse bilayer PLEDs. Results of these measurements are presented in Fig. 5.8 and Table 5.3, which show that light intensity affects the V_{bi} of reverse bilayer diodes comprising vapour-deposited Ca cathode in ways similar to those described above. Fig. 5.8 (a) and (b) show the results of V_{bi} measurements on a PEDOT:PSSH/F8BT/TFB/Ca reverse bilayer diode at 10 K. Fig. 5.8 (b) shows that at 10 K and using low EA probe beam intensity ($\sim$ 0.06 mW/cm^2), the V_{bi} of TFB ($\sim$ 2.7 V) is identical to the V_{bi} of F8BT ($\sim$ 2.8 V) within the error limit of EA technique. But at high probe beam intensity ($\sim$ 0.8 – 1 mW/cm^2), the V_{bi} of the TFB layer *decreases* to $\sim$ 2.6 V; while the V_{bi} of the F8BT layer *increases* to $\sim$ 3.0 V thereby causing a V_{bi} offset of $\sim$ 0.4 V across the F8BT/TFB heterojunction.

We also found that temperature affects our measurement results of the same device. Fig. 5.8 (c) and (d) show that although the EA probe beam intensities are identical to those used at 10 K, the V_{null} values of TFB and F8BT at room temperature are higher than their respective V_{bi} at 10 K. These observations may be attributed to the convolution of sub-gap spectral absorptions with EA spectral component as described earlier. These observations prompted us to rely on the V_{bi} data measured at 10 K for understanding the built-in field distributions in the reverse bilayer devices.
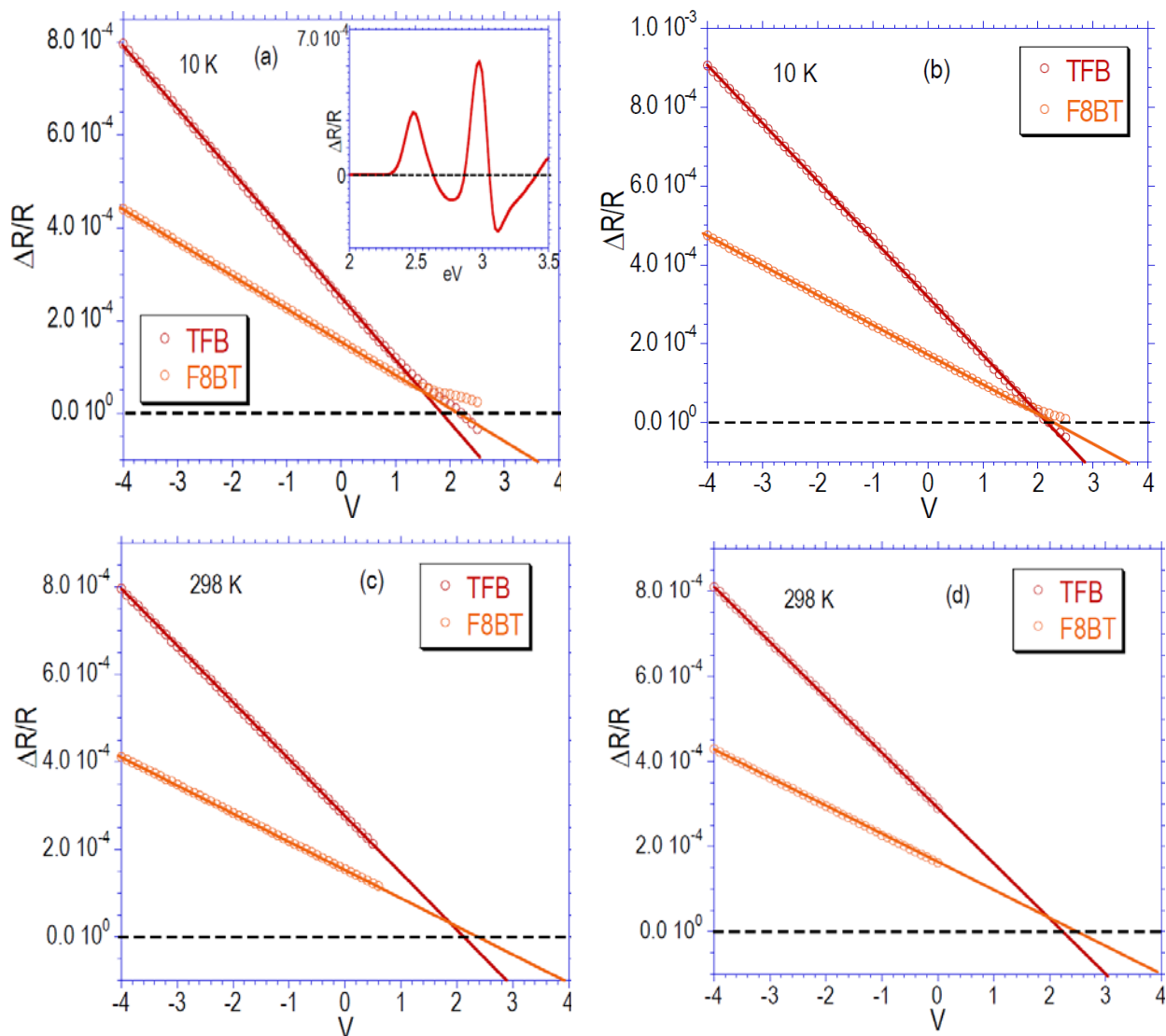
Figure 5.8: V_{bi} measurements of F8BT (2.48 eV) and TFB (2.98 eV) components in a PEDOT:PSSH/F8BT/TFB/Ca bilayer PLED at different temperatures. The monochromatic EA probe beam intensity is set at $0.8 - 1$ mW/cm^2 [(a) and (c)] and $0.06 - 0.07$ mW/cm^2 [(b) and (d)]. The device is modulated with $0.70 V_{rms}$ at 216.1 Hz frequency. The EA spectrum of the diode is similar to the inset of Fig. 5.7 (a) and is not shown.

Temperature (K)	Illumination Intensity (mW/cm^2)	Polymer OSC	V_{bi} or V_{null} ($\pm$ 0.1 V)
298	0.8 – 1	F8BT	3.2
		TFB	3.0
	0.06 – 0.07	F8BT	3.1
		TFB	2.9
10	0.8 – 1	F8BT	3.0
		TFB	2.6
	0.06 – 0.07	F8BT	2.8
		TFB	2.7

Table 5.3: Results of V_{bi} or V_{null} measurements of PEDOT:PSSH/F8BT/TFB/Ca bilayer PLEDs obtained with different EA probe beam intensities and at different temperatures.

5.5.3.3   PEDOT:PSSH/TFB/F8BT/Al

We have determined the effects of EA probe intensity on the V_{bi} of normal TFB/F8BT bilayer PLEDs with an Al cathode. Results of V_{bi} measurements conducted at 10 K with different EA probe beam intensities are shown in Fig. 5.9 and Table 5.4. The EA spectrum typically seen for normal bilayer PLEDs is shown in the inset of Fig. 5.9 (a). Several observations can be noted from Fig. 5.9 (a) and (b). Firstly, the built-in field of normal bilayer PLEDs varies with the intensity of the EA probe beam at 10 K. Specifically, increasing the EA probe beam intensity *decreases* the V_{bi} of the TFB layer to ~ 1.4 V; whereas the V_{bi} of the F8BT layer (~ 1.9 V) remains unchanged. Secondly, lowering the EA probe beam intensity over more than an order of magnitude does *not* eliminate the V_{bi} offset across the TFB/F8BT interface. Rather the V_{bi} of the TFB layer (~ 1.6 V) remains ~ 0.3 V lower than the V_{bi} of the F8BT layer (~ 1.9 V).

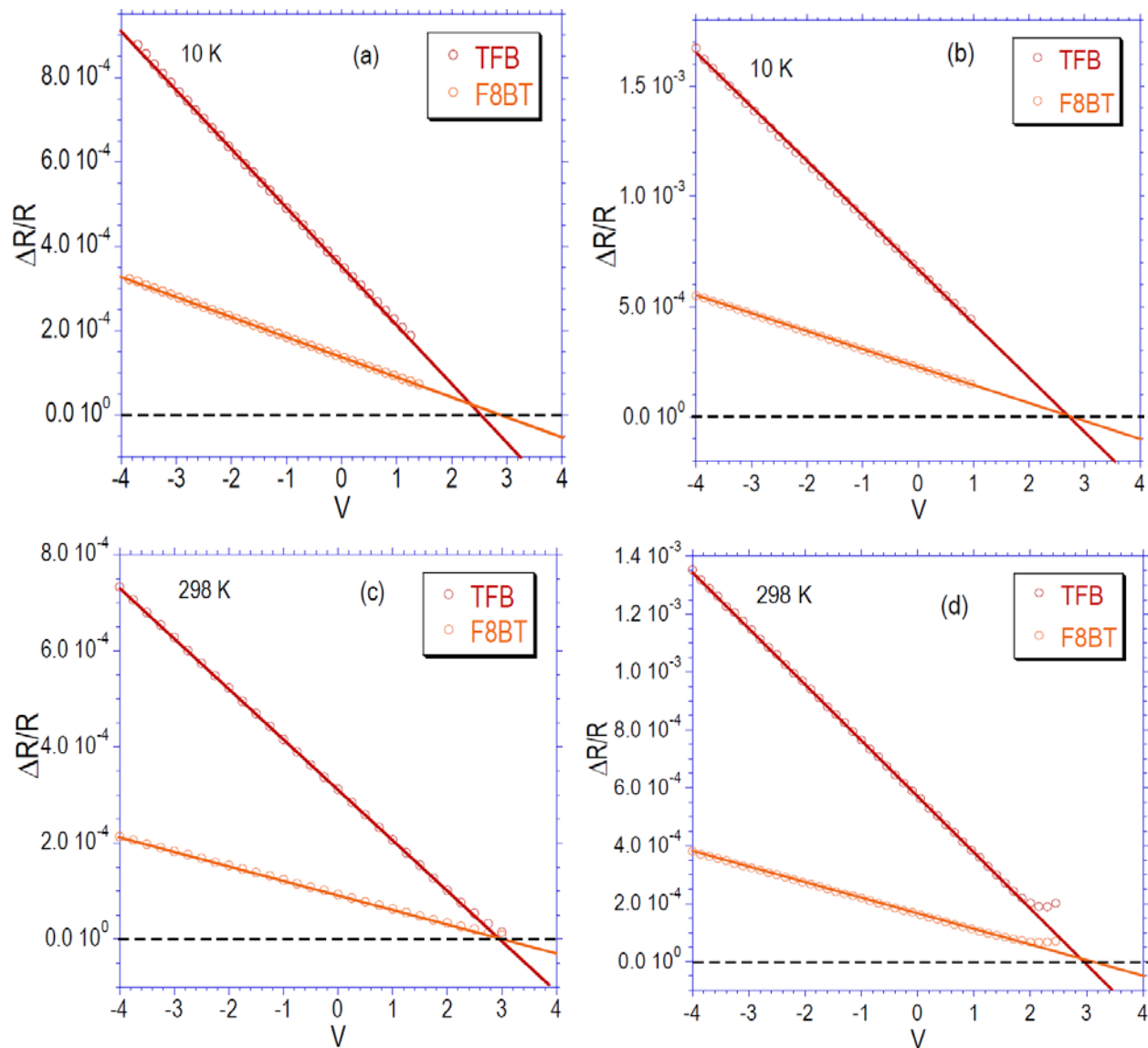Figure 5.9: V_{bi} measurements of F8BT (2.47 eV) and TFB (2.97 eV) components in a PEDOT:PSSH/TFB/F8BT/Al bilayer PLED at different temperatures. The monochromatic EA probe beam intensity is set at $0.06 - 0.07$ mW/cm^2 [(a) and (c)] and $0.8 - 1$ mW/cm^2 [(b) and (d)]. The device is modulated with $0.30V_{rms}$ at 216.1 Hz frequency. Inset in (a) shows the EA spectrum of the device at - 2 V and 10 K.

We have also determined the effects of temperature on the V_{null} of the same device. Results of V_{null} measurements performed at 298 K are shown in Fig. 5.9 and Table 5.4. The probe beam intensities employed in V_{null} measurements at 298 K are identical to those used at 10 K. Fig. 5.9 (c) – (d) show that the 1ω electromodulation signals of TFB and F8BT layers at 298 K do not vary linearly with applied V_{dc}. Rather, their deviations from linearity grow increasingly pronounced as the device approaches flat-band condition despite an attentuation of illumination intensities. This observation shows that the 1ω EA signal at 298 K are convoluted with bias-dependent charge absorption components *[49, 98, 168]* probably due to ohmic charge injection across the TFB/PEDOT:PSSH interface [see Chapter 4].

Temperature (K)	Illumination Intensity (mW/cm²)	Polymer OSC	V_{bi} or V_{null} (± 0.1 V)
298	0.8 – 1	F8BT	1.9
		TFB	1.9
	0.06 – 0.07	F8BT	2.5
		TFB	2.6
10	0.8 – 1	F8BT	1.9
		TFB	1.4
	0.06 – 0.07	F8BT	1.9
		TFB	1.6

Table 5.4: Results of V_{bi} or V_{null} measurements of PEDOT:PSSH/TFB/F8BT/Al bilayer PLEDs obtained with different EA probe beam intensities and at different temperatures.

To determine V_{null} by linear extrapolation of the 1ω electromodulation signals at 298 K, we ignore data in the V_{dc} ranging from - 1.5 V to 0 V as these data are contaminated by charge-modulation features. Table 5.4 shows that spectral contamination at 298 K leads to convergence

of the V_{null} values of TFB and F8BT layers, which is not observed in V_{bi} measurements obtained at 10 K. Interestingly, reducing illumination intensities at 298 K increases the V_{null} in TFB and F8BT layers by ~ 0.7 V; but reducing measurement temperature at fixed illumination intensities decreases the V_{null}. This phenomenon shows that EA spectral contamination influences the V_{null} measurements in ways opposite to the illumination intensities.

5.5.3.4   PEDOT:PSSH/TFB/F8BT/Ca

We have determined the effects of EA probe intensity on the built-in fields in normal TFB/F8BT bilayer PLEDs with a Ca cathode at 10 K. Several observations are noted from Fig. 5.10 and Table 5.5. Firstly, the 1ω EA signal of TFB and F8BT at 10 K varies *non-linearly* with V_{dc} ranging from - 3 V to - 4 V, showing that the internal field is *not* uniformly distributed when the device is subjected to reverse biases. This observation indicates the presence of space charge in the device prior to the application of external driving voltage. Secondly, at 10 K the V_{null} of both TFB and F8BT layers appear less sensitive to changes in illumination intensity. To determine V_{null} by linear extrapolation of the 1ω electromodulation signals at 10 K, we ignore data in the V_{dc} ranging from - 2.5 V to - 4 V as the internal fields are affected by redistribution of charges in this bias range. The V_{null} of TFB (~ 1.5 V) and F8BT (~ 2.1 V) remains unchanged (within the error limit of EA spectrometer) despite increasing the EA probe beam intensity by more than an order of magnitude. Thirdly, the V_{null} offset at the F8BT/TFB interface is not eliminated by attenuating the illumination intensity at 10 K. Rather, the V_{null} in TFB remains to be ~ 0.50 V lower than that of F8BT [see Table 5.5].

We have also determined the effects of temperature on the V_{null} of the same device. The probe beam intensities employed in V_{null} measurements at 298 K are identical to those used at 10 K. Fig. 5.10 (c) – (d) show that the 1ω electromodulation signals of TFB and F8BT layers at 298 K do not vary linearly with applied V_{dc} in a way similar to that shown in Fig. 5.9 (c) – (d), thus confirming that the EA 1ω signals are contaminated with charge-modulation components at room temperature.
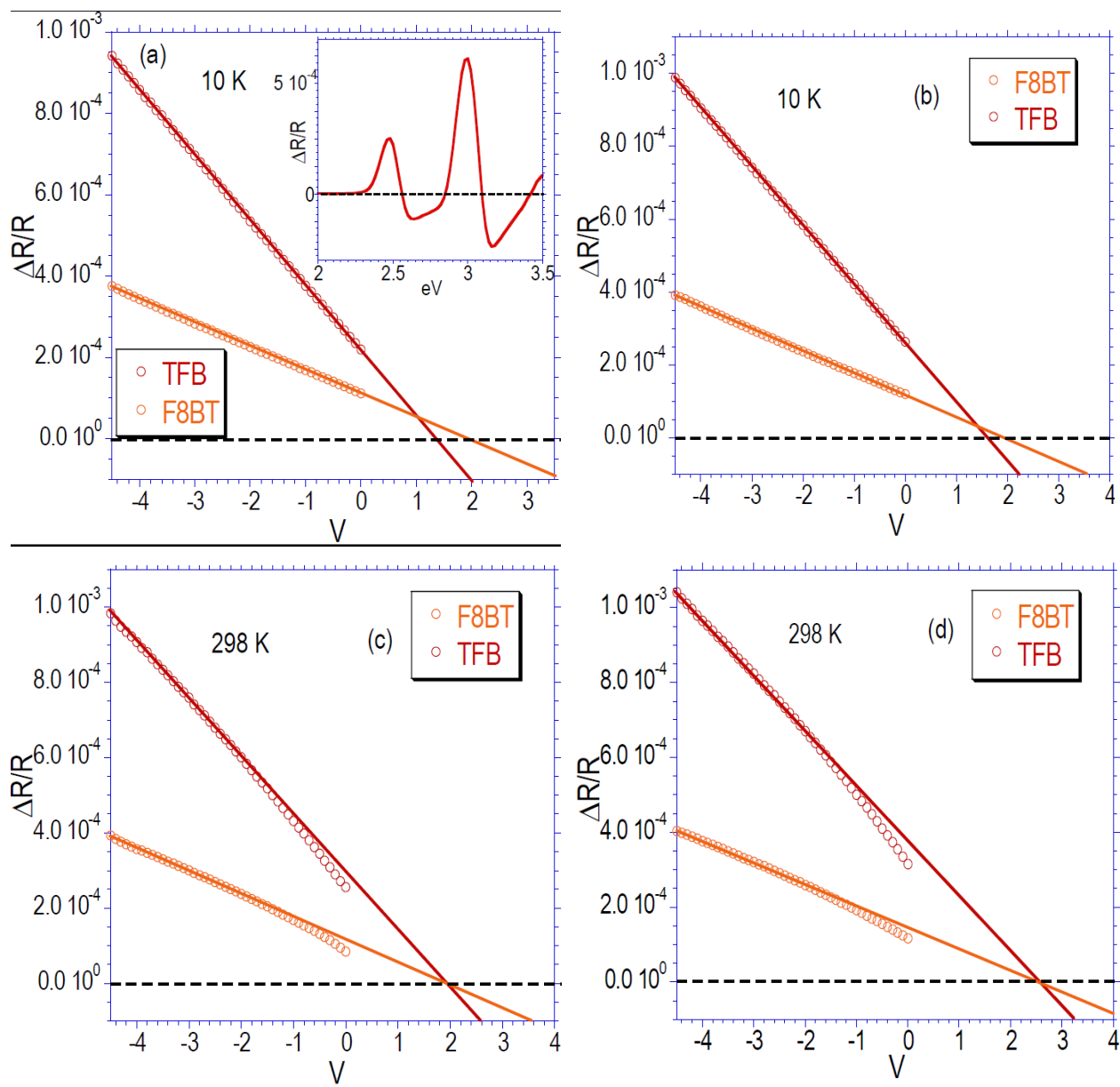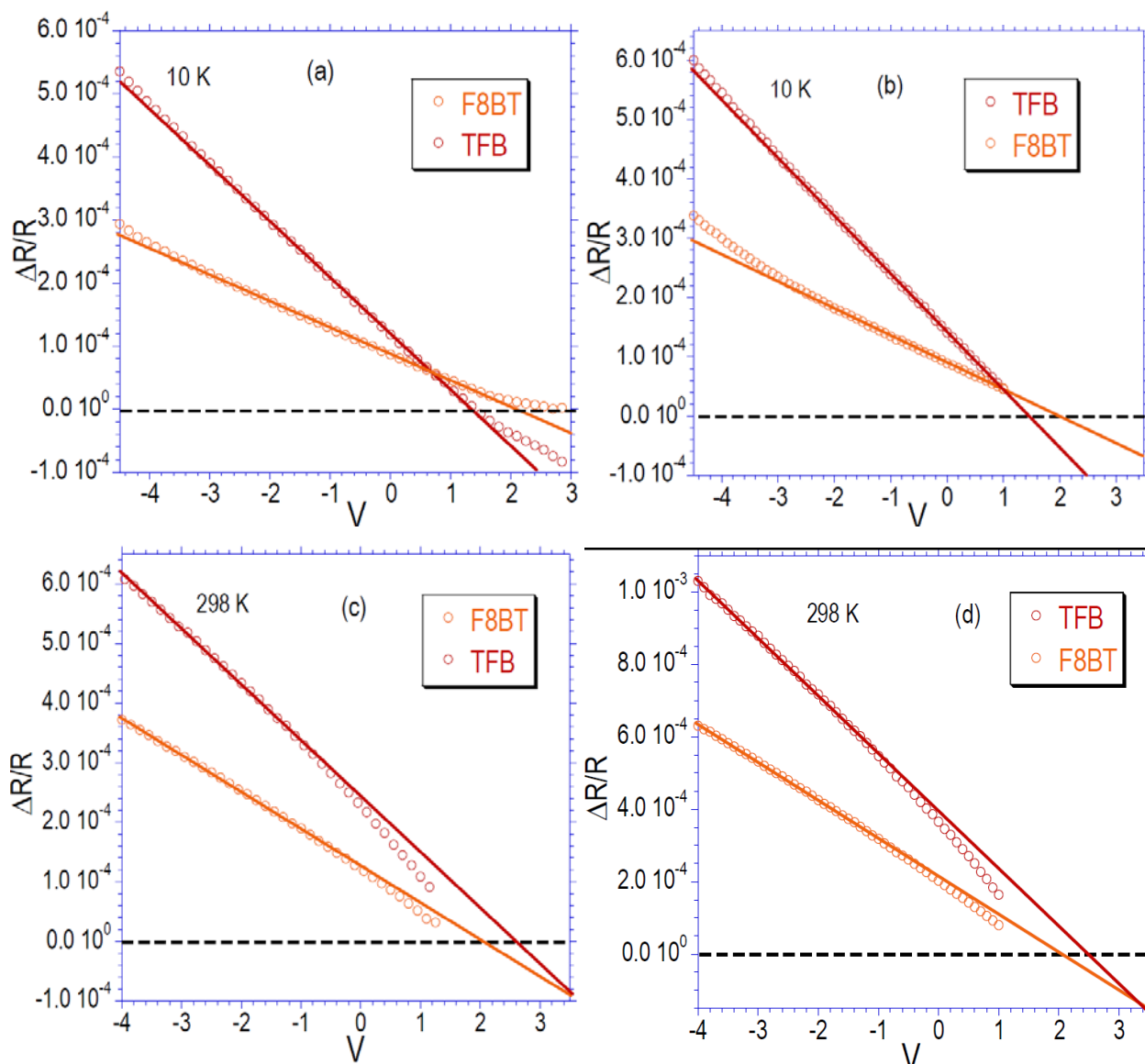
Figure 5.10: V_{bi} measurements of F8BT (2.46 eV) and TFB (2.96 eV) layers in a PEDOT:PSSH/TFB/F8BT/Ca bilayer PLED at different temperatures. The monochromatic EA probe beam intensity is set at $0.8 - 1$ mW/cm^2 [(a) and (c)] and $0.06 - 0.07$ mW/cm^2 [(b) and (d)]. The device is modulated with $0.50V_{rms}$ at 216.1 Hz frequency. The EA spectrum of the diode is similar to inset of Fig. 5.9 (a) and is not shown.

Interestingly reducing illumination intensities by more than an order of magnitude at 298 K does not change the V_{null} of TFB layer, but lowering the measurement temperatures from 298 K to 10 K reduces the V_{null} of TFB by ~ 1 V [see Table 5.5]. This phenomenon shows that EA spectral contamination influences the V_{null} measurements in an opposite way to the illumination intensity. Results of our measurements clearly show that EA spectral contamination undermines the reliability of V_{null} determination and that low-temperature EA measurement is necessary for accurate measurements of internal fields in working devices.

Temperature (K)	Illumination Intensity (mW/cm^2)	Polymer OSC	V_{bi} or V_{null} ($\pm$ 0.1 V)
298	0.8 – 1	F8BT	2.0
		TFB	2.5
	0.06 – 0.07	F8BT	2.1
		TFB	2.5
10	0.8 – 1	F8BT	2.1
		TFB	1.4
	0.06 – 0.07	F8BT	2.0
		TFB	1.5

Table 5.5: Results of V_{bi} or V_{null} measurements of PEDOT:PSSH/TFB/F8BT/Ca bilayer PLEDs obtained with different EA probe beam intensities and at different temperatures.

5.6 Discussions of EA Studies on PLEDs with F8BT/TFB Heterojunctions

5.6.1 Effects of Illumination Intensities on EA Studies of Reverse Bilayer Diodes

The phenomenon of a light intensity-dependent V_{bi} can be explained by examining the energy level schematic of a reverse F8BT/TFB bilayer diode [see Fig. 5.11]. Similar to organic photovoltaics *[118, 147]*, illuminating the EA probe beam (~ 2.98 eV in energy) onto the F8BT/TFB bilayer structure promotes photoinduced charge transfer across the F8BT/TFB interface at 10 K. This interfacial charge transfer causes local electron accumulation at the low-lying LUMO of F8BT and hole accumulation at the high-lying HOMO of TFB at 10 K, thereby leading to a "photoinduced dipole" that partly offsets the built-in field *[120, 224]* and decreases the V_{bi} of TFB layer. Photogeneration of dipole at the TFB/F8BT interface is related to the fact that the energy range corresponding to the TFB EA maximum (~ 2.93 – 2.98 eV) overlaps with the F8BT absorption spectrum [see Fig. 5.1]. Excitons are generated through absorption in the bulk of the F8BT layer upon illuminating the reverse bilayer device with an EA probe beam of 2.93 – 2.98 eV in energy. F8BT bulk excitons generated within the diffusion range (>10 nm *[115, 225]*) readily diffuse towards the F8BT/TFB interface, where they undergo charge transfer to form interfacial geminate electron-hole pairs *[118]*. With the aid of the built-in electric field in the reverse bilayer devices (~ 2.8 – 3.4 x 10^7 V/m), a small fraction of these geminate electron-hole pairs may separate into free electrons and holes. Otherwise these interfacial electron-hole pairs relax into the neutral exciplex state that recombines radiatively (with red-shifted emission) *[118, 218]* or non-radiatively assisted by intersystem crossing to form triplets *[226]*. At room temperature thermally activated exciton regeneration from the exciplex state also occurs *[218]*.

At 10 K, however, this cyclical process of exciton regeneration across the TFB/F8BT heterojunction must be completely frozen out *[223]*. The low temperature may also significantly extend the lifetime of the geminate pairs to millisecond timescale or beyond, thus making their effects on the V_{bi} detectable by steady-state EA spectroscopy. Indeed V_{bi} of the TFB layer in the PEDOT:PSSH/F8BT/TFB/Ca device is *not* affected by EA probe beam intensities at 165 K (data

not shown) and at room temperature [see Fig. 5.8 (c) and (d)]. These observations suggest that when temperature reaches 165 K or higher, the exciplex state that is generated from photoinduced charge-transfer during EA measurements are thermally reactivated to regenerate radiative F8BT excitons *[218]*. But at 10 K exciton regeneration is forbidden and we consider only the field-assisted dissociation of the interfacial geminate electron-hole pairs *[218]*, which modify the internal electric field in the device *[223]*.
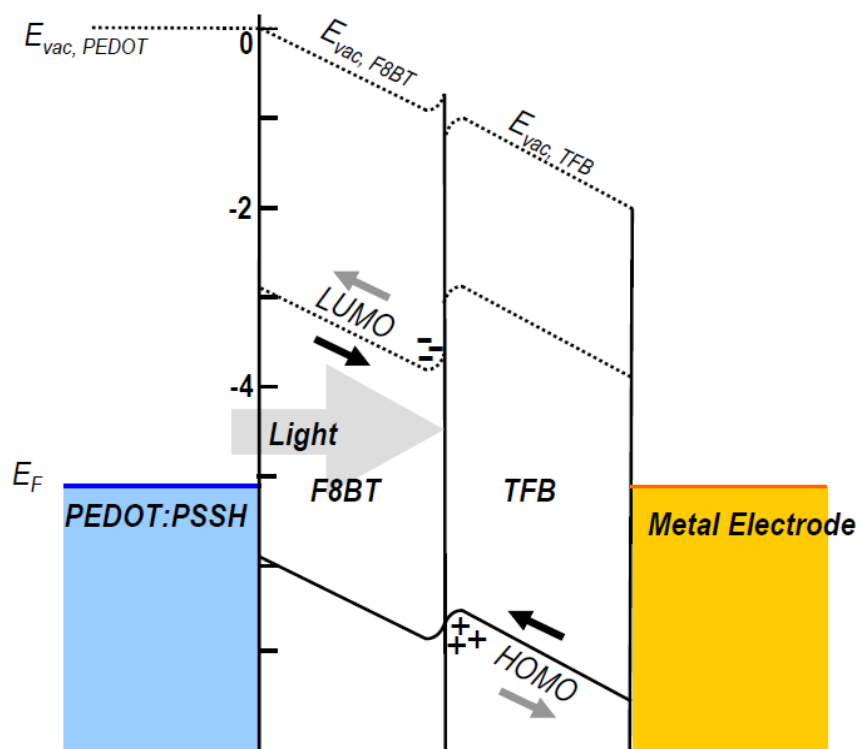
Figure 5.11: Energy band diagram of a PEDOT:PSSH/F8BT/TFB/metal reverse bilayer diode when illuminated by a monochromatic EA probe beam with photon energy corresponding to the EA maximum of TFB (~ 2.93 – 2.98 eV). Photogenerated excitons in F8BT undergo charge transfer at the F8BT/TFB interface to form interfacial electron-hole pairs that may dissociate into free charges or relax to form an exciplex. The built-in field in the reverse bilayer diode device favours local accumulation of the geminate pairs close to the F8BT/TFB interface. E_{vac} denotes the vacuum level of a material. E_{vac} of the vapour-deposited metal is not shown since dipole may present at the metal-on-OSC interface. The black and grey arrows indicate the directions of the built-in field and diffusion current, respectively.

Fig. 5.11 represents a complication that only affects V_{bi} measurements of the larger energy-gap OSC (i.e. TFB) of bilayer diodes. The V_{bi} of the lower energy-gap OSC (i.e. F8BT) is unlikely to be affected since both TFB and F8BT are transparent or slightly absorbing at ~ 2.48 eV (i.e. F8BT's EA maximum). Indeed comparing Fig. 5.7 (a) with Fig. 5.7 (b) shows that the V_{bi} of the F8BT at 10 K in the PEDOT:PSSH/F8BT/TFB/Al device is unaffected by the EA probe beam intensity. The slight increase in the V_{bi} of the F8BT in the PEDOT:PSSH/F8BT/TFB/Ca device [see Fig. 5.8 (a) and (b)] at high probe beam intensity (~ 2.48 eV) is unlikely to be due to the photoinduced dipole outlined in Fig. 5.11. Unfortunately direct confirmation of this hypothesis is difficult as the V_{bi} variation approaches the accuracy limit of the EA spectrometer.

We have attempted to estimate the photogenerated charge density introduced by EA measurement across a type II heterojunction. The areal charge density at the TFB/F8BT interface may be estimated by standard electrostatics:

$$\sigma = \frac{C \Delta V_{bi}}{q} = \frac{\varepsilon_r \varepsilon_0 \Delta V_{bi}}{qd} \tag{5.2}$$

where σ is the areal charge density, C is the double-layer capacitance, ε_r is the relative dielectric constant of polymer OSC, ΔV_{bi} is the difference in built-in voltages of F8BT and of TFB (~ 0.3 – 0.4 V), q is the unit charge of a single charge-carrier (i.e. 1.602 X 10^{-9}) and d is electron-hole separation within a geminate pair (after thermalisation) at the F8BT/TFB heterojunction. By assuming ε_r of both F8BT and TFB to be ~ 3.5 and d to be ~ 2.2 nm [see ref. *[218, 227]*], we estimate that photogenerated charge density across a planar F8BT/TFB heterojunction is ~ 2.6 – 3.5 x 10^{12} cm^{-2}. This amounts to ~ 4.9 – 6.6 x 10^{10} charges generated over the EA probe beam area (~ 1.9 x 10^{-2} cm^2). Remarkably the estimated charge density is comparable to the maximum charge densities encountered at OSC/OSC interfaces in multilayered organic LEDs during significant charge injection when subjected to high forward bias (~ 6 x 10^5 V/cm) *[123]*.

But in practice, photogenerated charges are likely to stay very close to the TFB/F8BT heterojunction with their effective accumulation widths being ~ 20 Å or so (i.e. ~ one or two

monolayers of the polymer) owing to orientation of the heterojunction with respect to direction of the built-in field. Based on the unit cell reported for semicrystalline F8BT films using X-ray diffraction *[228]*, the volume occupied by each F8BT monomer unit is ~ 1.3 nm^3. By assuming a charge accumulation width of ~ 20 Å from the TFB/F8BT interface, we estimated the *local* optical doping concentration to be ~ 2 – 3 % of the F8BT repeat units in one monolayer of F8BT (i.e. one charge for every 37 – 50 F8BT repeat units). But if the charge accumulation width extend to the entire vertical thickness of the device, EA measurement would induce optical doping of ~ 0.5 – 0.9 % of the repeat units in one monolayer of F8BT.

5.6.2 Effects of Illumination Intensities on EA Studies of Normal Bilayer Diodes

Similar influences of light intensity (with energy corresponding to TFB's EA maximum) over V_{bi} of the polymer active layers are observed in normal bilayer PLEDs, in which orientation of the F8BT/TFB bilayer heterojunction (relative to the electrodes) is reversed. Fig. 5.12 illustrates the effects of reversing the TFB/F8BT heterojunction on spatial distribution of photogenerated polarons in the device. As shown by Fig. 5.12, illuminating the EA probe beam (~ 2.93 – 2.98 eV in energy) onto the normal bilayer structure leads to a photoinduced dipole across the TFB/F8BT heterojunction. The physics underlying the formation of photoinduced dipole is described in the preceding section. With the aid of the built-in field in the normal bilayer PLEDs (~ 2.4 x 10^7 V/m), a small fraction of the geminate electron-hole pairs dissociate into unbound polarons *[218]*. At 10 K these charges may locally accumulate at the TFB/F8BT interface due to their reduced mobilities, thus establishing a charge concentration gradient that modifies the internal fields in these devices.

We note that the influence of illumination intensity on the V_{bi} of normal bilayer PLEDs appears less pronounced compared to that on the V_{bi} of reverse bilayer PLEDs. This observation may be related to the directions of the built-in fields [see Fig. 5.12] and of the diffusion currents in the normal bilayer PLEDs, both of which favour redistribution of photogenerated polarons from the TFB/F8BT heterojunction to the metal/polymer interfaces. This phenomenon may diminish the photoinduced dipole generated by the EA probe beam illumination in direct contrast to the built-

in field in reverse bilayer diodes, which favours accumulation of geminate pairs near the TFB/F8BT interface [see Fig. 5.11]. As such the reverse bilayer structures has the virtue of enabling accurate estimation of charges that arise purely from photoexcitation in bilayer diodes during EA measurements, which is not attainable for normal bilayer PLEDs as the distribution profiles of photogenerated polarons are not well determined.
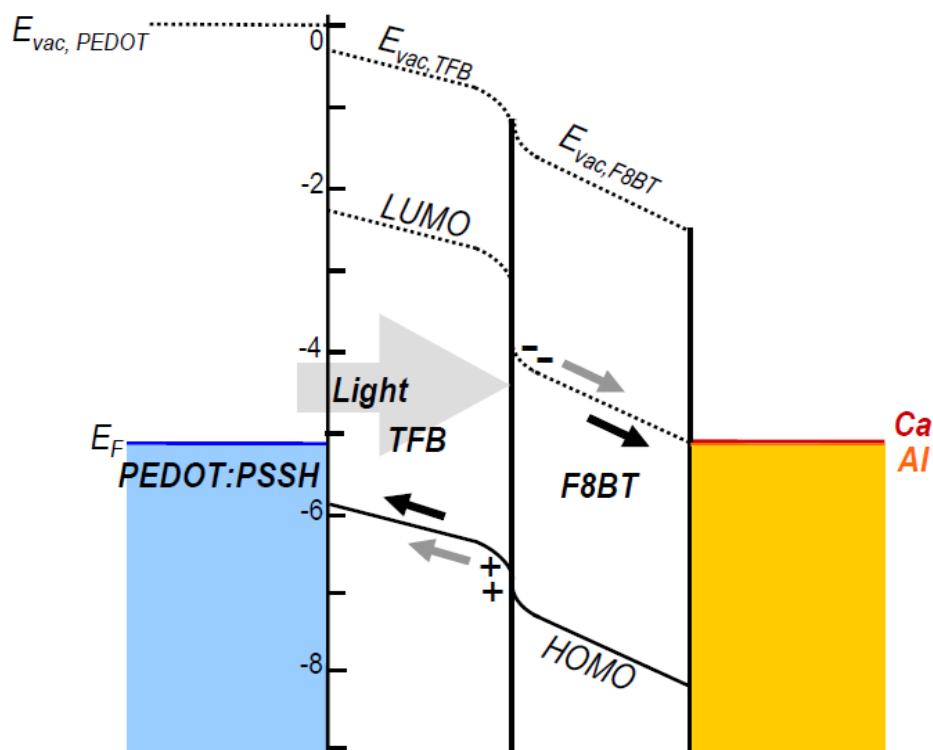
Figure 5.12: Energy band diagram of the PEDOT:PSSH/TFB/F8BT/metal (i.e. Ca or Al) normal bilayer PLEDs (at 10 K) when illuminated by a monochromatic EA probe beam with photon energy corresponding to the EA maximum of TFB ($\sim$ 2.93 – 2.98 eV). Photogenerated excitons in F8BT undergo charge transfer at the F8BT/TFB interface to form interfacial electron-hole pairs that may dissociate into free charges or relax to form an exciplex. At 10 K, geminate pairs may locally accumulate near the TFB/F8BT interface due to reduced charge mobility, thus modifying the internal field in the TFB layer. Work functions of the vapour-deposited Ca and Al are used to construct the diagram. E_{vac} denotes the vacuum level of a material. UPS confirms that a 0.3-eV E_{vac} misalignment exists at the PEDOT:PSSH/TFB interface [see Fig. 4.4]. E_{vac} of the vapour-deposited Ca and Al are not shown since dipoles may present at these metal-on-OSC interfaces. The black and grey arrows indicate the directions of the built-in field and diffusion current, respectively.

We emphasise that the process shown in Fig. 5.12 only affects the V_{bi} of the larger energy-gap OSC (i.e. TFB) of bilayer PLEDs. V_{bi} of the lower energy-gap OSC (i.e. F8BT) is unlikely to be affected since both polymer OSCs are transparent or slightly absorbing at ~ 2.48 eV (i.e. F8BT's EA maximum). Accordingly the ~ 0.1-V increase in V_{bi} of the F8BT layer in the PEDOT:PSSH/TFB/F8BT/Ca device, which occurs upon illuminating the device with 2.48-eV photons with 0.8 – 1 mW/cm^2 in intensity [Fig. 5.10 (a)], might not be due to photogeneration across TFB/F8BT interface but weak photoexcitation in the bulk of the F8BT layer. Direct confirmation of this is difficult as change in V_{bi} approaches the error limit of the EA spectrometer.

Our results shown here highlight the strong interference of the EA probe beam illumination at 10 K on the internal field distribution in bilayer PLEDs comprising type II heterojunctions, which are also found in organic photovoltaics *[147, 223]*. Optical doping of the device can be effectively circumvented by attenuating the EA probe beam over more than an order of magnitude from the intensity of ~ 1 mW/cm^2. Our results clearly show that EA probe beam intensity (~ 0.06 – 0.07 mW/cm^2) is crucial for the purpose of accurate V_{bi} determination in blended or multilayered PLEDs.

5.6.3   Effects of Illumination Intensities on EA Studies of Blended PLED

Studies of bilayer devices with a single planar F8BT/TFB interface enable us to understand the influence of TFB/F8BT orientation on results of V_{bi} measurements of blended PLED. Fig. 5.6 show that the V_{bi} values of TFB and F8BT in blended PLED are identical and are *not* affected by EA probe beam intensity. This is in stark contrast to V_{bi} values in bilayer PLEDs, which may be changed by as much as ~ 0.4 V through changing EA probe beam intensity over two orders of magnitude. This phenomenon is related to the morphologies of F8BT/TFB heterojunctions in blended and bilayer devices. The TFB/F8BT heterojunctions in bilayer PLEDs are planar and well defined in their directions of orientation; but orientations of TFB/F8BT interfaces encountered in blended

PLEDs are relatively random owing to complex polymer phase separation behaviour during film formation [see Fig. 5.2 and ref. *[63, 116, 221]*]. Photogenerated dipoles across randomly oriented TFB/F8BT interfaces in blended PLED readily cancel each other and give rise to V_{bi} values that are unaffected by changes in photoexcitation intensity. Interestingly, results of V_{bi} measurements obtained with attenuated light intensity show that the built-in field is equally distributed in the TFB and the F8BT components of the blended PLED. These observations are discussed in subsequent section.

5.6.4   Energy Level Alignments in Bilayer PLEDs via EA Spectrocopy

Having clarified the influence of light intensity on the internal field of reverse bilayer diodes, we can now examine the energy level alignment in these devices. For reasons outlined above, we rely on the V_{bi} obtained with minimal EA probe beam intensities ($\sim$ 0.06 – 0.07 mW/cm^2) to construct energy band diagrams of reverse and normal bilayer diodes.

In the case of blended or multilayered polymeric diodes comprising two or more polymer OSC components, V_{bi} of each polymer OSC component (at 10 K) in the device is generally related to the *surface* work functions of the electrodes by:

$$eV_{bi} = \Phi_{anode/OSC} - \Phi_{cathode/OSC} \tag{5.3}$$

where $\Phi_{cathode/OSC}$ and $\Phi_{anode/OSC}$ denote the *surface* work functions of cathode and anode near to charge-injecting interfaces, respectively. Eq. (5.3) expresses the relationship between *surface* work functions of the electrodes and V_{bi} of the finished diode provided that the electrode work functions lie within polaronic gap of *all* polymer OSC components (i.e. Schottky-Mott limit). Deviations from eq. (5.3) indicate presence of interface dipole(s) or electronic doping across one or both metal/polymer interface(s), which give rise to E_f pinning at these interfaces (Bardeen's limit).   In this case V_{bi} of each polymer OSC component in a blended/multilayered device is related to the *surface* work functions of its electrodes by:

$$eV_{bi} = [(\Phi_{anode/OSC} - \delta_{anode/OSC}) - (\Phi_{cathode/OSC} - \delta_{cathode/OSC})] \tag{5.4}$$

where $\delta_{anode/OSC}$ and $\delta_{cathode/OSC}$ denote vacuum level misalignments across anode/OSC and cathode/OSC junctions, respectively. The direction of $\delta_{metal/OSC}$ is the same direction as that of V_{bi} in the device. Note that $\delta_{metal/OSC}$ provides *no* information on the nature of the physical processes contributing to vacuum level misalignment.

5.6.4.1 PEDOT:PSSH/F8BT/TFB/Metal (Metal = Ca or Al)

Results of our V_{bi} measurements are summarised in Fig. 5.13, which shows the energy band diagrams of reverse bilayer F8BT/TFB diodes with different metal electrodes. Fig. 5.13 (a) and (b) show that the built-in fields in the F8BT and the TFB layers in PEDOT:PSSH/F8BT/TFB/metal (Ca or Al) devices are identical (within the error limit of EA spectrometer). This observation confirms that TFB and F8BT in reverse bilayer structures resemble charge-free dielectrics with identical built-in field, which is consistent with the absence of charge transfer across the F8BT-on-PEDOT:PSSH and the metal-on-TFB interfaces in the bilayer devices [see Chapter 4]. It is worth noting that the EA spectrometer measures the electric field intensity needed to cancel the built-in field in an OSC layer of a bilayer device *[123]*, which is independent on the thickness of the OSC layer [see eq. (2.28) in Chapter 2]. But an energy band diagram depicts the electrostatic potential in the bilayer device, which is a function of the material's thickness. Accordingly Fig 5.13 shows that eV_{bi} in a bilayer device is equally distributed in both polymer layers.

We have attempted to determine the surface work function of the vapour-deposited cathode in reverse bilayer diodes. Using eq. (5.3) and the fact that the PEDOT:PSSH/F8BT interface obeys the Schottky-Mott limit [see Fig. 4.3], the interface work function of vapour-deposited Al ($\Phi_{Al/F8BT}$) is found to be ~ 3.0 eV. This value is very close to $\Phi_{Al/F8BT}$ in single layer F8BT diodes (~ 3.2 eV) reported in Chapter 4. The 0.2-eV discrepancy in work function can be attributed to the slightly different vacuum deposition environment encountered during actual device fabrications. Similarly analysis on reverse bilayer diodes with a Ca cathode shows that the interface work function of Ca ($\Phi_{Ca/TFB}$) is ~ 2.4 eV at the TFB/Ca interface, which is identical to $\Phi_{Ca/TFB}$ of single layer TFB diode [see Chapter 4 for discussions].

Our V_{bi} measurements on reverse bilayer F8BT/TFB diodes lead us to several conclusions. Firstly, built-in fields in bilayer devices are determined by the work functions of vapour-deposited metals at the metal/polymer *interfaces*, which differ from work functions of atomically clean metals by at least 0.5 eV. Secondly, vacuum level alignment exists across the solution-

processed, type II TFB/F8BT heterojunction in bilayer devices comprising only Schottky metal/polymer OSC contacts. Interchain π-electronic interactions between TFB and F8BT are probably decoupled by a thin physisorbed hydrocarbon intervening layer introduced during device fabrication *[26, 71]*. Lastly, the ~ 0.3 – 0.4 eV V_{bi} offset may be generated through photoinduced charge-transfer across the type-II TFB/F8BT heterojunction simply by illuminating EA probe beam upon the diodes. This phenomenon undermines accurate determination of electronic structures in multilayered devices and may be avoided by attenuating the EA probe beam intensity. Importantly, these observations enable detailed understanding of interfacial electronic structures in normal bilayer PLEDs, which is discussed at length in the following section.
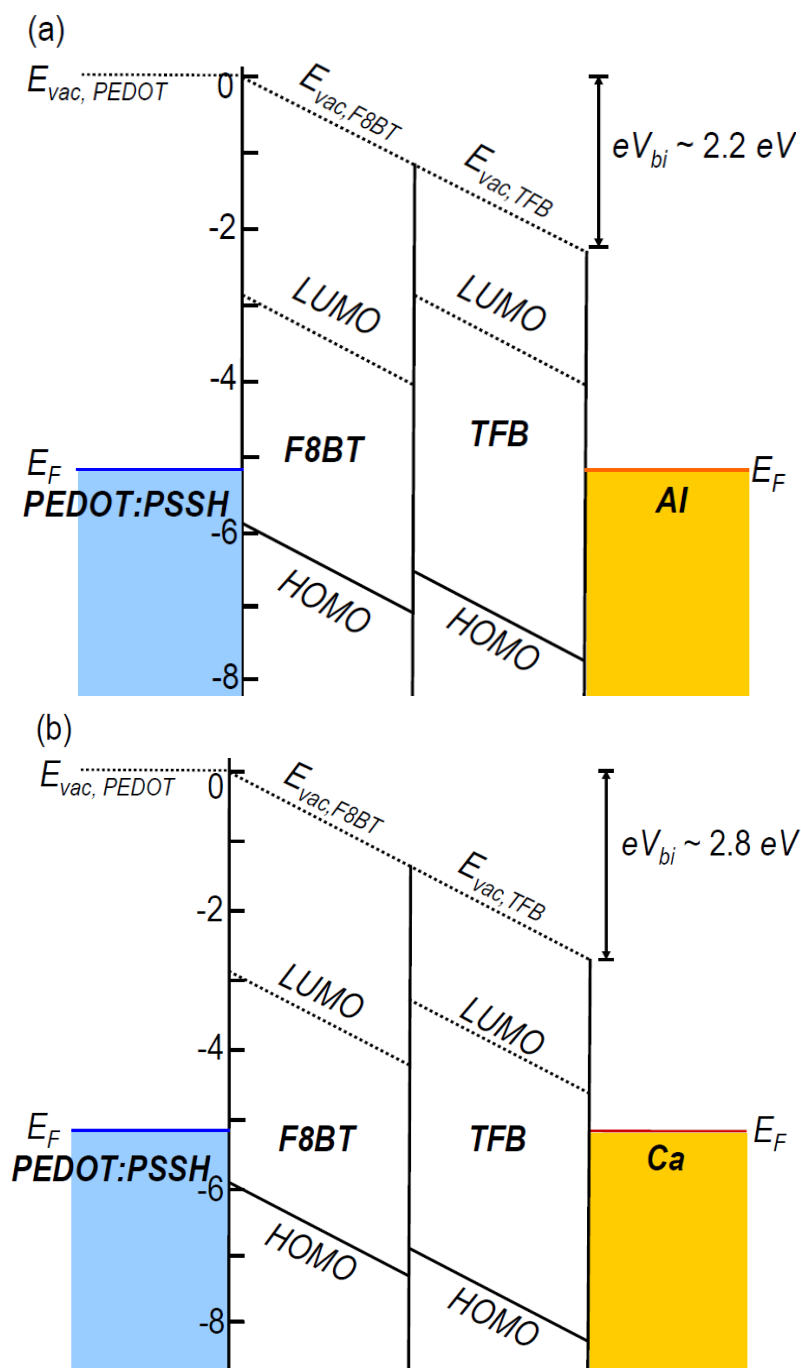
Figure 5.13: Energy band diagrams of (a) the PEDOT:PSSH/F8BT/TFB/Al reverse bilayer device; and (b) the PEDOT:PSSH/F8BT/TFB/Ca reverse bilayer device at electrical equilibrium. Both metal/polymer OSC interfaces are Schottky contacts, so F8BT and TFB layers resemble charge-free dielectrics with rigid energy bands and uniform distribution of built-in field. $\Phi_{Ca/TFB}$ (2.4 eV) and $\Phi_{Al/TFB}$ (3.0 eV) determined from the V_{bi} measurements at 10 K are used to construct the energy band diagrams. E_{vac} denotes the vacuum level of a material. E_{vac} of the vapour-deposited metals are not shown since dipoles may present at the metal-on-OSC interfaces.

5.6.4.2   PEDOT:PSSH/TFB/F8BT/Metal (Metal = Ca or Al)

(a)   PEDOT:PSSH/TFB/F8BT/Al

In order to construct the energy band diagram of a PEDOT:PSSH/TFB/F8BT/Al device, it is essential to understand consider the correlation between data obtained via both the *EA* and the ultraviolet photoemission spectroscopic (UPS) techniques. UPS measurement has confirmed that the TFB-on-PEDOT:PSSH interface is ohmic due to spontaneous hole doping of TFB chains by the PEDOT:PSSH *[68, 182]*. Accordingly a ~ 0.30-eV local band bending exists near the TFB/PEDOT:PSSH interface in the normal bilayer structure prior to cathode deposition. We note that the E_{vac} misalignment near the TFB/PEDOT:PSSH interface affects the energy level alignment in a finished bilayer device in several ways, which are discussed upon as follow.

Our earlier studies on reverse bilayer devices [see Fig. 5.13] have confirmed that E_{vac} of a TFB film aligns with E_{vac} of F8BT in finished bilayer diodes via EA spectroscopy. Accordingly the ~ 0.3-eV local band bending *[68, 100]* near the TFB/PEDOT:PSSH interface in a normal bilayer structure may increase the surface electron affinity of the F8BT layer from ~ 2.8 – 2.9 eV to ~ 3.1 – 3.2 eV, thereby resulting in an ohmic Al-on-F8BT contact in the bilayer PLED. Interestingly, this speculation is consistent with the V_{bi} of the F8BT layer (~ 1.9 V) in the device, which agrees well with eq. (5.4) by assuming that $\delta_{PEDOT/TFB}$ as ~ 0.30 eV, $\Phi_{Al/F8BT}$ as ~ 3.0 eV and $\Phi_{PEDOT/TFB}$ as ~ 5.2 eV. J-V measurements in Fig. 5.3 (a) and Fig. 5.3 (d) also reveal that the current traversing a blended PLED with an Al cathode, which has a normal bilayer structure due to vertical phase segregations *[63, 116]*, is close to the current traversing a normal bilayer PLED with a Ca cathode. Results of V_{bi} measurements [see Table 2] give further support to our speculation by showing that the F8BT V_{bi} in the normal bilayer device saturates at ~ 1.9 V upon replacing Al with Ca cathode.   These observations lead us to conclude that vapour-deposited Al may form an ohmic contact with F8BT like the case of vapour-deposited Ca. Chapter 4 has discussed this phenomenon at length.

Vapour-deposited Al is unlikely to form a simple electrical contact with F8BT. Photoemission spectroscopic studies of many Al-on-polymer OSCs contacts prepared in UHV environments (~ 10^{-9} – 10^{-10} mbar) *[93, 156, 174, 189, 190, 229-231]* show that Al atoms diffuse into the polymer chains near the interface and form covalent bonds with the conjugated backbone. In the case of polythiophene systems Al atoms (which are strong electron donors) selectively react with the electron deficient α-carbon atoms of thiophene units *[189, 230]*. Such Al – C_α covalent bond formation results in electron transfer from the Al atoms to the sp^3-hybridised α-carbon atoms along the polythiophene chain and breaks the π–conjugation at these points of bonding. Disruption of π–conjugation, in conjunction with strongly localised charges gained from vapour-deposited Al, result in an interfacial barrier layer (with thickness approaching ~ 60 Å *[230]* or electron tunneling distance *[4, 66, 174]*) where charge mobility is significantly reduced *[231]*. Similar chemical reactions occur at Al-on-polyfluorene-based OSCs interfaces in UHV environment. Greczynski *et. al.* *[156]* showed that π-conjugation near the poly(9,9'-dioctylfluorene) (F8) surface is disrupted due to the formation of Al–C complexes upon coating F8 with 3Å of Al. Independent X-ray photoemission spectroscopic (XPS) studies of Al-on-TFB contacts *[100]* also reveal formation of electron-deficient Al species during the early stage of Al deposition, which is in excellent agreement with early measurements of Al-on-polythiophene interfaces *[189, 230]*. These observations confirm that charge transfer occurs from Al to TFB chains upon contact formation in UHV environment.

Although direct measurements of the Al/F8BT interface in UHV are not available, vapour-deposited Al atoms probably interact with F8BT chains at the interface since F8BT shares a similar chemical structure with those of F8 and of TFB. π electronic conjugation along the F8BT backbone may be disrupted by site-selective reactions between Al atoms and α-carbon atoms of fluorene and benzothiadiazole (BT) units in the polymer, resulting in a barrier layer at the Al-on-F8BT interface with reduced charge mobility. In our case Al vacuum deposition was conducted at ~ 10^{-6} – 10^{-7} mbar, so the F8BT surface is probably contaminated with physisorbed hydrocarbons and oxygen *[108, 156, 229, 232]* of sub-monolayer thickness. Accordingly the Al-on-F8BT interface encountered in our bilayer devices should more closely resemble Al/AlOx/F8BT. In practice, interfacial composition across an Al-on-F8BT contact is likely to be

spatially non-uniform and is highly sensitive to the actual vapour-deposition environment *[232]*. So in some areas of an Al-on-F8BT contact F8BT chains are shielded from vapour-deposited Al by an AlO$_x$ intervening layer; whereas a low-conductivity interfacial barrier layer may be found in the remaining areas. Effects of this barrier layer on device characteristic are discussed in the subsequent section. Based on the above analysis, we consider the energy band diagram in the PEDOT:PSSH/TFB/F8BT/Al bilayer diodes ("Al-based diodes") at electrical equilibrium, which is shown in Fig. 5.14.
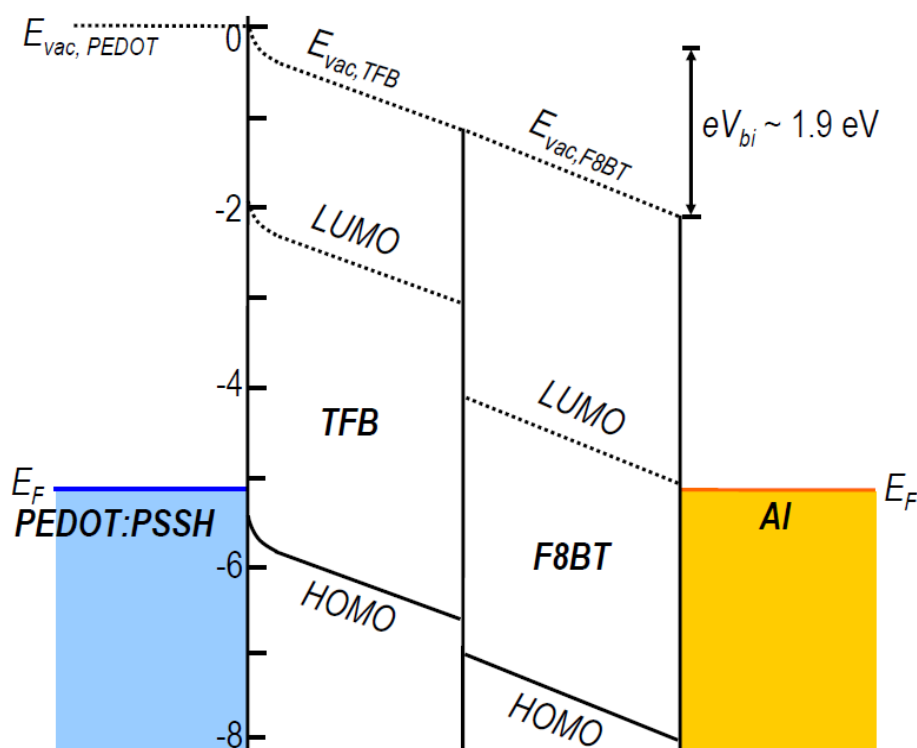
Figure 5.14: Energy band diagram of PEDOT:PSSH/TFB/F8BT/Al normal bilayer PLEDs based on the V_{bi} measurements at 10 K and with illumination intensity of ~ 0.06 – 0.07 mW/cm^2. E_{vac} denotes the vacuum level of a material. A 0.3-eV E_{vac} misalignment ($\delta_{PEDOT/TFB}$), which is confirmed by UPS measurements, exists near the PEDOT:PSSH/TFB contact and partly offsets the built-in field in the bulk of TFB layer. $\Phi_{Al/F8BT}$ and $\Phi_{PEDOT/TFB}$ are taken to be ~ 3.0 eV and ~ 5.2 eV, respectively. Although the V_{bi} in the bilayer device is ~ 1.9 V, the built-in fields in the bulk F8BT layer (~ 1.9 V/m) is larger than that in the bulk TFB layer (~ 1.6 V/m). E_{vac} of the vapour-deposited Al is not shown since a dipole may present at the Al-on-F8BT interface.

As illustrated in Fig. 5.14, the 0.3-eV E_{vac} misalignment near the TFB/PEDOT:PSSH contact arises from local band bending due to spontaneous charge-transfer across the interface *[68, 100]*. Therefore it also affects the built-in field in the TFB layer in a PEDOT:PSSH/TFB/F8BT/Al bilayer device. Spontaneous charge transfer electronically dopes the TFB chains near the PEDOT:PSSH/TFB contact with hole polarons, thus reducing the built-in field in the bulk of the TFB from ~ 1.9 V/m to ~ 1.6 V/m. This phenomenon is explained by the facts that: i) hole transfer across the TFB/PEDOT:PSSH interface is inherently confined to near the hole-injecting interface *[68, 100]* at 10 K; ii) the EA 1ω signal is proportional to the integral electric field in undoped portions of the TFB layer; and iii) the EA spectrometer measures the built-in field in a bilayer device, which is independent on the thickness of the polymer layer [see eq. (2.28) in Chapter 2]. Accordingly a thin hole-doped layer near the TFB/PEDOT:PSSH interface is depicted in Fig 5.14, which partly offsets the bulk internal field in the TFB film by ~ 0.3 V/m.

Fig. 5.14 clearly shows that the differential built-in fields in the F8BT layer and the undoped portion of TFB bulk account for the ~ 0.3-eV E_{vac} misalignment across the PEDOT:PSSH/TFB interface. Accordingly we conclude that the E_{vac} of TFB aligns with the E_{vac} of F8BT in a normal bilayer structure, which is in excellent agreement with results of our V_{bi} measurements on the reverse bilayer devices in Fig. 5.13. Hole transfer across the TFB/PEDOT:PSSH interface is equivalent to electronic reduction of PEDOT^{+} chains in PEDOT:PSSH, which may decrease the surface work function of PEDOT:PSSH by altering the internal dipole in the material *[108, 109]*. Assuming that the 0.3 V/m offset in built-in field is solely due to hole-doping of TFB and assuming d in eq. (5.2) to be ~ 2 – 4 nm, the hole density is estimated to be ~ 1.5 – 3 x 10^{12} cm^{-2} or ~ 8 – 16 x 10^{10} holes across the PLED's active area (1.5 x 3.5 mm).

(b) PEDOT:PSSH/TFB/F8BT/Ca

We now consider the energy level alignment across the PEDOT:PSSH/TFB/F8BT/Ca bilayer diodes ("Ca-based diodes") [see Fig. 5.15]. Our results in Fig. 5.10 show several important features: firstly, replacing the Al with Ca cathode increases the V_{bi} offset across the TFB/F8BT interface by ~ 0.2 V. Secondly, the ~ 0.2 V increase in V_{bi} offset is mainly due to a corresponding decrease in the built-in field in TFB layer (~ 1.5 V/m), which suggests enhanced hole-transfer across the PEDOT:PSSH/TFB interface. In contrast, the built-in field in F8BT layer (~ 2.0 V/m) remains almost unchanged upon replacing Al with Ca cathode, showing that the Al-on-F8BT interface in the bilayer PLED is as nearly an ohmic contact as the Ca-on-F8BT interface. Thirdly, 1ω electromodulation signals of TFB and F8BT vary *non-linearly* with applied *reverse* bias at 10 K despite the clear absence of charge injection from PEDOT:PSSH and Ca electrodes.   This last observation is in stark contrast to the EA 1ω signals of Al-based diodes, reverse bilayer diodes and blended PLEDs with a Ca cathode, which exhibit linear dependences on applied bias.

We examine the influences of applied reverse bias on the F8BT 1ω electromodulation signal of the Ca-based diodes. As shown by Fig. 5.10 (b), the F8BT 1ω electromodulation signal in Ca-based diodes varies *non-linearly* with applied reverse bias at 10 K. The non-linear EA 1ω signal is not related to leakage current since currents traversing the Ca-based diode and Al-based diode at - 4 V applied bias and at 10 K are found to be ~ 2 x 10^{-11} A/cm^2 (data not shown). Similar observations were also noted on *freshly-made* Ca-based diodes of different batches. Early V_{bi} measurements on single layer diodes with PEDOT:PSSH/F8BT/metal (Al or Ca) structures [see Chapter 4] have shown that the F8BT EA 1ω signal varies linearly with applied bias, which confirm that *Im* $\chi^{(3)}$ of F8BT is not changed by cathode deposition. These observations lead us to conclude that the F8BT layers in *pristine* Ca-based diodes (i.e. not subjected to charge injection before V_{bi} measurements) are doped with electrons and that the 1ω electromodulation spectral signal of F8BT is contaminated by charge modulation components at 10 K.

We now consider the nature of electron doping of F8BT in Ca-based diodes. To do so, it is important to first examine the chemical interaction between vapour-deposited Ca and F8BT. Electronic doping of F8BT may occur by charge transfer from E_f of vapour-deposited Ca to electron polaron levels of F8BT *[176]*, which differs from extrinsic n-doping of F8BT *[219]* in that it occurs spontaneously upon Ca/F8BT contact formation to equilibrate E_f across the diode structure *[27, 100, 117, 176, 229]*. XPS studies of Ca-on-F8BT interface prepared in UHV environment *[176]* show that vapour-deposited Ca atoms diffuse into the near surface region of F8BT and transfer charges to electron-withdrawing S and N atoms of the BT units to form calcium sulphide and calcium nitride with Ca–N covalent bonds, respectively. Consequently most Ca exists as electron deficient species in the early stage of vapour deposition to maintain overall electrostatic neutrality across the Ca/F8BT interface, similar to other Ca-coated polymer OSCs in UHV *[4, 174, 176, 180, 197, 229]*. But the fluorene units and phenylene groups of the F8BT conjugated backbones are not affected by vapour-deposited Ca. This observation is complemented by UPS studies *[176]*, which show that no occupied polaron or bipolaron state is formed in the energy gap of F8BT upon Ca deposition in UHV in direct contrast with many alkali metal-coated conjugated polymers *[66, 175, 178, 180, 197, 229]*. Photoemission spectroscopic measurements clearly show that charges donated by Ca are strongly localised at the electron-withdrawing sulphur and nitrogen sites of the BT moieties near F8BT surface and do not contribute to electrical conduction.

Interestingly vapour-deposited Ca also forms eletronically stable interfaces with other polymer OSCs. In-situ XPS measurements were conducted to study interface formation between vapour-deposited Ca and a poly(p-phenylene vinylene) (PPV) derivative containing 1,3,4-oxadiazole pendants during metal deposition in UHV *[233]*. No occupied electronic state is observed in the polymer's energy gap as electrons donated by Ca are localised at the electron-withdrawing oxadiazole rings rather than delocalised along the π-conjugated backbone. In contrast, vacuum depositing Ca over a MEH-PPV polymer (which contains electron-donating alkoxy MEH pendants) in UHV induces new polaron states in the polymer's energy gap, showing that π-electronic conjugation in MEH-PPV is affected by Ca deposition. These measurements demonstrate that electron-withdrawing moieties and/or pendant groups incorporated into the

polymer chains can serve as "in-built" buffer layers that protect the π-electronic conjugation from being disrupted by vapour-deposited Ca. Similarly, in the case of Ca-on-F8BT interface the electron-withdrawing BT moieties of F8BT enable vapour-deposited Ca to form a stable interface with F8BT in UHV without modifying electronic structures of its charge-transport levels *[176]*.

In practice, vapour deposition of Ca is conducted in HV environment (i.e. ~ 10^{-6} – 10^{-7} mbar) in which the solution-processed F8BT surface is contaminated by physisorbed hydrocarbons, moisture and oxygen *[101, 108, 174, 229]*. Independent photoemission spectroscopic measurements *[174, 191, 192, 229, 232]* on PPV derivatives confirm that vapour-deposited Ca first reacts with surface oxygen impurities to form an insulating CaO_x layer (~ 20 – 30 Å in thickness *[4]*) during early stages of contact formation. Further deposition of Ca result in progressive depletion of oxygen impurities on the PPV surface and a gradual increase in the metallic character of the Ca overlayer *[229]*. As a result, a CaO_x interlayer with a graded composition along its thickness direction is formed between the pure metallic Ca and the bulk PPV polymer. It is highly possible that similar processes occur while the F8BT surface is coated with vapour-deposited Ca in HV. In line with this reasoning we speculate that the CaO_x interlayer might have inhibited strong interfacial chemical interactions between the BT units of F8BT and the vapour-deposited Ca in the Ca-based diodes.

We emphasise that absence of Ca induced gap states at the Ca-on-F8BT interface *[176]* does not indicate absence of charge transfer across the heterojunction because charges can tunnel through the metal oxide to achieve E_f equilibrium across the diode structure *[26, 68, 100, 102, 234]*. In-situ XPS studies confirm that even when a PPV substrate is contaminated by oxygen-containing surface adsorbents, charge transfer across a 15 – 20 Å CaO interlayer readily occurs after the surface impurities are exhausted by interacting with vapour-deposited Ca *[229]*. In the case of Ca-on-F8BT interface *[176]*, charges transferred from vapour-deposited Ca may not be delocalised along the π–electronic conjugation of F8BT but are known to cause local charge accumulation and hence band bending near the heterojunction *[51, 229]*. These experimental evidences lead us to speculate that tail gap states *[10, 100, 113, 114]* at ~ 0.4 – 0.5 eV below the

LUMO edge ($\sim 2.8 - 2.9$ eV) of F8BT chains may be doped with electrons transferred from vapour-deposited Ca to equilibrate the E_f through the Ca-based diodes. Electron doping of F8BT may be electrostatically balanced by a thin layer of positive image charge (rather than Ca^{2+} ions) that accumulate at the surface region of Ca electrode adjacent to F8BT. Fig. 5.15 summarises the above descriptions on the electronic structures of Ca-based diodes in the form of an energy band diagram.
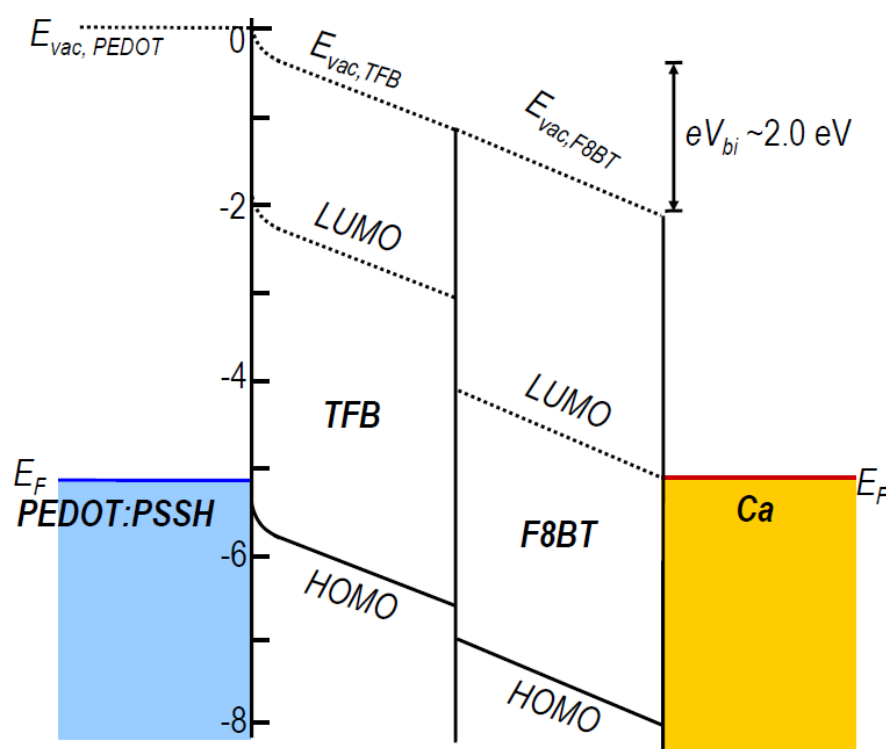
Figure 5.15: Energy band diagram of PEDOT:PSSH/TFB/F8BT/Ca normal bilayer PLEDs based on V_{bi} measurements at 10 K and with illumination intensity of $\sim 0.06 - 0.07$ mW/cm^2. E_{vac} denotes the vacuum level of a material. E_{vac} misalignment ($\delta_{PEDOT/TFB}$), which is confirmed by UPS measurements, exists near the PEDOT:PSSH/TFB contact and partly offsets the built-in field in the bulk of TFB layer. EA measures the bulk electric fields in the F8BT layer (~ 2.0 V/m) and in the undoped portions of TFB layer (~ 1.5 V/m), but the overall V_{bi} in the bilayer device is ~ 1.9 V. $\Phi_{PEDOT/TFB}$ is taken to be ~ 5.2 eV. E_{vac} of the vapour-deposited Ca is not shown since a dipole may present at the Ca-on-F8BT interface. Charge transfer due to E_f pinning at the Ca/F8BT contact may dope the F8BT bulk with electron polarons, thus resulting in non-linear variation of the bulk electric field in F8BT with applied bias.

It is interesting to consider the charge accumulation width near the Ca-on-F8BT interface in our bilayer device. Although the charge accumulation width near Ca-on-F8BT interface is unavailable, it is possible to approximate its length scale using measurements on other metal/polymer OSC systems. Hwang et. al. *[68]* demonstrate that the charge accumulation width near a TFB-on-PEDOT:PSSH contact, which contributes to ~ 0.3 eV E_{vac} misalignment, is ~ 16 nm. Similar measurement by Park *et. al.* *[197]* shows that local band bending near a phenylene vinylene oligomer (5PV)-on-Ca interface, which contributes to 0.5 eV E_{vac} misalignment, is ~ 10 nm. In the case of Ca-on-F8BT, the E_f of vapour-deposited Ca is substantially higher than the LUMO edge of F8BT [see Chapter 4] so charge transfer at the Ca-on-F8BT interface is probably much more significant than the TFB-on-PEDOT:PSSH and (5PV)-on-Ca interfaces. Accordingly charge accumulation width near the Ca-on-F8BT interface probably exceed ~ 16 nm or even approach the vertical thickness of F8BT layer (~ 40 nm) at room temperature. We therefore suspect that polaron clusters due to charge transfer from vapour-deposited Ca might diffuse through the entire F8BT layer at 298 K, thus contributing to the non-linear field dependence of the F8BT 1ω electromodulation signal [see Fig. 5.10 (b)].

The observation that the V_{bi} of the TFB layer decreases upon replacing the Al cathode with vapour-deposited Ca suggests that Ca-doping of F8BT might enhance hole transfer across the TFB/PEDOT:PSSH contact at the other side of the device. But the apparent reduction in TFB V_{bi} is likely to be attributed to spectral contamination of 1ω electromodulation TFB signal with a charge-modulation components, which also results in the non-linear field dependence of the TFB electromodulation signal [see Fig. 5.8 (b)]. The non-linear TFB 1ω electromodulation signal at 10 K implies that the bulk of the TFB layer is doped with mobile polaronic charges at room temperature. Such a hypothesis is consistent with independent UPS measurements on TFB-on-PEDOT:PSSH contacts *[68]*, where spontaneous hole transfer results in a ~ 16 nm thick local band bending region that extends into the bulk of TFB layer. Reasons contributing towards coupling of electronic structures across both charge-injecting interfaces of bilayer devices are under investigation. The effects of electron doping of F8BT on J-V-L characteristics of Ca-based diode are discussed in subsequent section.

Our V_{bi} measurements and independent photoemission spectroscopic studies show that the electronic structure near the Ca-on-F8BT contact is very different from the interfacial energetics at the Al-on-F8BT contact which comprises a thin insulating barrier interlayer with large injection barrier height and reduced charge mobility *[174, 189, 230, 231]*. The contrasting nature of Ca-on-F8BT and Al-on-F8BT interfaces suggests that polaron doping of the polymer OSCs, rather than eliminating charge-injection barriers, holds the key to realise high-performance PLEDs *[145, 156, 157, 171, 215, 219, 235, 236]*. But manual chemical doping of polymer OSCs is cumbersome and demands tight control over detailed fabrication procedures *[145, 157, 219, 236, 237]*, which are not conducive for large-scale industrial fabrication. Fortuitously doping of polymer OSCs can occur spontaneously during electrode deposition by optimising materials used for electrodes and OSC active layers *[156, 175, 180, 237, 238]*. Electrode-induced OSC doping explains the ongoing interests in employing novel metal electrodes to introduce charge carriers into light-emitting active layer for realising high-performance PLEDs *[48, 51, 143, 171, 172, 215, 239]*.

5.6.5 Correlations of EA Measurements with Device Characteristics

We now attempt to understand the physics underlying the J-V-L performance characteristics of Al-based diodes and Ca-based diodes by considering their energy band diagrams derived from low-temperature EA measurements. Although the energy level alignment of Al-based diodes [see Fig. 5.14] is similar to that of Ca-based diodes [see Fig. 5.15], the J-V-L performance characteristics of these devices are very different from each other. Fig. 5.3 (a) shows that the $V_{injection}$ and V_{on} in Ca-based diodes occur at ~ 1.5 V and ~ 2.1 V, respectively; whereas the $V_{injection}$ and V_{on} of Al-based diodes (data not shown) are ~ 1.9 – 2 V and ~ 3 V, respectively. The J-V-L characteristics of Al-based diodes are very similar to that of PEDOT:PSSH/TFB/F8T2/Al bilayer devices reported in ref. *[216]*. These observations indicate that the J-V-L characteristics of Al-based diodes are inferior to that of Ca-based diodes although our V_{bi} measurements show that the Al-on-F8BT interface is nearly as ohmic as the Ca-on-F8BT interface. Therefore minimising the energetic difference between the metal E_f and F8BT electron polaron levels appear not sufficient to realise bilayer PLEDs with optimal J-V-L characteristics. These observations motivate us to examine the correlations between low-temperature V_{bi} measurements and J-V-L performance characteristics of finished devices at room temperature.

V_{on} of single layer diodes have been widely assumed to be the applied biases needed to cancel built-in fields in these devices (i.e. $V_{on} \approx V_{bi}$) *[27, 49, 52, 76, 98, 116]*, which is valid if all metal/polymer interfaces in these devices are ohmic contacts [see Fig. 2.4]. Recently this model has been extended to understand the energy level alignments in blended and multilayered PLEDs comprising two or more polymers *[97, 116, 142, 168, 216]*. Specifically Lane *et. al. [97]* proposed that the V_{bi} of a blended PLED is given by the V_{on} and optical absorption gaps (E_g) of the light-emitting polymer (i.e. $eV_{bi} \approx eV_{on} \approx E_g$) if both metal/polymer interfaces in the device are ohmic contacts. Our V_{bi} measurements described above indicate that the empirical $eV_{bi} \approx eV_{on} \approx E_g$ relationship is not valid in understanding the device characteristics of PEDOT:PSSH/TFB/F8BT/Ca and PEDOT:PSSH/TFB/F8BT/Al bilayer PLEDs, both of which comprise ohmic metal/polymer contacts with barrierless charge injection across the heterojunctions. Indeed the V_{bi} of the F8BTlayer (~ 1.9 V) in Al-based diodes does not match the

E_g of the polymer (~ 2.7 eV) or the V_{on} of the device (~ 3 V). The absence of a direct correlation between V_{bi}, V_{on} and E_g is also seen in the J-V-L characteristics of the PEDOT:PSSH/TFB/F8T2/Al bilayer diode reported elsewhere *[216]*.

We account for this phenomenon by proposing that the $V_{injection}$ of a bilayer device is controlled by the OSC layer with the largest V_{bi} or the highest potential barrier against charge transport through the device. This hypothesis is supported by the fact that the $V_{injection}$ of Al-based diodes (~ 1.9 – 2.0 V) coincides with the V_{bi} of the F8BT layer (~ 1.9 V). Fig. 5.16 illustrates the correlation between the low-temperature V_{bi} measurements and the J-V-L characteristics of Al-based diodes. Fig. 5.16 (a) shows that at an applied bias of 1.6 V, the TFB layer in the device reaches flat-band while the F8BT layer is subjected to - 0.3 V *reverse* bias (i.e. 1.6 V − V_{bi} of F8BT). Increasing the applied bias to 1.9 V causes the F8BT layer to approach flat-band and subjects the TFB layer (V_{bi} ~ 1.6 V) to 0.3 V *forward* bias (i.e. 1.9 V − V_{bi} of TFB). Fig. 5.16 (b) shows that at an external applied bias of 1.9 V, holes originated from charge transfer near the PEDOT:PSSH/TFB contact (i.e. $\delta_{PEDOT/TFB}$) are drifted towards the TFB/F8BT interface, where they are locally confined by the 0.4-eV HOMO offset across the type II heterojunction. The resulting hole accumulation near TFB/F8BT interface leads to local band bending at the heterojunction, which facilitates hole diffusion from the TFB into the F8BT towards the Al cathode by reducing the HOMO offset at the TFB/F8BT interface *[4, 234, 240]*. Hole collection by the Al cathode probably contribute to the commencement of injection current through the device at ~ 1.9 – 2 V applied bias, which is in excellent agreement with the J-V-L characteristics of PEDOT:PSSH/TFB/F8T2/Al bilayer PLEDs reported in *[216]*. Although electron injection commences at the F8BT/Al interface at 1.9 V applied bias, electron transport in the bulk of F8BT is dispersive in nature *[40]*. Therefore electron accumulation at the Al/F8BT interface of the device, which is depicted as local band bending in Fig. 5.16 (b), is likely to occur at 1.9 V applied bias.
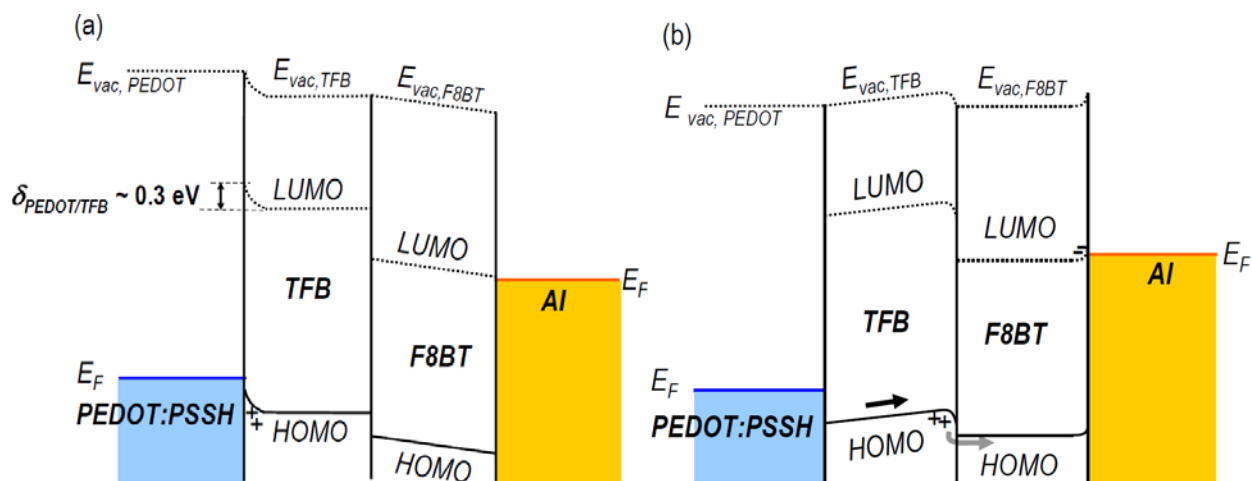
Figure 5.16: Energy band diagrams of PEDOT:PSSH/TFB/F8BT/Al bilayer diodes when subjected to external applied biases of: (a) 1.6 V and (b) 1.9 V at 298 K. $\Phi_{PEDOT/TFB}$ ($\sim$ 5.2 eV), $\Phi_{Al/F8BT}$ ($\sim$ 3.0 eV) and built-in fields in the device are determined by low-temperature V_{bi} measurements using probe beam intensities of $\sim$ 0.06 – 0.07 mW/cm^2. $\delta_{PEDOT/TFB}$ is determined from UPS measurement. Black and grey arrows in Fig. 5.16 (b) represent drift and diffusion of hole current through the device, respectively. At 1.9 V applied bias, hole accumulation at the TFB/F8BT interface and electron injection at the Al/F8BT interface lead to local band bending in the device. E_{vac} denotes the vacuum level of a material. E_{vac} of the vapour-deposited Al is not shown since a dipole may present at the Al-on-F8BT interface.

Imbalanced hole and electron injections as described above mean that the electron density near the TFB/F8BT interface at 1.9 V applied bias is too low to achieve radiative recombination. Indeed no EL from PEDOT:PSSH/TFB/F8BT/Al bilayer devices is observed until the applied bias reaches $\sim$ 2.7 – 3 V, similar to the L-V characteristics of PEDOT:PSSH/TFB/F8T2/Al bilayer PLEDs *[216]*. The high V_{on} of Al-based diodes ($\sim$ 2.7 – 3 V) can be attributed to the dispersive and diffusive natures of electron transport in the bulk of F8BT *[40]* as well as the presence of a 1-eV LUMO offset at the TFB/F8BT interface. Accordingly applying an external bias ranging from 1.9 V to 3 V to the device causes local electron accumulation at the TFB/F8BT interface, which largely screens the electric field in the bulk of F8BT. At 1.9 – 3 V applied bias, electron transport in the F8BT layer is probably driven by diffusion under the influence of electron concentration gradient similar to PLEDs subjected to strong forward bias *[49, 64, 98, 126]* and ion-doped light-emitting electrochemical cells *[145, 157]*.

Another important contribution to the high V_{on} of Al-based diodes is the insulating barrier layer ($\sim 20 - 30$ Å in thickness), which probably exists at the Al-on-F8BT interface due to the Al–C complex formations. Although photoemission spectroscopic studies on the Al-on-F8BT interface are not available, vapour deposition of Al is known to disrupt π-electronic conjugations of polyfluorene-based OSCs and other polymers *[4, 93, 174, 230]*. Accordingly the process of depositing vaporised Al atoms over F8BT in HV environment may result in an intervening layer with large electron injection barrier height between the Al cathode and bulk F8BT in ways similar to an overly oxidised Ca-on-F8 contact *[65, 173]*.

The energy band diagrams in Fig. 5.16 lead us to propose the following empirical relationship for bilayer organic diodes comprising *ohmic* contacts at *both* metal/OSC interfaces:

$$V_{bi,max} \approx V_{injection} \tag{5.5}$$

where $V_{bi,max}$ denotes the highest V_{bi} value of a bilayer device measured using the low-temperature EA technique. Importantly, eq. (5.5) relies on the assumption that the OSC layer in question is not doped with charges and that it resembles a charge-free dielectric at electrical equilibrium. Therefore eq. (5.5) is not applicable when spontaneous charge transfers occur at both metal/OSC contacts in the bilayer devices, which is the case for Ca-based diodes.

We now consider the correlations between the low-temperature V_{bi} measurements and the J-V-L characteristics of Ca-based PLEDs at room temperature. Fig. 5.3 (a) shows that $V_{injection}$ and V_{on} of Ca-based PLEDs commence at ~ 1.45 V and ~ 2.10 V, respectively. Comparing the J-V-L characteristics of Ca-based PLEDs with the results of low-temperature V_{bi} measurements in Table 5.5, which are obtained with attenuated illumination intensities, show that: i) the $V_{injection}$ (~ 1.5 V) coincides with the V_{bi} of the TFB layer (~ 1.5 V); and ii) the V_{on} (2.1 V) is close to the V_{bi} of the F8BT layer (~ 2.0 V). Fig. 5.10 (b) also shows that the TFB and F8BT 1ω electromodulation signals at 10 K vary *non-linearly* with applied reverse bias, implying that polarons in these polymer layers are relatively mobile at room temperature. These observations, in conjunction with our studies on Al-based diodes, lead us to conclude that the superior J-V-L

characteristics of Ca-based PLEDs can be attributed to the spontaneous charge transfer across the Ca/F8BT and PEDOT:PSSH/TFB contacts in the devices.

When both OSC layers are doped with charges *before* subjecting the bilayer PLED to an external driving voltage, eq. (5.5) is not valid in describing the J-V-L characteristics of the device. The reason is that the low-temperature V_{bi} of an OSC layer that is highly doped with charges does not reflect the effective potential barrier against charge injection and transport through the material at 298 K. The electron polaron clusters in the F8BT layer of Ca-based PLEDs may give rise to graded Fermi levels near the F8BT/Ca interface, which greatly facilitate electron injection into the bulk through a multihop pathway that resembles climbing up an energy cascade *[47]*. Accordingly charge injection through a Ca-based PLED should be determined by the built-in field in the OSC layer that is less affected by charge-transfer doping (TFB in this case). This hypothesis is borne out by the fact that the $V_{injection}$ (~ 1.45 V) of Ca-based PLEDs coincides with the low-temperature V_{bi} of TFB layer (~ 1.5 V) but not with the low-temperature V_{bi} of F8BT layer (~ 1.9 V). Our observation is also supported by Fig. 5.10 (b), which shows that the TFB 1ω electromodulation signals varies more linearly than the F8BT 1ω electromodulation signals with applied reverse bias over the same voltage range.

The presence of mobile charge carriers in the TFB and F8BT layers crucially affects the J-V-L characteristics of Ca-based PLEDs. Fig. 5.17 illustrates the effects of charge-transfer dopings of the F8BT and TFB layers on the J-V-L characteristics of Ca-based PLEDs. Fig. 5.17 (a) shows that the bulk of TFB layer reaches flat-band when the device is subjected to an applied bias of ~ 1.5 V. Meanwhile the hole polarons in the bulk of TFB layer (due to charge transfer from the PEDOT:PSSH) diffuse towards the TFB/F8BT interface. These hole carriers locally accumulate near the TFB/F8BT interface, which leads to local band bending that reduces the effective HOMO barrier across the TFB/F8BT heterojunction. This phenomenon facilitates the diffusion of holes from the TFB into the F8BT towards the Ca cathode *[4, 234, 240]*, which results in an injection current that commences at ~ 1.5 V applied bias. At 1.5 V applied bias, electron diffusion through the TFB layer is not likely because a 1-eV LUMO offset that acts as an electron injection barrier is present at the TFB/F8BT interface. Nevertheless, applying 1.5 V to

Ca-based PLEDs probably causes electron polarons in the n-doped F8BT layer to accumulate near the TFB/F8BT heterojunction. Fig. 5.17 (a) shows that this phenomenon results in local band bending near the TFB/F8BT interface and substantial screening of the built-in field in the bulk of F8BT layer.
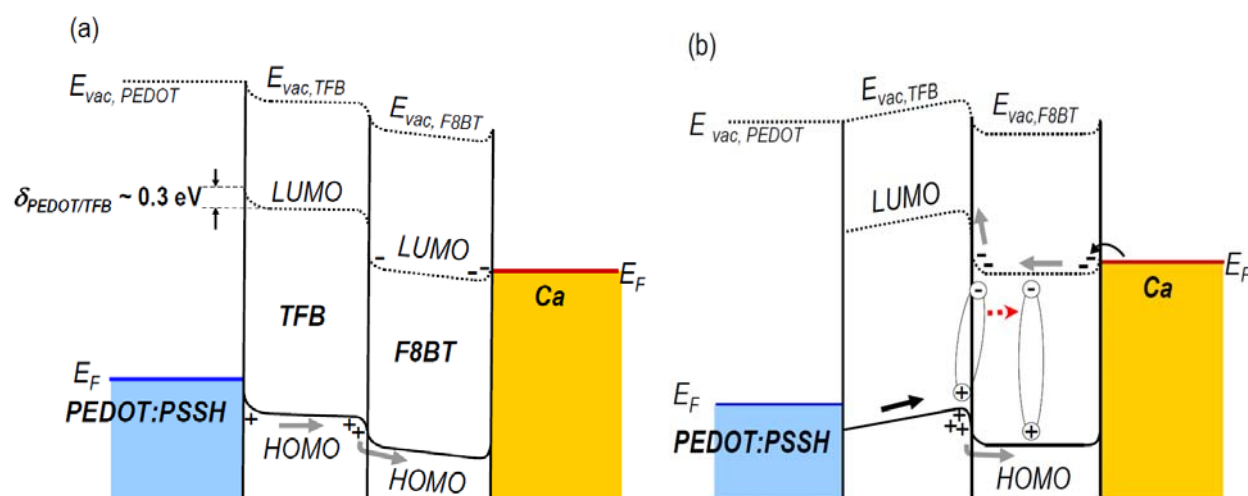

Figure 5.17: Energy band diagrams of PEDOT:PSSH/TFB/F8BT/Ca bilayer diodes when subjected to a driving voltage of: (a) 1.5 V and (b) 2.0 V at 298 K. Built-in fields in the device are determined by low-temperature V_{bi} measurements with illumination intensities of ~ 0.06 – 0.07 mW/cm². $\delta_{PEDOT/TFB}$ is determined from the UPS measurement. Black and grey arrows represent the drift and diffusion of charge carriers through the device, respectively. As the F8BT bulk reaches flat-band at ~ 2.0 V applied bias, electron-hole captures occur across the TFB/F8BT interface to form exciplexes, which undergo thermal activations (red arrow) to regenerate radiative F8BT bulk excitons. E_{vac} denotes the vacuum level of a material. E_{vac} of the vapour-deposited Ca is not shown since a dipole may present at the Ca-on-F8BT interface.

Fig. 5.17 (b) shows that increasing the applied bias to ~ 2.0 V causes the bulk of F8BT layer (V_{bi} ~ 2.0 V) to approach flat-band and subjects the TFB bulk (V_{bi} ~ 1.5 V) to a 0.5 V *forward* bias (i.e. 2.0 V − V_{bi} of TFB). Therefore applying a ~ 2.0 V external bias to the device sets up an electric field (~ 10⁶ V/cm) in the TFB bulk that drifts the hole carriers (due to charge transfer doping from the PEDOT:PSSH) towards the TFB/F8BT interface. These hole carriers subsequently diffuse across the HOMO barrier into the F8BT layer to the Ca cathode. As illustrated in Fig. 5.17 (b), applying ~ 2.0 V across the device also causes electron injection

across the ohmic Ca/F8BT contact. This is followed by electron diffusion through the bulk of F8BT layer and electron accumulation near the TFB/F8BT interface. Local electron confinement may facilitate electron diffusion into the TFB layer by lowering the effective LUMO barrier at the TFB/F8BT heterojunction, but a significant fraction of these charges undergo interfacial electron-hole captures to form exciplexes *[118, 218]*. At 298 K, interfacial exciplexes are thermally activated into bulk F8BT excitons that decay radiatively and contribute to EL of Ca-based bilayer PLEDs at 2.1 V applied bias [see Fig. 5.3 (a)]. Interestingly, independent L-V characterisations on Ca-based bilayer PLEDs with a thinner TFB layer (~ 10 nm in thickness) show that EL commences sharply when the driving voltages reach ~ 1.75 V *[116]* and ~ 2.0 V *[115]*. In order to achieve radiative recombinations, hole carriers at the TFB/F8BT interface must pass within a collision capture radius of at least one electron *[4]*. The latter process can occur immediately when or before the F8BT layer in the device reaches flat-band if the F8BT bulk is n-doped with electrons before subjecting the device to an external applied bias. Doping of F8BT is achieved through electrically spontaneous charge transfer that occurs upon the formation of the Ca-on-F8BT interface.

The operational mechanisms in Fig. 5.17 lead us to propose the following empirical relations to correlate the low-temperature V_{bi} measurements with the performance characteristics of bilayer organic LEDs:

$$V_{bi,min} \approx V_{injection} \tag{5.6}$$

$$V_{bi,max} \approx V_{on} \tag{5.7}$$

where $V_{bi,min}$ and $V_{bi,max}$ denote the lowest and highest low-temperature V_{bi} values of the OSC layers in the bilayer device, respectively. Importantly, eq. (5.6) and (5.7) are valid only if charge transfer occurs across both metal/OSC contacts in a bilayer device and is therefore not applicable to the Al-based bilayer diodes.

Interestingly, we find that the $eV_{bi} \approx eV_{on} \approx E_g$ relationship is also not valid in describing the performance characteristics of the PEDOT:PSSH/TFB:F8BT (50:50 w/w)/Ca PLEDs (i.e.

"blended PLEDs") although both metal/OSC interfaces are ohmic contacts. Table 5.1 shows that at 10 K, the V_{bi} of the TFB (~ 2.6 V) is identical to the V_{bi} of the F8BT (~ 2.6 V) in the blended PLEDs, which indicates that the bulk of F8BT:TFB layer are depleted with charge carriers at 10 K. But raising the temperature to 298 K causes the V_{null} of TFB (~ 2.3 V) to be larger than the V_{bi} of F8BT (~ 1.5 V). Comparing these observations with Fig. 5.3 (c) highlights the lack of correlation between the low-temperature V_{bi} and J-V-L device characteristics measured at 298 K. We consider the V_{bi} offset between the TFB and the F8BT since the complex, mesoscopic phase separations *[63, 116, 221]* in blended TFB/F8BT films prohibit interpretation of their absolute V_{bi} values. The V_{bi} offset is related to the mesoscopic phase separation in the blended films, which results in spatially interconnected networks of TFB/F8BT interfaces with their areas spanning across different length scales (~ 50 nm – 10 μm) *[63, 116, 221]*. At 10 K, polarons (due to charge transfer from the Ca and PEDOT:PSSH electrodes) locally accumulate near the TFB/PEDOT:PSSH and Ca/F8BT contacts, which results in identical built-in fields (~ 2.6 V/m) in both OSC components. But at 298 K, polarons near the two metal/OSC contacts diffuse towards the F8BT/TFB interfaces in the bulk of blended film and screen the built-in fields in the device. While the TFB in 50:50 blended films may form a continuous wetting layer (~ 5 – 10 nm) near the PEDOT:PSSH anode *[63, 116]*, F8BT does not form a continuous layer with vapour-deposited Ca because TFB capping layers are present in some areas within a Ca/F8BT contact *[116, 221]*. Accordingly electrons near the Ca/F8BT contact is likely to be more spatially confined than holes near the TFB/PEDOT:PSSH contact, which screens the V_{bi} in F8BT to a greater extent than the V_{bi} in TFB at 298 K.

Our investigations highlight the influences of charge-transfer at metal/polymer interfaces on the performance characteristics of bilayer polyfluorene-based PLEDs. Although V_{bi} measurements show both that the Al-on-F8BT contact is nearly as ohmic as the Ca-on-F8BT contact, they cannot account for the contrasting J-V-L characteristics of the respective bilayer devices. This phenomenon can be understood by considering the chemical and electronic interactions across the metal-on-F8BT interfaces. Our V_{bi} measurements provide evidences for the n-doping of F8BT by vapour-deposited Ca, which occur spontaneously upon the formation of the Ca/F8BT interface. Our studies show that doping of the OSC active layers in organic LEDs, rather than

minimising Schottky-barrier heights across the metal/OSC contacts, holds the key in optimising the J-V-L characteristics of the devices. This conclusion explains the ongoing interest in realising air-stable PLEDs with exceptional performance behaviours through doping of the light-emtting F8BT layer with transition metal-oxide electrodes *[171, 172, 220]*.

5.7   Conclusion

We have employed EA spectroscopy to perform detailed studies on the electronic structures in PLEDs comprising a type-II OSC/OSC heterojunction. Temperature and the EA probe beam intensity significantly affect V_{bi} measurements on PLEDs with a type-II OSC/OSC heterojunction. At low temperature, the EA measurements are found to introduce charge carriers with density $\sim 3 - 4 \times 10^{12}$ cm^{-2} through photoinduced charge transfer across a planar TFB/F8BT interface, which significantly redistributes the internal field across the type-II heterojunction. This phenomenon highlights the importance of conducting low-temperature EA measurements with attenuated EA probe beam intensities for accurate V_{bi} determination.

The knowledge gained from studying single layer diodes enables accurate determination of interfacial energetics across different bilayer diodes to within $\pm$ 0.1 eV accuracy. Comparing electronic structures in bilayer PLEDs comprising different metal cathodes show that electronic doping of the OSC active layers, rather than the elimination of Schottky barriers, holds the key in realising high-performance PLEDs with low EL turn-on voltages. Energy band diagrams of bilayer PLEDs, which are constructed based on results of low-temperature V_{bi} measurements, provide insights into understanding the detailed operational mechanisms of these devices. Our studies highlight the key influences of interfacial electronic interactions on device performance behaviours, which explains the ongoing interest in realising high-performance organic LEDs through doping of the OSC active layers with novel electrode materials.

REFERENCES

[1]   T. Ito, H. Shirakawa, S. Ikeda, *Journal of Polymer Science Part a-Polymer Chemistry* **1974**, *12*, 11.

[2]   H. Shirakawa, T. Ito, S. Ikeda, *Makromolekulare Chemie-Macromolecular Chemistry and Physics* **1978**, *179*, 1565.

[3]   J. H. Burroughes, D. D. C. Bradley, A. R. Brown, R. N. Marks, K. Mackay, R. H. Friend, P. L. Burns, A. B. Holmes, *Nature* **1990**, *347*, 539.

[4]   R. H. Friend, R. W. Gymer, A. B. Holmes, J. H. Burroughes, R. N. Marks, C. Taliani, D. D. C. Bradley, D. A. Dos Santos, J. L. Bredas, M. Logdlund, W. R. Salaneck, *Nature* **1999**, *397*, 121.

[5]   E. Moons, *Journal of Physics-Condensed Matter* **2002**, *14*, 12235.

[6]   H. Hoppe, N. S. Sariciftci, *Journal of Materials Research* **2004**, *19*, 1924.

[7]   H. Spanggaard, F. C. Krebs, *Solar Energy Materials and Solar Cells* **2004**, *83*, 125.

[8]   H. Sirringhaus, N. Tessler, R. H. Friend, *Synthetic Metals* **1999**, *102*, 857.

[9]   H. Sirringhaus, T. Kawase, R. H. Friend, T. Shimoda, M. Inbasekaran, W. Wu, E. P. Woo, *Science* **2000**, *290*, 2123.

[10]   H. Sirringhaus, *Advanced Materials* **2005**, *17*, 2411.

[11]   J. S. Kim, R. H. Friend, I. Grizzi, J. H. Burroughes, *Applied Physics Letters* **2005**, *87*, 023506.

 [12]   N. Corcoran, A. C. Arias, J. S. Kim, J. D. MacKenzie, R. H. Friend, *Applied Physics Letters* **2003**, *82*, 299.

[13]   N. Stutzmann, R. H. Friend, H. Sirringhaus, *Science* **2003**, *299*, 1881.

[14]   J. Z. Wang, Z. H. Zheng, H. W. Li, W. T. S. Huck, H. Sirringhaus, *Nature Materials* **2004**, *3*, 171.

[15]   M. Pope, C. E. Swenberg, *Electronic processes in organic crystals and polymers*, (Oxford University Press, New York **1999)**.

[16]   N. C. Greenham, S. C. Moratti, D. D. C. Bradley, R. H. Friend, A. B. Holmes, *Nature* **1993**, *365*, 628.

186

[17]   A. Kraft, A. C. Grimsdale, A. B. Holmes, *Angewandte Chemie-International Edition* **1998**, *37*, 402.

[18]   V. I. Arkhipov, H. Bassler, *Physica Status Solidi a-Applied Research* **2004**, *201*, 1152.

[19]   C. M. Ramsdale, N. C. Greenham, *Journal of Physics D-Applied Physics* **2003**, *36*, L29.

[20]   M. M. L. Grage, T. Pullerits, A. Ruseckas, M. Theander, O. Inganas, V. Sundstrom, *Chemical Physics Letters* **2001**, *339*, 96.

[21]   J. L. Bredas, J. C. Scott, K. Yakushi, G. B. Street, *Physical Review B* **1984**, *30*, 1023.

[22]   J. C. Scott, P. Pfluger, M. T. Krounbi, G. B. Street, *Physical Review B (Condensed Matter)* **1983**, *28*, 2140.

[23]   G. Greczynski, M. Fahlman, W. R. Salaneck, *Chemical Physics Letters* **2000**, *321*, 379.

[24]   J. L. Bredas, G. B. Street, *Accounts of Chemical Research* **1985**, *18*, 309.

[25]   J. L. Bredas, B. Themans, J. G. Fripiat, J. M. Andre, R. R. Chance, *Physical Review B* **1984**, *29*, 6761.

[26]   S. Braun, W. R. Salaneck, M. Fahlman, *Advanced Materials* **2009**, *21*, 1450.

[27]   I. H. Campbell, T. W. Hagler, D. L. Smith, J. P. Ferraris, *Physical Review Letters* **1996**, *76*, 1900.

[28]   J. L. Bredas, J. Cornil, A. J. Heeger, *Advanced Materials* **1996**, *8*, 447.

[29]   C. Tengstedt, W. Osikowicz, W. R. Salaneck, I. D. Parker, C. H. Hsu, M. Fahlman, *Applied Physics Letters* **2006**, *88*, 053502.

[30]   G. Crecelius, M. Stamm, J. Fink, J. J. Ritsko, *Physical Review Letters* **1983**, *50*, 1498.

[31]   T. C. Chung, J. H. Kaufman, A. J. Heeger, F. Wudl, *Physical Review B* **1984**, *30*, 702.

[32]   M. Wohlgenannt, X. M. Jiang, Z. V. Vardeny, R. A. J. Janssen, *Physical Review Letters* **2002**, *88*, 197401.

 [33]   A. Ioannidis, E. Forsythe, Y. L. Gao, M. W. Wu, E. M. Conwell, *Applied Physics Letters* **1998**, *72*, 3038.

[34]   E. M. Conwell, M. W. Wu, *Applied Physics Letters* **1997**, *70*, 1867.

[35]   H. Bassler, *Physica Status Solidi B-Basic Research* **1993**, *175*, 15.

[36]   Y. N. Gartstein, E. M. Conwell, *Chemical Physics Letters* **1995**, *245*, 351.

[37]   P. W. M. Blom, M. Vissenberg, *Physical Review Letters* **1998**, *80*, 3819.

[38]   M. Redecker, D. D. C. Bradley, M. Inbasekaran, W. W. Wu, E. P. Woo, *Advanced Materials* **1999**, *11*, 241.

[39]   M. Redecker, D. D. C. Bradley, M. Inbasekaran, E. P. Woo, *Applied Physics Letters* **1998**, *73*, 1565.

[40]   A. J. Campbell, D. D. C. Bradley, H. Antoniadis, *Applied Physics Letters* **2001**, *79*, 2133.

[41]   Y. Roichman, N. Tessler, *Applied Physics Letters* **2002**, *80*, 1948.

[42]   C. Tanase, E. J. Meijer, P. W. M. Blom, D. M. de Leeuw, *Physical Review Letters* **2003**, *91*, 216601.

[43]   M. Vissenberg, M. Matters, *Physical Review B* **1998**, *57*, 12964.

[44]   C. Tanase, P. W. M. Blom, D. M. de Leeuw, E. J. Meijer, *Physica Status Solidi a-Applied Research* **2004**, *201*, 1236.

[45]   R. N. Marks, J. J. M. Halls, D. D. C. Bradley, R. H. Friend, A. B. Holmes, *Journal of Physics-Condensed Matter* **1994**, *6*, 1379.

[46]   B. L. Groenendaal, F. Jonas, D. Freitag, H. Pielartzik, J. R. Reynolds, *Advanced Materials* **2000**, *12*, 481.

[47]   P. K. H. Ho, J. S. Kim, J. H. Burroughes, H. Becker, S. F. Y. Li, T. M. Brown, F. Cacialli, R. H. Friend, *Nature* **2000**, *404*, 481.

[48]   T. M. Brown, R. H. Friend, I. S. Millard, D. J. Lacey, J. H. Burroughes, F. Cacialli, *Applied Physics Letters* **2001**, *79*, 174.

[49]   P. A. Lane, J. C. deMello, R. B. Fletcher, M. Bernius, *Applied Physics Letters* **2003**, *83*, 3611.

[50]   P. A. Lane, P. J. Brewer, J. S. Huang, D. D. C. Bradley, J. C. deMello, *Physical Review B* **2006**, *74*, 125320.

 [51]   T. M. Brown, R. H. Friend, I. S. Millard, D. J. Lacey, J. H. Burroughes, F. Cacialli, *Applied Physics Letters* **2000**, *77*, 3096.

[52]   T. M. Brown, J. S. Kim, R. H. Friend, F. Cacialli, R. Daik, W. J. Feast, *Applied Physics Letters* **1999**, *75*, 1679.

[53]   J. S. Kim, R. H. Friend, F. Cacialli, *Flat-Panel Displays and Sensors: Principles, Materials and Processes* **2000**, *558*, 439.

[54]   J. S. Kim, R. H. Friend, F. Cacialli, *Applied Physics Letters* **1999**, *74*, 3084.

[55]   P. K. H. Ho, M. Granstrom, R. H. Friend, N. C. Greenham, *Advanced Materials* **1998**, *10*, 769.

[56]   I. H. Campbell, S. Rubin, T. A. Zawodzinski, J. D. Kress, R. L. Martin, D. L. Smith, N. N. Barashkov, J. P. Ferraris, *Physical Review B* **1996**, *54*, 14321.

[57]   Y. Cao, I. D. Parker, G. Yu, C. Zhang, A. J. Heeger, *Nature* **1999**, *397*, 414.

[58]   M. Wohlgenannt, K. Tandon, S. Mazumdar, S. Ramasesha, Z. V. Vardeny, *Nature* **2001**, *409*, 494.

[59]   J. S. Wilson, A. S. Dhoot, A. Seeley, M. S. Khan, A. Kohler, R. H. Friend, *Nature* **2001**, *413*, 828.

[60]   J. S. Wilson, N. Chawdhury, M. R. A. Al-Mandhary, M. Younus, M. S. Khan, P. R. Raithby, A. Kohler, R. H. Friend, *Journal of the American Chemical Society* **2001**, *123*, 9412.

[61]   F. Cacialli, R. H. Friend, N. Haylett, R. Daik, W. J. Feast, D. A. dosSantos, J. L. Bredas, *Applied Physics Letters* **1996**, *69*, 3794.

[62]   B. K. Crone, P. S. Davids, I. H. Campbell, D. L. Smith, *Journal of Applied Physics* **2000**, *87*, 1974.

[63]   J. S. Kim, P. K. H. Ho, C. E. Murphy, R. H. Friend, *Macromolecules* **2004**, *37*, 2861.

[64]   K. Murata, S. Cina, N. C. Greenham, *Applied Physics Letters* **2001**, *79*, 1193.

[65]   W. R. Salaneck, K. Seki, A. Kahn, J. Pireaux, Eds., *Conjugated Polymer and Molecular Interfaces* (Marcel Dekker, Inc., New York **2002)**.

[66]   W. R. Salaneck, S. Stafstrom, J. L. Bredas, *Conjugated Polymer Surfaces and Interfaces*, (Cambridge University Press, Cambridge, U.K. **1996)**.

[67]   N. C. Greenham, R. H. Friend, *Solid State Physics*, Vol. 49, (Academic Press, San Diego **1995)**.

[68]   J. Hwang, E. G. Kim, J. Liu, J. L. Bredas, A. Duggal, A. Kahn, *Journal of Physical Chemistry C* **2007**, *111*, 1378.

[69]   S. M. Sze, *The Physics of Semiconductor Devices* (Wiley, New York **1969)**.

[70]   R. T. Tung, *Physical Review Letters* **2000**, *84*, 6078.

[71]   H. Ishii, K. Sugiyama, E. Ito, K. Seki, *Advanced Materials* **1999**, *11*, 605.

[72]   J. C. Scott, *Journal of Vacuum Science & Technology A* **2003**, *21*, 521.

[73]   A. M. Cowley, S. M. Sze, *Journal of Applied Physics* **1965**, *36*, 3212.

[74]   H. Ishii, N. Hayashi, E. Ito, Y. Washizu, K. Sugi, Y. Kimura, M. Niwano, Y. Ouchi, K. Seki, *Physica Status Solidi a-Applied Research* **2004**, *201*, 1075.

[75]   A. Crispin, X. Crispin, M. Fahlman, M. Berggren, W. R. Salaneck, *Applied Physics Letters* **2006**, *89*, 213503.

[76]   I. D. Parker, *Journal of Applied Physics* **1994**, *75*, 1656.

[77]   I. H. Campbell, D. L. Smith, *Applied Physics Letters* **1999**, *74*, 561.

[78]   S. Barth, U. Wolf, H. Bassler, P. Muller, H. Riel, H. Vestweber, P. F. Seidler, W. Riess, *Physical Review B* **1999**, *60*, 8791.

[79]   V. I. Arkhipov, E. V. Emelianova, Y. H. Tak, H. Bassler, *Journal of Applied Physics* **1998**, *84*, 848.

[80]   U. Wolf, V. I. Arkhipov, H. Bassler, *Physical Review B* **1999**, *59*, 7507.

[81]   Y. N. Gartstein, E. M. Conwell, *Chemical Physics Letters* **1996**, *255*, 93.

[82]   J. C. Scott, G. G. Malliaras, *Chemical Physics Letters* **1999**, *299*, 115.

[83]   G. Rikken, D. Braun, E. G. J. Staring, R. Demandt, *Applied Physics Letters* **1994**, *65*, 219.

[84]   I. H. Campbell, P. S. Davids, D. L. Smith, N. N. Barashkov, J. P. Ferraris, *Applied Physics Letters* **1998**, *72*, 1863.

[85]   B. K. Crone, I. H. Campbell, P. S. Davids, D. L. Smith, *Applied Physics Letters* **1998**, *73*, 3162.

[86]   P. S. Davids, I. H. Campbell, D. L. Smith, *Journal of Applied Physics* **1997**, *82*, 6319.

[87]   L. Burgi, T. J. Richards, R. H. Friend, H. Sirringhaus, *Journal of Applied Physics* **2003**, *94*, 6129.

[88]   U. Wolf, S. Barth, H. Bassler, *Applied Physics Letters* **1999**, *75*, 2035.

[89]   F. Capasso, G. Margaritondo, *Heterojunction band discontinuities : physics and device applications* Elsevier Science Pub. Co., Amsterdam, North Holland **1987**.

[90]   J. Bardeen, *Physical Review* **1947**, *71*, 717.

[91]   M. Fahlman, D. Beljonne, M. Logdlund, R. H. Friend, A. B. Holmes, J. L. Bredas, W. R. Salaneck, *Chemical Physics Letters* **1993**, *214*, 327.

[92]   P. Dannetun, M. Fahlman, C. Fauquet, K. Kaerijama, Y. Sonoda, R. Lazzaroni, J. L. Bredas, W. R. Salaneck, *Synthetic Metals* **1994**, *67*, 133.

[93]   P. Dannetun, M. Logdlund, M. Fahlman, M. Boman, S. Stafstrom, W. R. Salaneck, R. Lazzaroni, C. Fredriksson, J. L. Bredas, S. Graham, R. H. Friend, A. B. Holmes, R. Zamboni, C. Taliani, *Synthetic Metals* **1993**, *55*, 212.

[94]   E. H. Rhoderick, R. H. Williams, *Metal-Semiconductor Contacts*, (Clarendon Press, Oxford **1988)**.

[95]   G. Wright, *Solid State Electronics* **1961**, *2*, 165.

[96]   G. H. Gelinck, H. E. A. Huitema, E. Van Veenendaal, E. Cantatore, L. Schrijnemakers, J. Van der Putten, T. C. T. Geuns, M. Beenhakkers, J. B. Giesbers, B. H. Huisman, E. J. Meijer, E. M. Benito, F. J. Touwslager, A. W. Marsman, B. J. E. Van Rens, D. M. De Leeuw, *Nature Materials* **2004**, *3*, 106.

[97]   P. A. Lane, P. J. Brewer, J. S. Huang, D. D. C. Bradley, J. C. deMello, *Physical Review B* **2006**, *74*, 125320

[98]   P. J. Brewer, P. A. Lane, J. S. Huang, A. J. DeMello, D. D. C. Bradley, J. C. DeMello, *Physical Review B* **2005**, *71*, 205209.

[99]   C. M. Heller, I. H. Campbell, *Journal of Applied Physics* **1997**, *81*, 3227.

[100]   J. Hwang, A. Wan, A. Kahn, *Materials Science & Engineering R-Reports* **2009**, *64*, 1.

[101]   W. Osikowicz, M. P. de Jong, S. Braun, C. Tengstedt, M. Fahlman, W. R. Salaneck, *Applied Physics Letters* **2006**, *88*, 193504.

[102]   M. Fahlman, A. Crispin, X. Crispin, S. K. M. Henze, M. P. de Jong, W. Osikowicz, C. Tengstedt, W. R. Salaneck, *Journal of Physics-Condensed Matter* **2007**, *19*, 183202.

[103]   W. Osikowicz, M. P. de Jong, W. R. Salaneck, *Advanced Materials* **2007**, *19*, 4213.

[104]   S. Braun, W. Osikowicz, Y. Wang, W. R. Salaneck, *Organic Electronics* **2007**, *8*, 14.

[105]   S. Braun, W. R. Salaneck, *Chemical Physics Letters* **2007**, *438*, 259.

[106]   R. J. Murdey, W. R. Salaneck, *Japanese Journal of Applied Physics Part 1-Regular Papers Short Notes & Review Papers* **2005**, *44*, 3751.

[107]   S. Rentenberger, A. Vollmer, E. Zojer, R. Schennach, N. Koch, *Journal of Applied Physics* **2006**, *100*, 053701.

[108]   N. Koch, *ChemPhysChem* **2007**, *8*, 1439.

[109]   N. Koch, A. Vollmer, A. Elschner, *Applied Physics Letters* **2007**, *90*, 043512.

[110]   W. Osikowicz, X. Crispin, C. Tengstedt, L. Lindell, T. Kugler, W. R. Salaneck, *Applied Physics Letters* **2004**, *85*, 1616.

[111]   C. Tengstedt, W. Osikowicz, W. R. Salaneck, I. D. Parker, C. H. Hsu, M. Fahlman, *Applied Physics Letters* **2006**, *88*, 053502.

[112]   L. Lindell, M. Unge, W. Osikowicz, S. Stafstrom, W. R. Salaneck, X. Crispin, M. P. de Jong, *Applied Physics Letters* **2008**, *92*, 163302.

[113]   I. N. Hulea, H. B. Brom, A. J. Houtepen, D. Vanmaekelbergh, J. J. Kelly, E. A. Meulenkamp, *Physical Review Letters* **2004**, *93*, 166601.

[114]   O. Tal, Y. Rosenwaks, Y. Preezant, N. Tessler, C. K. Chan, A. Kahn, *Physical Review Letters* **2005**, *95*, 256405.

[115]   J. S. Kim, R. H. Friend, I. Grizzi, J. H. Burroughes, *Applied Physics Letters* **2005**, *87*, 023506.

[116]   Y. J. Xia, R. H. Friend, *Advanced Materials* **2006**, *18*, 1371.

[117]   G. Greczynski, T. Kugler, W. R. Salaneck, *Journal of Applied Physics* **2000**, *88*, 7187.

[118]   A. C. Morteani, A. S. Dhoot, J. S. Kim, C. Silva, N. C. Greenham, C. Murphy, E. Moons, S. Cina, J. H. Burroughes, R. H. Friend, *Advanced Materials* **2003**, *15*, 1708.

[119]   A. C. Arias, N. Corcoran, M. Banach, R. H. Friend, J. D. MacKenzie, W. T. S. Huck, *Applied Physics Letters* **2002**, *80*, 1695.

[120]   C. M. Ramsdale, J. A. Barker, A. C. Arias, J. D. MacKenzie, R. H. Friend, N. C. Greenham, *Journal of Applied Physics* **2002**, *92*, 4266.

[121]   P. S. Davids, A. Saxena, D. L. Smith, *Journal of Applied Physics* **1995**, *78*, 4244.

[122]   I. H. Campbell, D. L. Smith, J. P. Ferraris, *Applied Physics Letters* **1995**, *66*, 3030.

[123]   I. H. Campbell, M. D. Joswick, I. D. Parker, *Applied Physics Letters* **1995**, *67*, 3171.

[124]   M. Cardona, *Modulation Spectroscopy*, (Academic, New York, **1969)**.

[125]   T. M. Brown, *PhD Thesis*, University of Cambridge, **2001**.

[126]   P. J. Brewer, P. A. Lane, A. J. deMello, D. D. C. Bradley, J. C. deMello, *Advanced Functional Materials* **2004**, *14*, 562.

[127]   P. A. Lane, J. C. de Mello, R. Fletcher, M. Bernius, *Organic Light-Emitting Materials and Devices Vii* **2004**, *5214*, 162.

[128]   M. Liess, S. Jeglinski, Z. V. Vardeny, M. Ozaki, K. Yoshino, Y. Ding, T. Barton, *Physical Review B* **1997**, *56*, 15712.

[129]   I. Hiromitsu, Y. Murakami, T. Ito, *Journal of Applied Physics* **2003**, *94*, 2434.

[130]   A. J. Cadby, P. A. Lane, H. Mellor, S. J. Martin, M. Grell, C. Giebeler, D. D. C. Bradley, M. Wohlgenannt, C. An, Z. V. Vardeny, *Physical Review B* **2000**, *62*, 15604.

[131]   L. S. Wang, J. Conceicao, C. M. Jin, R. E. Smalley, *Chemical Physics Letters* **1991**, *182*, 5.

[132]   K. Yoshino, X. H. Yin, K. Muro, S. Kiyomatsu, S. Morita, A. A. Zakhidov, T. Noguchi, T. Ohnishi, *Japanese Journal of Applied Physics Part 2-Letters* **1993**, *32*, L357.

[133]   A. Horvath, G. Weiser, G. L. Baker, S. Etemad, *Physical Review B* **1995**, *51*, 2751.

[134]   G. Weiser, A. Horvath, *Chemical Physics* **1998**, *227*, 153.

[135]   M. G. Harrison, S. Moller, G. Weiser, G. Urbasch, R. F. Mahrt, H. Bassler, U. Scherf, *Physical Review B* **1999**, *60*, 8650.

[136]   G. Weiser, *Physical Review B* **1992**, *45*, 14076.

[137]   A. Horvath, H. Bassler, G. Weiser, *Physica Status Solidi B-Basic Research* **1992**, *173*, 755.

[138]   A. Horvath, G. Weiser, C. LapersonneMeyer, M. Schott, S. Spagnoli, *Physical Review B* **1996**, *53*, 13507.

[139]   D. E. Aspnes, J. E. Rowe, *Physical Review B* **1972**, *5*, 4022.

[140]   M. Granstrom, K. Petritsch, A. C. Arias, A. Lux, M. R. Andersson, R. H. Friend, *Nature* **1998**, *395*, 257.

[141]   P. D. Prasad, D. J. Williams, *Introduction to Nonlinear Optical Effects in Molecules and Polymers* (John Wiley & Sons, New York **1991)**.

[142]   V. Bodrozic, T. M. Brown, S. Mian, D. Caruana, M. Roberts, N. Phillips, J. J. Halls, I. Grizzi, J. H. Burroughes, F. Cacialli, *Advanced Materials* **2008**, *20*, 2410.

[143]   T. M. Brown, R. H. Friend, I. S. Millard, D. J. Lacey, T. Butler, J. H. Burroughes, F. Cacialli, *Journal of Applied Physics* **2003**, *93*, 6159.

[144]   W. Y. Gao, A. Kahn, *Applied Physics Letters* **2003**, *82*, 4815.

[145]   J. C. deMello, J. J. M. Halls, S. C. Graham, N. Tessler, R. H. Friend, *Physical Review Letters* **2000**, *85*, 421.

[146]   C. Giebeler, S. A. Whitelegg, D. G. Lidzey, P. A. Lane, D. D. C. Bradley, *Applied Physics Letters* **1999**, *75*, 2144.

[147]   H. J. Snaith, A. C. Arias, A. C. Morteani, C. Silva, R. H. Friend, *Nano Letters* **2002**, *2*, 1353.

[148]   C. Lungenschmied, G. Dennler, H. Neugebauer, N. S. Sariciftci, E. Ehrenfreund, *Applied Physics Letters* **2006**, *89*, 223519.

[149]   D. Poplavskyy, J. Nelson, D. D. C. Bradley, *Applied Physics Letters* **2003**, *83*, 707.

[150]   T. van Woudenbergh, P. W. M. Blom, J. N. Huiberts, *Applied Physics Letters* **2003**, *82*, 985.

[151]   Newport_Corporation, in *Newport Resource Catalogue* **2007**, 1191.

[152]   B. W. D'Andrade, S. R. Forrest, *Advanced Materials* **2004**, *16*, 1585.

[153]   OPT301 Integrated Photodiode and Amplifier, Technical Data Sheet, Burr-Brown Corporation, United States **1994**.

[154]   V. Bodrozic, M. Roberts, N. Phillips, J. H. Burroughes, S. Mian, F. Cacialli, *Journal of Applied Physics* **2007**, *101*, 84507.

[155]   M. Zhou, L.-L. Chua, R.-Q. Png, C.-K. Yong, S. Sivaramakrishnan, P.-J. Chia, A. T. S. Wee, R. H. Friend, P. K. H. Ho, *Physical Review Letters* **2009**, *103*, 036601.

[156]   G. Greczynski, M. Fahlman, W. R. Salaneck, *Journal of Chemical Physics* **2000**, *113*, 2407.

[157]   Q. B. Pei, G. Yu, C. Zhang, Y. Yang, A. J. Heeger, *Science* **1995**, *269*, 1086.

[158]   J. S. Kim, P. K. H. Ho, C. E. Murphy, N. Baynes, R. H. Friend, *Advanced Materials* **2002**, *14*, 206.

[159]   J. S. Kim, P. K. H. Ho, C. E. Murphy, A. Seeley, I. Grizzi, J. H. Burroughes, R. H. Friend, *Chemical Physics Letters* **2004**, *386*, 2.

[160]   B. H. Cumpston, I. D. Parker, K. F. Jensen, *Journal of Applied Physics* **1997**, *81*, 3716.

[161]   I. Hiromitsu, G. Kinugawa, *Synthetic Metals* **2005**, *153*, 73.

[162]   P. A. Lane, J. Rostalski, C. Giebeler, S. J. Martin, D. D. C. Bradley, D. Meissner, *Solar Energy Materials and Solar Cells* **2000**, *63*, 3.

[163]   P. A. Lane, C. Giebeler, S. A. Whitelegg, S. J. Martin, A. Campbell, J. Rostalski, D. Meissner, D. D. C. Bradley, *Organic Photonic Materials and Devices Ii* **2000**, *3939*, 144.

[164]   I. D. Parker, Y. Cao, C. Y. Yang, *Journal of Applied Physics* **1999**, *85*, 2441.

[165]   A. C. Arias, J. D. MacKenzie, R. Stevenson, J. J. M. Halls, M. Inbasekaran, E. P. Woo, D. Richards, R. H. Friend, *Macromolecules* **2001**, *34*, 6005.

[166]   J. S. Kim, M. Granstrom, R. H. Friend, N. Johansson, W. R. Salaneck, R. Daik, W. J. Feast, F. Cacialli, *Journal of Applied Physics* **1998**, *84*, 6859.

[167]   Z. Xu, L. M. Chen, M. H. Chen, G. Li, Y. Yang, *Applied Physics Letters* **2009**, *95*, 013301.

[168]   P. J. Brewer, J. Huang, P. A. Lane, A. J. deMello, D. D. C. Bradley, J. C. deMello, *Physical Review B* **2006**, 74, 115202.

[169]   N. Koch, A. Elschner, R. L. Johnson, J. P. Rabe, *Applied Surface Science* **2005**, *244*, 593.

[170]   N. Koch, A. Kahn, J. Ghijsen, J. J. Pireaux, J. Schwartz, R. L. Johnson, A. Elschner, *Applied Physics Letters* **2003**, *82*, 70.

[171]   H. J. Bolink, E. Coronado, D. Repetto, M. Sessolo, *Applied Physics Letters* **2007**, *91*, 223501.

[172]   K. Morii, T. Kawase, S. Inoue, *Applied Physics Letters* **2008**, *92*, 213304.

[173]   L. S. Liao, L. F. Cheng, M. K. Fung, C. S. Lee, S. T. Lee, M. Inbasekaran, E. P. Woo, W. W. Wu, *Physical Review B* **2000**, *62*, 10004.

[174]   W. R. Salaneck, J. L. Bredas, *Advanced Materials* **1996**, *8*, 48.

[175]   G. Greczynski, M. Fahlman, W. R. Salaneck, N. Johansson, D. A. dos Santos, A. Dkhissi, J. L. Bredas, *Journal of Chemical Physics* **2002**, *116*, 1700.

[176]   M. K. Fung, S. L. Lai, S. W. Tong, S. N. Bao, C. S. Lee, W. W. Wu, M. Inbasekaran, J. J. O'Brien, S. T. Lee, *Journal of Applied Physics* **2003**, *94*, 5763.

[177]   M. K. Fung, S. L. Lai, S. N. Bao, C. S. Lee, J. J. O'Briein, M. Inbasekaran, W. W. Wu, S. T. Lee, *Synthetic Metals* **2002**, *128*, 97.

[178]   L. S. Liao, L. F. Cheng, M. K. Fung, C. S. Lee, S. T. Lee, M. Inbasekaran, E. P. Woo, W. W. Wu, *Chemical Physics Letters* **2000**, *325*, 405.

[179]   Y. Park, V. Choong, E. Ettedgui, Y. Gao, B. R. Hsieh, T. Wehrmeister, K. Mu¨llen, *Applied Physics Letters* **1996**, *69*, 1080.

[180]   Y. Park, V. E. Choong, B. R. Hsieh, C. W. Tang, Y. Gao, *Physical Review Letters* **1997**, *78*, 3955.

[181]   M. Stoessel, G. Wittmann, J. Staudigel, F. Steuber, J. Blassing, W. Roth, H. Klausmann, W. Rogler, J. Simmerer, A. Winnacker, M. Inbasekaran, E. P. Woo, *Journal of Applied Physics* **2000**, *87*, 4467.

[182]   J. Hwang, A. Wan, A. Kahn, *Materials Science & Engineering R-Reports* **2009**, *64*, 1.

[183]   J. Y. Hwang, A. Kahn, *Organic Light Emitting Materials and Devices X* **2006**, *6333*, 33310.

[184]   K. Seki, N. Hayashi, H. Oji, E. Ito, Y. Ouchi, H. Ishii, *Thin Solid Films* **2001**, *393*, 298.

[185]   G. Greczynski, T. Kugler, W. R. Salaneck, *Journal of Applied Physics* **2000**, *88*, 06801.

[186]   S. F. Alvarado, P. F. Seidler, D. G. Lidzey, D. D. C. Bradley, *Physical Review Letters* **1998**, *81*, 1082.

[187]   S. Janietz, D. D. C. Bradley, M. Grell, C. Giebeler, M. Inbasekaran, E. P. Woo, *Applied Physics Letters* **1998**, *73*, 2453.

[188]   J. C. Sancho-Garcia, C. L. Foden, I. Grizzi, G. Greczynski, M. P. de Jong, W. R. Salaneck, J. L. Bredas, J. Cornil, *Journal of Physical Chemistry B* **2004**, *108*, 5594.

[189]   R. Lazzaroni, J. L. Bredas, P. Dannetun, C. Fredriksson, S. Stafstrom, W. R. Salaneck, *Electrochimica Acta* **1994**, *39*, 235.

[190]   P. Dannetun, M. Logdlund, C. Fredriksson, R. Lazzaroni, C. Fauquet, S. Stafstrom, C. W. Spangler, J. L. Bredas, W. R. Salaneck, *Journal of Chemical Physics* **1994**, *100*, 6765.

[191]   Y. Gao, K. T. Park, B. R. Hsieh, *Journal of Chemical Physics* **1992**, *97*, 6991.

[192]   P. Broms, J. Birgersson, N. Johansson, M. Logdlund, W. R. Salaneck, *Synthetic Metals* **1995**, *74*, 179.

[193]   V. Choong, Y. Park, Y. Gao, T. Wehrmeister, K. Mullen, B. R. Hsieh, C. W. Tang, *Applied Physics Letters* **1996**, *69*, 1492.

[194]   P. J. Brewer, A. J. deMello, J. C. deMello, P. A. Lane, D. D. C. Bradley, R. Fletcher, J. O. Brien, *Journal of Applied Physics* **2006**, *99*, 114502.

[195]   V. Heine, C. H. Hodges, *Journal of Physics C: Solid State Physics* **1972**, *5*, 225.

[196]   *Handbook of Chemistry and Physics 75th Edition*, Chemical Rubber Company, Boca Raton **1994**.

[197]   Y. Park, V. Choong, E. Ettedgui, Y. Gao, B. R. Hsieh, T. Wehrmeister, K. Mullen, *Applied Physics Letters* **1996**, *69*, 1080.

[198] N. D. Lang, W. Kohn, *Physical Review B* **1971**, *3*, 1215.

[199] N. D. Lang, W. Kohn, *Physical Review B* **1973**, *7*, 3541.

[200] Mi Zhou, Lay-lay Chua, P. K. H. Ho, *private communication*

[201] Mi Zhou, Sankaran Sivaramakrishnan, Lay-lay Chua, P. K. H. Ho., *Private communication*.

[202] G. Greczynski, T. Kugler, M. Keil, W. Osikowicz, M. Fahlman, W. R. Salaneck, *Journal of Electron Spectroscopy and Related Phenomena* **2001**, *121*, 1.

[203] Y. Vaynzof, T. J. Dennes, J. Schwartz, A. Kahn, *Applied Physics Letters* **2008**, *93*, 103305.

[204] R. I. R. Blyth, S. A. Sardar, F. P. Netzer, M. G. Ramsey, *Applied Physics Letters* **2000**, *77*, 1212.

[205] M. W. Roberts, B. R. Wells, *Surface Science* **1967**, *8*, 453.

[206] J. Hwang, A. Wan, A. Kahn, *Materials Science & Engineering R-Reports* **2009**, *64*, 1.

[207] A. J. Campbell, D. D. C. Bradley, H. Antoniadis, *Journal of Applied Physics* **2001**, *89*, 3343.

[208] J. Cornil, I. Gueli, A. Dkhissi, J. C. Sancho-Garcia, E. Hennebicq, J. P. Calbert, V. Lemaur, D. Beljonne, J. L. Bredas, *Journal of Chemical Physics* **2003**, *118*, 6615.

[209] L. L. Chua, J. Zaumseil, J. F. Chang, E. C. W. Ou, P. K. H. Ho, H. Sirringhaus, R. H. Friend, *Nature* **2005**, *434*, 194.

[210] R. B. Fletcher, *PhD Thesis*, University of Sheffield **2000**.

[211] M. A. Stevens, C. Silva, D. M. Russell, R. H. Friend, *Physical Review B* **2001**, *63*, 165213.

[212] Y. F. Li, Y. Cao, J. Gao, D. L. Wang, G. Yu, A. J. Heeger, *Synthetic Metals* **1999**, *99*, 243.

[213] A. Wan, J. Hwang, F. Amy, A. Kahn, *Organic Electronics* **2005**, *6*, 47.

[214] H. Peisert, M. Knupfer, J. Fink, *Applied Physics Letters* **2002**, *81*, 2400.

[215] D. Kabra, M. H. Song, B. Wenger, R. H. Friend, H. J. Snaith, *Advanced Materials* **2008**, *20*, 3447.

[216] R. Jin, P. A. Levermore, J. S. Huang, X. H. Wang, D. D. C. Bradley, J. C. Demello, *Physical Chemistry Chemical Physics* **2009**, *11*, 3455.

[217]   G. Fichet, N. Corcoran, P. K. H. Ho, A. C. Arias, J. D. MacKenzie, W. T. S. Huck, R. H. Friend, *Advanced Materials* **2004**, *16*, 1908.

[218]   A. C. Morteani, P. Sreearunothai, L. M. Herz, R. H. Friend, C. Silva, *Physical Review Letters* **2004**, *92*, 247402.

[219]   S. Sivaramakrishnan, M. Zhou, A. C. Kumar, Z. L. Chen, R. Q. Png, L. L. Chua, P. K. H. Ho, *Applied Physics Letters* **2009**, *95*, 213303.

[220]   D. Kabra, L. Lu, M. H. Song, H. J. Snaith, R. H. Friend, *Advanced Materials*, *In press*.

[221]   C. R. McNeill, B. Watts, L. Thomsen, W. J. Belcher, N. C. Greenham, P. C. Dastoor, *Nano Letters* **2006**, *6*, 1202.

[222]   L. H. Slooff, A. Polman, F. Cacialli, R. H. Friend, G. A. Hebbink, F. van Veggel, D. N. Reinhoudt, *Applied Physics Letters* **2001**, *78*, 2122.

[223]   A. C. Morteani, P. K. H. Ho, R. H. Friend, C. Silva, *Applied Physics Letters* **2005**, *86*, 163501.

[224]   C. Yin, B. Pieper, B. Stiller, T. Kietzke, D. Neher, *Applied Physics Letters* **2007**, *90*, 133502.

[225]   S. Westenhoff, I. A. Howard, R. H. Friend, *Physical Review Letters* **2008**, *101*, 016102.

[226]   S. Westenhoff, I. A. Howard, J. M. Hodgkiss, K. R. Kirov, H. A. Bronstein, C. K. Williams, N. C. Greenham, R. H. Friend, *Journal of the American Chemical Society* **2008**, *130*, 13653.

[227]   M. Yokoyama, Y. Endo, A. Matsubara, H. Mikawa, *Journal of Chemical Physics* **1981**, *75*, 3006.

[228]   C. L. Donley, J. Zaumseil, J. W. Andreasen, M. M. Nielsen, H. Sirringhaus, R. H. Friend, J. S. Kim, *Journal of the American Chemical Society* **2005**, *127*, 12890.

[229]   Y. Gao, K. T. Park, B. R. Hsieh, *Journal of Applied Physics* **1993**, *73*, 7894.

[230]   P. Dannetun, M. Boman, S. Stafstrom, W. R. Salaneck, R. Lazzaroni, C. Fredriksson, J. L. Bredas, R. Zamboni, C. Taliani, *Journal of Chemical Physics* **1993**, *99*, 664.

[231]   R. Lazzaroni, M. Logdlund, A. Calderone, J. L. Bredas, P. Dannetun, C. Fauquet, C. Fredriksson, S. Stafstrom, W. R. Salaneck, *Synthetic Metals* **1995**, *71*, 2159.

[232]   E. Ettedgui, B. R. Hsieh, Y. Gao, *Polymers for Advanced Technologies* **1997**, *8*, 408.

[233]   D. W. Lee, K. Kim, J. I. Jin, Y. Park, *Synthetic Metals* **2004**, *143*, 181.

[234]   E. Ettedgui, H. Razafitrimo, Y. Gao, B. R. Hsieh, *Applied Physics Letters* **1995**, *67*, 2705.

[235]   H. J. Bolink, E. Coronado, D. Repetto, M. Sessolo, E. M. Barea, J. Bisquert, G. Garcia-Belmonte, J. Prochazka, L. Kavan, *Advanced Functional Materials* **2008**, *18*, 145.

[236]   K. Walzer, B. Maennig, M. Pfeiffer, K. Leo, *Chemical Reviews* **2007**, *107*, 1233.

[237]   M. Kroger, S. Hamwi, J. Meyer, T. Riedl, W. Kowalsky, A. Kahn, *Organic Electronics* **2009**, *10*, 932.

[238]   Y. Nakayama, K. Morii, Y. Suzuki, H. Machida, S. Kera, N. Ueno, H. Kitagawa, Y. Noguchi, H. Ishii, *Advanced Functional Materials* **2009**, *19*, 3746.

[239]   M. H. Song, D. Kabra, B. Wenger, R. H. Friend, H. J. Snaith, *Advanced Functional Materials* **2009**, *19*, 2130.

[240]   E. Tutis, D. Berner, L. Zuppiroli, *Journal of Applied Physics* **2003**, *93*, 4594.

APPENDIX